SLAC-382
UC-414
(T/E)

Search for Doubly Cabibbo Suppressed Decays Of The Charged *D* Meson*

Jonathan Freeman Labs

Stanford Linear Accelerator Center
Stanford University, Stanford, CA 94309

March 1992

Prepared for the Department of Energy
under contract number DE-AC03-76SF00515

Printed in the United States of America. Available from the National Technical Information Service, U.S. Department of Commerce, 5285 Port Royal Road, Springfield, Virginia 22161.

*Ph.D. Thesis

Abstract

The doubly Cabibbo suppressed decays $D^+ \to K^+\pi^-\pi^+$, $D^+ \to K^+\pi^0$ and $D^+ \to K^{*+}\pi^0$ are searched for in a 9.56 pb^{-1} data sample of e^+e^- annihilation events collected near the $\psi(3770)$ resonance with the Mark III detector at the SPEAR storage ring, at the Stanford Linear Accelerator Center. These rare weak decays are naively expected at a rate of $\tan^4\theta_c$ ($\cong 3\times10^{-3}$) relative to corresponding Cabibbo allowed decays. In the context of presently accepted models of hadronic weak decays, however, they are anticipated to be enhanced, making their experimental detection feasible in the Mark III data set.

The experimentally simplest decay channel $D^+ \to K^+\pi^-\pi^+$ is searched for inclusively through conventional analysis techniques. A signal of approximately 2.5σ significance is obtained. An independent analysis is performed to establish examples of this decay and of $D^+ \to K^+\pi^0$ and $K^{*+}\pi^0$ by full reconstruction of D^+D^- events. Exploiting the two body kinematics of $\psi(3770) \to D\overline{D}$, this second approach obtains significantly smaller backgrounds than the inclusive study. Consistent with the inclusive results, three $D^+ \to K^+\pi^-\pi^+$ candidate events are observed with an expected background of $1.2^{+0.4}_{-0.2}\pm0.4$ events. No events are observed for either $D^+ \to K^+\pi^0$ or $K^{*+}\pi^0$.

The branching fraction for $D^+ \to K^+\pi^-\pi^+$ is measured, and limits are established on the branching fractions for $D^+ \to K^+\pi^0$ and $K^{*+}\pi^0$. These results are used to confront the theoretical predictions from models of the weak hadronic decays of charmed mesons.

Acknowledgments

This work is the culmination of five and a half years of education at Stanford University and in the Mark III and SLD collaborations at the Stanford Linear Accelerator Center. It is difficult to give proper recognition to all who have in some way contributed to my education and thesis. I apologize upfront to those deserved people I have overlooked in these acknowledgments.

Foremost, I want to thank my advisor, Rafe Schindler, for his guidance, encouragement and attention to detail over the years. I greatly appreciate the many opportunities he has provided for developing my skills. It was a unique experience to have been his first graduate student.

I have enjoyed working with my Mark III collaborators Tom Browder, Dave Coward, Gerald Eigen, Gary Gladding, Joe Izen, Peter Kim, Bill Lockman, Usha Mallik, Dale Pitman, Ian Stockdale, Walter Toki, Bill Wisniewski, and especially fellow graduate students G. Dubois, Fritz DeJongh, Tim Freeze, Chris Matthews, Bijan Nemati, Larry Parrish, and Steve Wasserbaech. I thank them and many others for allowing me to join and work in the collaboration.

Karen Heidenreich and Ramon Berger deserve special credit for maintaining the Mark III software and data, even after the Mark III group (Group D) at SLAC had been terminated. It would not have been possible to complete this thesis without their support.

I have also greatly benefited from work with fellow SLD collaborators Iris Abt, Jack Hoeflich, Allan Honma, Mike Huffer, J. J. Russell, and Eric Vella. I have especially enjoyed the camaraderie over the last few years with my fellow SLD office mates Tom Junk, Homer Neal and Pablo Saez.

I also value the friendships with my fellow graduate students at Stanford, especially Rob Elia, Bob Jacobsen, Dale Koetke, Adrian Lee, and Brian Sterling.

I wish to thank my friends Mark Hamilton, John Renner and Tom Steele for convincing me to use the Macintosh and for supporting me with software and special fonts. They have made the writing painless.

I especially want to thank my parents, Linford and Eleanor Labs, for their freedom and support in the pursuit of my goals in high energy physics.

Most significantly, I want to thank Peter Kuykendall for his encouragement, support and generous assistance over the years, especially in completing this thesis.

Table of Contents

Chapter 3

Chapter 4

Chapter 5

Chapter 7

Chapter 8

Appendix 1

Appendix 2

Appendix 3

List of Tables

List of Figures

Chapter 1

Introduction

Since their discovery in 1976, much data and knowledge has been gathered on the weak decays of the charmed pseudoscalar mesons, D^0 and D^+. One phenomena of these particles--a difference in their lifetimes--initially came as a surprise in light of the naive model first used to describe their decays; the D^+ exists approximately 2.5$\times$ longer than the D^0, when it was expected that their lifetimes should be the same. It is now widely believed that this lifetime difference is a result of interference effects which are occurring in the D^+ decays at the quark level and which are causing a suppression in the overall D^+ decay rate.

The picture of charmed weak decays, however, is far from complete. One of the difficulties and challenges of studying charmed meson decays is the fact that these weak processes occur in a region where the strong interaction effects, as described by Quantum Chromodynamics, is largely nonperturbative. Several models therefore have been introduced to describe these decays, and they have been tested and modified by measured production rates of exclusive D decay channels. Some of the more widely accepted models account for the effects of interference in the D^+ decays, and further understanding and improvement lie both in studying other decay channels and in improving the experimental precision.

Although the experimental precision cannot be improved with the Mark III experiment, other decay channels can be studied. This thesis describes searches for a particular class of D decays, the doubly Cabibbo suppressed decays. Direct evidence for the interference effect currently comes from the measured production rates of only a couple D^+ decay

channels, and the D^+ doubly Cabibbo suppressed decays can provide an additional probe in the effect.

This thesis is broken down as follows. Chapter 2 provides a theoretical overview of charmed weak decays and expands on the motivation for studying the doubly Cabibbo suppressed decays of the D^+ meson. Chapter 3 discusses the Mark III detector and the initial processing done on the data collected with the detector. Chapters 4 through 7 discuss the various searches for D^+ doubly Cabibbo suppressed decays and include discussions of the efficiency estimates, the extensive background studies, and the resulting measurements or limit calculations on the branching fractions. Finally, Chapter 8 provides a summary of the analyses and discusses conclusions.

Chapter 2

Theory and Motivation for Analysis

2-1 Introduction to Charm

In 1964 Bjorken and Glashow proposed a model to extend the $SU(3)$ flavor symmetry of the up, down and strange quantum numbers to an $SU(4)$ flavor symmetry, introducing a fourth flavor--charm![1] Among its achievements, the model presented a symmetry between leptons and hadrons. A few years later, Weinberg and Salam developed an $SU(2) \otimes U(1)$ gauge theory which unified the electromagnetic and weak interactions of leptons![2] To extend this model to the quarks, Glashow, Iliopoulos and Maiani again found a fourth flavor was required![3] Their model, now referred to as the GIM mechanism, explains the K^0-$\overline{K}^0$ mass difference and the suppression of strangeness changing neutral current processes such as $K_L^0 \rightarrow \mu^+\mu^-$.

Finally, in 1974 the J/ψ resonance was discovered at SLAC![4] and Brookhaven![5] providing experimental evidence for the existence of charm. The J/ψ is considered to be a $J^{PC} = 1^{--}$ bound state of a charm quark and anticharm quark. The discovery of the next charmonium resonance, the $\psi(3685)$, followed shortly thereafter![6]

In 1976 the charmed D^0 and D^+ mesons were discovered at SPEAR by the SLAC-LBL collaboration![7] The D_s^+ (formerly the F^+) was conclusively found by CLEO in 1983;[8] completing the $SU(3)$ flavor triplet of charmed pseudoscalar states. Table 2.1 lists some fundamental properties of these mesons.

Much progress has been made over the past ten years in understanding charm weak decays. However, as will be discussed below, several issues and problems remain to be resolved. The balance of this chapter is divided into two parts: Section 2-2 reviews

Table 2.1 D meson properties.

Meson	C	S	I	I_3	J	P	Mass (MeV/c^2)	Lifetime (ps)
D^0	1	0	1/2	−1/2	0	−1	1864.5±0.5	0.421±0.010
D^+	1	0	1/2	1/2	0	−1	1869.3±0.4	1.062±0.028
D_s^+	1	1	0	0	0	−1	1968.8±0.7	$0.445^{+0.035}_{-0.029}$

some of the current issues and theories behind charm weak decays, and Section 2-3, in light of the theory discussion, motivates the analysis pursued for this thesis.

2-2 Theory

2-2.1 The Standard Model of Electroweak Interactions

The Weinberg-Salam model has evolved to what is known today as the Standard Model of Electroweak interactions. In its current form, it has succeeded at explaining and predicting a wide variety of phenomenon in particle physics, such as nuclear beta decay, neutrino scattering, and W and Z physics.

The model is based on a local $SU(2) \otimes U(1)$ gauge theory, where the six quarks--u(up), d(down), s(strange), c(charm), b(bottom) and t(top)--and the six leptons--e(electron), ν_e(electron neutrino), μ(muon), ν_μ(muon neutrino), τ(tau) and ν_τ(tau neutrino)-are considered to be the fundamental constituents of matter. Their interactions are mediated by four vector gauge bosons, the $W^\pm$, Z^0 and γ, which correspond to the 3 + 1 generators of $SU(2) \otimes U(1)$. The $W^\pm$ and Z^0 mediate the weak interactions while the γ mediates the electromagnetic. Quarks and leptons are spin 1/2 particles referred to as fermions and are represented the theory by spinor fields or spinors. The symmetry properties of the spinors depend upon their helicity; left-handed fields transform as weak isospin doublets of $SU(2)$:

$$\begin{bmatrix} u \\ d' \end{bmatrix}_L \qquad \begin{bmatrix} c \\ s' \end{bmatrix}_L \qquad \begin{bmatrix} t \\ b' \end{bmatrix}_L$$

$$\begin{bmatrix} e \\ \nu_e \end{bmatrix}_L \qquad \begin{bmatrix} \mu \\ \nu_\mu \end{bmatrix}_L \qquad \begin{bmatrix} \tau \\ \nu_\tau \end{bmatrix}_L$$

while right-handed fields transform as isospin singlets:

$$u_R, d_R \qquad c_R, s_R \qquad t_R, b_R$$

$$e_R \qquad \mu_R \qquad \tau_R$$

Neutrinos have been assumed to have no mass and therefore no right-handed components.

The isospin doublets illustrate the quark-lepton symmetry in the Standard Model; quark and lepton doublets pair-off to form a family or generation. Currently only three generations have been observed, and recent Z^0 width measurements[9] strongly suggest that only three generations do exist, in the absence of massive neutrinos.

The d', s' and b' spinors are weak eigenstates which mix to form the mass eigenstates d, s and b, via the Cabibbo-Kobayashi-Maskawa (CKM) matrix:

$$\begin{bmatrix} d' \\ s' \\ b' \end{bmatrix} = \begin{bmatrix} V_{ud} & V_{us} & V_{ub} \\ V_{cd} & V_{cs} & V_{cb} \\ V_{td} & V_{cs} & V_{tb} \end{bmatrix} \begin{bmatrix} d \\ s \\ b \end{bmatrix}$$

Several of the CKM matrix elements have been measured experimentally[10]: $|V_{ud}|$ from nuclear beta decay; $|V_{us}|$ from $Ke3$ and semileptonic hyperon decays; $|V_{cd}|$ from $\nu_\mu d \rightarrow \mu^- c$, charmed particle production by neutrinos, and semileptonic D decays; $|V_{cs}|$ from $D \rightarrow Ke\nu$ decays; $|V_{ub}|/|V_{cb}|$ from the leptonic energy spectrum in semileptonic B decays; and $|V_{cb}|$ from $B \rightarrow Dl\nu_l$ decays. Assuming only three generations of quark flavors and imposing unitarity constraints, the 90% confidence intervals on all matrix element magnitudes are obtained[11]:

$$\begin{bmatrix} 0.9747-0.9759 & 0.218-0.224 & 0.001-0.007 \\ 0.218-0.224 & 0.9734-0.9752 & 0.030-0.058 \\ 0.003-0.019 & 0.029-0.058 & 0.9983-0.9996 \end{bmatrix}$$

The small values for the off-diagonal terms show that the mixing is small. In the limit of no mixing with the third generation, the CKM matrix reduces to the original Cabibbo matrix for four flavors:

$$\begin{bmatrix} d' \\ s' \end{bmatrix} = \begin{bmatrix} \cos\theta_c & \sin\theta_c \\ -\sin\theta_c & \cos\theta_c \end{bmatrix} \begin{bmatrix} d \\ s \end{bmatrix}$$

This representation is still used in the discussion of charm physics; decays which occur through the transition $c \rightarrow sW^+$ are labelled *Cabibbo allowed*, while those which occur through $c \rightarrow dW^+$ are termed *Cabibbo suppressed.*

According to the Standard Model, charm and the other quarks decay weakly through charged current interactions, described by the Lagrangian

$$L_{cc} = -\frac{g}{2\sqrt{2}} \sum_i \bar{\chi}_L^{(i)} (T^+ W^- + T^- W^+) \chi_L^{(i)}$$

where g is the weak coupling constant, $\chi_L^{(i)}$ is the left-handed doublet for the ith quark or lepton family, T^+ and T^- are the raising and lowering operators of weak isospin and $W^\pm$ are the vector boson fields.

2-2.2 Quantum Chromodynamics

The Standard Model picture of quark decays is relatively simple. However, no quarks have been observed free; they are all bound within hadronic states. The study of the weak decays of heavy flavor quarks, therefore, necessarily includes the study of strong interactions among two or more quarks, which are described by the theory of Quantum Chromodynamics (QCD).

Quantum Chromodynamics is a local gauge theory based on $SU(3)$ symmetry. Analogous to the electric charge in QED, quarks in QCD carry one of three possible "color charges", which are often designated in the literature as r (red), g (green) and b (blue). The three color charges together form an $SU(3)$ color triplet. Color interactions are mediated by gluons, the gauge bosons of the local gauge theory. Eight different gluons correspond to the eight generators of $SU(3)$ and form a color octet. The non-Abelian nature of $SU(3)$ allows gluons to carry color, and consequently gluons can interact not only with quarks but with other gluons.

The gluon self-interaction leads to a QCD effective coupling constant, $\alpha_s(Q^2)$, which decreases with increasing momentum transfer or decreasing interaction distances. This property of *asymptotic freedom* is illustrated by the one loop approximation for $\alpha_s(Q^2)$:

$$\alpha_s(Q^2) = \frac{12\pi}{(33-2n_f)\ln(Q^2/\Lambda^2_{QCD})}$$

where n_f refers to the number of flavors that exist below the Q^2 value and Λ^2_{QCD} is a cut-off constant, determined experimentally to be about 200 MeV. For $Q^2 >> \Lambda^2_{QCD}$, QCD can be applied perturbatively, and conversely, for $Q^2 \sim \Lambda^2_{QCD}$, QCD is nonperturbative.

At the charm mass scale, $\alpha_s \sim 0.3$,[12] and hadronization has been found to play an important role in weak hadronic charm decays. This has made charmed meson decays difficult to fully understand but at the same time interesting in that they are a unique laboratory in which to study the interface between the perturbative and non-perturbative QCD regimes.

2-2.3 The Spectator Model and Its Experimental Confrontation

Charmed meson decays can occur through four types of processes: external W-emission, internal W-emission, W-exchange and W-annihilation. All four processes are illustrated in Figure 2.1. Processes involving the so-called "penguin" diagrams can also

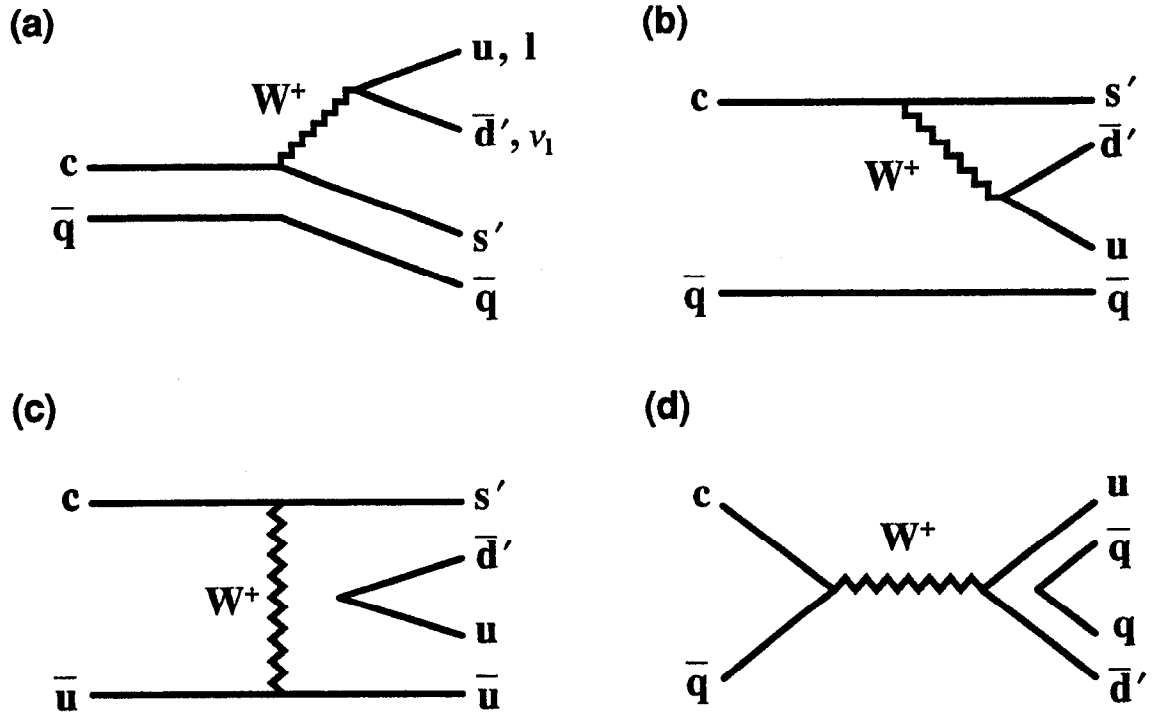

Figure 2.1 Charm weak decay processes: (a) external *W*-emission, (b) internal *W*-emission, (c) *W*-exchange (D^0 only) and (d) *W*-annihilation (D^+ and D_s^+ only).

occur but are highly suppressed because the transitions involve the CKM matrix element V_{ub}[13]; they will not be discussed further here. The dominant process was initially believed to be external *W*-emission; internal *W*-emission involves color matching between the quark lines to form color singlet states, while *W*-exchange and *W*-annihilation are "helicity suppressed" at the light quark-*W* vertex. The extent to which these latter processes are suppressed is not easily determined due to the influence of strong interaction effects. Considering only the first process and ignoring strong interaction effects, one obtains the so-called Spectator Model, where the properties of charmed mesons are assumed to be determined by the decay of the charm quark alone, and the light valence quark remains a spectator.

Although the Spectator Model is a naive picture, it is able to obtain the correct order of magnitude for the D meson lifetimes; scaling the expression for the muon lifetime to the c quark mass:

$$\tau_{D^0} = \tau_{D^+} = \tau_{D_s^+} = 5\frac{G_F^2 m_c^5}{192\pi^3} = \sim 9\times10^{-13}\,\text{sec}$$

compared with the experimentally established lifetimes[11]:

$$\tau_{D^0} = (4.21\pm0.10)\times10^{-13}\ \text{sec}$$

$$\tau_{D^+} = (10.62\pm0.28)\times10^{-13}\ \text{sec}$$

$$\tau_{D_s^+} = (4.45^{+0.35}_{-0.29})\times10^{-13}\ \text{sec}$$

Immediately, however, one sees the failure of the Spectator Model in predicting the pattern of differing lifetimes: $\tau_{D^+} \approx 2.5\times\tau_{D^0},\ \tau_{D_s^+}$. This discrepancy has been the focus of much study of the nonleptonic decays over the past ten years.

Some insight into the lifetime difference is obtained by examining the semileptonic branching fractions of the charmed mesons. Given

$$B(D^0 \to e^+X) = (7.7\pm1.2)\%\text{[11]}$$

$$B(D^+ \to e^+X) = (19.2^{+1.7}_{-1.4})\%\text{[11]}$$

$$B(D_s^+ \to e^+X) = (5.0\pm5.0\pm2.0)\%\text{[14]}$$

and $\Gamma^{sl} = (\Gamma^{sl}/\Gamma_D)\times\Gamma_D = B(D \to e^+X)/\tau_D$, then

$$\Gamma_{D^0}^{sl} = (1.83\pm0.29)\times10^{13}\ \text{sec}^{-1}$$

$$\Gamma_{D^+}^{sl} = (1.81^{+0.17}_{-0.14})\times10^{13}\ \text{sec}^{-1}$$

$$\Gamma_{D_s^+}^{sl} = (1.1\pm1.2)\times10^{13}\ \text{sec}^{-1}$$

The semileptonic partial widths are consistent with being equal, as the Spectator Model would predict, since there is no QCD influence to the semileptonic decay transition.

Therefore the lifetime difference must come from differences in the nonleptonic widths, wherein QCD can play an important role.

2-2.4 Nonleptonic Quark Decay Processes

The pattern of lifetime differences observed--$\tau_{D^0} \approx \tau_{D_s^+} \ll \tau_{D^+}$--may arise from either an enhancement of the D^0 and D_s^+ nonleptonic widths, a suppression of the D^+ nonleptonic width, or some combination of the two. Two processes have been suggested to induce these effects: quark annihilation and destructive interference of the decay amplitudes.

Quark annihilation involves the non-spectator processes *W*-exchange and *W*-annihilation. These decay mechanisms are "helicity suppressed" at the tree level, i. e. in the limit of massless quarks, the weak interaction will not couple to a J = 0 $c\bar{q}$ state wherein both the c and $\bar{q}$ must either be left- or right-handed. This suppression can be lifted when other partons, e.g. gluons, are present, placing the valence quarks into a non-zero relative spin state. The *W*-exchange diagram for the D^0 and the *W*-annihilation diagrams for the D^+ and D_s^+ are shown in Figure 2.2. Since *W*-annihilation is Cabibbo suppressed for the D^+, these processes would increase largely only the D^0 and D_s^+ hadronic partial widths. The decay $D^0 \rightarrow \bar{K}^0\phi$ was suggested[15] to be a clear signature for D^0 *W*-exchange, and has been observed with a significant branching fraction of approximately 1 %![16] Complicating the issue, however, is the possibility that this final state can be produced via one of the larger spectator decay modes, e. g. $D^0 \rightarrow K^-\rho^+$†, with *final state interactions*;[17][18] as illustrated in Figure 2.3. This class of interactions is discussed further below. Other possible signatures for quark annihilation, $D_s^+ \rightarrow \rho^0\pi^+$ and $\omega\pi^+$, have not been observed![19] suggesting that quark annihilation is unlikely to be a dominant effect in the lifetime differences.

† Throughout this thesis, a reference to a particle state also implies reference to its charge conjugate.

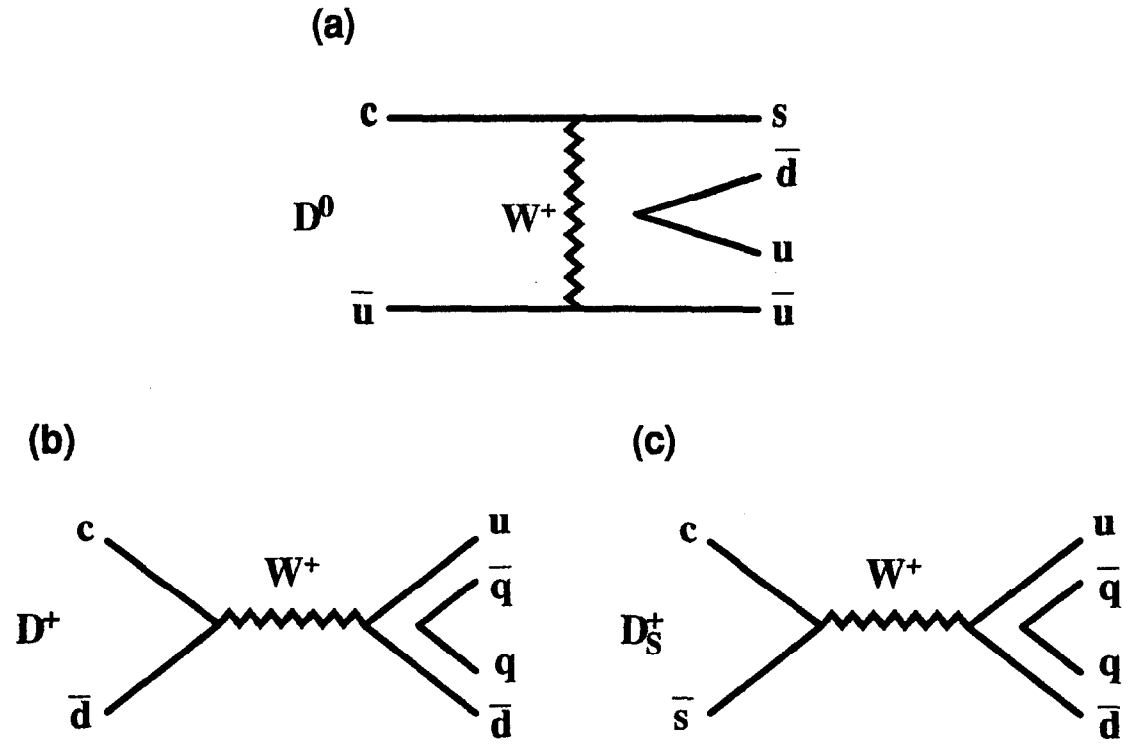

Figure 2.2 (a) The W-exchange diagram for the D^0; (b) the W-annihilation diagram for the D^+; (c) the W-annihilation diagram for the D_s^+.

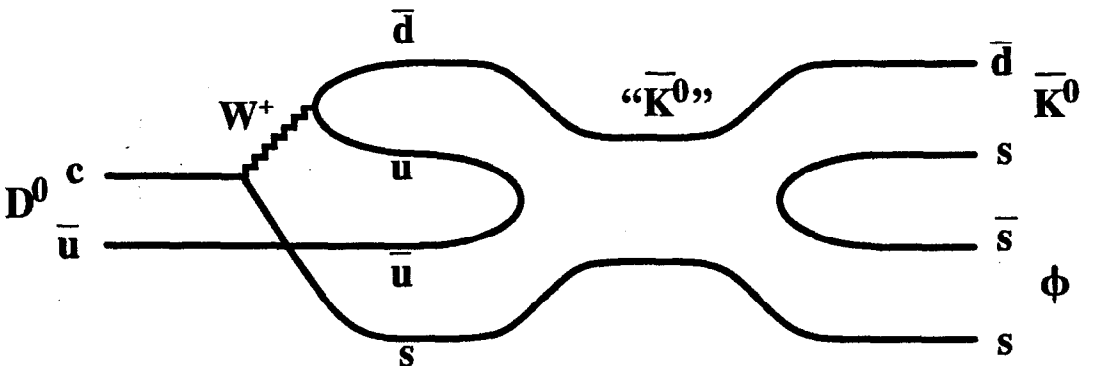

Figure 2.3 A final state interaction contributing to $D^0 \rightarrow \bar{K}^0\phi$.

Destructive interference involves the two spectator processes, external W-emission and internal W-emission. For Cabibbo allowed D^+ decays, both diagrams lead to the same final state with two identical $\bar{d}$ quarks, as illustrated in Figure 2.3(a). By Fermi-Dirac

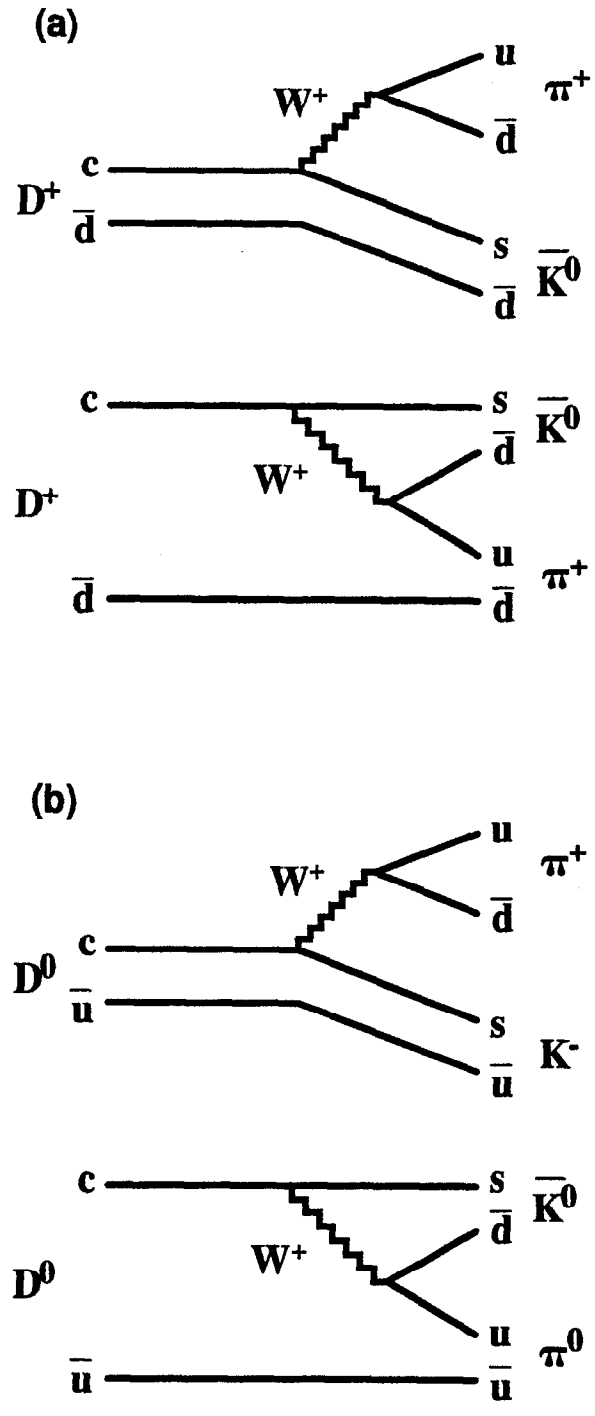

Figure 2.3 The two spectator diagrams leading to (a) $D^+ \to \bar{K}^0\pi^+$ and (b) $D^0 \to K^-\pi^+$ and $D^0 \to \bar{K}^0\pi^0$.

statistics, the two amplitudes are expected to interfere destructively. Since a similar effect cannot occur in the Cabibbo allowed D^0 or D_s^+ decays (Figure 2.3(b)), destructive interference, if significant, would suppress the D^+ nonleptonic width while leaving the D^0 and D_s^+ widths unaffected. Corroborating evidence for destructive interference has been observed in the Cabibbo-suppressed decays of the D^+.[20] Interference is possible for the decay $D^+ \to \pi^0\pi^+$ and not for $D^+ \to \bar{K}^0K^+$, implying the relations $B(D^+ \to \bar{K}^0K^+) \gg B(D^+ \to \pi^0\pi^+)$ and $B(D^+ \to \bar{K}^0K^+) \gg B(D^+ \to \bar{K}^0\pi^+)\times\tan^2\theta_c$, if the effect is significant. This prediction is consistent with the experimental numbers:

$$\frac{B(D^+ \to \bar{K}^0K^+)}{B(D^+ \to \bar{K}^0\pi^+)} = 0.317 \pm 0.086 \pm 0.048$$

$$\frac{B(D^+ \to \pi^0\pi^+)}{B(D^+ \to \bar{K}^0\pi^+)} < 0.21@90\%\ \text{CL}$$

In the limit of $SU(3)$ symmetry, the Spectator Model predicts the second ratio to be of the order $\frac{1}{2}\tan^2\theta_c \cong 0.026$.

Strong interactions clearly influence and mask the roles these processes play, and the fact that QCD is non-perturbative in charm weak decays complicates the interpretations further. Final state interactions are particularly difficult to estimate. As already seen, channel mixing may be behind the large branching fraction for $D^0 \to \bar{K}^0\phi$. Since the D mesons lie in a mass region with many nearby resonances, many other decay channels are also likely to be affected by final state interactions where the outgoing mesons rescatter through a nearby resonance possessing the same quantum numbers. For example, the $K\pi$ states from $D^0 \to K^-\pi^+$ and $\bar{K}^0\pi^0$ contain 3/2 and 1/2 isospin components, of which the latter could rescatter through a $I(J^P) = 1/2(0^+)$ resonance such as the $K_0^*(1430)$. Rescattering is manifested by isospin phase shifts. The isospin amplitudes for $D \to \bar{K}\pi$ decays are

Table 2.2 Isospin decomposition for Cabibbo allowed $D \to PP$, PV and VV modes.

Mode	$\lvert A_{1/2}/A_{3/2}\rvert$	$\delta_{1/2}-\delta_{3/2}$	Ref.
$\bar{K}\pi$	3.67±0.27	77°±11°	22
$\bar{K}\rho$	3.12±0.40	0°±26°	22
$\bar{K}^*\pi$	3.22±0.97	84°±13°	22
$\bar{K}^*\rho$	3.4±0.9	61°±37°	23

$$A(D^+ \to |+1/2;+1\rangle) = \sqrt{3}A_{3/2}\, e^{i\delta_{3/2}}$$

$$A(D^0 \to |-1/2;+1\rangle) = \sqrt{\frac{1}{3}}\left(A_{3/2}\, e^{i\delta_{3/2}} + \sqrt{2}A_{1/2}\, e^{i\delta_{1/2}}\right)$$

$$A(D^0 \to |+1/2;\,0\rangle) = \sqrt{\frac{1}{3}}\left(\sqrt{2}A_{3/2}\, e^{i\delta_{3/2}} - A_{1/2}\, e^{i\delta_{1/2}}\right)$$

The Mark III measurements have been used to obtain values for $|A_{1/2}/A_{3/2}|$ and $\delta_{1/2}-\delta_{3/2}$ for these channels and $D \to \bar{K}\rho$, $\bar{K}^*\pi$ and $\bar{K}^*\rho$, for which the formulae also apply. The numbers, listed in Table 2.2, show that the isospin phase shifts can indeed be very large.

2-2.5 The QCD Corrected Hamiltonian

The long distance, soft gluon effects, like hadronization and final state interactions, are difficult to estimate from first principles. The short distance, hard gluon effects, however, are still calculable using the methods of perturbation theory in QCD. These corrections are discussed here, following the seminal work of Rückl [13].

At the bare quark level, weak transitions are described by the Hamiltonian

$$H_W^{(0)} = -\frac{g^2}{8i}\int d^4x\, D_{\mu\nu}(x, M_W^2)T\left[J_+^\mu(x)J_-^\mu(0) + \text{h.c.}\right]$$

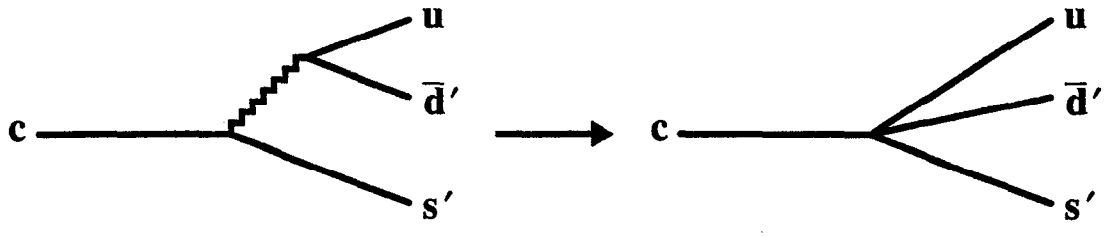

Figure 2.4 The low energy approximation for c quark weak decays.

For a c quark decaying to three light quarks or a light quark and a lepton pair, the momentum transfer is much smaller than the W boson mass. In the limit $M_W \to \infty$, the Hamiltonian reduces to

$$H_W^{(0)} = -\frac{G_F}{\sqrt{2}}\left[J_+^{\mu}(0)J_{-\mu}(0) + \text{h.c.}\right]$$

from which the $\Delta c = -1$ component is extracted

$$H_W^{(0)}(\Delta c = -1) = -\frac{G_F}{\sqrt{2}}(\bar{s}'c)_L\left[(\bar{u}d')_L + (\bar{\nu}_e e) + (\bar{\nu}_\mu \mu) + (\bar{\nu}_\tau \tau)\right]$$

where $G_F = g^2/(\sqrt{32}M_W)$ is the Fermi constant, and $(\bar{q}_1 q_2)_L = \sum_{\alpha=1}^{3} \bar{q}_{1\alpha}\gamma^{\mu}(1-\gamma^5)q_{2\alpha}$, α being the color index. This low energy approximation is illustrated in Figure 2.4. (In this limit W-exchange and W-annihilation reduce to the same diagram; hence the joint classification "quark annihilation" in Section 2-2.4)

To first order in α_s, the hard gluon corrections to the weak Hamiltonian involve the one-loop diagrams shown in Figure 2.5.Other one-loop diagrams affect the renormaliztion of G_F and the quark wave functions, and therefore need not be considered. Calculation of the diagrams yields

$$\Delta H_W^{(1)} = -\frac{G_F}{\sqrt{2}}\frac{3\alpha_s}{8\pi}\ln\frac{M_W^2}{\mu^2}(\bar{s}'\lambda^{\alpha}c)_L(\bar{u}\lambda^{\alpha}d')_L$$

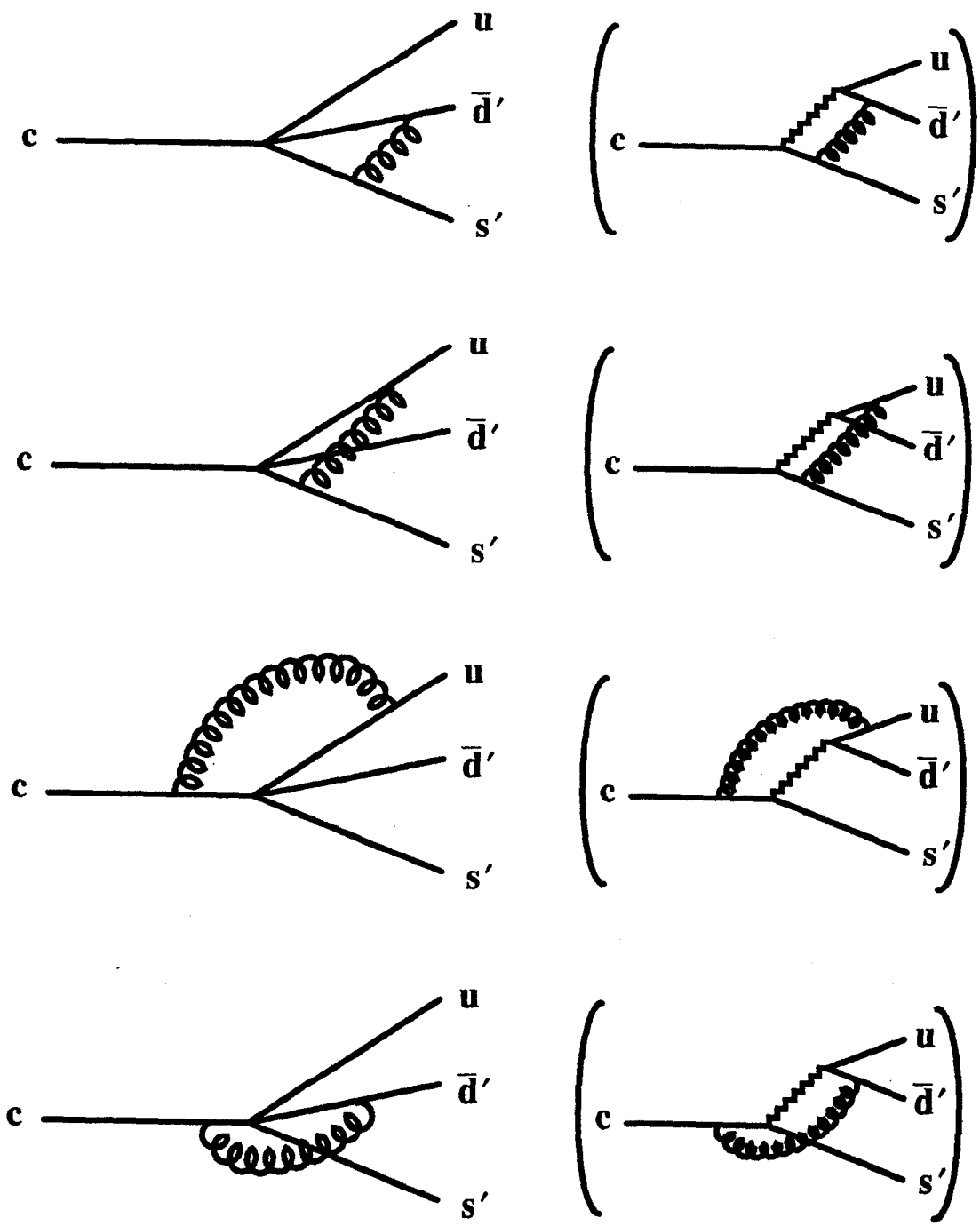

Figure 2.5 The one-loop corrections to the weak decays of a heavy quark. The diagrams in the parentheses are the corrections without low energy approximation.

where all quarks are approximated to be massless but off-shell by an amount μ^2 and λ^α {α = 1, 2,... 8} are the $SU(3)$ matrices. The calculation uses M_W for the ultraviolet cutoff and retains only the terms logarithmic in $(M_W/\mu)^2$. This result reveals that hard gluon effects induce weak color octet currents containing the same chirality and flavor structure as color singlet currents in $H_W^{(0)}$. A more intuitive interpretation can be made after applying the Fierz transformation:

$$\left[\gamma_\mu(1-\gamma_5)\right]_{\alpha\beta}\left[\gamma^\mu(1-\gamma_5)\right]_{\delta\varepsilon} = -\left[\gamma_\mu(1-\gamma_5)\right]_{\alpha\varepsilon}\left[\gamma^\mu(1-\gamma_5)\right]_{\delta\beta}$$

with the color relation

$$\sum_{a=1}^{8}\lambda^a_{ij}\lambda^a_{kl} = -\frac{2}{3}\delta_{ij}\delta_{kl} + 2\delta_{il}\delta_{kj}$$

to obtain

$$\begin{aligned} H_W^{(1)} &= H_W^{(0)} + \Delta H_W^{(1)} \\ &= \frac{G_F}{\sqrt{2}}\left[\left(1+\frac{\alpha_s}{4\pi}\ln\frac{M_W^2}{\mu^2}\right)(\bar{s}'c)_L(\bar{u}d')_L - \frac{3\alpha_s}{4\pi}\ln\frac{M_W^2}{\mu^2}(\bar{s}'d')_L(\bar{u}c)_L\right] \end{aligned}$$

where the leptonic terms in $H_W^{(0)}$ have been dropped. The first term represents the renormalized charged current interaction. The second term describes a new, *effective neutral current* interaction. These two types of transitions are compared in Figure 2.6.

By the operator product expansion and renormaliztion group theory, the short distance corrections can be calculated to all orders in α_s. After the operator product expansion, the effective Hamiltonian becomes

$$H_W^{\text{eff}} = \frac{G_F}{\sqrt{2}}[c_+O_+ + c_-O_-]$$

where $O_\pm$ are the four-quark operators

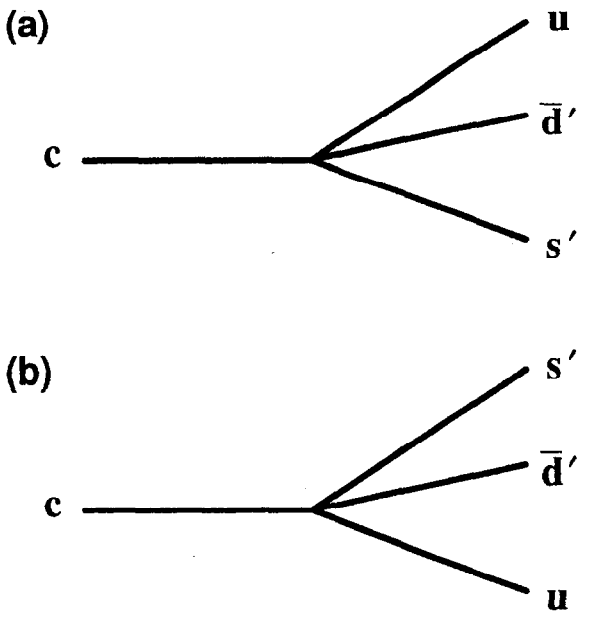

Figure 2.6 (a) The effective charged current. (b) The effective neutral current.

$$O_{\pm} = \frac{1}{2}\left[(\bar{s}'c)_L(\bar{u}d')_L \pm (\bar{s}'d')_L(\bar{u}c)_L\right]$$

and $c_{\pm}$ are "Wilson coefficients". In the leading log (LL) approximation

$$c_{\pm} = \left[\frac{\alpha_s(\mu^2)}{\alpha_s(M_W^2)}\right]^{\frac{d_{\pm}}{2b}} = \left[\frac{\ln(M_W^2/\Lambda_{QCD}^2)}{\ln(\mu^2/\Lambda_{QCD}^2)}\right]^{\frac{d_{\pm}}{2b}}$$

where $b = 11 - 2n_f/3$ and $d_{\pm}$ are the anomalous dimensions. Since $d_+ = -2d_-$, one obtains the relation $c_+ = 1/\sqrt{c_-}$. In the asymptotic limit, $c_+ = c_- = 1$, and H_W^{eff} reduces to $H_W^{(0)}$. Figure 2.7 plots c_+ and c_- as a function of μ; for $\mu = m_c \cong 1.5$ GeV/c^2:

$$c_+ \cong 0.74 \qquad c_- \cong 1.8$$

A calculation in the next-to-leading-log approximation suggests that further corrections to $c_{\pm}$ are small.[21] When quark masses are taken into account the corrections are also small.

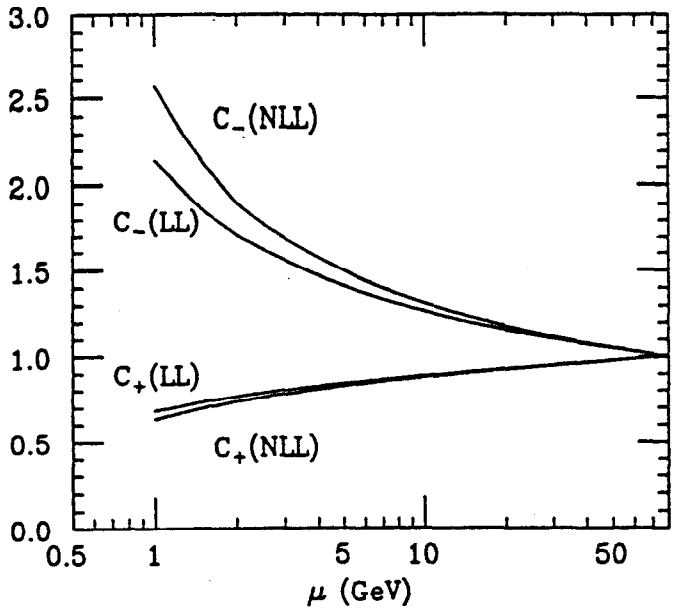

Figure 2.7 The dependence of the Wilson coefficients c_+ and c_- on the mass scale μ.

Expressing explicitly the charged and neutral currents terms, the effective Hamiltonian becomes

$$H_W^{\text{eff}} = \frac{G_F}{\sqrt{2}}[c_1(\bar{s}'c)_L(\bar{u}d')_L + c_2(\bar{s}'d')_L(\bar{u}c)_L]$$

where

$$c_1 \equiv (c_+ + c_-)/2 \cong 1.27$$

$$c_2 \equiv (c_+ - c_-)/2 \cong -0.53.$$

One effect of the QCD corrections to the weak Hamiltonian is an overall enhancement of the nonleptonic widths (Γ_{NL}) of the D mesons but no change in the semileptonic widths (Γ_{SL}), if the soft gluon effects, such as hadronization, are neglected. This shift occurs equally for all charmed mesons. Considering the Cabibbo allowed decays only, the Spectator Model predicts the widths to be $\Gamma_{\text{NL}} = 3\Gamma_0$ and $\Gamma_{\text{SL}} = \Gamma_0$, resulting in the semileptonic branching ratio

$$B(D \rightarrow l^{+}X) = 20\%$$

with Γ_0 being the muon decay rate scaled to the mass of the c quark. With the effective Hamiltonian the nonleptonic width is increased to

$$\Gamma_{NL} = 3\left(\frac{2c_{+}^{2} + c_{-}^{2}}{3}\right)\Gamma_0 \approx 4.3\Gamma$$

and the semileptonic branching ratio is correspondingly reduced to

$$B(D \rightarrow l^{+}X) = \frac{1}{2 + 2c_{+}^{2} + c_{-}^{2}} \cong 16\%$$

Using the next-to-leading log values for c_+ and c_- and including phase space and radiative gluon corrections, $B(D \rightarrow l^{+}X) \sim (13\text{-}15)\%$. This result is to be compared with the experimental values in Section 2-2.3; it is now closer to the average semileptonic branching ratio of the D^0, D^+ and D_s^+.

2-2.6 Exclusive Two-body Hadronic *D* Decays--A Phenomenological Approach

Most models on exclusive D decays are limited to the two-body modes PP, PV and VV, where P represents a pseudoscalar meson and V a vector meson. A wealth of information from high precision, heavy quark experiments have disclosed that the exclusive decays do appear to be dominated by two-body channels and these are largely of the classes PP, PV and VV. A comparison with theory has provided a deeper understanding of the weak decay mechanism in heavy quark physics.

The Factorization Hypothesis

One approach used by several authors to model heavy meson weak decays is to assume that the long distance QCD effects occur largely in the initial and final state configurations (Figure 2.8). This is referred to as the factorization hypothesis because it allows the decay amplitudes to be written as a product of current matrix elements, e. g.

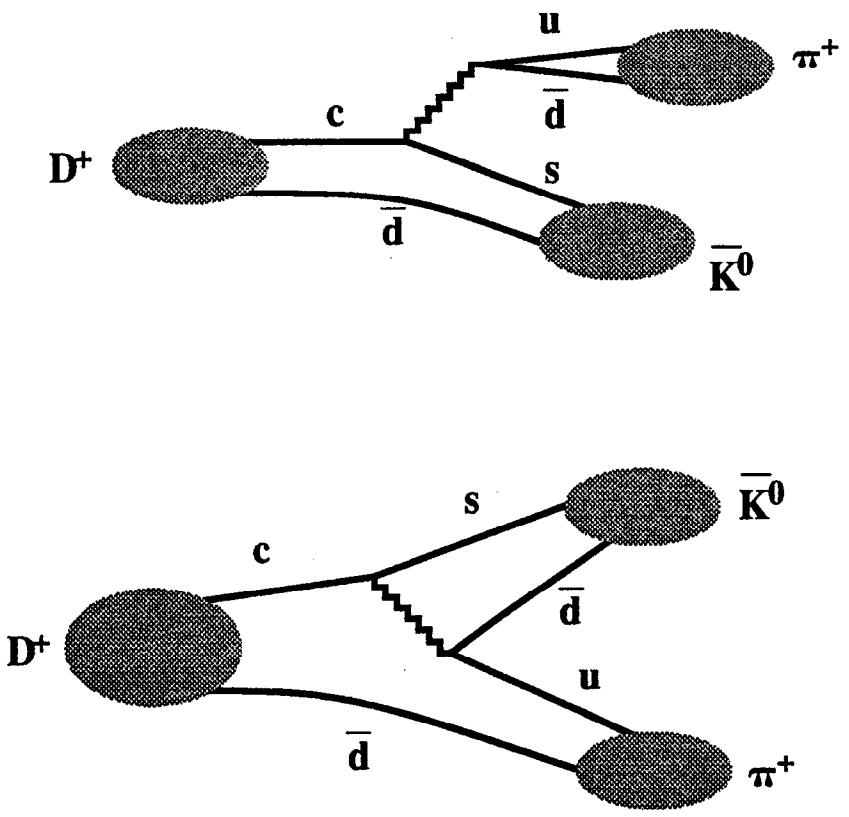

Figure 2.8 The factorization hypothesis, demonstrated for $D^+ \rightarrow \bar{K}^0\pi^+$.

$A(D^0 \rightarrow K^-\pi^+) \propto \langle K^-|J_\mu|D^0\rangle \times \langle \pi^+|j^\mu|0\rangle$. This is similar to the manner in which semileptonic decay amplitudes are constructed; $A(D^0 \rightarrow K^- l^+ \nu_l) \propto \langle K^-|J_\mu|D^0\rangle \times \langle \nu_l|\gamma^\mu(1-\gamma^5)|l^+\rangle$. Factorization occurs automatically for semileptonic decays since no strong coupling occurs between the leptons and quarks.

The BSW Model

The model that has met the most success with the factorization hypothesis is the model of Bauer, Stech and Wirbel (BSW).[18] Short distance effects are accounted for by using the effective weak Hamiltonian, discussed in Section 2-2.5. The initial charmed meson and final two-body states, which absorb the long distance effects, are described by harmonic oscillator wave functions.

Consider the example, $D^+ \to \overline{K}^0\pi^+$, which when factorized, leads to the matrix element

$$\left\langle \overline{K}^0\pi^+ \middle| H_W^{\text{eff}} \middle| D^+ \right\rangle = \frac{G_F}{\sqrt{2}}\cos^2\theta_c \Big[a_1 \left\langle \overline{K}^0 \middle| (\bar{s}c)_L \middle| D^+ \right\rangle \left\langle \pi^+ \middle| (\bar{u}d)_L \middle| 0 \right\rangle + a_2 \left\langle \overline{K}^0 \middle| (\bar{s}d)_L \middle| 0 \right\rangle \left\langle \pi^+ \middle| (\bar{u}c)_L \middle| D^+ \right\rangle \Big]$$

In the absence of hadronization and other long distance effects,

$$a_1 = c_1 + \xi c_2 \qquad a_2 = c_2 + \xi c_1$$

with $\xi = 1/n_c$ and $n_c = 3$ is the number of colors. The terms proportional to ξ in a_1 and a_2 arise from "color mismatched" contributions of the effective neutral and charged currents, respectively, and are obtained by applying a Fierz transformation and dropping the resulting octet current component.

The current matrix elements with pseudoscalar mesons are defined as

$$\left\langle P \middle| J_\mu \middle| 0 \right\rangle = -if_P\, p_\mu$$

$$\left\langle P' \middle| J_\mu \middle| D \right\rangle = \left(d + p' - \frac{M_D^2 - M_{P'}^2}{q^2} q \right)_\mu F_1(q^2) \; + \; \frac{M_D^2 - M_{P'}^2}{q^2} q_\mu F_0(q^2)$$

The first matrix element describes pseudoscalar coupling to the vacuum; f_P and p_μ are, respectively, the four-momentum and conventional weak decay constant of the pseudoscalar meson P. The second matrix element describes the hadronic current between the D and pseudoscalar P' mesons; d^μ and M_D (p'^μ and $M_{P'}$) are the four-momentum of the $D(P')$ meson, $q_\mu = d_\mu - p'_\mu$ and $F_1(q^2)$ and $F_0(q^2)$ are Lorentz invariant form factors which have the relation $F_1(0) = F_0(0)$. In the case of vector mesons

$$\left\langle V \middle| J_\mu \middle| 0 \right\rangle = \varepsilon_\mu F_V M_V$$

$$\langle V'|J_\mu|D\rangle = \frac{2}{M_D+M_{V'}}V(q^2)\,\varepsilon_{\mu\nu\rho\sigma}\,\varepsilon'^{*\nu}\,d^\rho\,v'^\sigma \;+\; i(M_D+M_{V'})A_1(q^2)\varepsilon'^*_\mu$$
$$-\frac{i}{M_D+M_{V'}}A_2(q^2)(\varepsilon'^*\cdot d)(d+v')_\mu \;-\; \frac{2iM_V}{q^2}A_3(q^2)(\varepsilon'^*\cdot d)q_\mu$$
$$+\frac{2iM_V}{q^2}A_0(q^2)(\varepsilon'^*\cdot d)q_\mu$$

where F_V is the decay constant for meson V and $A_0(q^2)$, $A_1(q^2)$, $A_2(q^2)$, $A_3(q^2)$ and $V(q^2)$ are form factors which obey the relations $A_3(0) = A_0(0)$ and

$$2M_{V'}A_3(q^2) = (M_D+M_{V'})A_1(q^2) - (M_D-M_{V'})A_2(q^2)\,;$$

M_V, v^μ, and ε^μ ($M_{V'}$, v'^μ, and ε'^μ) are the mass, four-momentum and polarization vector of V (V'). A single pole-dominance functional form is assumed for the form factors--e.g.

$$F_0^{D\to K}(q^2) = \frac{F_0^{D\to K}(0)}{1-q^2/M_{D_S^+}^2}$$

in $\langle\bar{K}^0|J_\mu|D^+\rangle$--and a relativistic harmonic oscillator model is used to evaluate the form factors at $q^2 = 0$.

BSW define three types of weak transitions: Class I which are proportional to $|a_1|^2$; Class II which are proportional to $|a_2|^2$; and Class III which are proportional to $|a_1+\alpha a_2|^2$, where α varies for each mode and is found to be > 0 in most cases. Because of the uncertainty in long distance effects, BSW treat a_1 and a_2 as free parameters which they evaluate by fitting the predicted amplitudes for the $D \to K\pi$ channels to the experimentally measured branching fractions. Final state interactions are accounted for in an ad hoc manner by using the isospin decomposition of the $K\pi$ states.

Under these assumptions, they obtain

$$a_1 = 1.2 \qquad a_2 = -0.5$$

Table 2.3 Measured and predicted branching ratios for Cabibbo allowed $D \to PP$, PV, and VV decays.

Decay Mode	Branching Fraction (%)	Ref.	BSW	BSW[a]
Class I:				
$D^0 \to K^-\pi^+$	4.2±0.4±0.4	24	6.0	4.7
$K^-\rho^+$	10.8±0.4±1.7	22	11	11
$K^{*-}\pi^+$	5.3±0.4±1.0	22	3.1	2.8
$K^{*-}\rho^+$	6.2±2.3±2.0	23	21	17
Class II:				
$D^0 \to \bar{K}^0\pi^0$	1.9±0.4±1.7	62	0.8	2.1
$\bar{K}^0\rho^0$	0.8±0.1±0.5	22	0.3	0.3
$\bar{K}^{*0}\pi^0$	2.6±0.3±0.7	22	1.0	1.3
$\bar{K}^{*0}\rho^0$	1.9±0.3±0.7	23	1.9	5.8
Class III:				
$D^+ \to \bar{K}^0\pi^+$	3.2±0.5±0.2	24	3.6	3.6
$\bar{K}^0\rho^+$	6.9±0.8±2.3	22	15.1	15.1
$\bar{K}^{*0}\pi^+$	5.9±1.9±2.5	22	0.3	0.3
$\bar{K}^{*0}\rho^+$	4.8±1.2±1.4	23	17	17

a. Corrected for isospin phase shifts.

If ξ were 1/3, then $a_1 = 1.27 - \xi \times 0.53 \cong 1.09$ and $a_2 = -0.53 + \xi \times 1.27 \cong -0.11$, i. e. they find that effectively $\xi \cong 0$ or $n_c \to \infty$, implying the "color mismatched" contribution can be ignored. Another important result from these numbers is that $a_1/a_2 < 0$. Among the Cabibbo allowed transitions, only the D^+ fall into Class III, namely $|a_1+\alpha a_2|^2 \approx |a_1-|\alpha| a_2|^2$, and thus destructive interference in D^+ decays is manifestly present in the model. Table 2.3 compares predicted branching ratios against the measured values for Cabibbo allowed $D \to PP$, PV and VV decays. In the last column the predictions are recalculated to include the isospin phase shifts determined from experiment. For most of the $D \to PP$ and PV

Table 2.4 Branching Fractions in the BSW model for $D \rightarrow VV$, using experimental values of form factors.[23]

Mode	Branching Fraction (%)	BSW 0[a]	BSW 1[b]	BSW 2[c]
$K^{*-}\rho^+$	6.2±2.3±2.0	17	4.7±1.6	8.0±3.1
$\bar{K}^{*0}\rho^0$	1.9±0.3±0.7	5.8	6.1±2.3	10.4±4.3
$\bar{K}^{*0}\rho^+$	4.8±1.2±1.4	17	2.1±0.8	3.6±1.5

a. Using theoretical form factors.
b. Using form factors from E691, Reference [26].
c. Using the E691 form factors after scaling by the square root of the Mark III $D^+ \rightarrow \bar{K}^{*0}e^+\nu_e$ branching fraction, Reference [25].

decays, the numbers are in reasonable agreement. Recall, however, that three channels were used to determine a_1 and a_2.

For $D \rightarrow VV$ the model tends to overestimate the branching ratios. This problem, however, may be due not so much with the factorization ansatz as with the choice of form factors, which are another critical hypothesis of this model. Form factors have been treated theoretically by several authors and found to vary as much as 30-40% When the theoretical form factors calculated for these modes are replaced by experimentally measured form factors, obtained independently from studies of semileptonic decays‡ better agreement is found (Table 2.4)

Overall, the BSW model obtains a smaller hadronic width for the D^+ than the D^0. This result suggests that the lifetime difference can be explained largely by interference effects in the D^+ decays.

‡ Specifically, the form factors are derived from the experimental measurements of $D^+ \rightarrow \bar{K}^{*0}e^+\nu_e$ including the $\bar{K}^*$ polarization. There has been some experimental uncertainty; Mark III measurements[25] disagree with those from E691 at Fermilab.[26] The form factors used in this test are from the latter experiment.

2-2.7 Exclusive Two-body Hadronic *D* Decays--More Fundamental Approaches

The $1/n_c$ Expansion

Buras, Gérard and Rückl[27] have applied the $1/n_c$ expansion to two-body charm decays and have developed a diagrammatic scheme to determine the order to which a particular decay diagram will contribute in $1/n_c$. Again the effective Hamiltonian is used, and the expansion is performed on the hadronic matrix elements $\langle \text{final}|H_W^{\text{eff}}|D\rangle$, where $\langle \text{final}|$ represents a given final state. They find that

1) Mesons are represented by their valence quarks to leading order.

2) All leading order contributions to the hadronic matrix elements are factorizable into current matrix elements. However, not all factorizable terms enter to leading order.

3) Final state interactions enter as next-to-leading order contributions.

The counting rules are given in Figure 2.9. Again taking $D^+ \to \bar{K}^0\pi^+$ as an example, the leading and some next-to-leading diagrams for this decay are shown in Figure 2.10. In calculating the hadronic matrix element, the procedure then is to consider all terms up to some order in $1/n_c$. Buras *et al.* keep only the leading terms:

$$\left\langle \bar{K}^0\pi^+\left|H_W^{\text{eff}}\right|D^+\right\rangle = \frac{G_F}{\sqrt{2}}\cos^2\theta_c\left[c_1\left\langle \bar{K}^0\left|(\bar{s}c)_L\right|D^+\right\rangle\left\langle \pi^+\left|(\bar{u}d)_L\right|0\right\rangle + c_2\left\langle \bar{K}^0\left|(\bar{s}d)_L\right|0\right\rangle\left\langle \pi^+\left|(\bar{u}c)_L\right|D^+\right\rangle\right]$$

This matrix element is the same as that obtained by the BSW model, if $a_1 = c_1$ and $a_2 = c_2$; the $1/n_c$ expansion therefore gives a justification argument for $\xi \equiv 0$ obtained in the phenomenological fit of BSW. Current matrix elements are evaluated as in the BSW model, with the exception that Buras *et al.* normalize all form factors to one at $q^2 = 0$.

In predicting the exclusive decay branching ratios, $1/n_c$ expansion approach is not as successful as the BSW model, due in part to the fact that final state interactions and

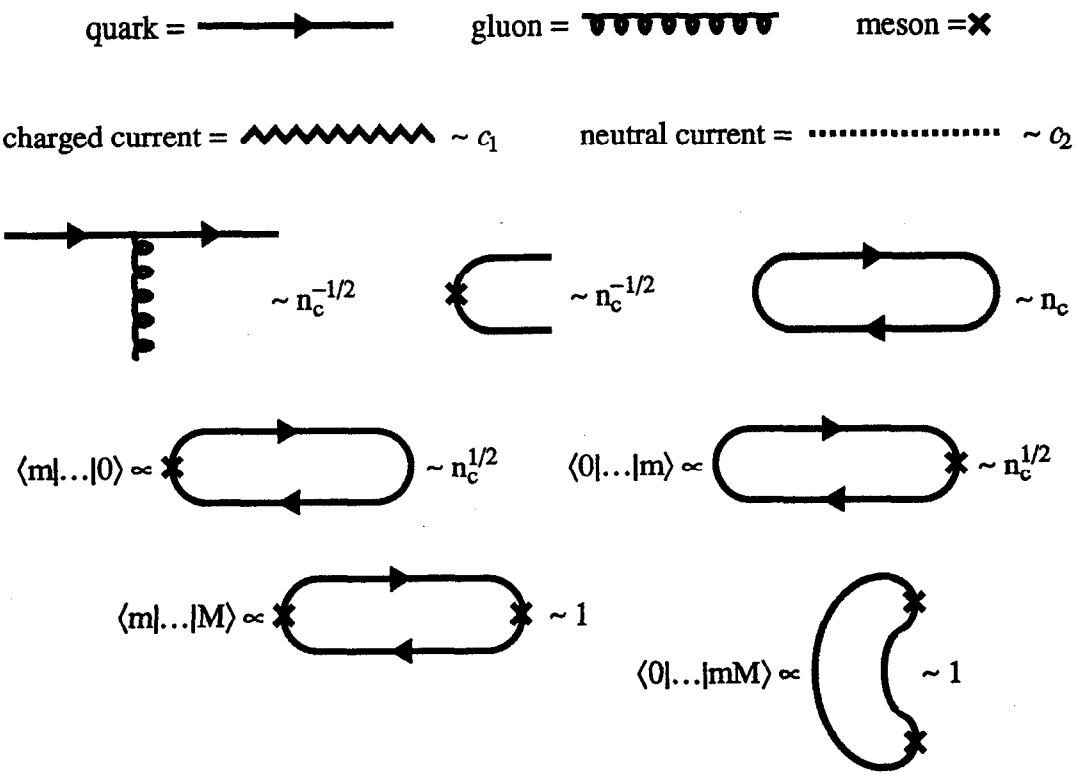

Figure 2.9 Counting rules in the $1/n_c$ expansion.

W-exchange diagrams do not enter at leading order. As with the BSW model, it also relies phenomenologically on form factors. However, the predictions by Buras *et al.* can in principle be improved by considering higher corrections in the expansion.

QCD Sum Rules

Blok and Shifman (BS) have taken a more fundamental approach by applying QCD sum rules to nonleptonic weak decays of the charmed mesons.[28] Their objective was to calculate the two-body amplitudes, including specifically the non-factorizable parts, which have been ignored in the BSW model and dropped in the $1/n_c$ approach. They find that the non-factorizable parts are parametrized by three universal numbers (M_1, M_2 and M_3)

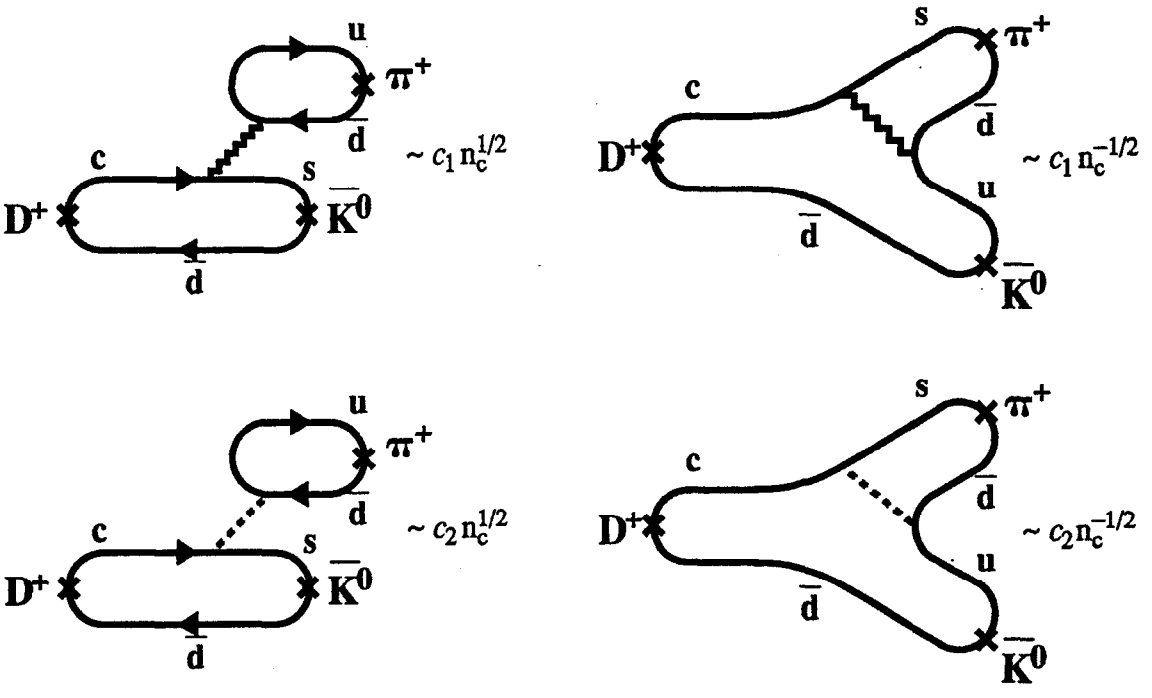

Figure 2.10 Leading and next-to-leading diagrams for $D^+ \to \bar{K}^0\pi^+$.

$$A = A_{\text{fact}} + \sum_{i=1}^{3} \alpha_i M_i$$

where A is the total amplitude, A_{fact} is the factorizable contribution and the coefficients α_i depend on the quark content of the mesons. The M_i parameters correspond to the quark annihilation diagram and the non-factorizable parts of the two spectator diagrams in the $M_W \to \infty$ limit. BS calculated the M_i's for the $D \to PP$ and PV decays (six numbers total).

BS find for most decays that the non-factorizable contribution nearly cancels with the terms proportional to $1/n_c$ in A_{fact}, thus providing a possible explanation why $\xi \cong 0$ in the BSW model and a justification for only considering the leading-order terms in the $1/n_c$ expansion approach. Interference is present in the model since A_{fact} is calculated in general factorization approach. They also find that the annihilation mechanism is not compensated, inducing an approximately 20% increase in the D^0 nonleptonic width. This would

further decrease the semileptonic branching fractions from the predictions that were obtained using only the QCD-corrected spectator model, making them agree more closely with experiment. This annihilation contribution in principle includes final state interactions such as channel mixing and rescattering.[29] For $D^0 \to \bar{K}^0\phi$, BS obtain a branching ration of 1.3 %, to be compared with the experimental number $0.99 \pm 0.24 \pm 0.14$ %.[30]

The Heavy Quark Approximation

Over the last few years, much interest and activity has arisen in the area of the "effective heavy quark theory."[31] The discussion here follows the excellent review in Reference [32].

The basic ansatz of the theory is to expand QCD in powers of $1/m_Q$, where m_Q is the mass of a heavy quark (c or b). In the limit $m_Q \to \infty$, hadronic structure becomes flavor and spin independent, resulting in an $SU(4)$ symmetry:

$$b\uparrow, b\downarrow, c\uparrow, c\downarrow \Rightarrow SU(4)_{\text{flavor-spin}}$$

The heavy quark then becomes a static source of color fields, and the internal dynamics involving the gluons and light quarks becomes independent of the mass and spin of the heavy quark. Hadrons with different spin, e. g. D and D^*, become degenerate states, and the mass splittings arise from perturbative effects in $1/m_Q$. An analogy can be drawn from the picture of the atom in non-relativistic quantum mechanics.[33] The heavy quark is akin to the atomic nucleus, QCD interactions to electromagnetic interactions, and the light quark degrees of freedom to the electrons and the electromagnetic field. If the nucleus has spin S, the atomic states then have a degeneracy of $2S + 1$. This degeneracy is lifted by the hyperfine structure, which enters at m_e/m_N, where m_e is the electron mass and m_N is the mass of the nucleus.

The heavy quark effective Lagrangian is

$$L_{HQ} = \bar{h}_v^{(b)} iv^\mu D_\mu h_v^{(b)} + \bar{h}_v^{(c)} iv^\mu D_\mu h_v^{(c)} + O(1/m_Q)$$

which together with the QCD lagrangian for the gluons and light quarks describes the structures of hadrons. It is derived from the Dirac Lagrangian as follows. In the rest frame of a D meson, the heavy charm quark wave function would have a component proportional to the four-spinor eigenstate

$$u_c^{(s)} = \sqrt{\frac{E+m_c}{2E}} \begin{pmatrix} \chi^{(s)} \\ \frac{\sigma \cdot p}{E+m_c} \chi^{(s)} \end{pmatrix} e^{-i(p^\mu x_\mu)}$$

where $\chi^{(s)}$ is a two component spinor, $p^\mu = (E, p)$ is the four-momentum of the charm quark and σ_i are the Pauli spin matrices. In the large m_c limit, $E \to m_c$, normalization is unity and the lower component vanishes. In effect $u^{(s)}$ is being applied by the projection operator

$$\left(\frac{1+\gamma_0}{2}\right) = \begin{pmatrix} 1 & 0 \\ 0 & 0 \end{pmatrix}$$

$$\left(\frac{1+\gamma_0}{2}\right) u_c^{(s)} \approx u_c^{(s)}$$

where γ_0 is the "time" Dirac matrix. A general Lorentz frame is characterized by its four-velocity

$$v^\mu = \frac{p^\mu}{m_c} = \frac{1}{\sqrt{1-v^2}}(1, \boldsymbol{v})$$

To boost to this frame the projection operator is first made Lorentz invariant

$$\left(\frac{1+\gamma_0}{2}\right) \to \left(\frac{1+\not{v}}{2}\right)$$

where $\not{v} = \gamma_\mu v^\mu$, and

$$e^{-i(p^\mu x_\mu)} = e^{-i(m_c v^\mu x_\mu)}$$

is already invariant. A new field is then defined with the leading mass dependence factored out

$$u_c^{(s)} = \left(\frac{1+\not{v}}{2}\right) u_c^{(s)} \equiv e^{-i(m_c v^\mu x_\mu)} h_v^{(c)}(x)$$

Given the Dirac equation

$$L_{Dirac} = \overline{\psi}_b(i\not{D} - m_b)\psi_b + \overline{\psi}_c(i\not{D} - m_c)\psi_c$$

one is then left with the algebra to obtain $\mathcal{L}_{HQ}$.

The theory is just beginning to be tested. The spin symmetry has been tested by relating $B \to De\nu$ to $B \to D^* e\nu$ and comparing predicted polarization quantities with experiment; agreement within the large experimental errors is found. The flavor symmetry has also been tested by relating the decay constants f_D and f_B and comparing results with lattice QCD calculations. The test here was less successful, the methods differed by a factor of 2-3. This may indicate that the charm quark is not massive enough, and higher order terms in the $1/m_c$ expansion need to be considered. More tests are needed. If the theory can be applied to the charm regime, it would be a powerful tool in improving the level of understanding of D physics.

2-3 Doubly Cabibbo Suppressed Decays

2-3.1 Introduction

This dissertation will explore the processes designated as doubly Cabibbo suppressed decays. These decays occur with two factors of $\sin\theta_c$ in the weak transition (Figure 2.11) and are therefore expected to be suppressed by $\sim 3\times10^{-3}$ in rate. Using the naive

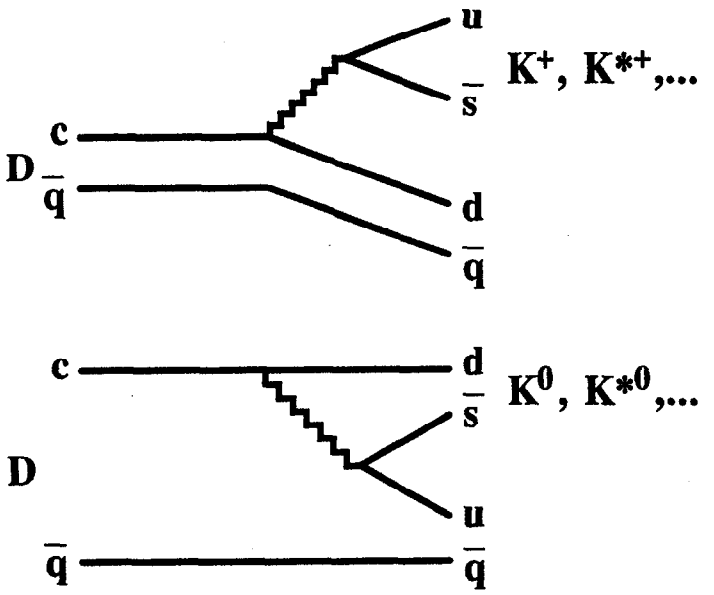

Figure 2.11 Doubly Cabibbo suppressed decays.

non-QCD corrected Spectator Model, one would argue that, for example, the doubly Cabibbo suppressed *PP* decay, $D^+ \to K^+\pi^0$, has a branching fraction of

$$B(D^+ \to K^+\pi^0) = \frac{1}{2}B(D^+ \to \overline{K}^0\pi^+) \times \tan^4\theta_c \approx 4\times10^{-3}\,\%$$

where the phase space corrections have been ignored. In the Mark III data set analyzed in this thesis, that number would correspond to 1.7 $K^+\pi^0$ *produced* events. It will be argued in the balance of this chapter, however, that while the amplitudes for Cabibbo allowed D^+ decays are suppressed by the effects of interference (Section 2-2.4, Section 2-2.6), this is not the case for D^+ doubly Cabibbo suppressed decays, making the experimental detection of these decays accessible.

2-3.2 Motivation for Studying D^+ Doubly Cabibbo Suppressed Decays

In the first half of this chapter destructive interference has been argued as the possible driving mechanism behind the lifetime difference between the D^+ and the D^0 and D_s^+

mesons. Some compelling experimental evidence--the singly Cabibbo suppressed branching fractions $B(D^+ \to \bar{K}^0 K^+)$ and $B(D^+ \to \pi^0 \pi^+)$--and theoretical evidence--the BSW model--for that process were discussed. Required now, experimentally, are additional signatures for interference in other exclusive D decays, and for that one turns to the doubly Cabibbo suppressed D^+ channels.

In all D^+ doubly Cabibbo suppressed decays, no identical quarks arise in the final state, as Figure 2.11 shows when $\bar{q} = \bar{d}$. Therefore, destructive interference cannot occur in those channels. If, however, interference is a dominant effect in the Cabibbo allowed decays, the relative weight of doubly Cabibbo suppressed decays could be enhanced. This effect would be reflected through the parameter

$$\bar{\rho} \equiv \frac{A(D \to DCSD)}{A(D \to CAD)} \times \frac{1}{\tan^2 \theta_c}$$

where *DCSD* represents a doubly Cabibbo suppressed channel and *CAD* the corresponding Cabibbo allowed channel. Interference would suppress the denominator, thus increasing the $\bar{\rho}$ parameters relative to their Spectator Model predictions.

Bigi[34] has demonstrated this enhancement by applying the $1/n_c$ expansion approach to obtain numbers for D^+ $|\bar{\rho}|^2$ parameters. His predictions are given in Table 2.5, showing that some parameters are as large as approximately 20. Both the numerator and denominator are from theory; the Cabibbo allowed experimental measurements are not used. The ranges reflect theoretical uncertainty; in the model, interference strongly suppresses $D^+ \to \bar{K}^{*0} \pi^+$ (in the denominators of $|\bar{\rho}_{K^{*0}\pi}|^2$ and $|\bar{\rho}_{K^*\pi^0}|^2$), and it is sensitive to the model parameters. Included in the table for comparison are the Spectator Model predictions.

It is also instructive to compare predictions for D^0 doubly Cabibbo suppressed decays (Table 2.5) against the numbers for the D^+ doubly Cabibbo suppressed decays.

Table 2.5 Theoretical predictions for $D^+ |\bar{\rho}|^2$ parameters.

$\lvert\bar{\rho}\rvert^2$	Bigi[a]	Spectator Model
$\lvert\bar{\rho}_{K\pi^0}\rvert^2 \equiv \frac{B(D^+ \to K^+\pi^0)}{B(D^+ \to \bar{K}^0\pi^+)} \times \frac{1}{\tan^4\theta_c}$	3	0.5
$\lvert\bar{\rho}_{K^{*0}\pi}\rvert^2 \equiv \frac{B(D^+ \to K^{*0}\pi^+)}{B(D^+ \to \bar{K}^{*0}\pi^+)} \times \frac{1}{\tan^4\theta_c}$	5-11	1.0
$\lvert\bar{\rho}_{K^{*+}\pi^0}\rvert^2 \equiv \frac{B(D^+ \to K^{*+}\pi^0)}{B(D^+ \to \bar{K}^{*0}\pi^+)} \times \frac{1}{\tan^4\theta_c}$	12-25	0.5
$\lvert\bar{\rho}_{K\rho^0}\rvert^2 \equiv \frac{B(D^+ \to K^+\rho^0)}{B(D^+ \to \bar{K}^0\rho^+)} \times \frac{1}{\tan^4\theta_c}$	0.35	0.5

a. Reference [34].

Table 2.6 Theoretical predictions for $D^0 |\bar{\rho}|^2$ parameters.

$\lvert\bar{\rho}\rvert^2$	Bigi[a]	Spectator Model
$\lvert\bar{\rho}_{K\pi}\rvert^2 \equiv \frac{B(D^0 \to K^+\pi^-)}{B(D^0 \to K^-\pi^+)} \times \frac{1}{\tan^4\theta_c}$	2	1.0
$\lvert\bar{\rho}_{K\rho}\rvert^2 \equiv \frac{B(D^0 \to K^+\rho^-)}{B(D^0 \to K^-\rho^+)} \times \frac{1}{\tan^4\theta_c}$	0.5	1.0
$\lvert\bar{\rho}_{K^*\rho}\rvert^2 \equiv \frac{B(D^0 \to K^{*+}\pi^-)}{B(D^0 \to K^{*-}\pi^+)} \times \frac{1}{\tan^4\theta_c}$	3	1.0

a. Reference [34].

Enhancements are also found for the D^0 $\bar{\rho}$ parameters, albeit not as large. Interference cannot influence either the D^0 Cabibbo allowed or doubly Cabibbo suppressed decays, and the increase here over Spectator Model predictions is found to arise largely from $SU(3)$ symmetry breaking effects--e. g. $f_K/f_\pi \equiv 1.22$. Breaking in $SU(6)$ symmetry is behind the suppression of $D^0 \to K^+\pi^-$ and $D^+ \to K^+\rho^0$.

Thus presented herein are searches for D^+ doubly Cabibbo suppressed decays in the 9.56 pb^{-1} data sample of e^+e^- annihilation events collected near the $\psi(3770)$ resonance with the Mark III detector at the SPEAR storage ring, at the Stanford Linear Accelerator Center. These searches are performed foremost to provide an additional probe into the possible phenomena of destructive interference in the D^+ decays. The specific modes searched for are

- $D^+ \to K^+\pi^-\pi^+$ (which consists of $D^+ \to K^+\rho^0$, $K^{*0}\pi^+$ and $K^+\pi^-\pi^+$ nonresonant)
- $D^+ \to K^+\pi^0$
- $D^+ \to K^{*+}\pi^0$

The results will be used to test the theoretical predictions for the $|\bar{\rho}|^2$ parameters in Table 2.5. Other doubly Cabibbo suppressed modes, $D^+ \to K^0\pi^+$ and $K^0\rho^+$, cannot be studied experimentally due to the confusion with the Cabibbo allowed modes, $D^+ \to \bar{K}^0\pi^+$ and $\bar{K}^0\rho^+$, when both K^0 and $\bar{K}^0$ decay via the weak eigenstates K_S^0 and K_L^0.

Using Bigi's predictions, the numbers of produced doubly Cabibbo suppressed events expected in the Mark III data set are 5.1 for $D^+ \to K^+\pi^0$, 32-70 for $D^+ \to K^{*0}\pi^+$, 76-160 for $D^+ \to K^{*+}\pi^0$ and 2.6 for $D^+ \to K^+\rho^0$. These decays may therefore be observable in this experiment.

2-3.3 The Current Experimental Status of Doubly Cabibbo Suppressed Decays

To date only one study has been performed experimentally for D^+ doubly Cabibbo suppressed decays. The SLAC-LBL Collaboration[35] at SPEAR searched for $D^+ \to K^+\pi^-\pi^+$ inclusively in 1.27 pb^{-1} and 1.63 pb^{-1} of data collected, respectively, at $\sqrt{s}$ = 4.03 and 4.41 GeV. They observed $0.0^{+4.7}_{-0.0}$ events over the combinatoric background with an efficiency of 0.16±0.03 and placed a 90% confidence level upper limits of <0.02 on

$\sigma \cdot B(D^+ \to K^+\pi^-\pi^+)$ and <0.05 on $B(D^+ \to K^+\pi^-\pi^+)/B(D^+ \to K^-\pi^+\pi^+)$.[11] This result corresponds to

$$|\bar{\rho}_{K\pi\pi}|^2 < 19 \text{ at } 90\% \text{ confidence level.}$$

Considerably more research has been done for D^0 doubly Cabibbo suppressed decays by virtue of searching for D^0-$\bar{D}^0$ mixing. Mixing in the K^0-$\bar{K}^0$, D^0-$\bar{D}^0$, B_d^0-$\bar{B}_d^0$ and B_s^0-$\bar{B}_s^0$ systems arises when the eigenstates of the flavor conserving strong and electromagnetic interactions, which produce the particles, are not eigenstates of the weak interactions, which cause the decay of the particles. Thus a particle produced as a D^0, containing a c quark, can decay into a state characteristic of a $\bar{D}^0$, containing a $\bar{c}$ quark. If CP is conserved in the D^0-$\bar{D}^0$ system, the two weak eigenstates are

$$|D_+\rangle = \frac{1}{\sqrt{2}}\left[|D^0\rangle + |\bar{D}^0\rangle\right]$$
$$|D_-\rangle = \frac{1}{\sqrt{2}}\left[|D^0\rangle - |\bar{D}^0\rangle\right]$$

characterized by even and odd CP, a mass difference $\Delta m = m_+ - m_-$ and width difference $\Delta\Gamma = \Gamma_+ - \Gamma_-$. A state prepared as $|D^0\rangle$ at $t = 0$ evolves as

$$|D^0(t)\rangle = \frac{1}{2}\left[e^{-im_+t-\frac{\gamma_+}{2}t} + e^{-im_-t-\frac{\gamma_-}{2}t}\right]|D^0\rangle \quad + \quad \frac{1}{2}\left[e^{-im_+t-\frac{\gamma_+}{2}t} - e^{-im_-t-\frac{\gamma_-}{2}t}\right]|\bar{D}^0\rangle$$

With the dimensionless variables

$$x \equiv \frac{\Delta m}{\Gamma} \qquad y \equiv \frac{\Delta\Gamma}{2\Gamma}$$

the amount of mixing is usually defined by the parameter

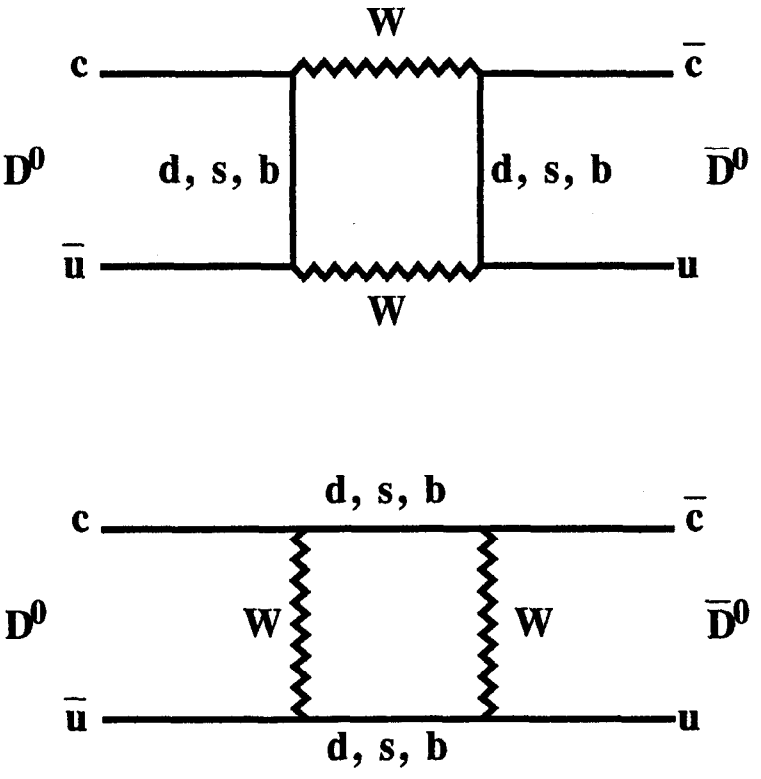

Figure 2.12 Box diagrams leading to D^0-$\bar{D}^0$ mixing.

$$r \equiv \frac{\int_0^\infty \left|\langle \bar{D}^0 | D^0(t) \rangle\right| dt}{\int_0^\infty \left|\langle D^0 | D^0(t) \rangle\right| dt} = \frac{x^2 + y^2}{2 + x^2 - y^2}$$

At the quark level, D^0-$\bar{D}^0$ mixing is a second order weak process represented by the box diagrams in Figure 2.12. In the Standard Model the effect of mixing from these diagrams is estimated to be small, $r \approx 10^{-7}$[36] largely because $\Delta\Gamma \ll \Delta m$ in the D^0-$\bar{D}^0$ and $\Delta m \propto f_D(m_s^2 - m_d^2)\tan^2\theta_c$ vanishes in the $SU(3)$ symmetry limit. Long distance effects, involving intermediate states such as $K\bar{K}$ and $\pi\pi$, may enhance mixing to as much as $r \approx 10^{-3}$[37] Physics outside the Standard Model could also enlarge r through extra box diagrams or first order flavor changing neutral currents.

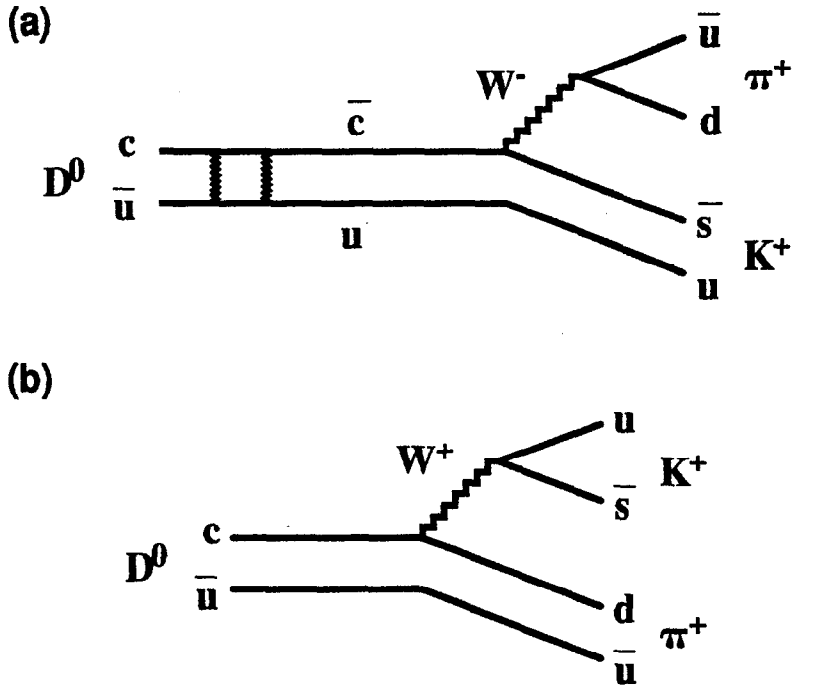

Figure 2.13 $D^0 \rightarrow K^+\pi^-$ produced by (a) D^0-$\bar{D}^0$ mixing and (b) D^0 doubly Cabibbo suppressed decays.

However, D^0 doubly Cabibbo suppressed decays are an unavoidable background in studies of D^0-$\bar{D}^0$ mixing. As shown in Figure 2.13, these decays produce the same final state as D^0-$\bar{D}^0$ mixing, when the latter are searched for in nonleptonic final states. One way to avoid this problem is to study mixing by the lepton tag method, where the sign of a lepton in the decay of a D marks the charm quantum number of the original meson.

Another approach to handling the background from doubly Cabibbo suppressed decays is to take advantage of the time dependence of D^0-$\bar{D}^0$ mixing. For example, the time evolution for $D^0 \rightarrow K^+\pi^-$ is given by[38]:

$$Rate(D^0(t) \to K^+\pi^-) \propto e^{-\Gamma t}\left[\left(\frac{\Gamma t}{2}\right)^2 (x^2+y^2) \;+\; |\bar{\rho}_{K\pi}|^2 \tan^4\theta_c \right.$$
$$+\; y\Gamma t \tan^2\theta_c \mathrm{Re}\left(\frac{1+\varepsilon}{1-\varepsilon}\bar{\rho}_{K\pi}\right)$$
$$\left. -\; x\Gamma t \tan^2\theta_c \mathrm{Im}\left(\frac{1+\varepsilon}{1-\varepsilon}\bar{\rho}_{K\pi}\right)\right]$$

where CP violation has been include in the ε parameter. The first term is due to mixing and is proportional to $t^2 e^{-\Gamma t}$. The second term is due to doubly Cabibbo suppressed decays and is proportional to the usual $e^{-\Gamma t}$. The third and fourth terms account for possible interference between mixing and doubly Cabibbo suppressed amplitudes. At sufficiently large decay times, therefore, mixing will dominate.

This approach was taken by the photoproduction experiment E691 at Fermilab.[39] The D^0's are observed through the reactions

$$\gamma + \mathrm{Be} \to D^{*+} + X$$
$$\hookrightarrow D^0\pi^+$$
$$\hookrightarrow K^-\pi^+, K^-\pi^+\pi^-\pi^+ \qquad \text{(right-sign)}$$
$$\hookrightarrow K^+\pi^-, K^+\pi^-\pi^+\pi^- \qquad \text{(wrong-sign)}$$

where the π^+ from the D^{*+} tags the charm of the D^0. With the time cut $t > 0.88$ ps, they plot for the remaining events the available energy Q versus the invariant mass M_{inv} of the $K\pi$ or $K\pi\pi\pi$ combinations and find in the signal regions one event for $D^0 \to K^+\pi^-$ with an estimated background of 2.7 events and two events for $D^0 \to K^+\pi^-\pi^+\pi^-$ consistent with background. Through a maximum likelihood fit using the Q, M_{inv} and t values for each event in a function describing the known dependence on these quantities for normal decays, mixing decays and doubly Cabibbo suppressed decays, they obtain an upper limit on mixing of $r < 3.7\times10^{-3}$ at 90% confidence level and upper limits on the doubly Cabibbo suppressed parameters $|\bar{\rho}_{K\pi}|$ and $|\bar{\rho}_{K\pi\pi\pi}|$ of:

$$|\bar{\rho}_{K\pi}|^2 < 5.7$$

$$|\bar{\rho}_{K\pi\pi\pi}|^2 < 6.8 \qquad \text{at } 90\% \text{ C. L.}$$

for $\tan\theta_c = 0.2267$. These limits are to be compared with the predictions in Table 2.5.

This experiment[40] has also studied D^0-$\bar{D}^0$ mixing by observing hadronic and semileptonic modes of the D^0 through the reactions

$$e^+e^- \rightarrow \psi(3770) \rightarrow D^0\bar{D}^0 \begin{cases} \rightarrow K\pi, K\pi\pi\pi, K\pi\pi^0, Ke\nu, K\mu\nu \\ \rightarrow K\pi, K\pi\pi\pi, K\pi\pi^0, Ke\nu, K\mu\nu \end{cases}$$

The exclusive final states are kinematically fitted to the hypothesis $e^+e^- \rightarrow X(\mathrm{M})\bar{X}(\mathrm{M}) \rightarrow$ (mode 1, mode 2), where M is a parameter of the fit and not constrained to the D^0 mass. Since D's with charm $C = +1$ typically decay to final states with strangeness $S = -1$, the vast majority of $D^0\bar{D}^0$ events have a final states with net $S = 0$. D's which decay by mixing or a doubly Cabibbo suppressed transition produce $S = +1$ states, and the events with these decays will have final states with a net $S = \pm 2$.

Because the D's are produced near threshold at the $\psi(3770)$, they are nearly at rest and time evolution can not be utilized in this analysis to reduce the background from doubly Cabibbo suppressed decays. One solution to the problem to consider only the events where both D's decay semileptonically. Another is to search for events where both D's decay to identical two-body final states. Doubly Cabibbo suppressed decays cannot contribute to such final states, a fact which follows from a quantum statistical argument due to Yamamoto[41] and Bigi and Sanda[42] Here the argument is specialized to the case $D^0\bar{D}^0 \rightarrow K^-\pi^+$. Since the $\psi(3770)$ is a spin one object, the two D mesons, each with spin zero, must be produced in a relative p wave state. In turn each $K^-\pi^+$ pair must be in a relative s wave state in order that the net spin be zero, and they can therefore be viewed as identical bosons. However, Bose-Einstein statistics require that these bosons have symmetric wave

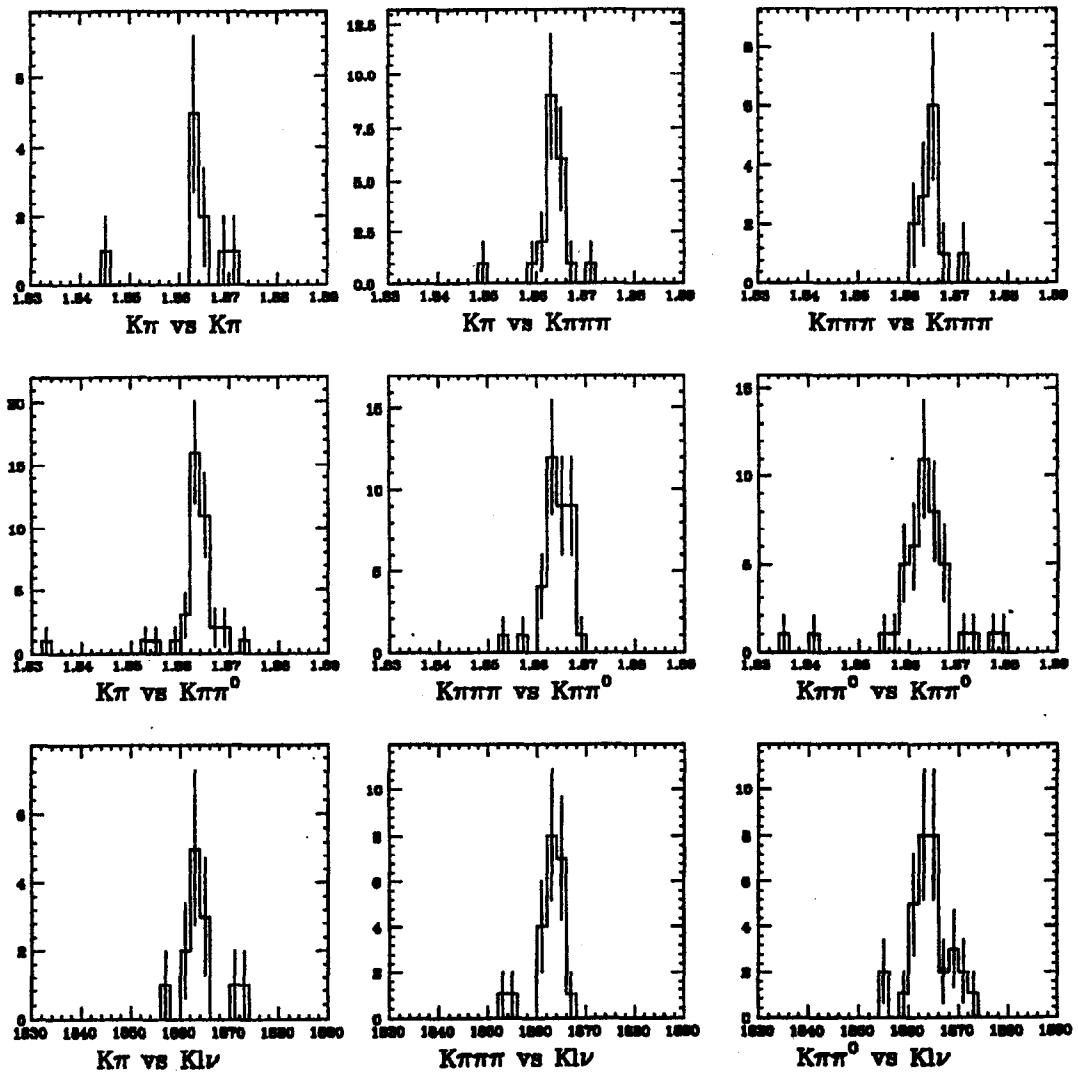

Figure 2.14 Mass distributions of the $S = 0$ and $S = \pm 2$ events observed in the Mark III experiment.

functions. Such final states cannot therefore be generated by doubly Cabibbo suppressed decays.

From the analysis, this experiment observes 224 events with $S = 0$ final states, whereas it observes three events with $S = \pm 2$ final states; the distributions are shown in Figure 2.14. Two of the $S = \pm 2$ events are reconstructed in the final states $K^{\pm}\pi^{\mp}\pi^{0}$ versus $K^{\pm}\pi^{\mp}\pi^{0}$, and a Dalitz plot analysis finds one to be consistent with $K^{-}\rho^{+}$ versus $K^{-}\rho^{+}$ and

the other consistent with $K^{*0}\pi^0$ versus $K^{*0}\pi^0$ ($D^0 \to K^-\pi^+\pi^0$ decays are dominated by the $D^0 \to K^-\rho^+$ and $\bar{K}^{*0}\pi^0$ channels; confer Table 2.3). The third event is observed in the final state $K^-\pi^+$ versus $K^-\pi^+\pi^0$. The expected background is 0.4±0.1 events, largely due to S = 0 events with particle misidentification. In the limiting case where the events are all due to mixing, a maximum likelihood analysis finds r = 1.2±0.6% or $r > 4\times10^{-3}$. If instead the E691 limit is assumed to be valid for mixing and $\bar{\rho}_{K\pi\pi^0} \gg \bar{\rho}_{K\pi}$ is assumed, then $|\bar{\rho}_{K\pi\pi^0}|^2$ = 7±4 or

$$|\bar{\rho}_{K\pi\pi^0}|^2 > 1.9 \qquad \text{at 90\% C. L.}$$

This lower limit is to be compared with the predictions in Table 2.5 for $|\bar{\rho}_{K\rho}|^2$ and $|\bar{\rho}_{K^*\pi}|^2$.

Finally, the CLEO Collaboration[43] at CESR has searched for the decays $D^0 \to K^+\pi^-$ and $K^+\pi^-\pi^+\pi^-$ as evidence for either mixing or double Cabibbo suppressed decays; no attempt was made to distinguish the two. Right- and wrong-sign candidates were identified through the decays

$$D^{*+} \to D^0\pi^+$$
$$\searrow\ K^-\pi^+,\ K^-\pi^+\pi^-\pi^+ \qquad \text{(right-sign)}$$
$$\searrow\ K^+\pi^-,\ K^+\pi^-\pi^+\pi^- \qquad \text{(wrong-sign)}$$

with stringent cuts applied to reduce all background. No statistically significant signals were observed for either $D^0 \to K^+\pi^-$ or $K^+\pi^-\pi^+\pi^-$, placing 90% confidence level limits of <4.3 and <6.5 events, respectively. With 420±21 events and 393±20 events observed, respectively, for $D^0 \to K^-\pi^+$ and $K^-\pi^+\pi^-\pi^+$, they obtain the limits $B(D^0 \to K^+\pi^-)/B(D^0 \to K^-\pi^+) < 0.011$ and $B(D^0 \to K^+\pi^-\pi^+\pi^-)/B(D^0 \to K^-\pi^+\pi^-\pi^+) < 0.018$. These results give

$$|\bar{\rho}_{K\pi}|^2 < 4.2$$

$$|\bar{\rho}_{K\pi\pi\pi}|^2 < 6.8 \qquad \text{at 90\% C. L.}$$

which are small improvements over the E691 results. The results also support the E691 limit on mixing.

In summary, the present data on doubly Cabibbo suppressed decays, and D^0-$\overline{D}^0$ mixing, is rather sparse; no unambiguous evidence has been found for any of these processes. Results from E691 and CLEO find mixing to be small, suggesting that the three $S = \pm 2$ events observed by Mark III are due to D^0 doubly Cabibbo suppressed decays with $|\bar{\rho}_{K\pi\pi^0}|^2 > 1.9$. This result further motivates the searches discussed in the remainder of this thesis; the need to understand $|\bar{\rho}|^2$ for doubly Cabibbo suppressed decays, as it influences our understanding and interpretations of mixing, provides further motivation for a search for these decays in the D^+ sector, wherein mixing cannot occur.

Chapter 3

The Mark III Detector and Data Processing

3-1 Introduction

The studies presented in this thesis use data collected by the Mark III detector,[44] the third solenoidal, general purpose detector designed for physics at the electron positron storage ring SPEAR (Figure 3.1). The primary objective of the experiment is to study and measure exclusive final states of charmonium and the charmed mesons produced from e^+e^- collisions in the 3 to 5 GeV center-of-mass energy range. Optimization of the detector involved (1) good solid angle coverage to detect particles efficiently, (2) good particle identification to distinguish e's, μ's, π's and K's and (3) high detection efficiency for low momentum photons, originating, for example, from low momentum π^0's.

The detector, shown in Figure 3.2, was located in the West Pit of SPEAR. Closest to the interaction point is a beryllium beam pipe 15cm in diameter with 1.5mm thick walls. Surrounding the beam pipe is the inner trigger chamber, also referred to as Layer 1, used in the particle tracking and trigger systems. After it is the main drift chamber,[45] providing the major tracking information and dE/dx information for particle identification. Surrounding the main drift chamber is a series of 48 scintillation counters which make up the time-of-flight system,[46] used for most of the particle identification. The electromagnetic calorimetry is divided into a barrel section[47] lying beyond the time-of-flight counters and two endcap sections.[48] The calorimetry is located inside the aluminum magnet coil, which supplies a nearly constant 0.4 Tesla B-field throughout the main drift chamber for measuring track momenta. Finally, two layers of muon counters make up the outermost detector system. The readout electronics for the various systems contain sample and hold circuits for temporary analog storage and microprocessor-controlled analog to

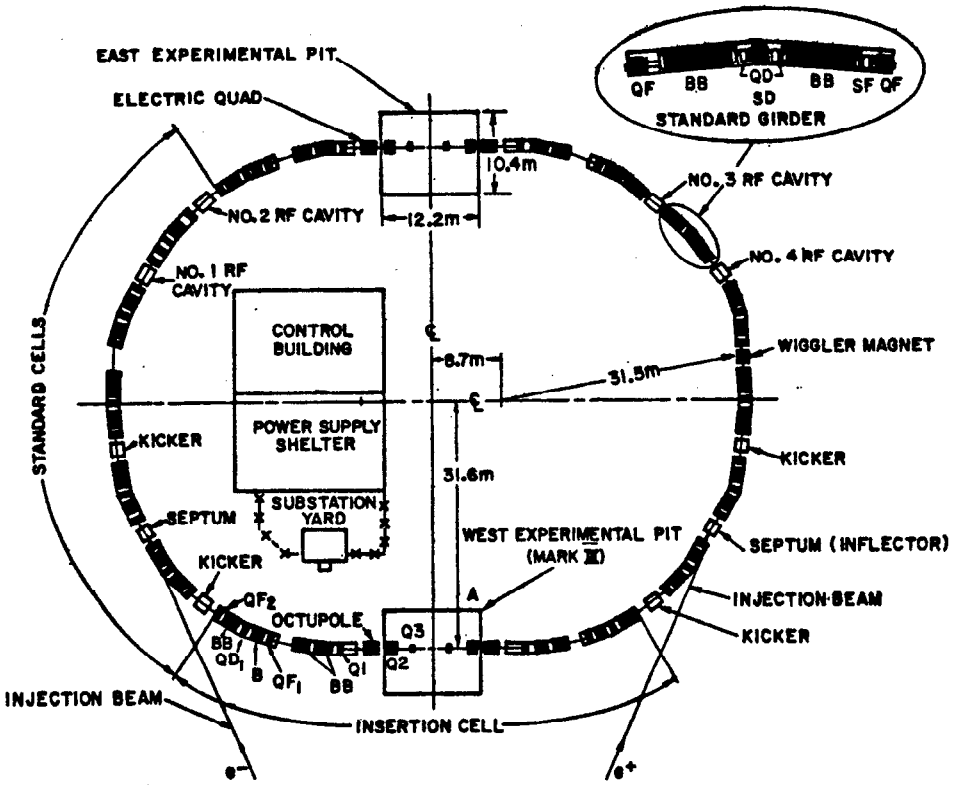

Figure 3.1 The electron positron storage ring SPEAR.

digital converters,[49] or BADC's, for digitization and online data calibration such as pedestal subtraction. Corrected data are read out and stored to tape by a dedicated VAX 11/780 computer. A hardware trigger system[50] provides interrupts to allow time for logging data and rejects backgrounds from cosmic rays and beam-gas scattering.

The analysis in this thesis uses the Mark III $\psi(3770)$ data samples and relies on the following detector components:

- the inner trigger chamber for charged track momenta;
- the main drift chamber for charged track momenta and for particle identification of low angle tracks;
- the time-of-flight system for particle identification;

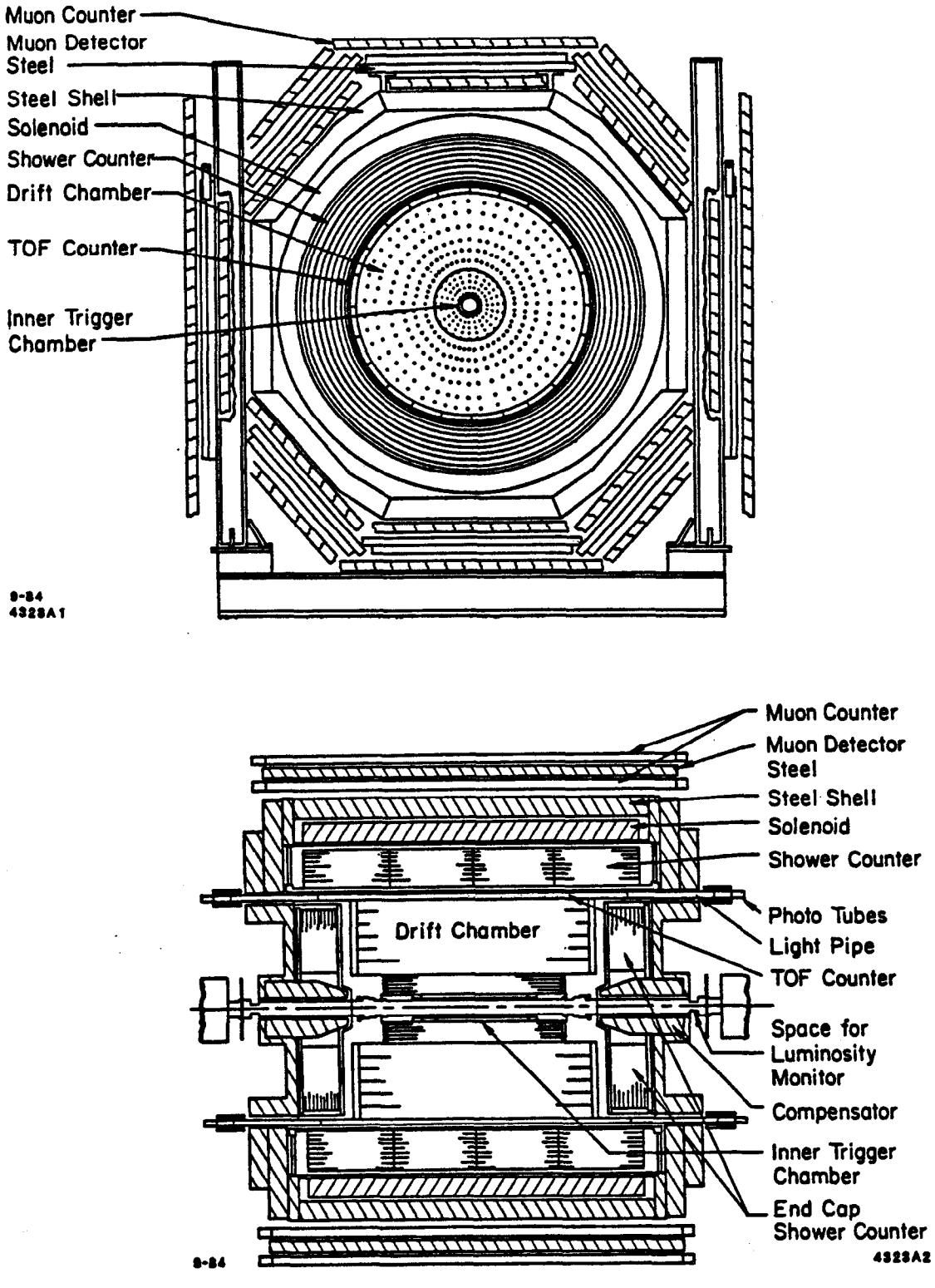

Figure 3.2 The Mark III Spectrometer.

- the electromagnetic shower counters for photon detection and π^0 reconstruction.

This chapter discusses in more detail these detector systems and their performance. This chapter also discusses the processing of the "raw" data collected with those systems and the preliminary event selection.

3-2 Overview of the Mark III Detector

3-2.1 The Inner Trigger Chamber

A precursor to today's vertex detectors, the inner trigger chamber, or Layer 1, provides tracking information close to the interaction region and therefore defines the location and time of the interactions. It is a small cylindrical drift chamber with an inner radius of 9.2 cm, an outer radius of 13.7 cm and a length of 110 cm; the coverage is 98% of 4π steradians. The chamber consists of four concentric planes of wires, divided into 32 drift cells. A drift cell is defined by one 38 μm stainless steel sense wire bordered on each side by 178 μm BeCu field wires. An end view is illustrated in Figure 3.3.

Each plane is staggered by half a cell relative to adjacent planes to provide a more efficient configuration for the trigger system. Tracks radiating from the interaction region will have different ionization drift times in the cells due to their orientation. However, as shown in Figure 3.3, the sum of drift times in neighboring cells of adjacent layers is nearly constant and equal to the maximum drift time in a single cell, ~250 ns. To obtain the sum in drift times, discriminated signals from neighboring cells in the first two planes of Layer 1 are transmitted into the opposite ends of a tapped delay line chronotron circuit.[51] The total drift time is determined by the coincidence circuit where the signals met. This scheme allowed the trigger system to use only a ~100 ns gate instead of the full 250 ns for the physics events.With beam crossings at SPEAR occurring every 780 ns, this reduced the total cosmic ray triggers by approximately a factor of 8.

The gas used in the chamber was a mixture of 70% argon and 30% ethane.

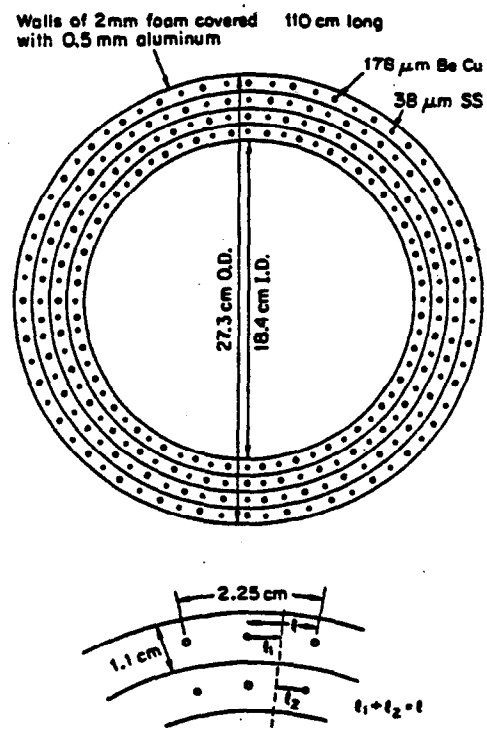

Figure 3.3 The transverse view of the inner trigger chamber.

3-2.2 The Main Drift Chamber

The main drift chamber is divided into two sections as shown in Figure 3.4. The inner region, referred to as Layer 2, contains sense wires at high density for tracking, momentum resolution and dE/dx measurement. The outer section contains Layers 3 through 8, which provide further tracking information, including z information.† The main drift chamber extends in radius from 14.47 cm out to 114.26 cm. In length, layers 3 through 8 are 238.8 cm, while layer 2 is only 182.9 cm; the indentation is needed for the compensating magnets.

Layer 2 is made up of 32 axial cells, each containing thirteen 20μm diameter tungsten sense wires bounded radially by two 57μm diameter stainless steel guard wires. The cells are separated azimuthally by 15 field shaping wires made from 175 diameter BeCu.

† The Mark III coordinate system is defined in relation to the SPEAR ring: the positive z axis is in the e^+ beam direction, the positive x axis points toward the center of the ring, and the y axis points upward. The e^- and e^+ beams circulate clockwise and counter-clockwise, respectively, as view from above.

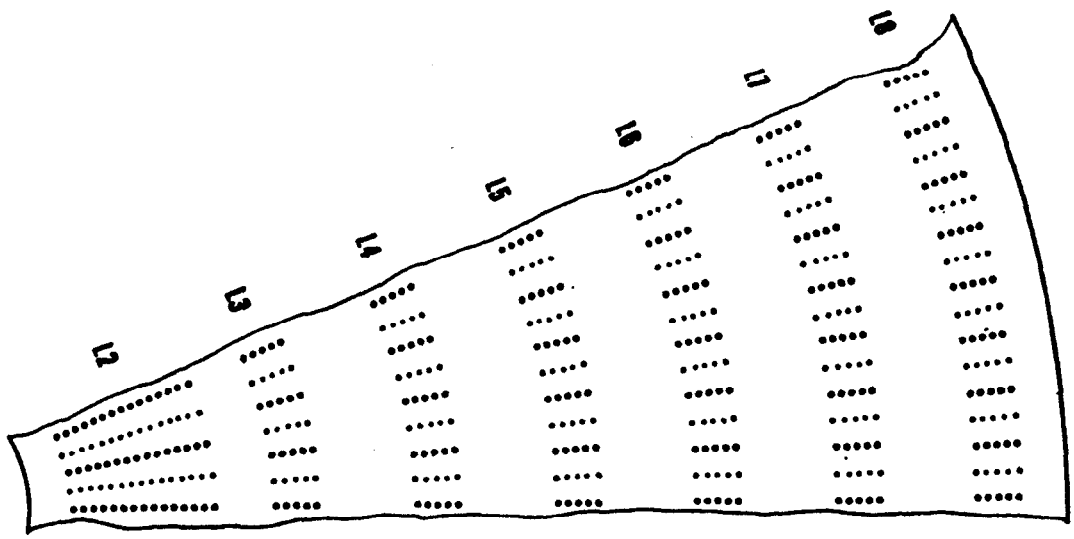

Figure 3.4 An axial view of 1/16th of the main drift chamber. The large dots, small dots and open circles represent the field wires, the sense wires and the guard wires, respectively.

The reasons for the high density of wires in this region are two-fold: (1) to obtain good resolution of displaced vertices from neutral particles such as Λ's and K_S^0's and (2) to extract information on the energy deposition of the steeply-dipped charged tracks. This latter information is obtained by operating the sense wires at low gas gain and reading out the signal pulse heights over a 1 μs gate. The sense wires are staggered by ± 150 μm with respect to the cell centers to resolve the ambiguity which arises when determining through which cell half a track has passed. This ambiguity is discussed further below in the discussion of the other drift chamber layers.

Layers 3 through 8 are divided into $N \times 16$ cells, where N is the layer number. This design makes each cell approximately equal in size. Each cell contains three 20 μm diameter tungsten sense wires and two 57μm diameter stainless steel guard wires which radially bound the sense wires. The cells are separated azimuthally by an equal number of

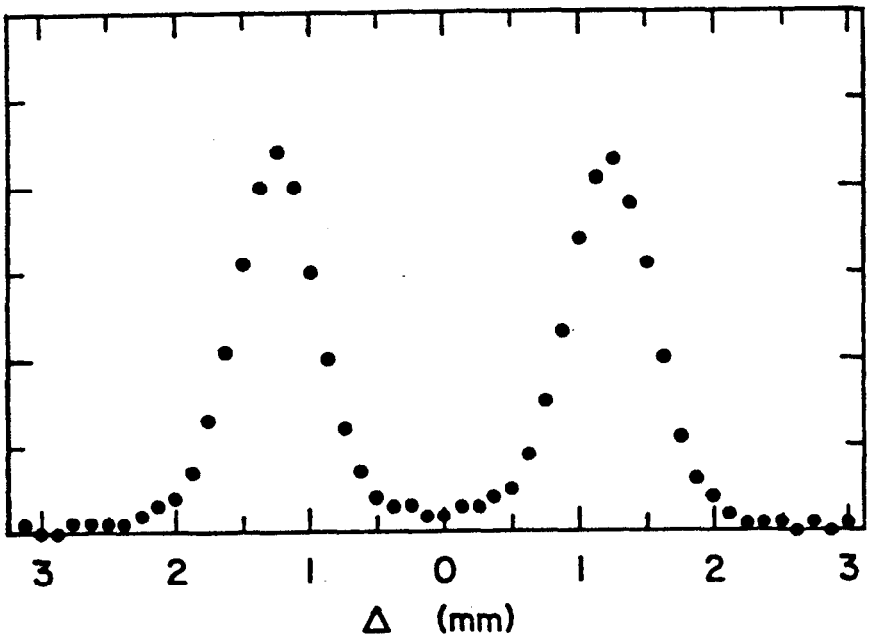

Figure 3.5 A distribution of $\Delta = v_{drift}\,[(t_1 + t_3)/2 - t_2]$ averaged over all cells in Layer 5. The two peaks correspond to tracks traversing the left and right halves of a cell, while the valley between them corresponds to tracks crossing a cell center.

175 diameter BeCu field wires. To obtain z information, Layers 4 and 6 were strung at stereo angles 7.7° and –9.0°, respectively. Additional z information is obtained from Layers 3, 5 and 7 by charge division in the guard wires.

The gas initially used for the chamber was a mixture of 89% argon, 10% CO_2 and 1% methane. During later runs water vapor was added to prolong the lifetime of the chamber.

Similar to the cell design for Layer 2, the three sense wires in each cell of Layers 3 through 8 are staggered by ±400 μm to resolve the left-right ambiguity. Without the stagger, the cells would be symmetric axially, leaving the determination of which cell half a particle has passed through for the offline track fitting algorithm. With the stagger the ambiguity can be resolved by calculating the quantity

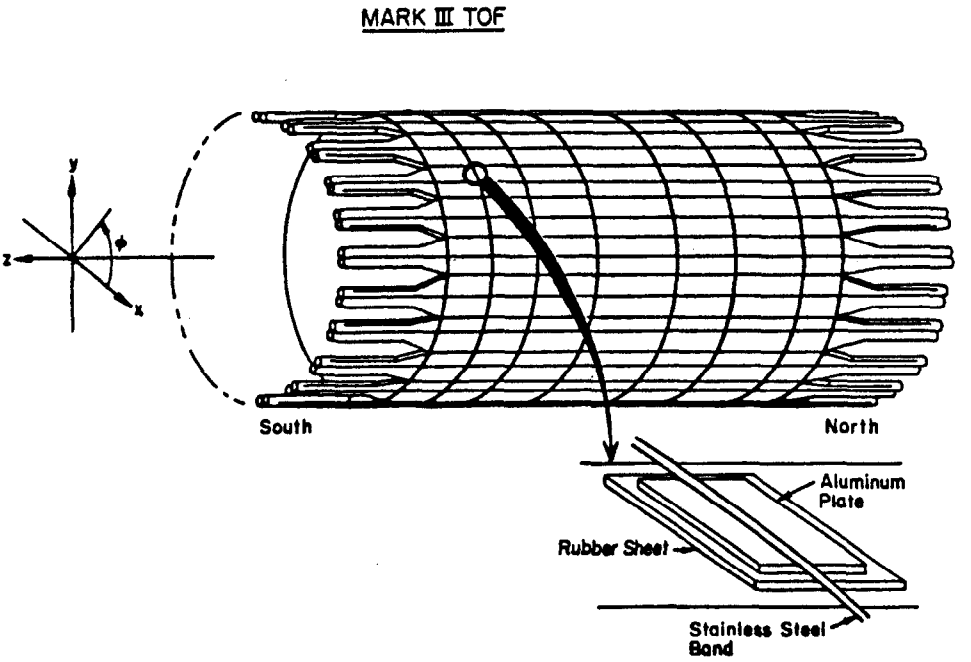

Figure 3.6 The time-of-flight system.

$$\Delta = v_{\text{drift}}\left[\frac{t_1 + t_3}{2} - t_2\right]$$

where v_{drift} is the drift velocity and t_1, t_2 and t_3 are the measured times on the three sense wires. The sign of Δ determines through which half of the cell the particle has passed. A Δ distribution is shown in Figure 3.5, where the two peaks corresponding to the left and right sides of a cell are cleanly resolved.

3-2.3 The Time-of-Flight System

The time-of-flight system consists of 48 scintillator counters 15.6cm wide, 5cm thick and 3.2m long, mounted parallel to the beam at a radius of 1.2m, thus providing a coverage of 80% of 4π steradians. Light generated from a particle traversing a counter is transmitted to the ends of the scintillator and fed by light guides into XP2020 photomultiplier tubes. The time-of-flight system is illustrated in Figure 3.6.

The time measurements are made relative to a beam crossing signal defined via pick-off electrodes in the storage ring. Discriminators measure times at the total pulse height and at two thresholds. An online calibration system consists of a pulser with variable voltage for calibrating the electronics and a N_2 laser system for calibrating the entire time-of-flight system.

3-2.4 The Shower Counters

One of the features that distinguished the Mark III from its predecessors was the electromagnetic calorimeter, or shower counter system, situated inside the magnetic coil. This configuration dramatically reduced the amount of material which interfered with low energy electron and photon detection. The system is a sampling calorimeter with proportional wire readout. Three sections, a barrel and two endcaps, provide a solid angle coverage of 94% of 4π steradians.

In the barrel shower counter, the radiator is a lead alloy of 6% antimony and 94% lead, while the ionizing medium is a gas mixture of 20% methane and 80% argon. The gas fills twenty-four layers of proportional cells, 1.27 cm thick. Each layer contains 360 cells circumreferentially, divided by I-shaped aluminum barriers. In each cell, an aluminum wire axially strung collects the deposited charge. Lead alloy sheets with a thickness of 0.28 cm, or 1/2 a radiation length, separate the 24 layers of proportional cells. Each of the lead sheets were fabricated in 10 azimuthal pieces and mounted on an aluminum spool 2.52 m in diameter and 3.85 m in length. Radial support is provided by five, longitudinally positioned aluminum ribs. Figure 3.7 shows the design of the barrel shower counter.

The endcap shower counters have a design similar to the barrel: 24 layers of proportional cells 1.17cm thick separated by 1/2 radiation length lead. In the endcaps, the proportional cells run vertically. To fit around the compensator magnets each endcap is divided into five sections as shown in Figure 3.8.

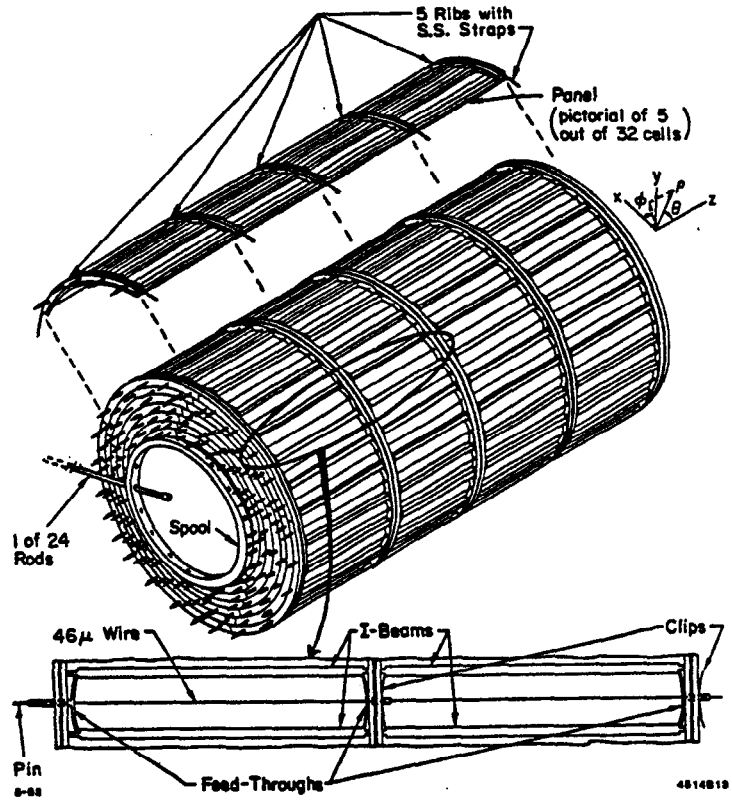

Figure 3.7 The barrel shower counter.

The wires in the first six layers of the barrel and endcap shower counters are read out individually to achieve maximum efficiency and resolution for low energy photons. Subsequent layers are readout in radial groups of three. Both ends of the wires are readout to obtain z information through charge division.

3-2.5 The Trigger

The trigger system for the Mark III uses information from the drift chamber and the time-of-flight system to discriminate physics events from the cosmic and beam gas backgrounds. Since the beams at SPEAR cross every 780 ns, the trigger makes decisions on two levels--Level 1 and Level 2--to minimize dead time. Failure to satisfy the trigger criteria at either level causes the electronics to be reset for the next beam crossing. Thirty milliseconds are required to read out the electronics when the trigger criteria is satisfied.

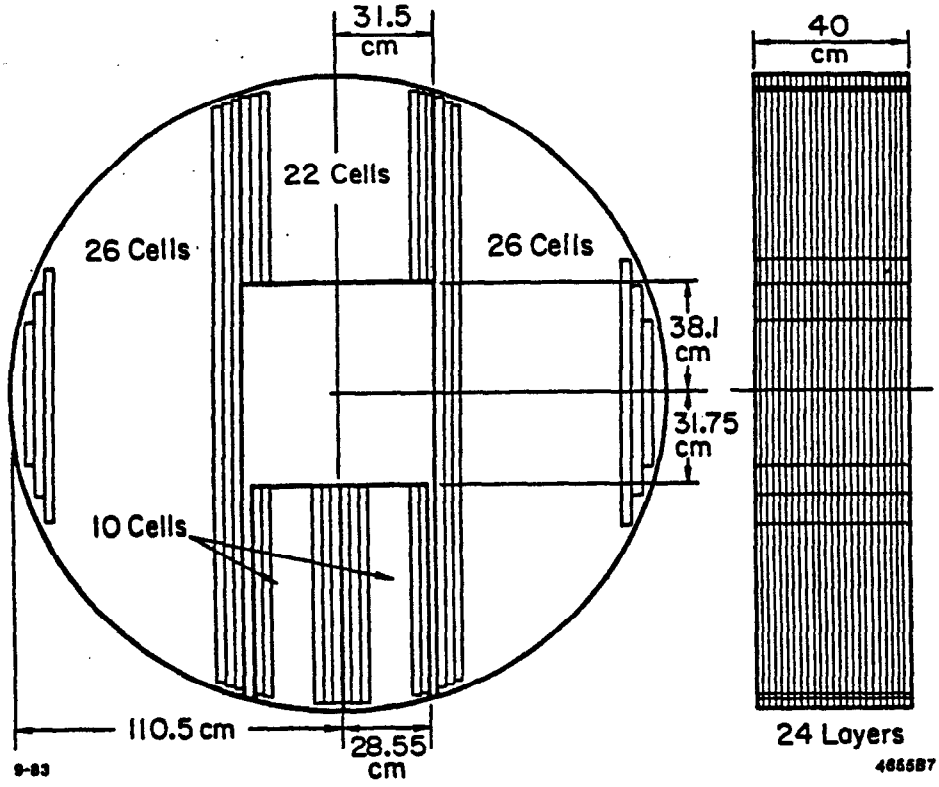

Figure 3.8 An endcap shower counter.

The Level 1 trigger can look for six different event configurations simultaneously. For the $\psi(3770)$ data runs, the "one-track" and "two-track" trigger configurations7 were enabled. The two-track trigger required two chronotron hits from Layer 1, while the one-track trigger required at least one chronotron hit in Layer 1 and a hit in a time-of-flight counter. The decision is made within 590 ns after the beam crossing, allowing enough time, should an event fail, for the capacitors in the sample and hold electronics to discharge before the next crossing. If an event satisfies the trigger criteria, the next beam crossing is sacrificed to allow time for the Level 2 trigger to process the event.

In the Level 2 trigger, rudimentary track reconstruction is performed with hits from drift chamber layers 1, 3 and 5. A circular track is defined by a coincidence between a cell in layer 5 and groups of cells in layers 1 and 3. These group patterns are identified by

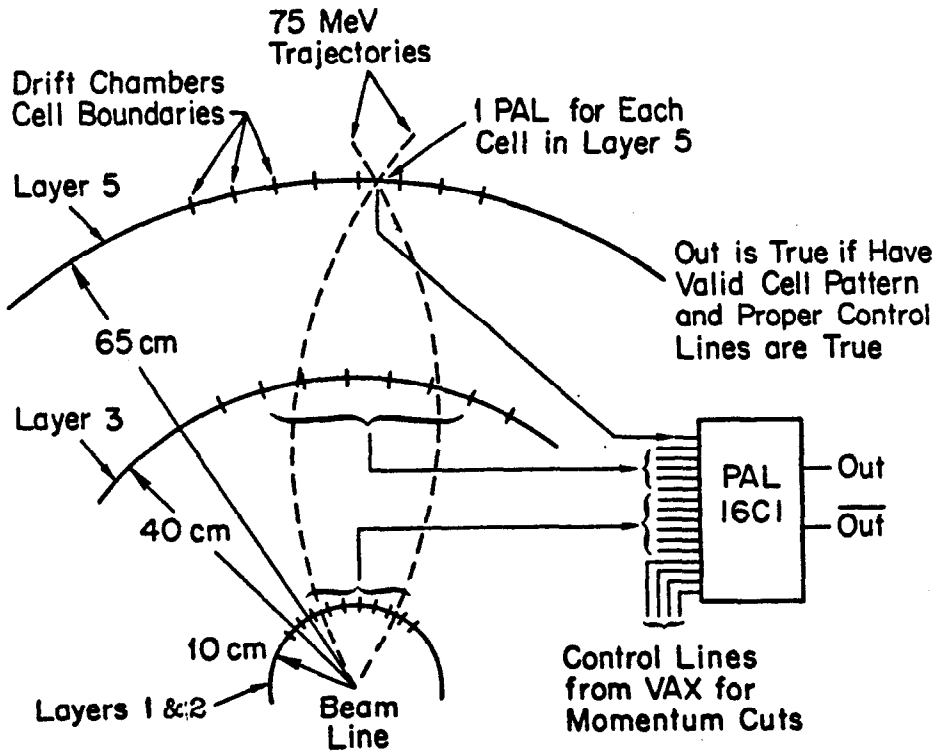

Figure 3.9 The Level 2 trigger track finding scheme.

80 programmable array logic IC's running in parallel; see Figure 3.9. The one-track trigger required only one of these group patterns, while the two-track trigger required two.

The trigger rate at the $\psi(3770)$ was 3.5 Hz with the Level 2 trigger. This rate resulted in a 10% dead time. Analysis of data taken at the $\psi(3680)$ determined that the trigger efficiency is 97%.

3-3 Offline Data Processing

3-3.1 The $\psi(3770)$ Data Samples

Figure 3.10 shows the e^+e^- hadronic cross section as a function of $\sqrt{s}$ around the charm threshold region. Lying ~40 MeV above the $D^0\overline{D}^0$ and D^+D^- thresholds, the $\psi(3770)$ resonance, also called the ψ'', has been established to be an unbound state of charm and anticharm with $J^{PC} = 1^{--}$. It resides below the $D\overline{D}^*$ and $D^*\overline{D}^*$ thresholds,

decaying dominantly to $D^0\overline{D}^0$ and D^+D^-.‡ The D's are consequently produced monochromatically, with total momenta of $P_{D^0} = 270$ MeV/c and $P_{D^+} = 242$ MeV/c. These kinematic properties have been exploited to obtain the model-independent D production cross section measurements, $\sigma_{D^0} = 5.8\pm0.5\pm0.6$nb and $\sigma_{D^+} = 4.2\pm0.6\pm0.3$nb.[24]

The Mark III $\psi(3770)$ data sample was taken during three separate running periods: in the fall of 1982, the spring of 1983 and the spring of 1984. The total integrated luminosity, as determined from the observed numbers of wide-angle Bhabha and dimuon events, is 9.56 pb^{-1} with a systematic error of 0.48pb^{-1}. With this luminosity, 27700±2400±2600 $D^0\overline{D}^0$ pairs and 20300± 2900±1100 D^+D^- pairs are estimated to have been produced.

3-3.2 The Filter

Although the Mark III trigger discriminates against events produced by beam gas and cosmic rays, a considerable number of these backgrounds are still logged with the interesting e^+e^- data; for the $\psi(3770)$ ~50% of the triggered events are from beam gas, ~40% from cosmics and only ~1% from e^+e^- interactions. To purify the sample and facilitate the offline data reconstruction, the raw data is processed by a filter program,[52] which classifies events as Bhabhas, dimuons, hadrons, cosmic rays or "junk" and discards events under the latter two classifications. The program first uses information from the time-of-flight and muon counters to distinguish dimuon events from cosmic ray events. It then examines the shower counter response and labels the events as Bhabha, hadronic, cosmic or junk based on the number of showers, the shower energy distribution and the total shower energy. Before rejection, cosmic and junk events are subjected to a fast track finding algorithm; an event is retained if it satisfies a loose set of criteria for track multiplicities and topologies. The efficiency of the filter program for retaining e^+e^- events is determined to be

‡ Some evidence exists for non-$D\overline{D}$ and non-charm decays. See, for example, Y. Zhu, Ph.D. thesis, California Institute of Technology (1988).

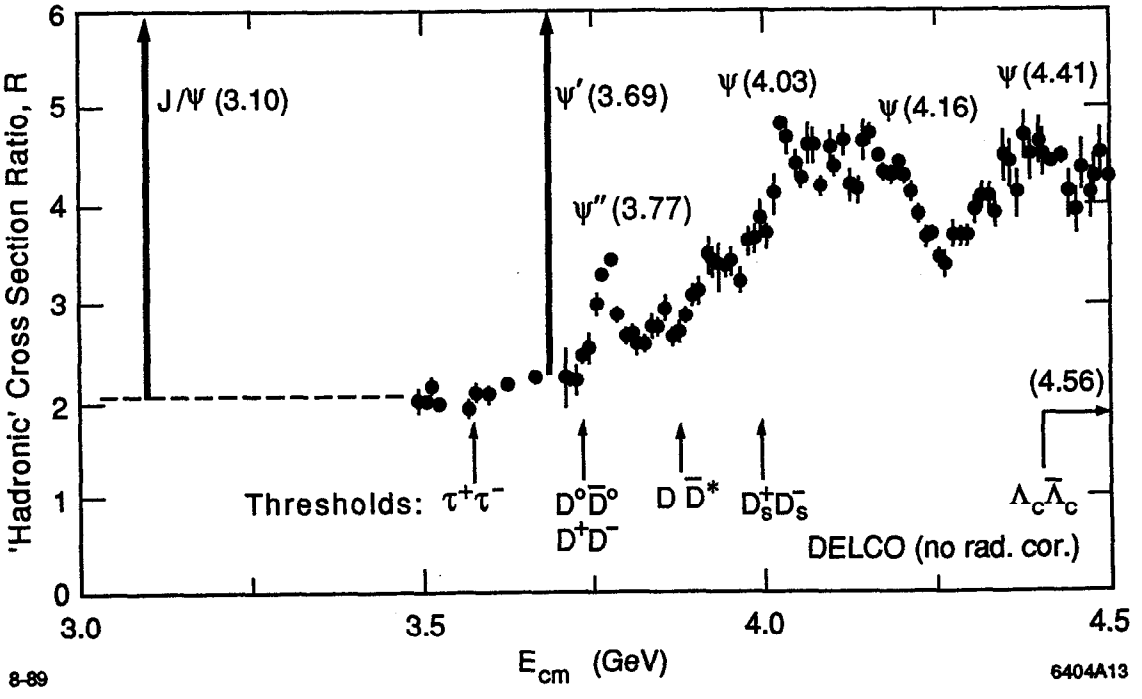

Figure 3.10 The charm sector showing the J/ψ, ψ(3680), ψ(3770), ψ(4040) and ψ(4160) resonances. Also shown are the various $D\bar{D}$, $D\bar{D}^*$ and $D^*\bar{D}^*$ thresholds.

better than 99%, based on checks which included scanning visually large samples of rejected events and varying the selection requirements.

3-3.3 Event Reconstruction

Drift Chamber Reconstruction

Charged particle trajectories in the drift chambers are found and fit by a fast, efficient track recognition algorithm.[53] The reconstruction is performed in four stages:

1) The first stage uses a non-numeric pattern recognition algorithm modelled after the online track finding trigger processor (see Section 3-2.5). Cell hits in the r-ϕ plane are registered in bit arrays. The arrays are then compared to a dictionary of 12832 possible hit patterns which would be produced by track from the event origin possessing a transverse momentum greater than 50 MeV/c.

2) At the second stage drift time information is used. Different tracks can lead to identical hit patterns, particularly when hit information is missing for a given layer. These ambiguities are resolved by analyzing local drift cell information, including track direction, curvature, and left-right cell location. In a few cases an approximate non-iterative circular fit is necessary to finally resolve the ambiguities. After all tracks are determined, the drift cell information and fast circle fit parameters are cached for the full helix fit.

3) The third stage involves z reconstruction. For 75% of the tracks the z information comes from the stereo layers 4 and 6. From these tracks the position of the event vertex is found. For those tracks with only one stereo layer information, approximately 11%, the z information is found from the stereo layer and the event vertex. For 1% of the tracks, no stereo information is present, and the vertex position and charge division from layers 1, 3, 5 and 7 are used. For some low angle tracks, approximately 4%, a shower in the endcap may be used in conjunction with the vertex position. For 4% of the tracks no z information can be obtained.

4) Finally in the fourth stage, a full piecewise iterative helix fit is performed. The values from the fast fit performed in the second stage are used as input values for the full fit. Track trajectories are parametrized by five helix parameters: $\phi \equiv$ azimuthal direction of $\vec{p}$ at the point of closest approach to the z-axis; $\kappa \equiv 1/p_{xy}$; $s \equiv \tan\lambda =$ the tangent of the dip angle; $\xi \equiv x\sin\phi - y\cos\phi =$ signed distance of closest approach to the z-axis; and $\eta \equiv z$ position at closest approach.

A momentum resolution of

$$\left(\frac{\Delta p}{p}\right)^2 = (0.015)^2\,(1+p^2)$$

has been achieved, where p is in GeV/c. The first term reflects the uncertainties due to energy losses and multiply scattering in the material before the drift chamber (Table 3.1). The angular resolutions achieved are

$$\Delta\phi = 0.002$$

Table 3.1 The materials traversed by particles; thicknesses in radiation lengths.

Material	Number of Radiation Lengths
Beam pipe	0.0040
Inner trigger chamber	0.0068
Inner wall of drift chamber	0.0016
Drift chamber gas	0.0075
Drift chamber wires	0.0015
Total	0.0214

$$\Delta \tan\lambda = 0.011.$$

After the helix fit, corrections due to energy losses are applied to the track parameters and the correlation matrix. The losses are assumed to be a function of β only[54]:

$$\Delta p = \begin{cases} \overline{\Delta p}_{\min} \sec\lambda \left(\frac{\beta}{0.94}\right)^{-2.74} & (\beta < 0.94) \\ \overline{\Delta p}_{\min} \sec\lambda & (\beta \geq 0.94) \end{cases}$$

where $\overline{\Delta p}_{\min}$ is the mean momentum loss for a minimum ionizing particle. Additional corrections are made for the uncertainty introduced by multiple scattering.[55] These corrections are calculated for each track assuming e, π, μ, K and p mass hypotheses.

Further improvements to the momentum resolution can be achieved by performing a *beam fit*, where the origin of a track is constrained to the beam location.[56] The beam fit minimizes the r-ϕ distance between the beam crossing spot and the reconstructed track orbit and is applied after the energy loss and multiple scattering corrections. After the fit the track parameters and correlation matrix are recalculated, and a χ^2 is obtained which can be used to determine good event tracks. In this thesis, $P(\chi^2) > 0.01\%$ defines a good track.

Figure 3.11 compares the results of the helix fit, energy loss corrections and beam fit corrections. The plots show how the corrections reduce the non-Gaussian tails which can arise in the mass distributions and how the corrections improve the resolution.

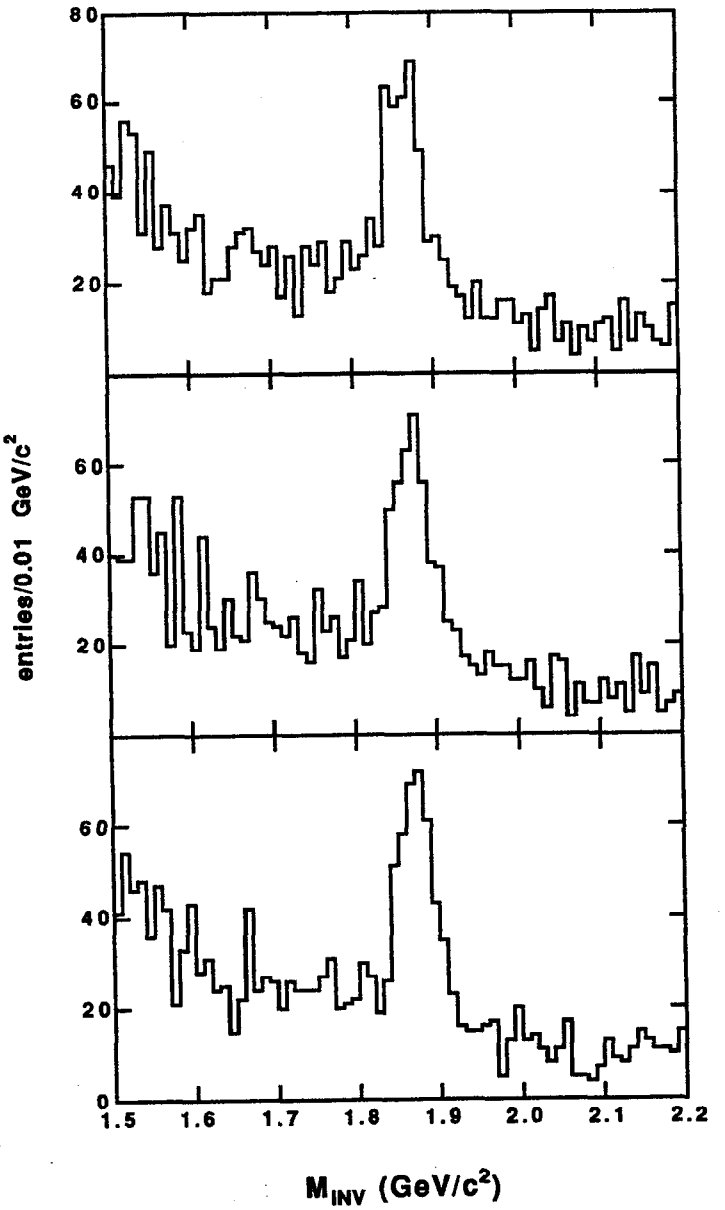

Figure 3.11 The invariant mass of $D^+ \to K^-\pi^+\pi^+$ candidates using (a) the track momenta from the helix fit, (b) the track momenta corrected for energy losses and (c) the track momenta obtained from the beam fit.

The pulse height measurements from Layer 2 are used to provide dE/dx ionization information, which can in turn be used for particle identification. The raw pulse heights are corrected for the gains and pedestals in the electronics, fluctuations in the pressure and temperature of the gas, signal arrival times and track angles within the cells. The measured energy loss is then determined from an average of the lowest 75% of the corrected pulse

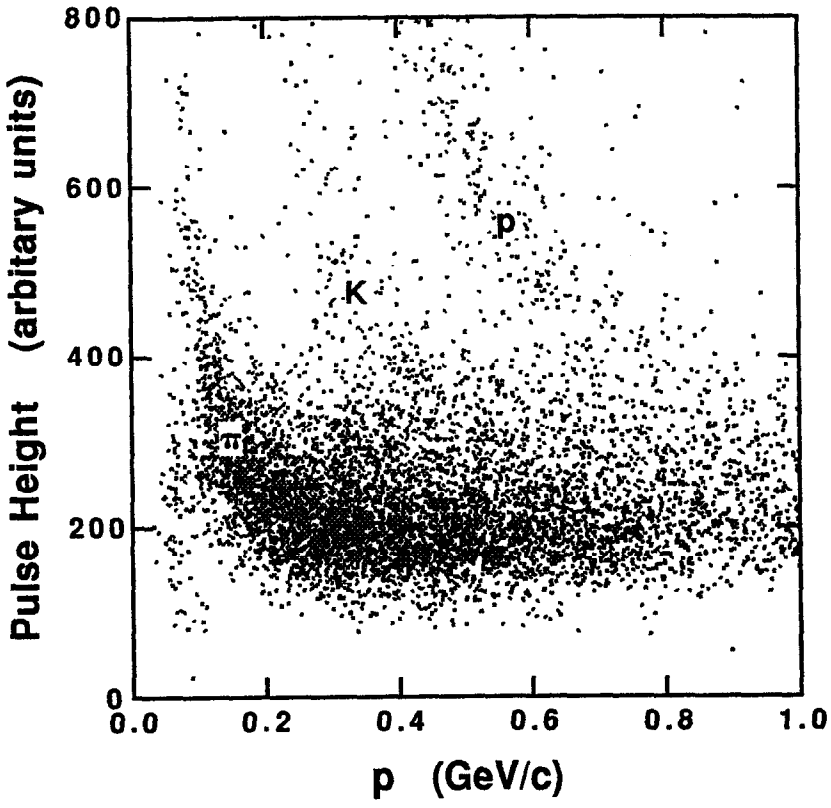

Figure 3.12 Average pulse height from layer 2 as a function of track momentum. Tracks were required to have at pulse height measurements from at least six wires.

heights; the highest 25% of the pulse heights are due to the larger asymmetric Landau fluctuations. The performance of the dE/dx system is illustrated in Figure 3.12 where the average pulse height is plotted against momentum. Clear π, K and p bands are shown. Particle identification with the dE/dx information involves studies of the residuals

$$\Delta E_i / \sigma \equiv (E_i^{pred} - E^{meas})/\sigma$$

where E_i^{pred} is the predicted energy loss assuming mass hypothesis i, E^{meas} is the measured energy loss, and σ is the resolution in E^{meas}. The predicted energy loss is calculated using the Landau formula with the Sternheimer-Peierls modification for the density effect:[57]

$$\frac{dE}{dx} = \frac{N}{\beta^2}\,[9.0 + \ln\gamma^2 - \beta^2 - \delta]$$

where δ parametrizes the density effect and N provides the normalization based on the number of pulse height measurements. The energy resolution depends on the number of pulse height measurements and is determined from Monte Carlo simulations. Separation of pions and kaons are possible up to about 0.625 GeV/c.

Time-of-Flight Reconstruction

The raw time-of-flight data consists of the timing signals extracted from the photo-multiplier tubes on each end of the time-of-flight counters. Reconstruction involves first applying calibration. Calibration constants are determined using samples of Bhabha events collected by the filter program. These corrections account for effects such as light propagation times, time variations due to differing cable lengths, and time walks associated with varying pulse heights. The reconstruction continues by associating time-of-flight hits with tracks reconstructed in the drift chamber. For each combination a χ^2 is formed between the z positions measured by the time-of-flight and by the drift chamber and is used to label the quality of the time-of-flight information for that track. Best time-of-flight z information is obtained when only one particle traverses a counter.

Particle identification by time-of-flight involves a comparison of the measured time T^{meas} with the predicted time, T_i^{pred}, assuming mass hypothesis i:

$$\begin{aligned}\Delta T_i &\equiv T_i^{\text{pred}} - T^{\text{meas}} \\ &= \frac{l}{c}\sqrt{\left(\frac{m_i c}{p}\right)^2 + 1} \; - \; T^{\text{meas}}\end{aligned}$$

where l and p are the path length and momentum of the track, determined from the drift chamber measurements, and m_i is the hypothesized mass. The time residual uncertainty, σ_i, contains factors from the time resolution of the time-of-flight counter, the uncertainty

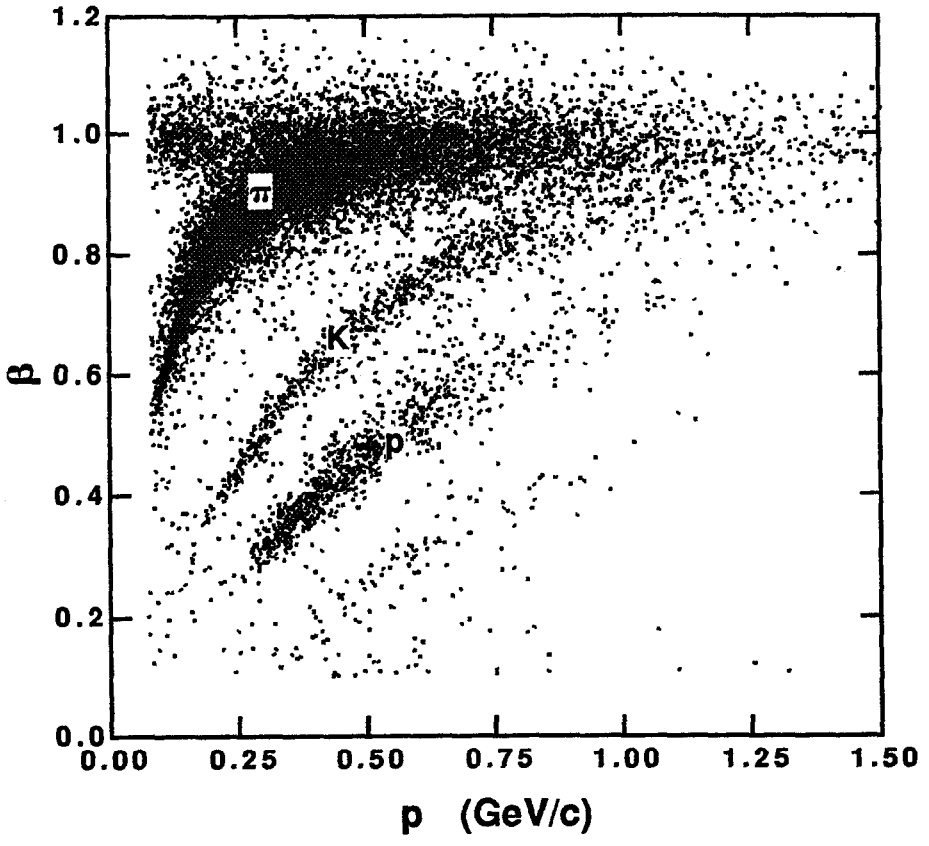

Figure 3.13 β vs.momentum for tracks in the ψ(3770) data. The π, K and p bands are clearly distinguished below $p = 1$ GeV/c. The electrons can also be seen at low momenta with $\beta = 1$.

in the predicted time arising from the drift chamber resolution, the finite size of the e^+e^- beams.

The time-of-flight resolution obtained for hadrons in the ψ(3770) data samples is ~190 ps.The performance of the system is illustrated in Figure 3.13. At least 3σ π-K separation has been achieved for tracks up to 0.8 GeV/c.

The Shower Counter Reconstruction

The shower reconstruction involves identification of hits as shower clusters. The positions of the clusters along the proportional tubes are determined by charge division; this measurement is in z for the barrel and in y for the endcaps. Clusters may be then

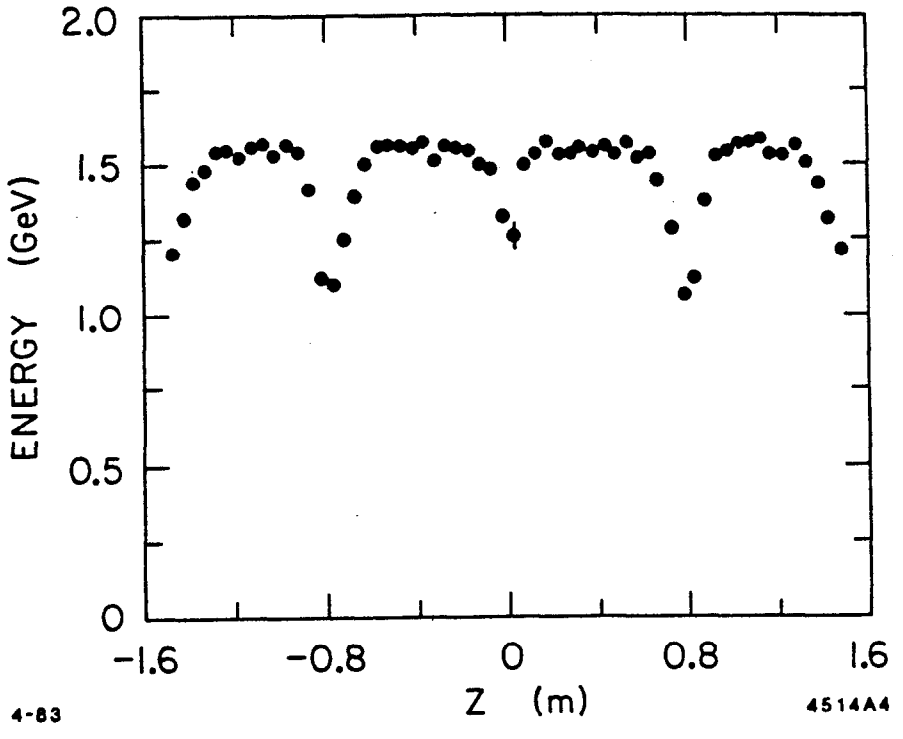

Figure 3.14 Energy deposited in the shower counters by Bhabha scattered e^+e^- pairs as a function of z.

associated with tracks seen in the drift chamber. The energy measurement is obtained by integrating the collected charge.

The performance of the shower counters is investigated using electrons from Bhabha events and photons from kinematically constrained $J/\psi \rightarrow \pi^+\pi^-\pi^0$ events. A degradation in detection efficiency about the ribs is shown in Figure 3.14. The efficiency for detecting photons as a function of photon energy is shown in Figure 3.15. The counters are fully efficient for photons down to 100 MeV in energy. The energy resolution obtained is

$$\frac{\sigma_E}{E} = \frac{18\%}{\sqrt{E}}$$

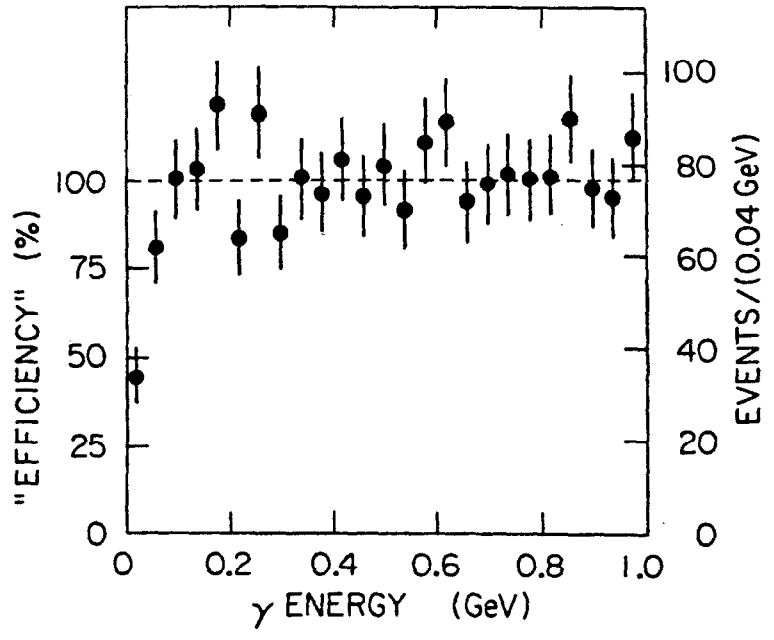

Figure 3.15 Efficiency for detecting photons as a function of photon energy.

where E is in units of GeV. The resolutions in azimuthal angle and z are $\sigma_t = 7$ mrad and $\sigma_z = 44$ mm, respectively.

3-3.4 The Hadronic Event Filter

A post-filter program exploits the fully reconstructed event information to remove the cosmic and beam-gas events that survived the initial filter program. Loose requirements are imposed on the event vertex position in both the r-ϕ plane and in z. Events with only two charged tracks must also pass cuts on p_{xy}, acolinearity, time-of-flight differences, and shower energy. Additionally, the dilepton events, found by the initial event filter, are separated out. This program reduces the event sample by approximately a factor of ten, but it has an efficiency better than 99% for retaining the interesting physics events.

3-3.5 Monte Carlo Event Generation and Detector Simulation

Monte Carlo simulation is used in this thesis to estimate efficiencies and study backgrounds. The Mark III Monte Carlo simulation involves both event generation and detector simulation.

The two generators used for the analyses in this thesis simulate the following reactions:

- $e^+e^- \rightarrow \psi(3770) \rightarrow D\bar{D}$
- $e^+e^- \rightarrow u\bar{u}(g), d\bar{d}(g), s\bar{s}(g)$

The first reaction is simulated by the Mark III $D\bar{D}$ event generator. The program produces pairs of D^0 and D^+ mesons at a specified center of mass energy with a specified energy spread; the nominal values, which correspond to the Mark III $\psi(3770)$ data sets, are 3.768 GeV/c^2 and 1.2 Mev/c^2, respectively. The D mesons are produced with a $\sin^2\theta$ angular distribution as required by the helicity constraints of $e^+e^- \rightarrow \psi(3770) \rightarrow D\bar{D}$. Each D is then "decayed" through a channel which is either specified by the user or selected randomly by the program from a dictionary of known D decay modes. When the decay channels are selected randomly, the channels are weighted by their branching ratios. The D^0 and D^+ dictionaries are listed in Table 3.2 and Table 3.3, respectively. The dictionaries contain some high multiplicity channels which have not yet been measured; these have been included in order to produce the inclusive multiplicity and momentum distributions observed in the real data.[58] Daughter particles produced by the D decays are decayed according to their known modes.

For most D decay channels, the four vectors of the daughter particles are distributed according to the density of states in the allowed phase space. For $D \rightarrow VP_1$, $V \rightarrow P_2P_3$, where V represents a vector particle and P a pseudoscalar particle, the four vectors are distributed instead with a $\cos^2\theta$ distributions, where θ is the angle between the D and either P_2 or P_3 in the rest frame of the daughters of V.

Table 3.2 The D^0 Monte Carlo dictionary.

Decay Mode	Branching Ratio (%)	Decay Mode	Branching Ratio (%)
$K^-\pi^+$	4.200	$\bar{K}^0\pi^0$	1.900
K^-K^+	0.510	$\bar{K}^0K^0$	0.255
$\pi^-\pi^+$	0.140	$\pi^0\pi^0$	0.140
$\bar{K}^0\eta$	1.500	$\pi^0\eta$	0.008
$\eta\eta$	0.016	$\bar{K}^0\eta'$	0.061
$\pi^0\eta'$	0.004	$K^-\rho^+$	8.450
$\bar{K}^0\rho^0$	0.860	$\bar{K}^0\phi$	0.860
$K^{*-}\pi^+$	5.230	$\bar{K}^{*0}\pi^0$	1.060
$\phi\pi^0$	0.026	$\bar{K}^0\omega$	3.200
$K^{*-}K^+$	0.860	$K^-\pi^+\pi^0$	2.470
$\bar{K}^0\pi^+\pi^-$	2.000	$\bar{K}^0\pi^0\pi^0$	0.800
$K^-\pi^+\pi^-\pi^+$	9.100	$K^-\pi^+\pi^0\pi^0$	14.90
$\pi^-\pi^+\pi^-\pi^+$	1.470	$\bar{K}^0\pi^+\pi^-\pi^0$	9.800
$\bar{K}^0\pi^0\pi^0\pi^0$	0.750	$\bar{K}^0\pi^+\pi^-\pi^+\pi^-$	0.850
$K^-\pi^+\pi^-\pi^+\pi^-\pi^+$	2.350	$K^-K^+\bar{K}^0$	0.850
$\phi\pi^+\pi^-$	0.170	$K^-K^+\pi^-\pi^+$	0.072
$\bar{K}^0K^-\pi^+$	0.870	$\pi^-\pi^+\pi^0$	1.110
$K^-\pi^+\pi^-\pi^+\pi^0$	8.280	$K^-\pi^+\pi^-\pi^+\pi^0\pi^0$	0.650
$K^-\pi^+\pi^0\pi^0\pi^0$	3.400	$K^-e^+\nu_e$	3.400
$K^-\mu^+\nu_\mu$	3.400	$K^{*-}e^+\nu_e$	3.400
$\pi^-e^+\nu_e$	0.300	$\pi^-\mu^+\nu_\mu$	0.300
$\rho^-e^+\nu_e$	0.300		

The reactions, $e^+e^- \rightarrow u\bar{u}(g)$, $d\bar{d}(g)$, $s\bar{s}(g)$, are simulated with the Lund Jetset 6.2 generator,[59] which is based on the Lund string fragmentation model. This generator is used to estimate backgrounds arising from the non-charm continuum. The program

Table 3.3 The D^+ Monte Carlo dictionary.

Decay Mode	Branching Ratio (%)	Decay Mode	Branching Ratio (%)
$\bar{K}^0\pi^+$	3.200	$\bar{K}^0K^+$	1.010
$\pi^0\pi^+$	0.100	$\pi^+\eta'$	0.080
$\bar{K}^{*0}\pi^+$	3.670	$\bar{K}^0\rho^+$	7.540
$\phi\pi^+$	0.770	$\bar{K}^{*0}K^+$	0.440
$K^-\pi^+\pi^+$[nr]	6.650	$\bar{K}^0\pi^+\pi^0$	1.440
$K^-K^+\pi^+$[nr]	0.540	$\pi^+\pi^-\pi^+$	0.380
$\bar{K}^0\pi^+\pi^-\pi^+$	6.600	$K^-\pi^+\pi^+\pi^0$	6.200
$\bar{K}^0\pi^+\pi^0\pi^0$	5.000	$K^-\pi^+\pi^+\pi^-\pi^+$	4.960
$\bar{K}^0\pi^+\pi^-\pi^+\pi^-\pi^+$	1.000	$K^-\pi^+\pi^+\pi^-\pi^+\pi^-\pi^+$	3.300
$\bar{K}^0\pi^+\pi^-\pi^+\pi^-\pi^+\pi^-\pi^+$	0.500	$K^-\pi^+\pi^+\pi^0\pi^0$	3.820
$\bar{K}^0\pi^+\pi^-\pi^+\pi^0$	5.800	$\bar{K}^0\pi^+\pi^0\pi^0\pi^0$	10.20
$\bar{K}^0e^+\nu_e$	8.100	$\bar{K}^0\mu^+\nu_\mu$	8.100
$\bar{K}^{*0}e^+\nu_e$	7.500	$\pi^0e^+\nu_e$	0.600
$\pi^0\mu^+\nu_\mu$	0.600	$\rho^0e^+\nu_e$	0.600
$\bar{K}^{*0}\mu^+\nu_\mu$	7.500	$\rho^0\mu^+\nu_\mu$	0.600

calculates the cross section for these processes to be 14.94 nb^{-1} at the ψ(3770). This number is used to normalize the background estimates. For the studies in this thesis the parameters of the model are left unadjusted.

After event generation, the final state particles via their four-vectors are propagated through the detector simulation. The detector responses account for the system efficiencies, including the effects of dead channels, and system resolutions. Also included are the effects due to energy loss, multiple Coulomb scattering, hadronic interactions in the detector material, photon conversions, and e bremsstrahlung. For the time-of-flight simulation, real dimuon events are used to determine the time residual distributions for each of the

time-of-flight counters. For the shower simulation a library of real showers taken from $J/\psi \rightarrow \rho\pi$ is used.[60]

The detector simulation generates the Monte Carlo raw event data in the same format as real event data. The same reconstruction and analysis programs can thus be used on both Monte Carlo and real data.

For initial background studies in this thesis, 199K $D^0\overline{D}^0$ events and 157K D^+D^- events were generated and stored on tape. These samples contain approximately 7.75× and 7.20× the numbers of $D^0\overline{D}^0$ and D^+D^- pairs estimated in the real data. For higher statistic studies specific event topologies are generated with at least 10× the number of events with that topology. For the u, d, s background studies, 1400K events were generated with the Lund Monte Carlo and stored on tape.

Chapter 4

The Tagged Event Sample

4-1 Introduction

The general technique used in this thesis for full event reconstruction is referred to as *tagging*. Since the $\psi(3770)$ decays dominantly to $D^0\overline{D}^0$ and D^+D^- pairs, fully reconstructing a D decay from a subset of tracks in an event therefore guarantees that the remaining tracks originated from the recoiling $\overline{D}$. The reconstructed D is referred to as the *tagged D* or simply the *tag*, while everything not associated with the tag is referred to as the *recoil*. Once a tag has been obtained, the recoil tracks can be analyzed for the decay modes of interest, in this case the doubly Cabibbo suppressed modes.

This chapter discusses the tagging procedure used in the balance of the thesis. Section 4-2 discusses the kinematics of $\psi(3770)$'s at rest which are exploited by the tagging procedure. Section 4-3 details the tagging event selection. Section 4-4 describes the method for estimating signals and backgrounds with tagged events. Finally, Section 4-5 discusses the kind of backgrounds which remain by tagging $D\overline{D}$ events.

4-2 Kinematics at the $\psi(3770)$

The conventional method of observing resonant signals in particle physics analyses is by selecting a set of tracks and studying plots of the invariant mass (M_{inv}):

$$M_{inv} \equiv \sqrt{\left(\sum E_i\right)^2 - \left(\sum p_i\right)^2}$$

where $(E,\ p)_i$ are the energy and three-momenta of the track i. For reconstructing D decays at the $\psi(3770)$ in the Mark III, the resolution of the invariant mass is typically 15 to 20 MeV if the modes contain only charged tracks and somewhat worse, ~30 MeV, if the

modes contain a π^0. The resolution is largely due to errors on the momentum and not on errors on the track angles. Improvements can be obtained by exploiting the pair production kinematics of D mesons near threshold. Since the D's are pair produced at the $\psi(3770)$ and the laboratory frame is also the rest frame of the resonance, each D is produced with an energy equal to that of the beam in the laboratory frame. Another mass quantity known as the beam-constrained mass (M_{beam}) can therefore be constructed by replacing the energy of the D with the energy of the beam:

$$M_{beam} \equiv \sqrt{E_{beam}^2 - \left(\sum p_i\right)^2} = \sqrt{E_{beam}^2 - P_D^2}$$

This mass quantity is simply a function of the total momentum of the decay products, $P_D = \sum p_i$. Because of the smaller energy spread of the beam (~1.2 MeV) and the low value of P_D (270 MeV/c for the D^0, 242 MeV/c for the D^+) and its error, δP_D (~10 MeV), resolutions of M_{beam} are of the order 2-3 MeV.

Another advantage of having a second independent mass variable lies in the reduction of background from misidentification. The invariant mass is sensitive to the mass hypotheses made on the decay products, while the beam-constrained mass requires that they have the correct momentum (the measured momentum is dependent on the mass-hypotheses only to the extent that the small dE/dx corrections are mass dependent). Imposing a cut on one quantity, conventionally the invariant mass, leaves the other quantity to be examined to search for a "signal".

4-3 The D^+ Tagged Event Selection

To obtain the largest tag data sample, seven of the dominant decay channels are used to form the tagged D; these modes and their measured branching fractions are listed in Table 4.1. All neutral kaons are detected through the decay chain $\overline{K}^0 \to K_S^0 \to \pi^+\pi^-$, and all neutral pions through the decay $\pi^0 \to \gamma\gamma$. The general procedure and analysis techniques used to extract a signal for each of the channels are described here. Loose criteria

Table 4.1 The D^+ tag channels and their branching fractions. The branching fraction for $K^-K^+\pi^+$ is derived from $B(D^+ \to \phi\pi^+) = 0.77 \pm 0.22 \pm 0.11\%$, $B(D^+ \to \bar{K}^{*0}K^+) = 0.44 \pm 0.20 \pm 0.10$, and $B(D^+ \to K^-K^+\pi^+[\text{nr}]) = 0.54 \pm 0.25 \pm 0.09\%$

Tag Mode	BR(%)	Reference
$\bar{K}^0\pi^+$	$3.2 \pm 0.5 \pm 0.2$	24
$K^-\pi^+\pi^+$	$9.1 \pm 1.3 \pm 0.4$	24
$\bar{K}^0\pi^+\pi^-\pi^+$	$6.6 \pm 1.5 \pm 0.5$	24
$\bar{K}^0\pi^+\pi^0$	$10.2 \pm 2.5 \pm 1.6$	24
$\bar{K}^0K^+$	$1.01 \pm 0.32 \pm 0.17$	24, 20
$K^-K^+\pi^+$	$1.21 \pm 0.33 \pm 0.13$	24, 20
$K^-\pi^+\pi^+\pi^0$	$5.8 \pm 1.2 \pm 1.2$	23

has been chosen to maximize the efficiency. Knowing the tag efficiency is not critical--only proper counting of the detected tags for the "denominator" is important.

Tag reconstruction begins with the charged track selection. All charged tracks must have a good helix fit with a well measured momentum Z component. Their parameters must also be corrected for energy losses and multiple scattering according to the assigned mass hypotheses. Tracks not associated with K^0_S reconstruction are further required to have a successful beam fit. No requirement is made on the track with respect to the fiducial volume of the detector.

To reduce the combinatoric backgrounds, loose particle identification is imposed with the TOF or dE/dx measurements. The following algorithm is used to determine if a track is consistent with a given mass hypothesis:

- If the TOF measurement has a good quality flag it must satisfy the requirement

$$\left|\frac{\Delta T_i}{\sigma_i}\right| < 5$$

where ΔT_i is the difference between T_i^{pred} and T^{meas} for mass hypothesis i, and σ_i is the mass-dependent uncertainty on ΔT_i.

- If no identification has been made with TOF then the dE/dx measurement is considered, provided the momentum of the track is less than 0.625 GeV/c and the measurement was obtained from six or more track hits. With a good dE/dx measurement, the track must satisfy the requirement:

$$-3.0 < \left|\frac{\Delta E_i}{\sigma}\right| < 4.5$$

where ΔE_i is the difference between E_i^{pred} and E^{meas} for mass hypothesis i, and σ is the resolution of E^{meas}.

If no identification is made with either system, the track is defaulted to the pion hypothesis. This algorithm allows a track to be identified as *both* a kaon and a pion if the hypotheses are consistent. If K and π identifications are made, both hypothesis are considered in reconstructing the D decays. The issue of double counting that this introduces will be discussed below.

This standard algorithm is used in all cases except the Cabibbo suppressed D^+ tag $K^-K^+\pi^+$ where the background in the invariant mass plot peaks near the mass of the D^+. To improve on the signal-to-noise in this channel, tighter particle identification cuts are imposed on the kaon identification:

- $\Delta T_K > -0.6$ns ($\sim 3\sigma$) if identified by TOF,
- $\Delta E_K > -1.5\,\sigma$ if identified by dE/dx.

In the identification of neutral tracks in the shower counters (photons from the physics events), one has to address a number of processes which can produce both real and

spurious showers. The major source of these "fake photons" arises from hadronic interactions between π's or K's and the lead material in the shower counter; the secondary particles from these interactions can "split-off" and create a shower which the pattern recognition does not associate to the main shower. Other sources of fake photons are particle decays, back splash (albedo), and electronic noise. Although none of these processes are modelled by the Monte Carlo, a standard set of selection criteria has been established which significantly suppresses these fake photons. A shower is selected as an *isolated* photon if

- the energy of the shower E_γ is greater than 30 MeV
- number of layers hit is two or more
- the first layer hit is before layer seven, i.e. within ~3 radiation lengths from the inner radius of the counter
- $|\cos\theta| < 0.95$ where θ is the angle between the shower momenta and the momenta of the nearest charged track.

Once a set of charged tracks and isolated photons have been selected, multiplicity requirements are imposed. The number of charged tracks and the number of isolated photons must be greater than or equal to the numbers required by the tag decay mode.

Tag reconstruction proceeds with the reconstruction of K_S^0's. For each pair of oppositely charged tracks with consistent pion hypotheses, the crossing points of the track circles are located in the xy plane. The correct crossing point is chosen, and the track parameters and error matrices are recalculated at the secondary vertex. A pair is then retained as a K_S^0 combination if

- $|M_{\pi\pi} - M_{K0}| < 30$ MeV/c^2, where $M_{\pi\pi}$ is the invariant $\pi^+\pi^-$ mass with the recalculated track parameters and $M_{K0} = 497.671$ MeV/c^2.
- the displacement of the decay vertex transverse to the beam, l_{xy}, is greater than 2mm

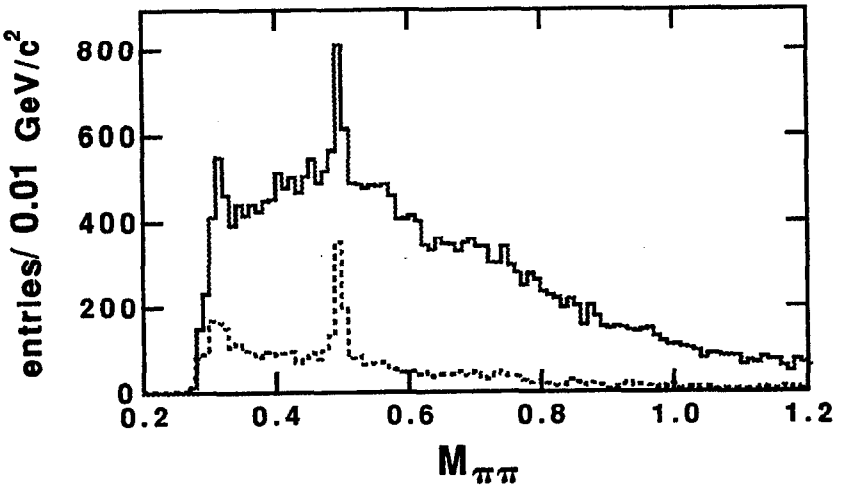

Figure 4.1 Inclusive $\pi^+\pi^-$ mass distribution before (solid) and after (dotted) the cuts on l_{xy} and $P(\chi^2_{xy})$ (see text). The peek near the $\pi^+\pi^-$ threshold is the result of misidentified photon conversions in the detector.

- the momentum vector of the $\pi^+\pi^-$ pair aligns with the position vector of the decay vertex crossing point in the transverse plane. This condition is imposed by requiring $P(\chi^2_{xy}) > 0.01$, where χ^2_{xy} is the chi-square between the two vectors in the xy plane.

The latter two cuts are imposed to reduce the combinatoric background under the K^0_S mass peak as demonstrated in Figure 4.1.

In the π^0 reconstruction, to improve on the modest energy resolution of the shower counters, all photon pairs are subjected to a one-constraint kinematic fit in which the energies and positions of the showers are adjusted, within errors, to form an invariant mass equal to the π^0 mass. The fit is considered successful if the confidence value for the χ^2 is greater than 0.1. After the fit, an additional cut on the fitted photon energies is imposed to reduce the background which arises when fake showers or incorrect photons have replaced the real, lower energy photons in the very asymmetric π^0 decays. For the $\overline{K}^0\pi^+\pi^0$ tag, the fitted energies must be greater than 50 MeV, while for the $K^-\pi^+\pi^+\pi^0$ tag, because of the larger backgrounds observed, the fitted energies must be greater than 150 MeV.

Photon pairs which pass these cuts are retained as π^0 candidates, and the fitted photon momenta are used in the full reconstruction of the D tag. The multiple counting problem introduced by the possibility of more than one two-photon combination satisfying this criteria is discussed below.

Finally for the full D reconstruction, all tracks with consistent mass hypotheses and, if appropriate, reconstructed K_S^0's and π^0's are permuted to form the invariant and beam-constrained masses. A cut on the invariant mass from 1.819 to 1.919 GeV/c^2, corresponding to about 2.5 σ around the nominal D mass, is imposed to extract a signal in the beam-constrained mass plot.

As mentioned above the loose particle identification criteria and the π^0 reconstruction can allow an event to be counted more than once as a tag candidate. The multiple counting can occur in two ways:

1) Two or more different tag channels can be reconstructed for a given event; this can occur, for example, when both D's in an event can be reconstructed.

2) Two or more possible combinations of tracks can yield a consistent tag for a given channel; tag modes with higher multiplicity like $D^+ \rightarrow \bar{K}^0\pi^+\pi^-\pi^+$ and those containing a π^0 tend to be more susceptible to this problem.

To count the actual number of tagged events in an unbiased manner, the following criteria is used to select only one tag combination per event:

1) If more than one tag channel can be reconstructed, select the channel with the largest signal-to-noise ratio; the tag modes are listed in Table 4.1 according to the selection order.

2) For the all charged tags, $D^+ \rightarrow \bar{K}^0\pi^+$, $K^-\pi^+\pi^+$, $\bar{K}^0\pi^+\pi^-\pi^+$, $\bar{K}^0K^+$, and $K^-K^+\pi^+$, if more than one combination of tracks forms the tag, choose

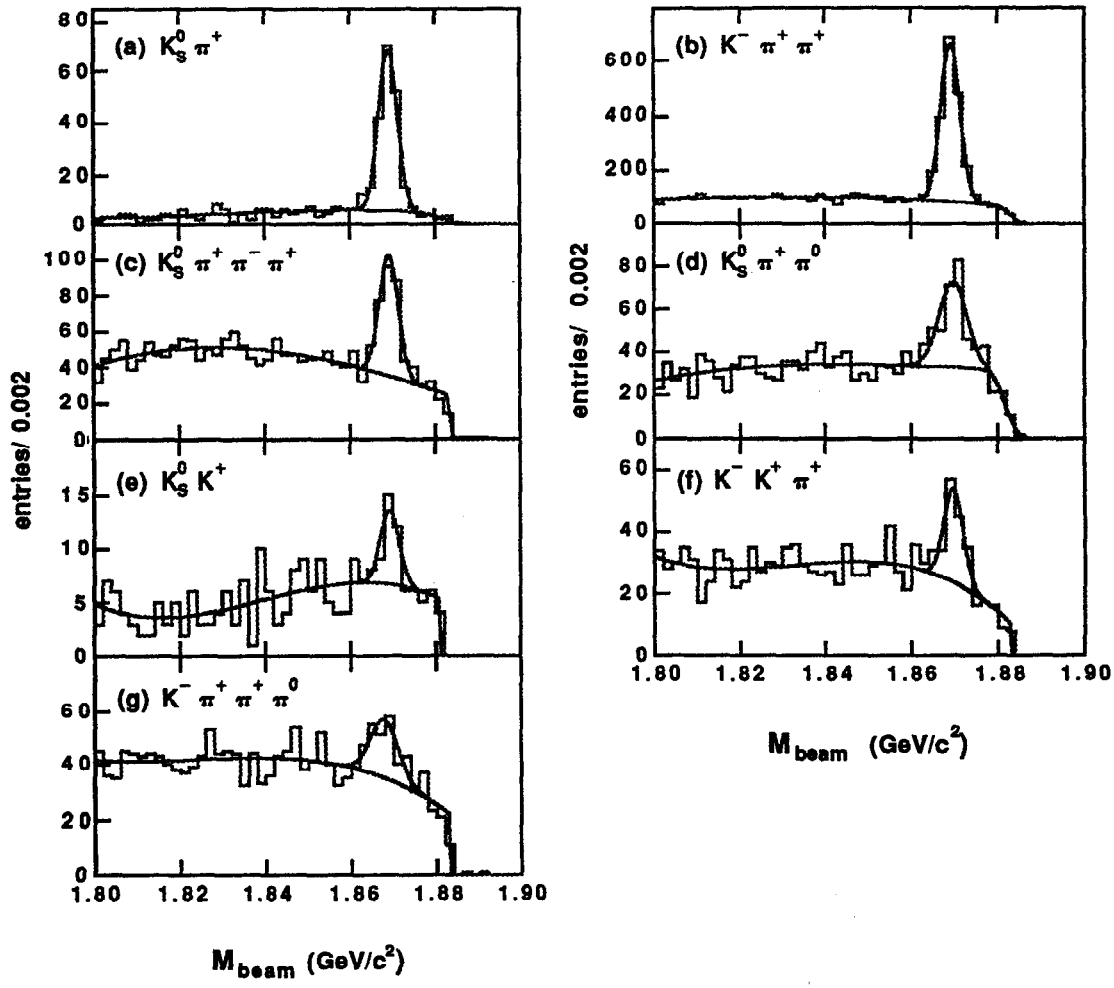

Figure 4.2 The D^+ tags.

the combination whose lowest momentum track has the largest momentum of all the combinations.

3) For the two tags containing neutrals, $D^+ \to \overline{K}^0\pi^+\pi^0$, $K^-\pi^+\pi^+\pi^0$, if more than one combination of photon pairs can reconstruct the tag, choose the combination with the lowest χ^2 from the π^0 fit.

The D^+ tag sample for each mode is displayed in Figure 4.2 after this selection procedure. The number of tags above background is determined by a binned log likelihood fit to a function of the form

Table 4.2 The number of D^+ tags.

Channel	Number of Events
$\bar{K}^0\pi^+$	$176 \pm 5 \pm 2$
$K^-\pi^+\pi^+$	$1601 \pm 19 \pm 29$
$\bar{K}^0\pi^+\pi^-\pi^+$	$182 \pm 10 \pm 16$
$\bar{K}^0\pi^+\pi^0$	$191 \pm 17 \pm 13$
$\bar{K}^0K^+$	$17 \pm 5 \pm 3$
$K^-K^+\pi^+$	$84 \pm 9 \pm 13$
$K^-\pi^+\pi^+\pi^0$	$98 \pm 13 \pm 9$
Total	$2350 \pm 33 \pm 40$

$$f(m;p_i) = \{1 + p_1 m + p_2 m^2 + p_3 m^2\}\frac{1-\mathrm{erf}[(m-m_1)/\sigma_1]}{2} + p_4 e^{\frac{(m-m_0)^2}{2\sigma_0^2}}$$

where m is the mass variable and $p_i \equiv \{p_1, p_2, p_3, p_4, m_0, \sigma_0, m_1, \sigma_1\}$ are the parameters of the fit. The polynomial in the first term describes the background, while the Gaussian term parametrizes the signal. The error function represents a Gaussian-smeared Heavyside function to account for the phase space cut-off near m = 1.884 GeV/c^2. For the tag modes without a π^0, a fit is first made to the $K^-\pi^+\pi^+$ distribution with all parameters free. This fit determines the resolution of the D signal for the all-charged modes; a value of 0.0022 ± 0.0001 GeV/c^2 was obtained. Fits for the remaining all-charged modes are then performed with σ_0 fixed at 0.0022 GeV/c^2. For the two modes with a π^0, the resolution was determined by a fit to Monte Carlo; a resolution of 0.0032 ± 0.0001 GeV/$c^2$was obtained. Fits to the data are then performed with σ_0 fixed to 0.0032 GeV/c^2.

The numbers of tags found in each of the seven channels are given in Table 4.2 with statistical and systematic errors respectively; a total of 2350±33±40 were obtained.The number for each mode is calculated by integrating the fitted background

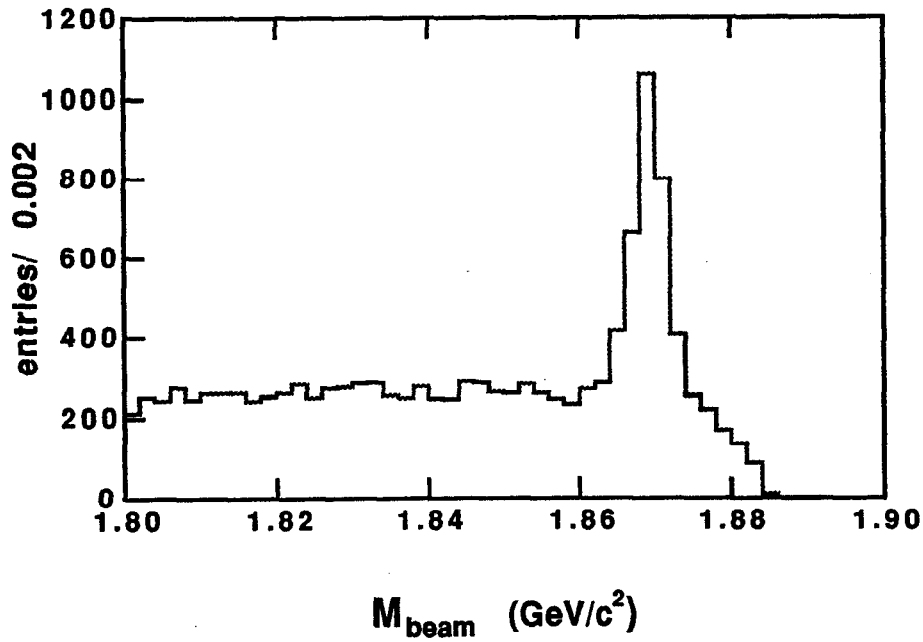

Figure 4.3 The sum of the seven tag samples.

function over the tag signal region and subtracting that number from the total number of events in the region. The signal region is defined to be between 1.862 and 1.876 GeV/c^2 for the all-charged modes and to be between 1.859 and 1.879 GeV/c^2 for the modes with a π^0; these regions are approximately $\pm 3\sigma$ intervals about the mass peak. Note that the statistical errors reflect the uncertainty in the number of background events under the peak. No contribution from the tags ($\sim\sqrt{n_{tag}}$) is present; one is only interested in the collected number of $D^{\pm}$ tags. For example, if there were no background, there would be no error on the number of tags. The systematic errors on the number of tags were determined by varying the polynomial in the background functions for each of the fits; polynomials of different orders were used as well as initial values for the function parameters.

Figure 4.3 combines the seven tag samples. The background level is low with a signal-to-noise ratio of 1.54.

4-4 Estimating Expected Numbers of Events

While the tagging procedure counts only one tag per event, all reconstructed tags are tested when searching for doubly Cabibbo suppressed candidates. The removal of candidates associated with multiple tags would introduce a systematic uncertainty from the multiple tag reconstruction efficiency. Instead, the number of events for a given signal is calculated according to:

$$n_s = n_{tag} B_s \varepsilon_s C$$

where n_s is the number of signal events, n_{tag} is the number of tags, B_s is the branching ratio of the signal decay mode, ε_s is the reconstruction efficiency, and C is a small correction for multiple counting:

$$C = \frac{1}{1 - \frac{1}{2}\sum_i \varepsilon_{tag.i} B_{tag.i}}$$

where $\varepsilon_{tag.i}$ and $B_{tag.i}$ are the reconstruction efficiency and the branching ratio for tag mode i, respectively.

The derivation of this formula follows. Let n_{tot} be the number of produced $D\overline{D}$ pairs. The number of produced D's is then $2n_{tot}$, and the number of produced D's that decay through the tag mode i is $2n_{tot}B_{tag.i}$. Of these D's, $2n_{tot}B_{tag.i}\varepsilon_{tag.i}$ are reconstructed. This number is the number of events where only one of the two D's has been reconstructed plus twice the number of events where both D's have been reconstructed. Since the tagging procedure only counts one tag per event, the number of events tagged twice has to be subtracted from $2n_{tot}B_{tag.i}\varepsilon_{tag.i}$ to reflect the number of tagged events. Since the number of events tagged twice is $n_{tot}B^2_{tag.i}\varepsilon^2_{tag.i}$, the number of tags in mode i is

$$2n_{tot}B_{tag\,i}\varepsilon_{tagi}\,(1 - \frac{1}{2}B_{tag.i}\varepsilon_{tag.i})$$

Generalizing to all tag modes, the number of tags, n_{tag}, becomes

$$n_{tag} = 2n_{tot}(\sum_i B_{tag.i}\varepsilon_{tag.i})(1 - \frac{1}{2}\sum_j B_{tag.i}\varepsilon_{tag.i})$$

Now, opposite a tag, consider reconstructing some signal decay mode with a branching ratio of B_s and an efficiency of ε_s (for simplification of this discussion, ε_s is assumed to be independent of the tag). The number of reconstructed events, n_s, is

$$n_s = 2n_{tot}B_s\varepsilon_s\sum_i \varepsilon_{tag.i}B_{tag.i}$$

$$= n_{tag}B_s\varepsilon_s\frac{1}{1-\frac{1}{2}\sum_i \varepsilon_{tag.i}B_{tag.i}}$$

$$= n_{tag}B_s\varepsilon_s C$$

thus obtaining the correction factor C.

For the analyses which use all the tags, the correction factor was found to be

$$C = 1.032.$$

For the analyses which use the tags containing only charged tracks, the correction factor was found to be

$$C = 1.028.$$

The uncertainties on these correction factors are considered negligible, since the uncertainties on n_s, for example will be dominated by the uncertainties from n_{tag}, ε_s and B_s.

4-5 Backgrounds in the Tagging Analyses

In the following analyses, where doubly Cabibbo suppressed decays are searched for opposite the tags, backgrounds arise from two production sources: (1) charm ($D\overline{D}$) production and (2) u, d and s production. Since the events are tagged, the major

backgrounds arise from the former. Two categories of $D\bar{D}$ backgrounds are defined: Class I and Class II.

Class I backgrounds are $D\bar{D}$ events where *one* of the two decay modes is correctly reconstructed to form the tag, while the other decay mode is incorrectly reconstructed as the desired signal. An example of a Class I background event for the $D^+ \to K^+\pi^0$ search (Chapter 6) would be an event produced as $D^+ \to \bar{K}^0 K^+$ vs. $D^- \to K^+\pi^-\pi^-$, where $\bar{K}^0 \to K_S^0 \to \pi^0\pi^0$, and detected as a D^- tag $\to K^+\pi^-\pi^-$ plus a D^+ incorrectly $\to K^+\pi^0$. Often the term, Class I background, will refer simply to the D decay which has been incorrectly reconstructed, e.g. $D^+ \to \bar{K}^0 K^+$ is a Class I background.

The number of Class I background events, $n^{\rm I}_{\rm back}$, which are expected to contribute to a signal, is calculated according to:

$$n^{\rm I}_{\rm back} = n_{\rm tag}\, B_{\rm b}\, \varepsilon_{\rm b}\, C$$

where $B_{\rm b}$ and $\varepsilon_{\rm b}$ are, respectively, the branching fraction and acceptance for the background process, and C is the correction factor for multiple counting, discussed in the previous section. Class I backgrounds are generally the dominant backgrounds in tagging analyses.

Class II backgrounds are $D\bar{D}$ events where both decay modes are incorrectly reconstructed. An example of a Class II background event for the $D^+ \to K^+\pi^-\pi^+$ analysis (Chapter 5) is $D^+ \to \bar{K}^0\pi^+\pi^-\pi^+$ vs. $D^- \to K^+\pi^-\pi^-$. Since the $\bar{K}^0$ is identified through the channel $\bar{K}^0 \to K_S^0 \to \pi^+\pi^-$, it can be misidentified as a K^0. Wrong combinatorics then yield the final state $K^0\pi^+\pi^-\pi^-$ vs. $K^+\pi^-\pi^+$. Both D^+D^- and $D^0\bar{D}^0$ events may contribute to Class II backgrounds, as will be subsequently shown. Since the tag is not correctly reconstructed, the number of Class II background events, $n^{\rm II}_{\rm back}$, is calculated according to

$$n^{\rm II}_{\rm back} = 2\, n_{D\bar{D}}\, B_{\rm b} B_{\bar{\rm b}} \varepsilon_{\rm b,\bar{b}}$$

where $n_{D\overline{D}}$ is the number of produced $D\,\overline{D}$ events, B_{b} and $B_{\overline{b}}$ are the branching fractions of the two D decay channels, and $\varepsilon_{b,\overline{b}}$ is the acceptance of the event topology as the signal.

Chapter 5

Search for $D^+ \to K^+\pi^-\pi^+$

5-1 Introduction

The first doubly Cabibbo suppressed decay mode that is searched for is $D^+ \to K^+\pi^-\pi^+$; it is experimentally, the most accessible mode of the D^+, having three charged particles and no neutrals in the final state. Of the three doubly Cabibbo suppressed final states evaluated in this thesis, it is the excellent mass resolution and modest combinatoric backgrounds for this final state only that allow it to be approached with *both* inclusive (untagged) and full reconstruction (tagged) analyses. The balance of the final states, having neutrals, can only be studied using the tagged technique and full event reconstruction.

The detailed results of the untagged analysis for $D^+ \to K^+\pi^-\pi^+$ are presented in Appendix 1. For clarity, they are summarized in Section 5-2 since they motivate the search for explicit candidates of fully reconstructed events. The balance of this chapter presents the tagged search for $D^+ \to K^+\pi^-\pi^+$, including the resonant channels $D^+ \to K^+\rho^0 \to K^+(\pi^-\pi^+)$ and $D^+ \to K^{*0}\pi^+ \to (K^+\pi^-)\pi^+$ and the nonresonant final state $D^+ \to K^+\pi^-\pi^+$. Section 5-3 describes the initial event selection for $K^+\pi^-\pi^+$. Section 5-4 discusses the major backgrounds that arise from charm production, and it describes the cuts added to reduce them. Section 5-5 gives the results of the analysis on the data and includes various analysis tests and estimates of the efficiency and level of remaining background. Section 5-6 uses those estimates to calculate the upper limit on the branching fraction for $D^+ \to K^+\pi^-\pi^+$. Finally, Section 5-7 describes the resonant substructure analysis performed to extract upper limits specifically for $D^+ \to K^+\rho^0$, $K^{*0}\pi^+$ and $K^+\pi^-\pi^+$[nr].

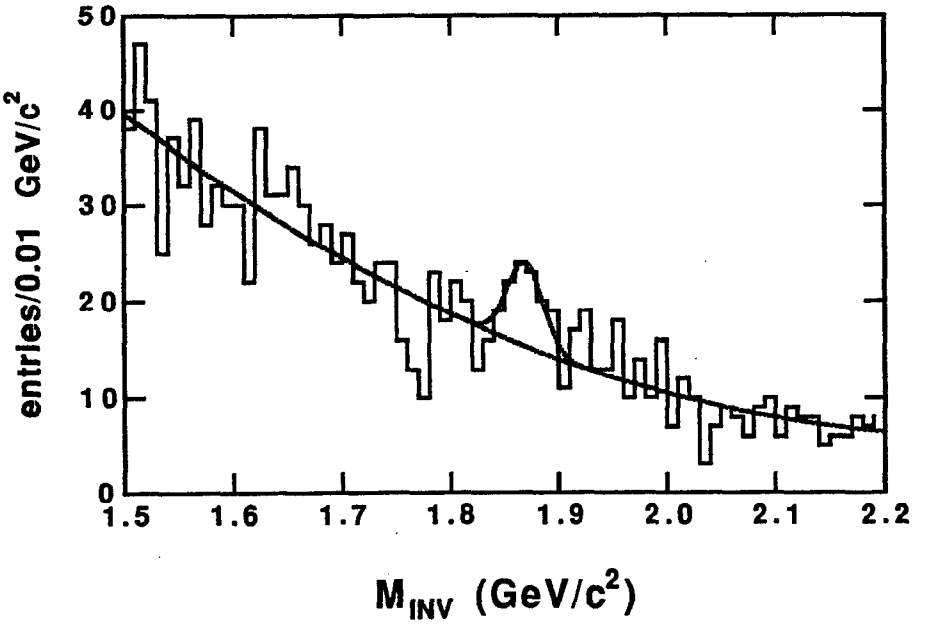

Figure 5.1 Invariant mass distribution for inclusive $K^+\pi^-\pi^+$.

5-2 Summary of Inclusive (Untagged) Analysis of $D^+ \to K^+\pi^-\pi^+$

In Appendix 1 the details of an analysis to isolate a signal for $D^+ \to K^+\pi^-\pi^+$ inclusively in the $\psi(3770)$ data set is presented. Strict fiducial and particle identification cuts are applied to reduce combinatoric background. A signal of 37.1±12.4±5.5 events above the combinatoric background is observed in this channel; see Figure 5.1. With the analysis cuts employed, only $2.5\pm0.9^{+1.0}_{-0.9}$ background events are expected to peak under this signal. This result represents only a ~2.5 σ significance above the smooth background. An efficiency of $22.0\pm0.3^{+2.1}_{-3.3}$% leads to an estimate of the branching fraction $B(D^+ \to K^+\pi^-\pi^+)$ = $0.39^{+0.09+0.09}_{-0.08-0.08}$%. Relative to the Cabibbo allowed decay, $D^+ \to K^-\pi^+\pi^+$, a value of $|\bar{\rho}_{K\pi\pi}|^2 = 18.3^{+3.6}_{-3.2}\pm4.0$ is calculated. This surprising result strongly motivates the search for fully reconstructed events in this channel and in other simple channels, in the balance of this thesis.

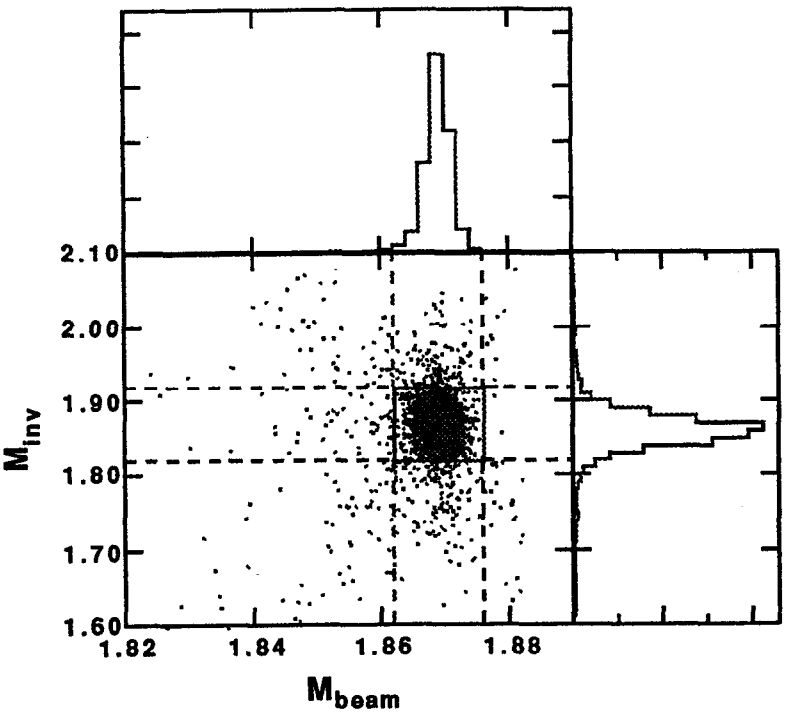

Figure 5.2 Monte Carlo $D^+ \to K^+\pi^-\pi^+$ (generated opposite $D^- \to K^0\pi^-$). The box delimits the signal region.

5-3 Tagged Analysis of $D^+ \to K^+\pi^-\pi^+$--Event Selection

Given a tagged event as described in Section 4-3, selection of $D^+ \to K^+\pi^-\pi^+$ candidate events proceeds as follows:

- Three charged tracks with a good helix fit must be found in the recoil. The tracks must also be corrected for energy losses and have a good beam fit.
- The net charge of the event must be zero.
- The recoil tracks are permuted according to the $D^+ \to K^+\pi^-\pi^+$ hypothesis; the mass hypotheses assigned to the tracks must be consistent with the TOF and dE/dx information. This *initial* particle identification is the same as that used in the tag event selection.

To observe a signal, a scatterplot of the invariant mass (M_{inv}) versus beam-constrained mass (M_{beam}) is made from the selected track combinations. Figure 5.2 shows the

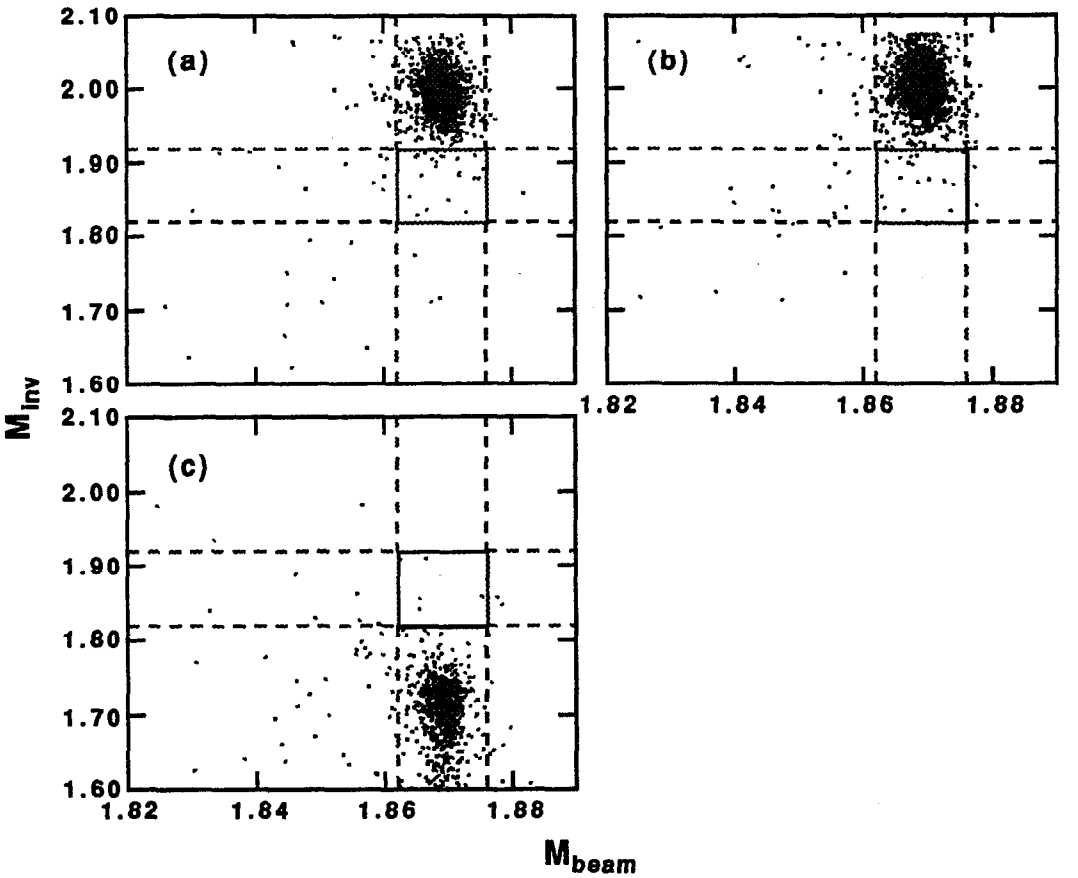

Figure 5.3 (a) $D^+ \to \bar{K}^0\pi^+$, $\bar{K}^0 \to K^0_S \to \pi^+\pi^-$; (b) $D^+ \to \pi^+\pi^-\pi^+$; and (c) $D^+ \to K^-K^+\pi^+$ when reconstructed as $D^+ \to K^+\pi^-\pi^+$.

scatterplot for the expected signal, along with the two projections. The scatterplot aids the identification and rejection of background events. True $D^{\mp}$ meson combinations will have a fixed momentum (242 ± 14 MeV/c^2) and therefore have a beam-constrained mass centered on the mass of the D^+, independent of errors in the particle mass assignments. The invariant mass provides the rejection against the backgrounds which occur from single particle misidentifications--specifically, $D^+ \to \pi^+\pi^-\pi^+$ (including $D^+ \to \bar{K}^0\pi^+$, $\bar{K}^0 \to K^0_S \to \pi^+\pi^-$) and $D^+ \to K^-K^+\pi^+$. With a correctly reconstructed tag, $\pi^+\pi^-\pi^+$ forms $K^+\pi^-\pi^+$ when a pion is misidentified, and $K^-K^+\pi^+$ forms $K^+\pi^-\pi^+$ when a kaon is misidentified. These backgrounds produce reflections at approximately ±120 MeV/c^2 from the D^+ invariant mass, as illustrated in Figure 5.3.

The signal region is defined by a $\pm 3\sigma$ cut in M_{beam} and a $\pm 2\sigma$ cut in M_{inv}:

- $1.819 < M_{inv} < 1.919$ GeV/c^2
- $1.862 < M_{beam} < 1.876$ GeV/c^2

Together the cuts retain approximately 88.4% of the Monte Carlo signal, while rejecting better than 98% of the backgrounds from single particle misidentifications.

Figure 5.7(a) shows the events retained after the initial event selection requirements. Twenty candidate events lie within the signal region, and 60 events lie outside. As anticipated, a vertical band is formed largely from particle misidentifications.

5-4 Major Backgrounds to $D^+ \to K^+\pi^-\pi^+$

In general, the major backgrounds to $D^+ \to K^+\pi^-\pi^+$ appear to arise from the occurrence of at least two errors in the event selection procedure, e.g. two particle misidentifications. These backgrounds are of the Class I category, where only the recoil is incorrectly reconstructed. Backgrounds also come from Class II category, where both the tag and recoil have been incorrectly reconstructed. The Class I backgrounds are discussed first (Section 5-4.1), followed by the Class II backgrounds (Section 5-4.2). The data reduction cuts introduced to remove the backgrounds are then discussed (Section 5-4.3). The application of these cuts on the data is postponed until Section 5-5.

5-4.1 The Class I Backgrounds

The major Class I backgrounds arise from two D^+ decay channels:

- $D^+ \to \bar{K}^0 K^+$, $\bar{K}^0 \to K^0_S \to \pi^+\pi^-$--a Cabibbo suppressed mode where the K^0_S is not identified.
- $D^+ \to K^-\pi^+\pi^+$--a Cabibbo allowed mode followed by a double misidentification between the kaon and a pion.

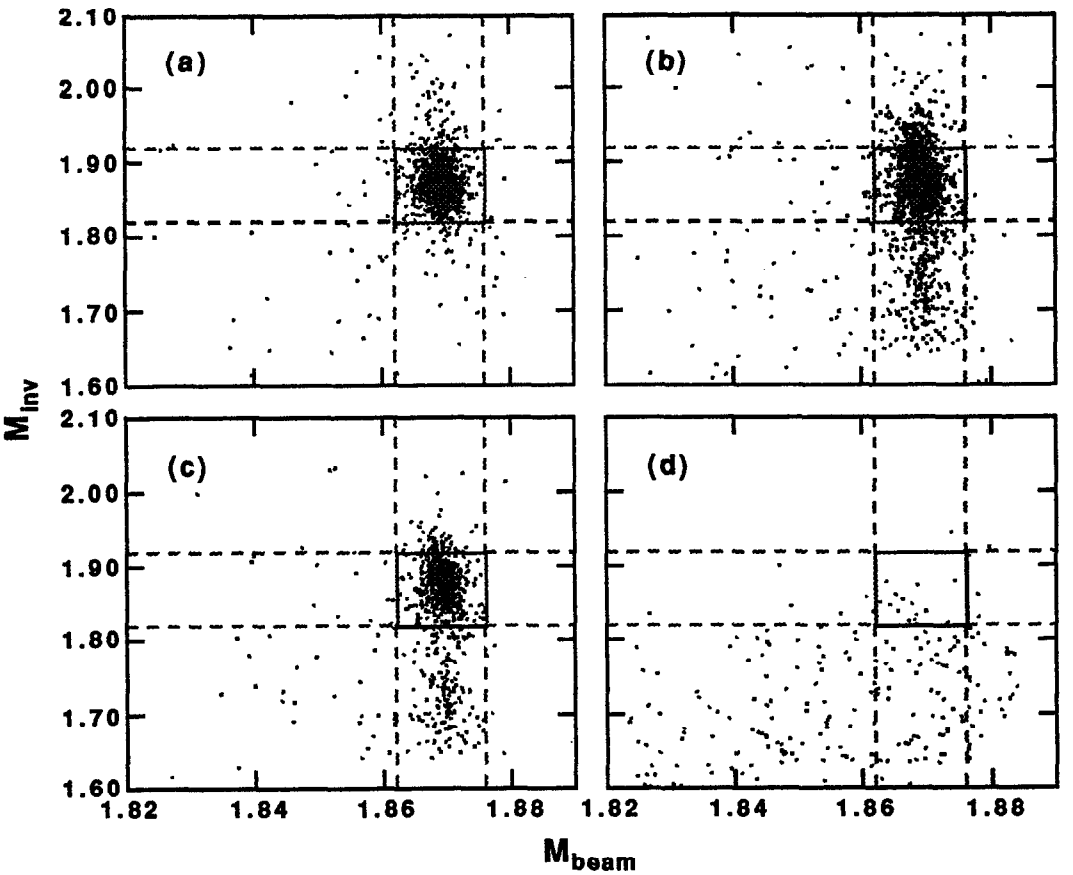

Figure 5.4 Monte Carlo of the Class I backgrounds to $D^+ \to K^+\pi^-\pi^+$: (a) $D^+ \to \bar{K}^0K^+ \to (\pi^+\pi^-)K^+$; (b) $D^+ \to K^-\pi^+\pi^+$[nr]; (c) $D^+ \to \bar{K}^{*0}\pi^+ \to (K^-\pi^+)\pi^+$; and (d) $D^+ \to \bar{K}^0\pi^+\pi^0 \to (\pi^+\pi^-)\pi^+\pi^0$.

The $K^-\pi^+\pi^+$ background has been studied through its resonant component $D^+ \to \bar{K}^{*0}\pi^+ \to (K^-\pi^+)\pi^+$ and its non-resonant component $D^+ \to K^-\pi^+\pi^+$[nr]. Another D^+ decay mode which contributes background is:

- $D^+ \to \bar{K}^0\pi^+\pi^0$, $\bar{K}^0 \to K_S^0 \to \pi^+\pi^-$--a Cabibbo allowed mode where the π^0 is lost and a pion is misidentified as a kaon to compensate the missing momentum.

Figure 5.4 displays the M_{inv} versus M_{beam} scatterplots for these backgrounds. The $\bar{K}^0K^+$ and $K^-\pi^+\pi^+$ peak in the signal region, while the $\bar{K}^0\pi^+\pi^0$ form a continuum which feeds into the signal region.

5-4.2 Class II Backgrounds

For this search, the major Class II backgrounds arise from both D^+D^- and $D^0\overline{D}^0$ events where only track misassociation occurs; no particle misidentification is involved.

Consider, for example, the following D^+D^- event:

$$D^+ \to \overline{K}^0\pi^+\pi^-\pi^+, \overline{K}^0 \to K^0_S \to \pi^+\pi^- \quad \text{vs.} \quad D^- \to K^+\pi^-\pi^-$$

Both D decay modes are Cabibbo allowed. In the attempt to reconstruct a tag and a $K^+\pi^-\pi^+$ recoil, a π^+ from the D^+ can be interchanged with a π^- from the D^-. If the pions are soft, such an interchange often does not significantly alter the kinematics. The event is then observed as

$$D^- \to K^0_S\pi^+\pi^-\pi^- \quad \text{vs.} \quad D^+ \to K^+\pi^-\pi^+$$

Characteristic of the situation, the unique constraint of strangeness is lost by the presence of the K^0_S.

As another example, consider a $D^0\overline{D}^0$ event produced as

$$D^0 \to \overline{K}^0\pi^+\pi^-, \overline{K}^0 \to K^0_S \to \pi^+\pi^- \quad \text{vs.} \quad \overline{D}^0 \to K^+\pi^-\pi^+\pi^-$$

In the attempt to reconstruct a $K^0_S\pi^+\pi^-\pi^+$ tag and a $K^+\pi^-\pi^+$ recoil, a π^- from the second D could be associated with the first. Again if the particle momenta are low, the kinematics is not greatly changed by the misassociation. The event is then observed as

$$D^- \to K^0_S\pi^+\pi^-\pi^- \quad \text{vs.} \quad D^+ \to K^+\pi^-\pi^+$$

The final state $K^0_S\pi^+\pi^-\pi^-$ vs. $K^+\pi^-\pi^+$ is most susceptible to these Class II backgrounds, since the pions are generally soft due to the high multiplicity. However, the final states with the tags $K^0_S\pi^+$, $K^0_S\pi^+\pi^0$, $K^0_SK^+$, and $K^+K^-\pi^+$ are also susceptible; in the first three tags the neutral kaon makes the strangeness of the decay ambiguous, while, similarly in the last tag, the net strangeness is zero.

Some other less obvious Class II backgrounds were found from studies of the D^+D^- and $D^0\overline{D}^0$ Monte Carlo sets (Section 3-3.5). These backgrounds involve topologies where an extra π^0 in the event is lost in the reconstruction. For example, one such topology is

$$D^0 \to K^{*-}\pi^+ \text{ vs. } \overline{D}^0 \to K^+\pi^-\pi^+\pi^-, K^{*-} \to K^-\pi^0, \pi^0 \to \gamma\gamma$$

reconstructed as

$$D^+ \to K^-K^+\pi^+ \text{ vs. } D^- \to K^-\pi^+\pi^-$$

where the π^0 is lost, a pion from the decay of the $\overline{D}^0$ is misidentified, and tracks are misassociated.

5-4.3 The Background Cuts

The Anti-K_S^0 Cut

This cut suppresses the $\overline{K}^0K^+$ background by discarding events with $K_S^0 \to \pi^+\pi^-$ candidates. For each $K^+\pi^-\pi^+$ track combination, the track parameters and error matrices of the $\pi^+\pi^-$ pair are recalculated at the point of closest approach and are then used to calculate the $\pi^+\pi^-$ invariant mass. An event is retained if

- $|M_{\pi\pi} - M_{K0}| > 30$ MeV/c^2

This criteria removes 88% of the $\overline{K}^0K^+$ background which survives the initial event selection, while retaining 94% of the signal. This cut is also found to remove 80% of the $\overline{K}^0\pi^+\pi^0$ background.

The Second Level Particle Identification Cuts

These cuts are introduced to suppress the $K^-\pi^+\pi^+$ backgrounds. The $\Delta T = T^{\text{pred}} - T^{\text{meas}}$ distributions are examined for those recoil tracks identified by the time of flight, and $\Delta E / \sigma \equiv (E^{\text{pred}} - E^{\text{meas}})/\sigma$ distributions for those identified by dE/dx. Figure 5.5 shows Monte Carlo plots of these distributions for $K^-\pi^+\pi^+$ (solid histograms) and $K^+\pi^-\pi^+$

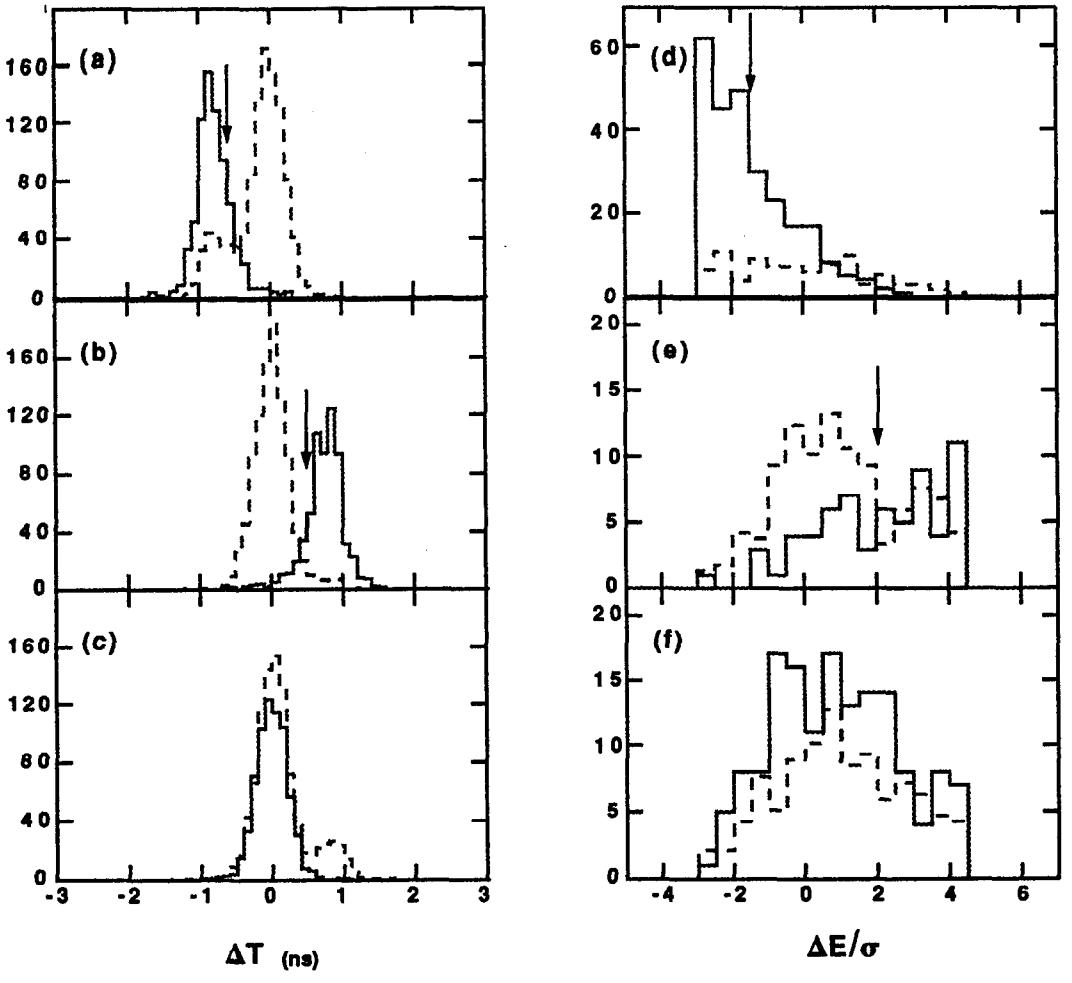

Figure 5.5 Double misidentification of $D^+ \to K^-\pi^+\pi^+$ when reconstructed as $K^+\pi^-\pi^+$. Plots (a)-(c) are ΔT distributions, respectively, for the K^+, π^- and π^+ tracks identified by TOF, while plots (d)-(f) are $\Delta E/\sigma$ distributions for the K^+, π^- and π^+ tracks identified by dE/dx. The solid histograms show the distributions for Monte Carlo $K^-\pi^+\pi^+$ and the dashed histograms show the distributions for the desired $K^+\pi^-\pi^+$ signal. The arrows indicate the second level particle identification cuts. (The small peaks offset from zero in the signal distributions arise from the double misidentification $K^+ \leftrightarrow \pi^+$).

(dashed histograms) events. In the ΔT distributions, Figures 4.5(a)-(c), correctly identified tracks produce peaks at zero, while misidentified pions and kaons produce peaks around –0.8 ns and +0.8 ns, respectively. A similar effect is observed in the $\Delta E/\sigma$ distributions, Figures 4.5(d)-(f).

The second level particle identification cuts impose tighter criteria on the tracks which the first level cuts have identified as the K^+ and the π^- in $K^+\pi^-\pi^+$. For a track to be retained as the K^+:

- $\Delta T_K > -0.6$ ns (~3σ) if the time-of-flight information has been used,
- $\frac{\Delta E_K}{\sigma} > -1.5$ if the dE/dx information has been used,

while for a track to be retained as the π^-:

- $\Delta T_\pi < 0.5$ ns (~2.5σ),
- $\frac{\Delta E_\pi}{\sigma} < 2.0$,

and the pion must now be identified by either the TOF or dE/dx. Since the π^+ in $D^+ \to K^+\pi^-\pi^+$ does not participate in the double misidentification, it is unnecessary to apply tighter criteria to that track. This criteria removes 97% of the $K^-\pi^+\pi^+$ background which survives the initial event selection, while retaining 81% of the signal. It is also removes about 90% of the $\bar{K}^0\pi^+\pi^0$ background which survives the anti-K^0_S cut.

The Topology Cuts

The major Class II backgrounds are identified and suppressed by reanalyzing the events for alternate $D\bar{D}$ hypotheses. The topologies which are examined are listed in Table 5.1 and Table 5.2. For each candidate event, the tracks are repermuted and the beam constrained masses are recalculated. The event is then considered consistent with the background topology and discarded if, for any of the combinations, the mass on both sides lies within 3σ of the nominal D mass. The efficiency of this procedure is demonstrated in Figure 5.6 .for the background $D^+ \to \bar{K}^0\pi^+\pi^-\pi^+$ opposite $D^- \to K^+\pi^-\pi^-$.

Effectively all of the Class II backgrounds are found to be removed by these cuts. The effect of these cuts on the signal depend strongly upon the final state being reconstructed: 85% of the signal is retained when reconstructed opposite a $K^0_S\pi^+$ tag, 49%

Table 5.1 D^+D^- topologies considered as background to tagged $D^+ \to K^+\pi^-\pi^+$.

Tag vs. $K^+\pi^-\pi^+$	D^+D^- background
$\bar{K}^0\pi^+$ vs. $K^-\pi^+\pi^-$	$K^0\pi^-$ vs. $K^-\pi^+\pi^+$
$\bar{K}^0\pi^+\pi^-\pi^+$ vs. $K^-\pi^+\pi^-$	$K^0\pi^-\pi^+\pi^-$ vs. $K^-\pi^+\pi^+$
$\bar{K}^0\pi^+\pi^0$ vs. $K^-\pi^+\pi^-$	$K^0\pi^-\pi^0$ vs. $K^-\pi^+\pi^+$
$\bar{K}^0K^+$ vs. $K^-\pi^+\pi^-$	$K^0\pi^-$ vs. $K^-K^+\pi^+$
$K^-K^+\pi^+$ vs. $K^-\pi^+\pi^-$	$K^+K^-\pi^-$ vs. $K^-\pi^+\pi^+$

Table 5.2 $D^0\bar{D}^0$ topologies considered as background to tagged $D^+ \to K^+\pi^-\pi^+$.

Tag vs. $K^+\pi^-\pi^+$	$D^0\bar{D}^0$ background
$\bar{K}^0\pi^+$ vs. $K^-\pi^+\pi^-$	$K^0\pi^-\pi^+$ vs. $K^-\pi^+$
$\bar{K}^0\pi^+\pi^-\pi^+$ vs. $K^-\pi^+\pi^-$	$K^0\pi^-\pi^+$ vs. $K^-\pi^+\pi^-\pi^+$
$\bar{K}^0\pi^+\pi^0$ vs. $K^-\pi^+\pi^-$	$K^0\pi^-\pi^+$ vs. $K^-\pi^+\pi^0$
$\bar{K}^0K^+$ vs. $K^-\pi^+\pi^-$	$K^0\pi^-\pi^+$ vs. K^-K^+
$K^-K^+\pi^+$ vs. $K^-\pi^+\pi^-$	K^+K^- vs. $K^-\pi^+\pi^-\pi^+$

when opposite $K^0_S\pi^+\pi^-\pi^-$, 85% when opposite $K^0_S\pi^+\pi^0$, 71% when opposite $K^0_SK^+$, and 69% when opposite $K^+K^-\pi^+$.

The Anti-Photon Cut

This cut is motivated by the $\bar{K}^0\pi^+\pi^0$ background and the less obvious Class II $D\bar{D}$ backgrounds with the extra π^0's. These residual backgrounds are suppressed by a cut on the number of isolated photons not participating in the event reconstruction; if one or more extra photons are found with energies exceeding 100 MeV, the event is discarded. To reduce confusion between photons from the event vertex and split-offs from charged tracks

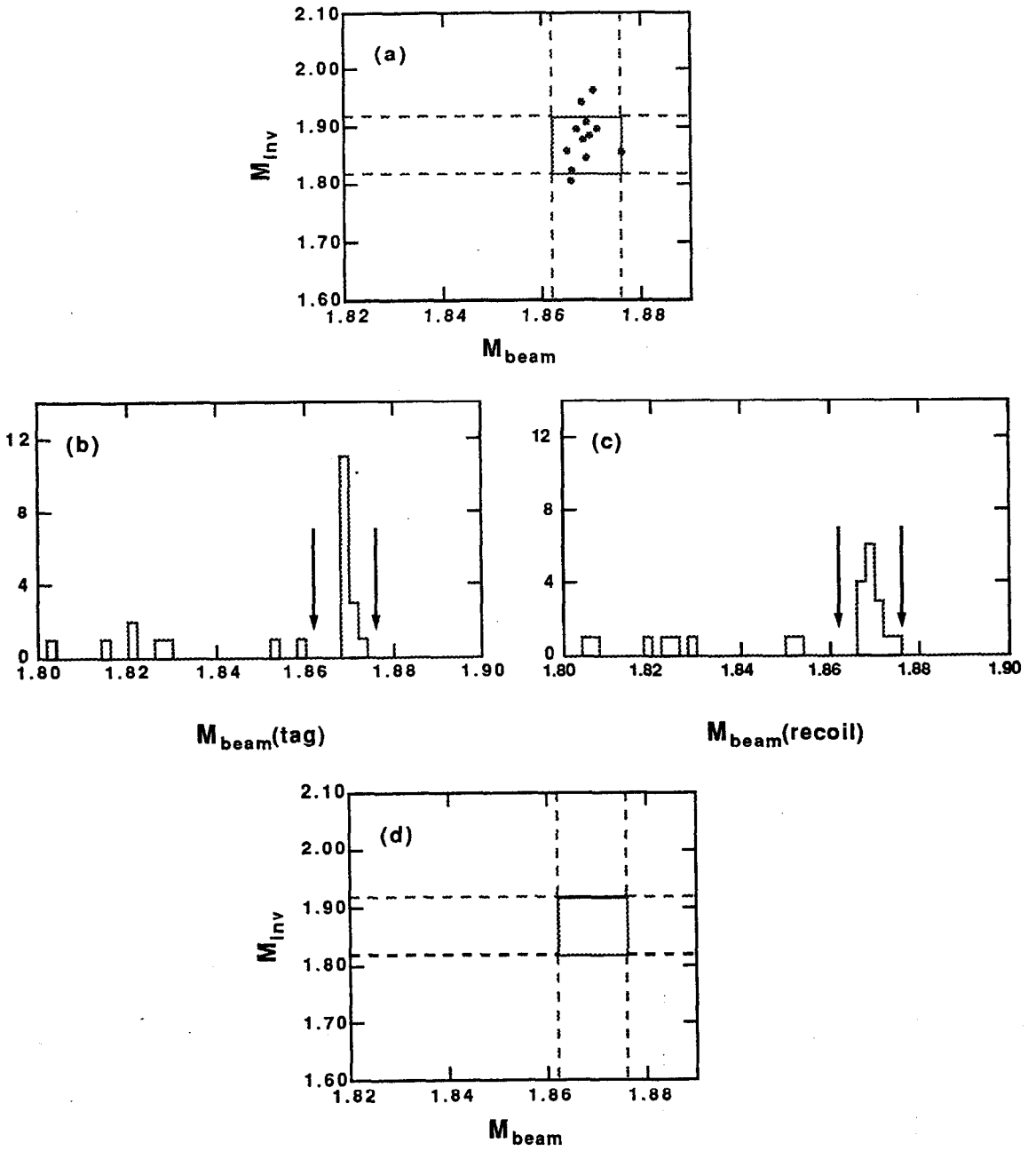

Figure 5.6 Monte Carlo $D^+ \to \overline{K}^0\pi^+\pi^-\pi^+, D^- \to K^+\pi^-\pi^-, \overline{K}^0 \to K^0_S \to \pi^+\pi^-$. (a) Events reconstructed as the signal $D^- \to K^0_S\pi^+\pi^-\pi^-$, $D^+ \to K^+\pi^-\pi^+$ after the second level particle identification cuts have been applied. (b), (c) The beam constrained mass plots from reanalyzing the events as $K^0_S\pi^+\pi^-\pi^+, K^+\pi^-\pi^-$ (with multiple entries per event); the arrows delimit the $\pm 3\sigma$ mass regions about the D^+ mass. (d) Events remaining after discarding those consistent with the $K^0_S\pi^+\pi^-\pi^+, K^+\pi^-\pi^-$ hypothesis.

interacting in the detector, the angle θ between their momentum and the momentum of the nearest charged track must give $\cos\theta < 0.95$. The disadvantage with applying this anti-photon cut is the systematic uncertainty--approximately 8%--introduced by the presence of the split-offs, which the Monte Carlo does not simulate.

5-5 Results

Figure 5.7 shows the application of the cuts to the data. After all cuts are applied three candidate events remain in the signal region and one falls directly outside the signal boundary. For the remaining discussions the events are labelled in Figure 5.7(e) as A, B, C and D.

5-5.1 Analysis Tests

Tests have been performed to check the analysis procedure of the $K^+\pi^-\pi^+$ search. The first two tests examine the initial event selection procedure by searching specifically for the two major Class I background channels: $D^+ \to K^-\pi^+\pi^+$ and $D^+ \to \bar{K}^0K^+$, $\bar{K}^0 \to K_S^0 \to \pi^+\pi^-$. The third test studies the background reduction cuts by predicting the numbers of events removed and comparing the results with the numbers that are removed.

Search for $D^+ \to K^-\pi^+\pi^+$

For this search, the initial selection criteria for $K^+\pi^-\pi^+$ is modified to account for the differing final state charged particles. The resulting scatterplot is shown in Figure 5.8. An expected cluster of events is seen around $M_{inv} = M_{beam} = 1.8693$ GeV/c^2 with little background in the surrounding regions; 107 candidate events fall within the signal region.

The detection efficiencies and expected numbers of events are calculated opposite each tag mode according to the procedure in Section 4-4. Although the resonant $K^-\pi^+\pi^+$ substructure is not well understood[22] (the non-$\bar{K}^{*0}\pi^+$ component is not uniform across the Dalitz plot), the numbers are determined from samples of $D^+ \to \bar{K}^{*0}\pi^+ \to (K^-\pi^+)\pi^+$ and $D^+ \to K^-\pi^+\pi^+$[nr], for lack of a better model. The branching fractions used are $B(D^+$

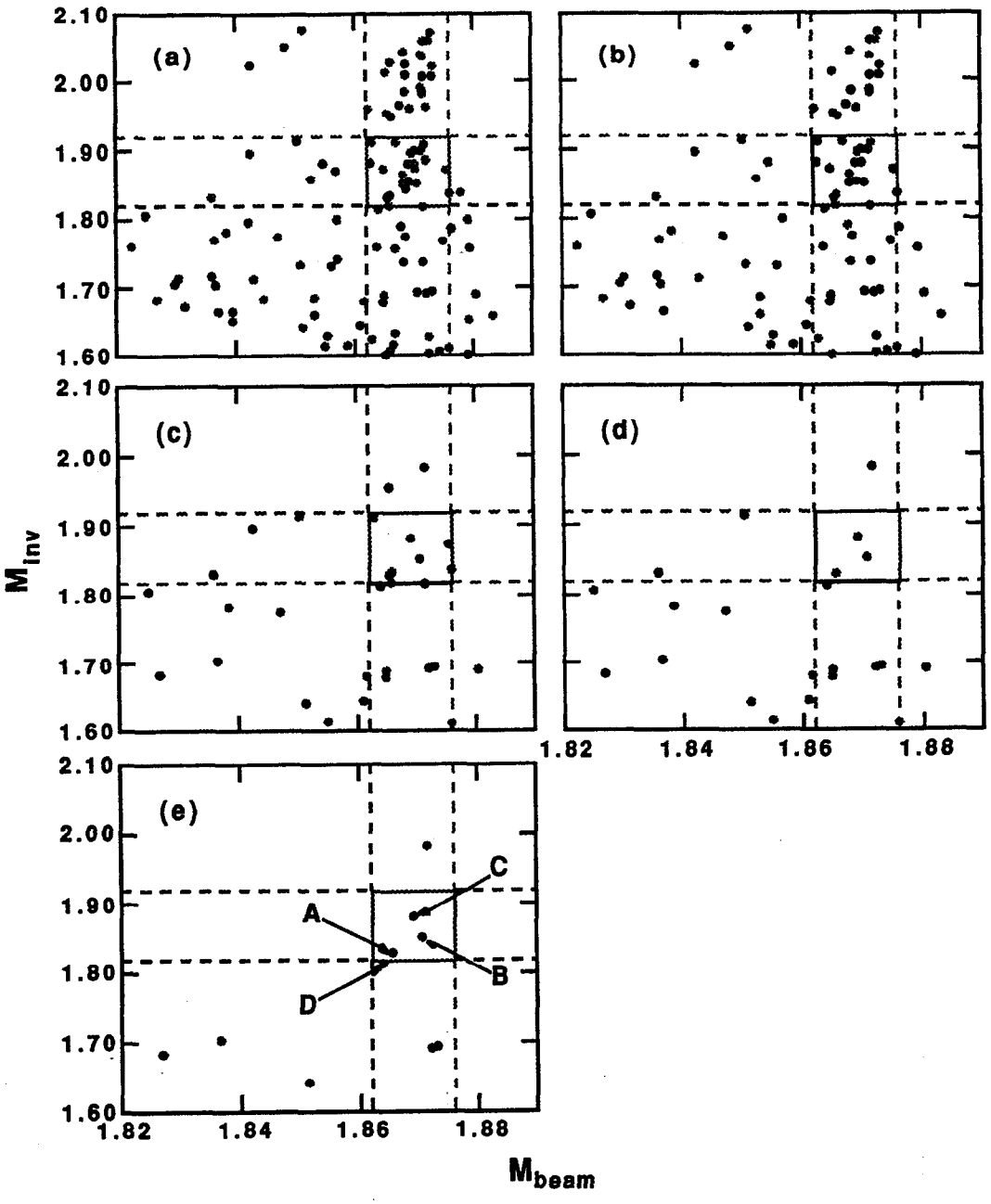

Figure 5.7 Data after: (a) the initial event selection; (b) the anti-K_S^0 cut; (c) the second level particle identification cuts; (d) the $D\bar{D}$ topology cuts; and (e) the isolated photon cut.

$\to K^-\pi^+\pi^+$[nr]) = 7.2±0.6±1.8%[22] and $B(D^+ \to \bar{K}^{*0}\pi^+ \to (K^-\pi^+)\pi^+)$ = 1.9±1.4±1.8%, where the latter branching fraction is derived from $B(D^+ \to \bar{K}^{*0}\pi^+ \to (K^-\pi^+)\pi^+) = B(D^+ \to K^-\pi^+\pi^+) - B(D^+ \to K^-\pi^+\pi^+$[nr]), using $B(D^+ \to K^-\pi^+\pi^+)$ =

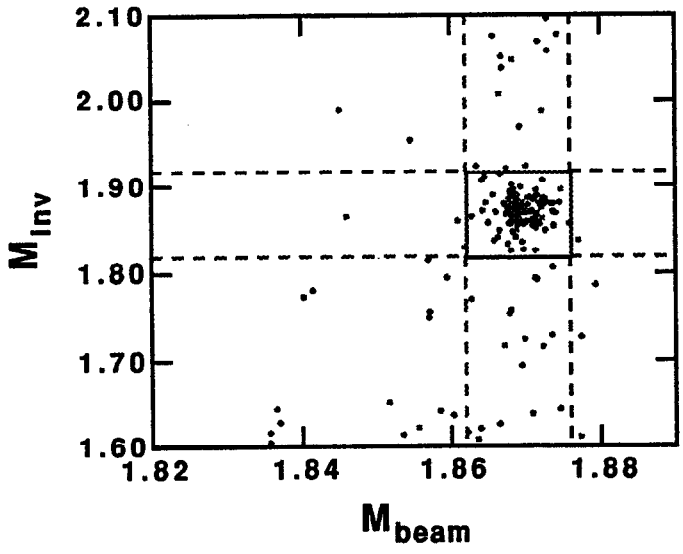

Figure 5.8 Candidate $D^+ \to K^-\pi^+\pi^+$ events.

$9.1\pm1.3\pm0.4\%$[24] and $B(D^+ \to K^-\pi^+\pi^+[\text{nr}])$. The correlation between $B(D^+ \to K^-\pi^+\pi^+[\text{nr}])$ and $B(D^+ \to \bar{K}^{*0}\pi^+ \to (K^-\pi^+)\pi^+)$ is accounted for when propagating errors.[61]

Table 5.3 summarizes the calculations and compares the expected numbers of events against the observed numbers. The total number expected, 110 ± 14 events, is in good agreement with 107 observed events, assuming no background. The uncertainty on the number of expected events is statistical only and reflects the uncertainty on the number of tags, the error on the branching fractions and the error on the Monte Carlo statistics. The number of expected background events is $1.5^{+0.5}_{-0.3}$, smaller than the error on the total number of expected events. The background arises from $D^+ \to \bar{K}^0K^+ \to K^0_SK^+ \to (\pi^+\pi^-)K^+$ events (where a double misidentification occurs between the K^+ and the π^-), from $D^+ \to K^-\pi^+\pi^+\pi^0$ events (where the π^0 is excluded from the reconstruction) and from the non-charm continuum (estimated by analyzing u, d, s events generated with Lund Monte Carlo Jetset 6.2).

Table 5.3 Analysis test of $D^+ \to K^-\pi^+\pi^+$. The efficiencies are averages of the efficiencies for $D^+ \to K^-\pi^+\pi^+$[nr] and $D^+ \to \bar{K}^{*0}\pi^+ \to (K^-\pi^+)\pi^+$, weighted by the branching fractions for the two channels.

Tag Mode	Efficiency (%)	Expected Number	Observed Number
$\bar{K}^0\pi^+$	45±2	7.5±1.0	10
$K^-\pi^+\pi^+$	50±1	75.6±9.6	72
$\bar{K}^0\pi^+\pi^-\pi^+$	57±2	9.8±1.3	8
$\bar{K}^0\pi^+\pi^0$	47±2	8.4±1.4	12
$\bar{K}^0K^+$	47±1	0.7±0.2	1
$K^-K^+\pi^+$	55±2	4.3±0.7	4
$K^-\pi^+\pi^+\pi^0$	45±1	4.1±0.8	0
Total $K^-\pi^+\pi^+$ Events		110±14	107

Search for $D^+ \to \bar{K}^0K^+$ and $D^+ \to \bar{K}^0\pi^+$

The procedure for finding $D^+ \to \bar{K}^0K^+$ is the same as that for $K^+\pi^-\pi^+$ except for the treatment of the $\pi^+\pi^-$ pair. For these tracks the K^0_S selection criteria from the tagging procedure (Section 4-3) is used. Figure 5.9 shows the resulting plot with four events in the signal region. A cluster of events is seen around M_{inv} = 2.0 GeV/c^2, M_{beam} = 1.8693 GeV/c^2 due to $D^+ \to \bar{K}^0\pi^+$ where the pion has been misidentified as a kaon, causing upward shift in mass. The detection efficiencies and expected numbers of events are given in Table 5.4, using $B(D^+ \to \bar{K}^0K^+) = 1.01\pm0.32\pm0.17\%$[24] A total of 3.0±1.0 events are expected; this number is consistent with the observed four events. The number of $D^+ \to \bar{K}^0\pi^+$ events expected in the high mass region is also checked, obtaining an estimated total of 10.8±1.7 events, which agrees well with 10 observed events. Table 5.4 provides the numbers for the high mass region. The measurement $B(D^+ \to \bar{K}^0\pi^+) = 3.2\pm0.5\pm0.2\%$[24] is used.

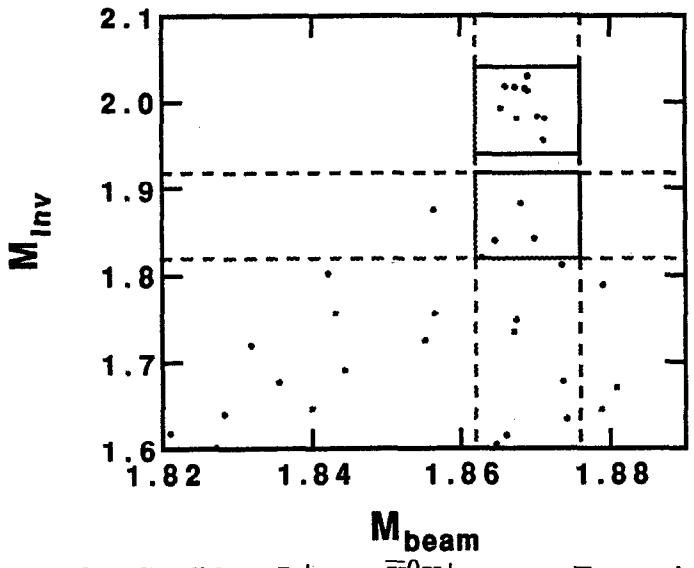

Figure 5.9 Candidate $D^+ \to \bar{K}^0K^+$ events. Events in the high mass region are reflections from $D^+ \to \bar{K}^0\pi^+$.

From these checks, it is concluded that the initial event selection procedure is well understood.

Test of the Background Cuts

In this test the numbers of events that are expected to be removed by each of the background cuts are calculated and compared to the numbers that are removed. This is done for three regions in the scatterplot of M_{inv} versus M_{beam}:

- Signal Region: $1.819 < M_{inv} < 1.919$ GeV/c^2, $1.862 < M_{beam} < 1.876$ GeV/c^2.

- Region I: $1.67 < M_{inv} < 1.77$ GeV/c^2, $1.862 < M_{beam} < 1.876$ GeV/c^2. This is the low invariant mass reflection region, containing 90% of the $D^+ \to K^-K^+\pi^+$ events which are misidentified as $K^+\pi^-\pi^+$. Other sources of events in this region are $D^+ \to \bar{K}^0\pi^+\pi^0$ and the tails from $D^+ \to K^-\pi^+\pi^+$.

- Region II: $1.94 < M_{inv} < 2.04$ GeV/c^2, $1.862 < M_{beam} < 1.876$ GeV/c^2. This is the high invariant mass reflection region, containing 90% of the

Table 5.4 Analysis check with $D^+ \to \bar{K}^0K^+ \to K^0_SK^+ \to (\pi^+\pi^-)K^+$.

Tag Mode	Efficiency (%)	Expected Number	Observed Number
$\bar{K}^0\pi^+$	37±2	0.23 ± 0.07	2
$K^-\pi^+\pi^+$	35±1	2.03 ± 0.64	1
$\bar{K}^0\pi^+\pi^-\pi^+$	36±3	0.24 ± 0.08	0
$\bar{K}^0\pi^+\pi^0$	40±4	0.27 ± 0.09	0
$\bar{K}^0K^+$	36±2	0.02 ± 0.01	0
$K^-K^+\pi^+$	36±2	0.11 ± 0.04	0
$K^-\pi^+\pi^+\pi^0$	35±3	0.12 ± 0.04	1
Total $\bar{K}^0K^+$ Events		3.0 ± 1.0	4

Table 5.5 Analysis check with $D^+ \to \bar{K}^0\pi^+ \to K^0_S\pi^+ \to (\pi^+\pi^-)\pi^+$ (for events in the high mass region $1.94 < M_{inv} < 2.04$ GeV/c^2, $1.862 < M_{beam} <$ 1.876 GeV/c^2 of Figure 5.9).

Tag Mode	Efficiency	Expected Number	Observed Number
$\bar{K}^0\pi^+$	40±2	0.81±0.13	0
$K^-\pi^+\pi^+$	41±2	7.38±1.22	9
$\bar{K}^0\pi^+\pi^-\pi^+$	40±3	0.82±0.15	0
$\bar{K}^0\pi^+\pi^0$	46±4	1.00±0.21	0
$\bar{K}^0K^+$	38±3	0.07±0.03	1
$K^-K^+\pi^+$	37±7	0.35±0.07	0
$K^-\pi^+\pi^+\pi^0$	34±10	0.37±0.10	0
Total $\bar{K}^0\pi^+$ Events		10.8±1.7	10

$D^+ \to \pi^+\pi^-\pi^+$ and $\bar{K}^0\pi^+$ events which are misidentified as $K^+\pi^-\pi^+$. Other sources of events in this region are the tails from $D^+ \to K^-\pi^+\pi^+$.

Table 5.6 Branching fractions of the Class I and Class II backgrounds to $D^+ \to K^+\pi^-\pi^+$

Mode	Branching Fraction (%)	Reference
$D^+ \to \bar{K}^0 K^+$	1.01±0.32±0.17	24, 20
$D^+ \to \bar{K}^{*0}\pi^+ \to (K^-\pi^+)\pi^+$	1.9±1.4±1.8	(see text)
$D^+ \to K^-\pi^+\pi^+$[nr]	7.2 ± 0.6 ± 1.8	22
$D^+ \to \bar{K}^0\pi^+\pi^0$	10.2±2.5±1.6	24
$D^+ \to K^-K^+\pi^+$	1.21 ± 0.33 ± 0.13	24, 20
$D^+ \to \bar{K}^0\pi^+$	3.2 ± 0.5 ± 0.2	24
$D^+ \to \pi^+\pi^-\pi^+$	0.38 ± 0.15 ± 0.09	24, 20
$D^+ \to \bar{K}^0\pi^+\pi^-\pi^+$	6.6 ± 1.5 ± 0.5	24
$D^0 \to K^-\pi^+$	4.2±0.4±0.4	24
$D^0 \to \bar{K}^0\pi^+\pi^-$	6.4±0.5±1.0	22
$D^0 \to K^-\pi^+\pi^-\pi^+$	9.1±0.8±0.8	24
$D^0 \to K^-\pi^+\pi^0$	13.3±1.2±1.3	24
$D^0 \to K^-K^+$	0.51±0.09±0.07	24, 20

For the checks Monte Carlo samples of the various backgrounds were generated with at least 10× the expected numbers of events in the $\psi(3770)$ data samples. The contribution of $\bar{K}^0\pi^+\pi^0$ and $K^-K^+\pi^+$ to the signal region is either small or negligible, and therefore these channels were generated according to phase space only. The decay $D^0 \to K^-\pi^+\pi^0$ (in the Class II backgrounds) is dominated by the quasi-two body mode $D^0 \to K^-\rho^+$, so this mode has been used to represent $K^-\pi^+\pi^0$.

Table 5.6 lists the background branching fractions used in the estimates. Correlations exist between several of the branching fractions. The branching fraction for $\bar{K}^0K^+$ is derived from measurements of the branching fraction ratio, $B(\bar{K}^0K^+)/B(\bar{K}^0\pi^+)$, and of the

absolute branching fraction for $B(\overline{K}^0\pi^+)$. Similar relations hold between $K^-K^+\pi^+$, $\pi^+\pi^-\pi^+$ and $K^-\pi^+\pi^+$ and between K^-K^+ and $K^-\pi^+$. These correlations are accounted for in the errors. The relation between $B(D^+ \to K^-\pi^+\pi^+[\text{nr}])$ and $B(D^+ \to \overline{K}^{*0}\pi^+ \to (K^-\pi^+)\pi^+)$ has been discussed above and is also accounted for here. Among the D^+ modes $\overline{K}^0\pi^+$, $K^-\pi^+\pi^+$, $\overline{K}^0\pi^+\pi^-\pi^+$, $\overline{K}^0\pi^+\pi^0$ and the D^0 modes $K^-\pi^+$, $K^-\pi^+\pi^-\pi^+$, $K^-\pi^+\pi^0$, correlated errors arise from the double tag analysis procedure used in the determination of the absolute branching fractions. These correlations are assumed to be small and have been neglected for these checks.

Included in the predicted numbers are the estimated contributions from *u*, *d*, *s* events, determined from an analysis of Lund Monte Carlo data. The analysis, shown in Figure 5.10, finds that the contribution from *u*, *d*, *s* production is not negligible. The tagging procedure constrains track combinations to the D momentum. When all generated particles in the event leave well-measured tracks in the detector, momentum conservation will then constrain the recoil tracks to the D momentum, causing events to fall in or around the signal region

Table 5.7 gives the total expected numbers of events lost and compares the results against the data. The total number of events expected to be lost from the signal region, 26.7±3.8, deviates by approximately 2σ from the observed number lost, 17, assuming Poisson statistics. Most of this discrepancy occurs at the second level particle identification cuts, where 22.2±3.6 events are expected to be lost versus 11 events observed to be lost. The deviation may be due to statistical fluctuations, but may also involve the fact that the resonant substructure of the $K^-\pi^+\pi^+$ background is not well understood.[22] A discrepancy is also found in Region II, where the observed number of events, 18, exceeds the predicted number, 11.6±1.7, by approximately 1.5σ. In Region I the predicted number, 7.4±1.4 events, agrees well with the observed number, 8 events.

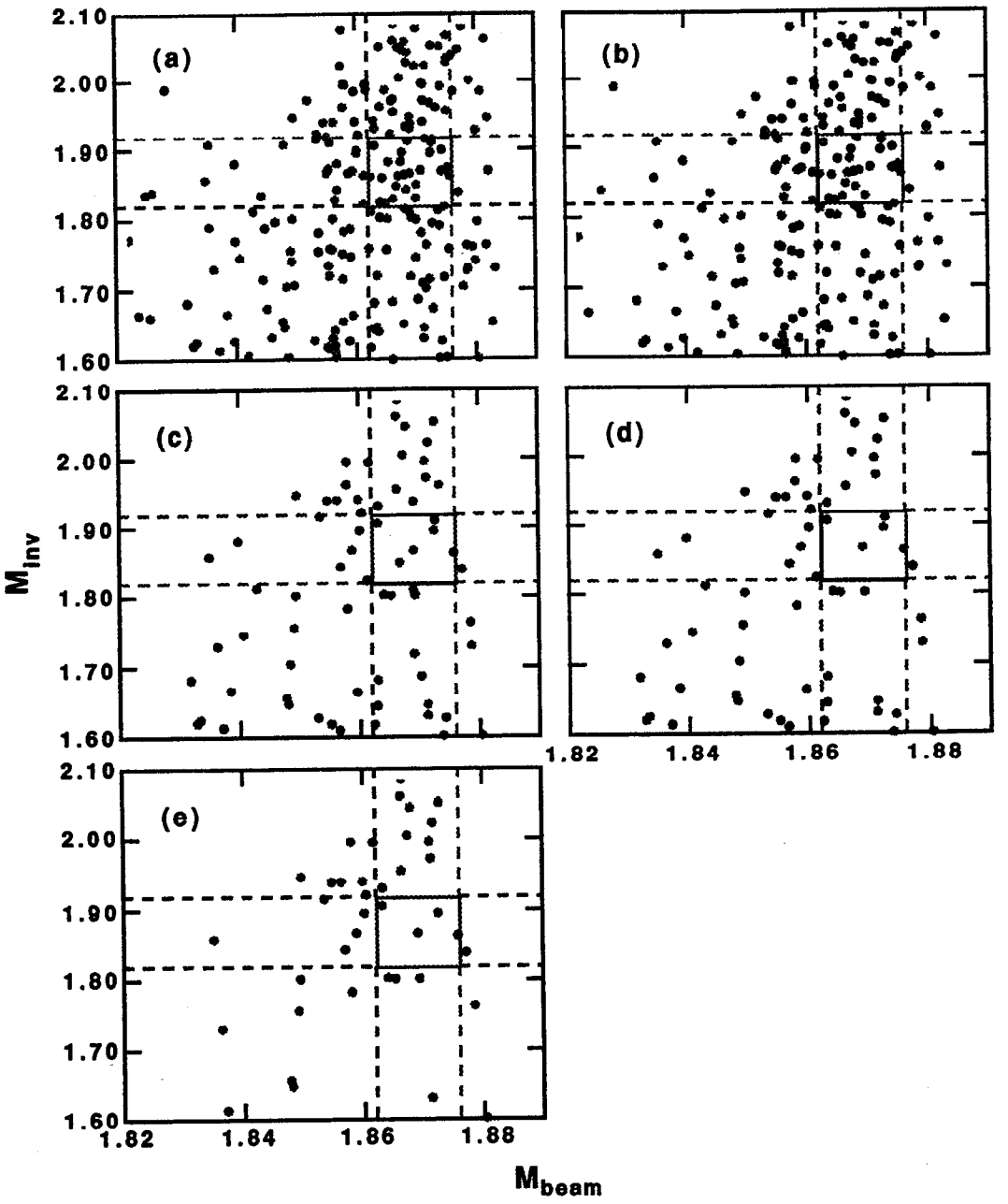

Figure 5.10 Analysis procedure applied to the Lund Monte Carlo: (a) after the initial event selection; (b) after the anti-K_S^0 cut; (c) after the second level particle identification cuts; (d) after the $D\overline{D}$ topology cuts; and (e) after the isolated photon cut.

5-5.2 Total Momentum and Energy Studies

No constraints on the total track momenta (P_{tot}) and energy (E_{tot}) have been imposed by either the event selection procedure or the data reduction cuts. Therefore, as a further check on the quality of the three events, P_{tot} and E_{tot} of the events are examined.

Table 5.7 Numbers of events observed and expected to be removed by the background cuts.

Cut	Region I		Signal Region		Region II	
	Obs.	Exp.	Obs.	Exp.	Obs.	Exp.
Anti-K^0_S	1	$1.0^{+0.4}_{-0.2}$	3	$3.0^{+0.4}_{-0.3}$	6	$4.5^{+0.7}_{-0.6}$
Second Level Particle Identification	5	5.7±1.2	11	22.2±3.6	11	6.8±1.4
Topology	0	$0.2^{+0.3}_{-0.1}$	3	$0.9^{+0.3}_{-0.1}$	1	$0.4^{+0.3}_{-0.1}$
Extra Photon	2	$0.5^{+0.5}_{-0.1}$	0	$0.5^{+0.5}_{-0.1}$	0	<0.23
Total Number	8	7.4±1.4	17	26.7±3.8	18	11.6±1.7

The expected values for these quantities are $P_{\rm tot} \equiv 0$ and $E_{\rm tot} = \sqrt{s} \equiv 3.77$ GeV/c^2. Significant discrepancies would indicate, for example, missing particles or tracks which escaped detection by travelling out through the beam pipe. Figure 5.11 shows distributions of $P_{\rm tot}$ and $\Delta E_{\rm tot} \equiv \sqrt{s} - E_{\rm tot}$ for the three candidate events and the boundary event. For comparison, the corresponding distributions for $D^+ \to K^-\pi^+\pi^+$ with the all-charged tags are superimposed.

Event D has the largest discrepancies in both $P_{\rm tot}$ (= 245 MeV/c) and $\Delta E_{\rm tot}$ (= 107 MeV/c^2). Because of this result and the fact it does lie outside the signal region, this event is removed from further consideration as a $K^+\pi^-\pi^+$ candidate.

In total momentum event C also has a significant discrepancy with $P_{\rm tot}$ = 130 MeV/c, placing it in the tail of the $D^+ \to K^-\pi^+\pi^+$ distribution. The missing momentum

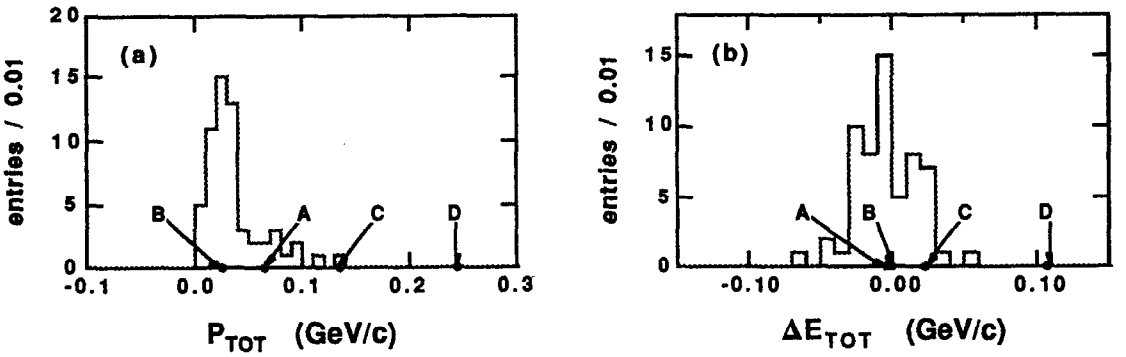

Figure 5.11 The total momentum (a) and the total energy (b) of the three $K^+\pi^-\pi^+$ candidate events and of the event on the signal boundary event. Superimposed are the total momentum and energy distributions for $D^+ \to K^-\pi^+\pi^+$.

for this event has $\cos\theta = 0.86$, not well along the direction of the beam pipe. However, a visual inspection of the event (Section 5-5.3) finds an isolated 61 MeV shower. If the shower is included, the missing momentum then has $\cos\theta = 0.99$ with $P_{tot} = 108$ MeV/c, well in the direction of the beam pipe. Nevertheless this event will be retained as a $K^+\pi^-\pi^+$ candidate.

5-5.3 Event Scans

To determine the quality of the events and to check against background, the three events within the signal region were examined visually; displays of the events are given in Figure 5.12 through Figure 5.14. Table 5.8 provides event information.

Event A

The tag is $K^-\pi^+\pi^+$, reconstructed from the tracks labelled 4, 2 and 6, respectively. Tracks 4 and 2 are strongly identified by time-of-flight, and the dE/dx information corroborates the mass hypotheses. For track 6, however, the time-of-flight information prefers the kaon hypothesis over the pion hypothesis; the dE/dx information confirms the kaon hypothesis, although the momentum of the track--0.651 GeV/c--just exceeds the 0.650 GeV/c cut above which dE/dx information is not considered reliable. The invariant and beam-constrained masses of the tag are $M_{inv} = 1.904$ GeV/c^2 and $M_{beam} = 1.8624$ GeV/c^2;

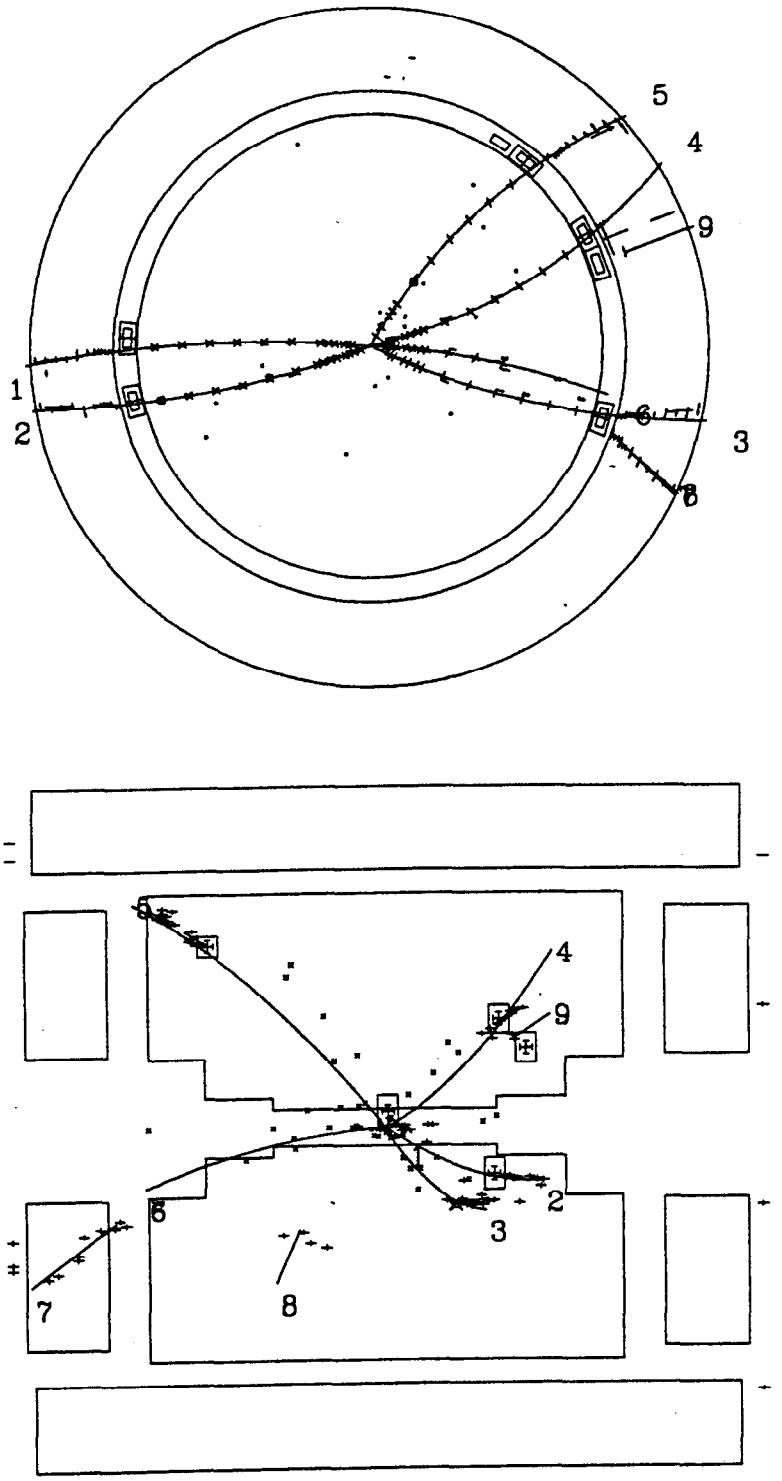

Figure 5.12 Event A.

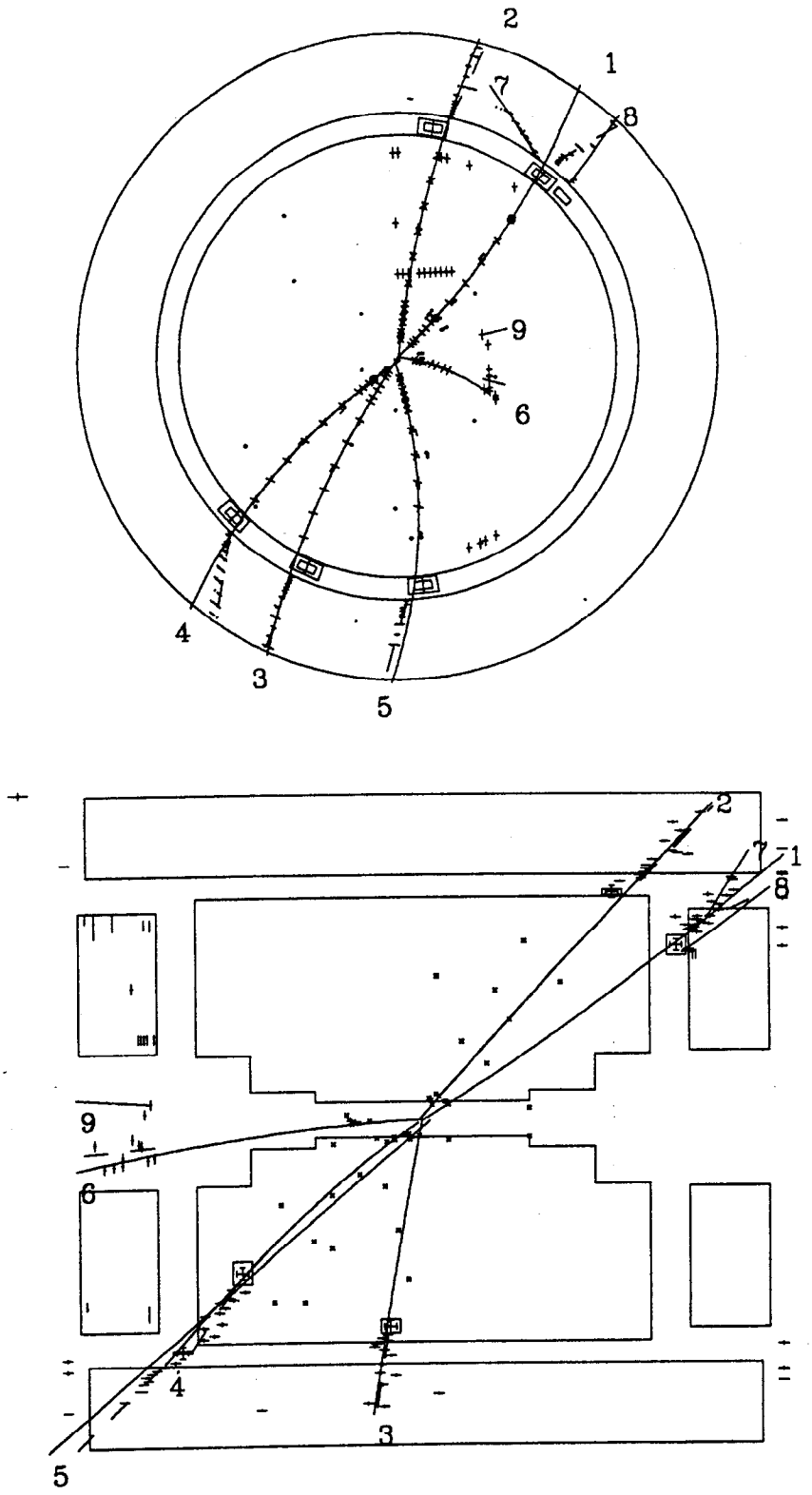

Figure 5.13 Event B.

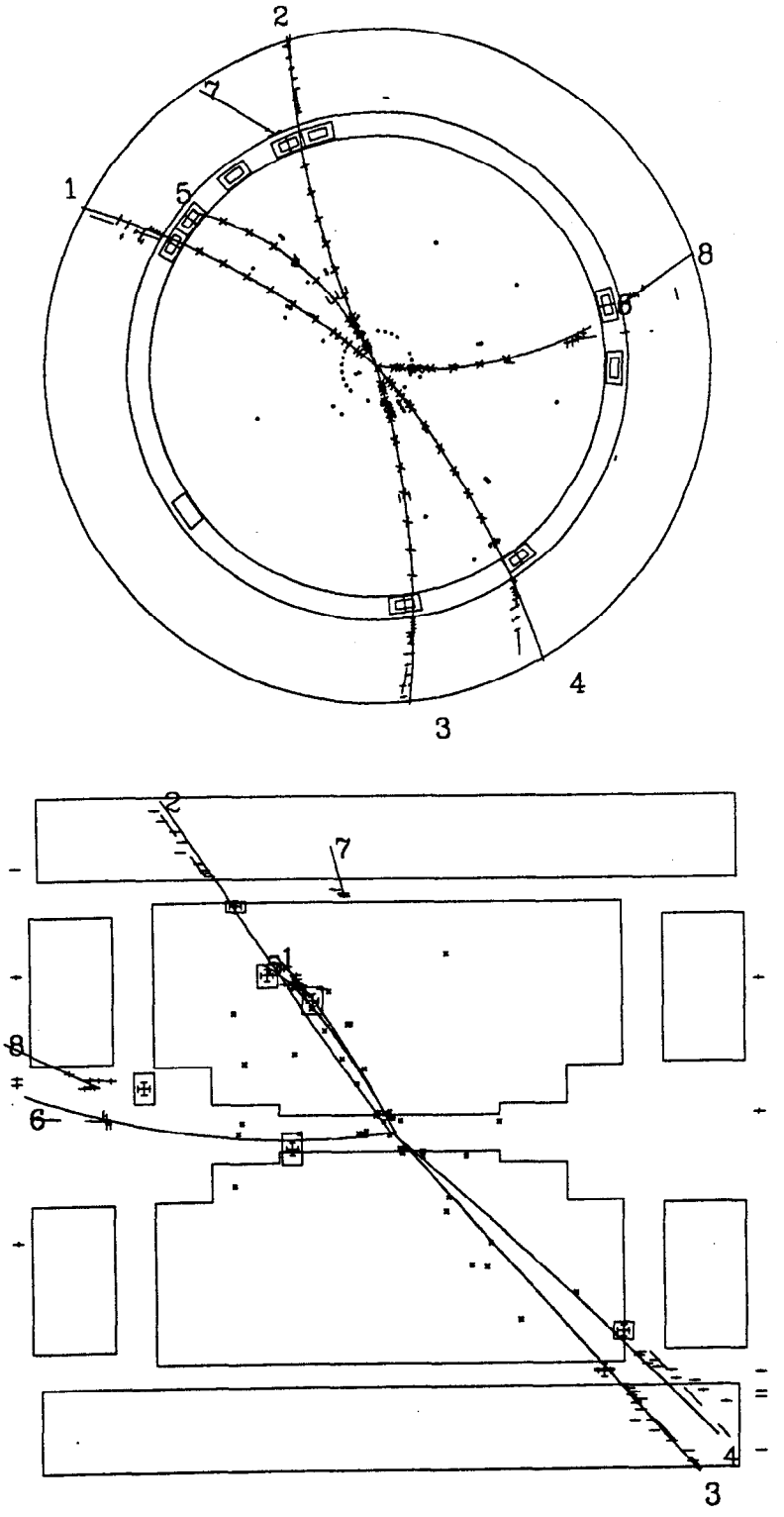

Figure 5.14 Event C.

Table 5.8 Event information on the three $D^+ \to K^-\pi^+\pi^-$ candidates.

	Event A			Event B			Event C		
Tag:									
Channel	$K^-\pi^+\pi^+$			$\bar{K}^0\pi^+ \to \pi^+\pi^-\pi^+$			$K^+K^-\pi^-$		
Tracks:	4	2	6	5	4	2	4	1	5
P(GeV/c)	0.363	0.648	0.651	0.490	0.467	0.889	0.722	0.538	0.192
$\Delta T_K/\sigma_K$	*03*	6.8	1.6	10.2	11.1	3.8	*31*	*22*	36.5
$\Delta T_\pi/\sigma_\pi$	14.0	*10*	*45*	*07*	*09*	*03*	2.4	10.3	*17*
$\Delta E_K/\sigma_K$	*00*	1.1	–	1.7	3.8	1.6	*21*	*10*	–
$\Delta E_\pi/\sigma_\pi$	8.3	*02*		*17*	*18*	*13*	1.4	2.0	
M_{inv} (GeV/c^2)	1.904			1.890			1.829		
M_{beam} (GeV/c^2)	1.8624			1.8704			1.8638		
Recoil:									
Channel	$K^-\pi^+\pi^-$			$K^-\pi^+\pi^-$			$K^+\pi^-\pi^+$		
Tracks:	1	5	3	1	6	3	2	6	3
P(GeV/c)	0.781	0.494	0.477	0.693	0.395	0.565	0.557	0.370	0.733
$\Delta T_K/\sigma_K$	*23*	14.1	8.9	*15*	–	6.1	*20*	–	3.2
$\Delta T_\pi/\sigma_\pi$	07	*14*	*15*	7.5		*05*	10.6		*07*
$\Delta E_K/\sigma_K$	*41*	–	0.8	*13*	3.3	1.4	*15*	3.6	2.6
$\Delta E_\pi/\sigma_\pi$	5.4		*28*	0.1	*11*	*08*	3.9	*00*	*22*
M_{inv} (GeV/c^2)	1.829			1.851			1.881		
M_{beam} (GeV/c^2)	1.8655			1.8707			1.8691		

the latter number lies directly above the lower cut on the beam-constrained mass for the all-charged tag modes (1.862 GeV/c^2). The remaining tracks, 1, 5 and 3, make up the recoil $K^+\pi^-\pi^+$, respectively. All recoil tracks are also identified by TOF. The pion tracks are strongly identified by their time-of-flight, but the kaon track is preferred to be a pion by time-of-flight; the momentum of the kaon track--781 MeV/c--excludes the use of dE/dx

information. The masses for the recoil are M_{inv} = 1.829 GeV/c^2 and M_{beam} = 1.8655 GeV/c^2. The invariant $\pi^+\pi^-$ mass is $M_{\pi^+\pi^-}$ = 0.707 GeV/c^2, well away from the mass of the K^0.

Event B

The tag is $K^0_S\pi^+$, reconstructed from tracks 5, 4 and 2; 5 and 4 form the K^0_S with an invariant mass of 0.506 GeV/c^2. The displaced K^0_S decay vertex can be seen in the axial view of the event. All tag tracks are well identified by time-of-flight, and the dE/dx information corroborates the mass hypotheses. The tag invariant and beam-constrained masses are M_{inv} = 1.890 GeV/c^2 and M_{beam} = 1.8704 GeV/c^2. The recoil $K^-\pi^+\pi^-$ tracks are 1, 6 and 3, respectively. Tracks 1 and 3 are strongly identified by time-of-flight with consistent dE/dx. Track 6 has a low angle with respect to the beam axis and does not hit the time-of-flight counters. It is identified by the dE/dx system, which does prefer the pion hypothesis. The recoil masses are M_{inv} = 1.851 GeV/c^2 and M_{beam} = 1.8707 GeV/c^2. The invariant $\pi^+\pi^-$ mass is $M_{\pi^+\pi^-}$ = 0.730 GeV/c^2, well away from the mass of the K^0.

Event C

The tag is $K^-K^+\pi^-$ reconstructed from tracks 1, 4 and 5, respectively. All tag tracks are identified by time-of-flight. Track 1 is strongly identified as a kaon, but track 4 is consistent with both pion and kaon hypotheses. For the tag M_{inv} = 1.829 GeV/c^2 and M_{beam} = 1.8638 GeV/c^2. The recoil $K^+\pi^-\pi^+$ tracks are 2, 6 and 3, respectively. Tracks 2 and 3 are strongly identified by time-of-flight with consistent dE/dx information. Track 6 is another one at low angle to the beam axis, and is strongly identified by the dE/dx information. For the recoil M_{inv} = 1.881 GeV/c^2 and M_{beam} = 1.8691 GeV/c^2. This event has an extra photon with an energy of 61 MeV, below the 100 MeV cut required for the event to be rejected by the isolated photon cut. The invariant $\pi^+\pi^-$ mass is $M_{\pi^+\pi^-}$ = 0.925 GeV/c^2, well away from the mass of the K^0.

In summary, of the three events, Event A would be the most likely to be a background. The time-of-flight information of two of the tracks prefers the opposite mass hypothesis, and the tag beam constrained mass is at the boundary for signal events.

5-5.4 Additional Topology Tests

The topology cuts remove events that are consistent only with those topologies listed in Table 5.1 and Table 5.2. Other topologies that can contribute are considered to be less significant because they include one or more D decays which are Cabibbo suppressed. For example, $K^-K^+K^+$ versus $\pi^+\pi^-\pi^-$ could be reconstructed as $K^-K^+\pi^-$ versus $K^+\pi^-\pi^+$. The three candidate events have been tested against these other topologies. Only Event A is found to be consistent with another topology--$K^0_S K^-$ versus $\pi^-\pi^+\pi^+$. The invariant masses of the event are 1.835 GeV/c^2 and 1.894 GeV/c^2, respectively, and the beam constrained masses are 1.8634 GeV/c^2 and 1.8654 GeV/c^2, respectively. However, the number of such events expected to have been produced in all the $\psi(3770)$ data sets is about 0.54 events, and it would be unlikely that one produced event with that topology could be reconstructed as both $K^0_S K^-$ versus $\pi^-\pi^+\pi^+$ and $K^0_S\pi^+$ versus $K^-\pi^+\pi^-$. Event A is therefore retained as a $K^+\pi^-\pi^+$ candidate.

5-5.5 Detection Efficiencies

Due to the selective nature of the background cuts, the reconstruction efficiency for $D^+ \to K^+\pi^-\pi^+$ must be determined separately opposite each of the seven tag modes. To estimate the efficiencies, the analysis procedures are applied to seven Monte Carlo samples, ~15,000 events apiece, with $D^+ \to K^+\pi^-\pi^+$ generated according to phase space. Table 5.9 lists the estimated efficiencies with the errors from the Monte Carlo statistics. The weighted efficiency, determined by the number of tags, is calculated to be $\bar{\varepsilon}_s$= 40.3±0.6%

Table 5.9 Detection efficiency for $D^+ \to K^+\pi^-\pi^+$ opposite each tag.

Tag Mode	Efficiency(%)
$\overline{K}^0\pi^+$	33.1 ± 0.7
$K^-\pi^+\pi^+$	43.8 ± 0.8
$\overline{K}^0\pi^+\pi^-\pi^+$	24.0 ± 0.9
$\overline{K}^0\pi^+\pi^0$	34.3 ± 1.4
$\overline{K}^0K^+$	27.9 ± 0.7
$K^-K^+\pi^+$	32.3 ± 0.9
$K^-\pi^+\pi^+\pi^0$	46.7 ± 3.0
Weighted Efficiency:	40.3 ± 0.6

5-5.6 Background Estimates

The dominant $D\overline{D}$ backgrounds after the data reduction cuts are the Class I backgrounds, $D^+ \to \overline{K}^0K^+ \to K^0_SK^+ \to (\pi^+\pi^-)K^+$, $D^+ \to K^-\pi^+\pi^+$[nr], and $D^+ \to \overline{K}^{*0}\pi^+ \to (K^-\pi^+)\pi^+$. As for the detection efficiency, the background acceptances and numbers of events must be estimated separately opposite each tag mode. The numbers are listed in Table 5.10, where the errors are statistical only, derived from the Poisson errors on the Monte Carlo statistics, the statistical errors on the background branching fractions, and the statistical errors on the number of tags. The total expected number is found to be $n_{b,D\overline{D}} = 0.81 \pm 0.21$

From the analysis of the Lund Monte Carlo data, the number of events from u, d, s production is determined to be $n_{b,uds} = 0.41^{+0.32}_{-0.12}$. This number is included in Table 5.10.

The number of expected events from all background sources is $n_b = 1.2^{+0.3}_{-0.2}$. Assuming Poisson statistics, the probability for 1.2 events to fluctuate to three events is 0.087.

Table 5.10 The expected numbers of background events to $D^+ \to K^+\pi^-\pi^+$, including the contribution from the continuum. The acceptances for the $D\bar{D}$ background are also included.

$D\bar{D}$ Background		Acceptance(%)	Number of Events
$D^+ \to K^-\pi^+\pi^+$[nr]	vs. $D^- \to K^0\pi^-$	$0.022^{+0.015}_{-0.006}$	$0.0028^{+0.0019}_{-0.0008}$
	$D^- \to K^+\pi^-\pi^-$	0.349±0.036	0.416±0.055
	$D^- \to K^0\pi^-\pi^+\pi^-$	$0.034^{+0.033}_{-0.010}$	$0.0045^{+0.0044}_{-0.0014}$
	$D^- \to K^0\pi^-\pi^0$	$0.108^{+0.065}_{-0.029}$	$0.0154^{+0.0094}_{-0.0045}$
	$D^- \to K^0K^-$	$0.085^{+0.028}_{-0.017}$	$0.0011^{+0.0005}_{-0.0004}$
	$D^- \to K^+K^-\pi^-$	$0.008^{+0.018}_{-0.002}$	$0.0005^{+0.0011}_{-0.0002}$
	$D^- \to K^+\pi^-\pi^-\pi^0$	$0.117^{+0.154}_{-0.037}$	$0.0085^{+0.0113}_{-0.0030}$
$D^+ \to \bar{K}^{*0}\pi^+$	vs. $D^- \to K^0\pi^-$	$0.012^{+0.012}_{-0.004}$	$0.0004^{+0.0005}_{-0.0003}$
	$D^- \to K^+\pi^-\pi^-$	0.888±0.088	0.279±0.207
	$D^- \to K^0\pi^-\pi^+\pi^-$	$0.038^{+0.030}_{-0.011}$	$0.0014^{+0.0015}_{-0.0011}$
	$D^- \to K^0\pi^-\pi^0$	$0.016^{+0.036}_{-0.005}$	$0.0006^{+0.0014}_{-0.0005}$
	$D^- \to K^0K^-$	$0.085^{+0.027}_{-0.016}$	0.0003±0.0002
	$D^- \to K^+K^-\pi^-$	$0.021^{+0.020}_{-0.006}$	$0.0003^{+0.0004}_{-0.0003}$
	$D^- \to K^+\pi^-\pi^-\pi^0$	$0.212^{+0.167}_{-0.061}$	$0.0041^{+0.0044}_{-0.0033}$
$D^+ \to \bar{K}^0K^+$	vs. $D^- \to K^0\pi^-$	0.602±0.089	0.0038±0.0013
	$D^- \to K^+\pi^-\pi^-$	0.991±0.116	0.0573±0.0192
	$D^- \to K^0\pi^-\pi^+\pi^-$	0.488±0.003	0.0032±0.0013
	$D^- \to K^0\pi^-\pi^0$	0.984±0.226	0.0068±0.0027
	$D^- \to K^0K^-$	0.758±0.081	0.0005±0.0002
	$D^- \to K^+K^-\pi^-$	0.879±0.136	0.0027±0.0010
	$D^- \to K^+\pi^-\pi^-\pi^0$	0.808±0.361	0.0029±0.0016
Total expected $D\bar{D}$ contribution			0.81±0.21
Total expected u, d, s contribution			$0.41^{+0.32}_{-0.12}$
Total expected number of events			$1.22^{+0.32}_{-0.24}$

Table 5.11 and Table 5.12 give the number of events for Regions I and Region II, respectively. The number of events expected in Region I is $0.33^{+0.24}_{-0.08}$, while two events are

Table 5.11 The expected numbers of background events for Region I, including the contribution from the continuum. The acceptances for the $D\bar{D}$ background are also included.

$D\bar{D}$ Background	Acceptance(%)	Number of Events
$D^+ \to K^-K^+\pi^+$ vs. $D^- \to K^0\pi^-$	0.51±0.08	0.011±0.004
$D^- \to K^+\pi^-\pi^-$	0.94±0.12	0.188±0.057
$D^- \to K^0\pi^-\pi^+\pi^-$	$0.36^{+0.14}_{-0.08}$	$0.008^{+0.004}_{-0.003}$
$D^- \to K^0\pi^-\pi^0$	$0.56^{+0.23}_{-0.13}$	$0.013^{+0.007}_{-0.005}$
$D^- \to K^0K^-$	$0.11^{+0.06}_{-0.03}$	$(2^{+2}_{-1})\times10^{-4}$
$D^- \to K^+K^-\pi^-$	0.47±0.08	0.005±0.002
$D^- \to K^+\pi^-\pi^-\pi^0$	$0.57^{+0.56}_{-0.17}$	$0.007^{+0.007}_{-0.003}$
Total expected $D\bar{D}$ contribution		0.23±0.07
Total expected u, d, s contribution		<0.23
Total expected number of events		$0.33^{+0.24}_{-0.08}$

actually observed. The variation in the predicted number is estimated to be ±2% when the resonant $K^-K^+\pi^+$ decay channels ($D^+ \to \phi\pi^+$ and $\bar{K}^{*0}K^+$) are considered. The numbers suggest, therefore, that some residual background for this region has not been accounted for, perhaps decay modes containing extra low momentum π^0's.The number of events expected in Region II is $1.46^{+0.53}_{-0.48}$, which is consistent with the observed number of one event.

5-5.7 Systematic Errors

Systematic errors are estimated for the detection efficiency of the signal, the number of $D\bar{D}$ background events and the number of u, d, s background events. Sources of error and their level of contribution is described below.

Table 5.12 The expected numbers of background events for Region II, including the contribution from the continuum. The acceptances for the $D\bar{D}$ background are also included.

$D\bar{D}$ Background		Acceptance(%)	Number of Events
$D^+ \to \bar{K}^0\pi^+$	vs. $D^- \to K^0\pi^-$	0.49±0.06	0.010±0.002
	$D^- \to K^+\pi^-\pi^-$	0.75±0.10	0.136±0.028
	$D^- \to K^0\pi^-\pi^+\pi^-$	0.46±0.96	0.010±0.003
	$D^- \to K^0\pi^-\pi^0$	0.57±0.17	0.012±0.004
	$D^- \to K^0K^-$	0.54±0.10	$(10\pm4)\times10^{-4}$
	$D^- \to K^+K^-\pi^-$	0.40±0.09	0.004±0.001
	$D^- \to K^+\pi^-\pi^-\pi^0$	1.48±0.49	0.016±0.006
$D^+ \to \pi^+\pi^-\pi^+$	vs. $D^- \to K^0\pi^-$	8.46±0.33	0.059±0.024
	$D^- \to K^+\pi^-\pi^-$	14.55±0.46	0.920±0.376
	$D^- \to K^0\pi^-\pi^+\pi^-$	5.70±0.41	0.041±0.017
	$D^- \to K^0\pi^-\pi^0$	8.88±0.69	0.067±0.029
	$D^- \to K^0K^-$	9.17±0.40	0.006±0.003
	$D^- \to K^+K^-\pi^-$	7.88±0.42	0.026±0.011
	$D^- \to K^+\pi^-\pi^-\pi^0$	12.7±1.52	0.049±0.022
Total expected $D\bar{D}$ contribution			1.36±0.48
Total expected u, d, s contribution			<0.23
Total expected number of events			$1.46^{+0.53}_{-0.48}$

Systematic Errors on $\bar{\varepsilon}_s$

The following sources are considered to contribute to the systematic error on the reconstruction efficiency of the signal. The errors are given in terms of the relative uncertainty.

1) Charged track reconstruction efficiency. For each charged track a relative uncertainty of −1% is attributed to the reconstruction efficiency. A −3% relative error is therefore given for $\bar{\varepsilon}_s$ to account for the reconstruction of the three recoil tracks. The charged track reconstruction efficiency is based on previous studies of the $\psi(3770)$ data.[62]

2) The effect of no cuts for the fiducial regions of the detector. In the tracking system, a comparison between simulated and real $\psi(3770)$ data finds no more than a –2% discrepancy in the number of detected tracks. Attributing a –1% error for each charged track yields an overall –3 % error for this effect. In the time-of-flight and dE/dx systems, the uncertainty is folded into the uncertainty in the particle identification, discussed next.

3) Particle Identification. The effects of the first and second level particle identification cuts on the $K^+\pi^-\pi^+$ signal in Monte Carlo and real data were compared by applying those cuts on samples of $K^-\pi^+\pi^+$ events. Inclusive samples were collected from all three charged track combinations with a net charge of ± 1 and $| P_{tot} - P_D | < 50$ MeV/c. The track with charge opposite to the net charge was given the kaon mass assignment, while the other two tracks were given the pion assignment. Monte Carlo and real data samples of 5294 and 1620 events were obtained, respectively. The particle identification criteria were then applied, and differences in efficiencies of ± 2%, ± 1% and ± 1% were found for the second level kaon identification, second level pion identification and first level pion identification, respectively. Added in quadrature, these numbers give an overall ± 2.4% uncertainty due to the particle identification.

4) Anti-photon cut. Although $D^+ \to K^+\pi^-\pi^+$ produces no extra photons, the anti-photon cut may reject real events when split-offs from charged tracks generate an isolated shower. The detector simulation does not model this effect. The –8% uncertainty introduced by this cut was estimated by applying the anti-photon cut on the tagged $K^-\pi^+\pi^+$ sample from the first analysis test in Section 5-5.1.

5) Mass cuts and definition of the signal region. Wide mass cuts were introduced by the anti-K^0_S and topology cuts, and the wide cuts about the D mass define the signal region. A ± 1% error is given to account for possible tails in the signal distribution.

6) Resonant substructure. The efficiency was estimated by generating $D^+ \to K^+\pi^-\pi^+$ according to phase space. Differences in efficiency of –1 %

Table 5.13 The systematic errors on the $K^+\pi^-\pi^+$ detection efficiency.

Source	Systematic Error (%)
Charged track efficiency	−1.2
Absence of fiducial cuts	−1.2
Particle Identification	±1.0
Anti-photon cut	−3.2
Mass and signal region cuts	±0.4
Resonant substructure	−2.8
Total Error	+1.1 / −8.5

and −7% were observed when $D^+ \to K^+\rho^0 \to K^+(\pi^-\pi^+)$ and $D^+ \to K^{*0}\pi^+ \to (K^+\pi^-)\pi^+$. Therefore a −7% error is attributed to this effect.

These errors are summarized in Table 5.13 in terms of the absolute error on the reconstruction efficiencies for $D^+ \to K^+\pi^-\pi^+$. The total errors are obtained by adding the biased errors linearly and the remaining errors in quadrature. Quoting both statistical and systematic errors, the weighted efficiencies for the signal is

$$\bar{\varepsilon}_s = 40.3 \pm 0.6^{+1.1}_{-8.5}\%$$

Systematic Errors on $n_{b,D\bar{D}}$

Several effects which contribute to the systematic uncertainty of the signal efficiency also introduce uncertainties to the number of D (Class I) background events. Discussion of these effects on the backgrounds follows, with the errors given in terms of the relative uncertainty on the number of events.

1) Charged track reconstruction efficiency. All backgrounds are detected with three charged tracks in the recoil; therefore a −3% error is attributed.

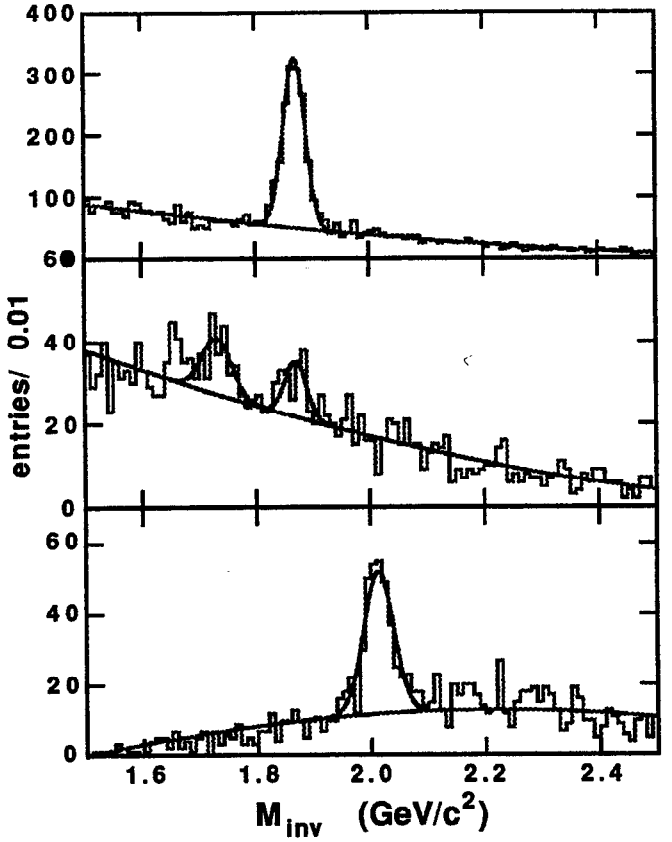

Figure 5.15 Forcing track misidentification with a sample of $D^+ \rightarrow K^-\pi^+\pi^+$: (a) the event sample; (b) kaon misidentification yielding a reflection peak at approximately 1.73 GeV/c^2 (the signal peak is due to $D^+ \rightarrow \bar{K}^0\pi^+$); (c) pion misidentification yielding a reflection peak at approximately 1.95 GeV/c^2.

2) The effect of no cuts for the fiducial regions of the detector. For three charged tracks, a –3% uncertainty is attributed.

3) Particle identification and misidentification. For the $\bar{K}^0K^+$ background, all tracks are identified correctly, and therefore a ±2% error is given to account for the uncertainty in particle identification for that background. For the $K^-\pi^+\pi^+$ backgrounds, the uncertainties in the kaon and pion misidentifications were estimated by modifying the particle identification study performed for the signal efficiency; for this study, the inclusive $K^-\pi^+\pi^+$ samples were again used, but tracks were assigned the opposite mass hypothesis before applying the first and second level particle identification criteria. This intentional misidentification is demonstrated in Figure 5.15. Uncertainties of approximately +6% and +9%

are estimated for the kaon and pion misidentifications, respectively. Including the ±1% uncertainty for correctly identifying the other pion track, an overall error in the particle identification for the $K^-\pi^+\pi^+$ backgrounds is estimated to be $^{+15}_{-1}$%, when the numbers are propagated linearly. Since the $K^-\pi^+\pi^+$ backgrounds dominate, the error on the total number of background events is $^{+14}_{-1}$%.

4) Anti-photon cut. The D backgrounds also do not produce extra photons. An error of –8% is therefore given.

5) Mass cuts and definition of the signal region. Wide mass cuts were introduced by the anti-K^0_S and topology cuts, and the wide cuts about the D mass define the signal region. A ±5% error is given to account for possible tails in the $M_{\pi^+\pi^-}$ and signal distributions.

The following additional sources have been considered in the systematic error on $n_{b\bar{D}D}$.

6) The branching fractions for the background processes. The relative systematic errors in the branching fractions for $\bar{K}^0K^+$ (17%), $K^-\pi^+\pi^+$[nr] (25%) and $\bar{K}^{*0}\pi^+ \to (K^-\pi^+)\pi^+$ (95%) propagate to a ±21.0% error in the number of background events, where the correlations between the latter two modes have been taken into account. The systematic error for the decay of the $\bar{K}^0$ is negligible.

7) The error on the number of tags. These systematic errors contribute a ±1.7% uncertainty on the total number of background events (refer to Table 4.2).

These errors are summarized in Table 5.15 in terms of the absolute error on $n_{b\bar{D}D}$. The total errors are obtained by adding the biased errors linearly and the remaining errors in quadrature. Quoting both statistical and systematic errors, the number of D background events is:

$$n_{b\bar{D}D} = 0.81 \pm 0.21^{+0.21}_{-0.24}$$

Table 5.14 The systematic errors on the number of $D\overline{D}$ background events.

Source	Error (#events)
Charged track efficiency	–0.02
Absence of fiducial cuts	–0.02
Particle identification	+0.11 / –0.01
Anti-photon cut	–0.12
Mass and signal region cuts	±0.01
Branching Fractions	±0.17
Number of tags	±0.01
Total uncertainty	+0.21 / –0.24

Systematic Errors on $n_{b.uds}$

Because of the limited statistics from the Lund Monte Carlo data, the various *u*, *d*, *s* event topologies which can leak into the signal are not well understood. To estimate the systematic errors for $n_{b.uds}$, some assumptions are made about the topologies and the misidentification mechanisms: for the majority of the topologies (1) the charged track multiplicity is six; and (2) the tracks identified as the recoil K^+ and the recoil π^- are, respectively, a pion and a kaon which have been misidentified. With these assumptions the relative systematic errors on the number of *u*, *d*, *s* background events follows.

1) Charged track reconstruction efficiency. For six charged tracks, a –6% error is attributed.

2) The effect of no cuts for the fiducial regions of the detector. For six charged tracks, a –6% uncertainty is attributed.

3) Particle identification. In the recoil, double track misidentification and one correct track identification contribute errors of $^{+15}_{-1}$%. Assuming the tracks in the tag are correctly identified contributes an additional ±2%

Table 5.15 The systematic errors on the number of u, d, s background events.

Source	Error (#events)
Charged track efficiency	–0.02
Absence of fiducial cuts	–0.02
Particle identification	+0.06 / –0.01
Anti-photon cut.	–0.03
Mass and signal region cuts	±0.02
Integrated Luminosity	±0.02
Total uncertainty	+0.07 / –0.08

uncertainty. Adding the errors in quadrature gives a total uncertainty of $^{+15}_{-3}$% from particle identification.

4) Anti-photon cut. Although some topologies may produce extra photons, an error of –8% is still given to account for the uncertainty in removing events with split-off showers.

5) Mass cuts and definition of the signal region. A ±5% error is given to account for effects of the mass cuts and the overlap of the background with the signal region.

6) Integrated Luminosity for the $\psi(3770)$ data set. This number contains a ±5% error which directly contributes to the systematic error on the number background events.

These errors are summarized in Table 5.15 in terms of the absolute error on the number of u, d, s background events. The total errors are obtained by adding the biased errors linearly and the remaining errors in quadrature. Quoting both statistical and systematic errors, the number of u, d, s background events is:

$$n_{b.uds} = 0.41^{+0.32+0.07}_{-0.12-0.08}$$

5-6 Upper Limit for $B(D^+ \to K^+\pi^-\pi^+)$

To obtain an upper limit for $B(D^+ \to K^+\pi^-\pi^+)$, a maximum likelihood fit is performed for observing three candidate events in the presence of background. The following notation is used to describe the likelihood functions:

- $\mu_s \equiv$ the true number of $D^+ \to K^+\pi^-\pi^+$ events.
- $\mu_{b.D\bar{D}}$ $(n_{b.D\bar{D}}) \equiv$ the true (estimated) number of background events for $K^+\pi^-\pi^+$ originating from charm production.
- $\mu_{b.uds}(n_{b.uds}) \equiv$ the true (estimated) number of background events for $K^+\pi^-\pi^+$ originating from u, d, s production.
- $n_{obs} \equiv$ the observed number of events for $K^+\pi^-\pi^+$.
- $\eta_s(\varepsilon_s) \equiv$ the true (estimated) reconstruction efficiency for $K^+\pi^-\pi^+$.
- μ_{tags} $(n_{tags}) \equiv$ the true (estimated) number of tags.
- $\sigma_{b.D\bar{D}}$, σ_s, $\sigma_{tags} \equiv$ the statistical standard deviations on $n_{b.D\bar{D}}$, ε_s, and n_{tags}, respectively.
- $p \equiv$ the set of true quantities $\{\eta_s, \mu_s, \mu_{b.D\bar{D}}, \mu_{b.uds}\}$
- $\hat{p} \equiv$ the set of estimated quantities $\{\varepsilon_s, n_{b.D\bar{D}}, n_{buds}, \sigma_s, \sigma_{b.D\bar{D}}\}$

The joint likelihood function is

$$\mathcal{L}(n_{obs}, p; \hat{p}) = \mathcal{P}(n_{obs}; \mu_s+\mu_{b.D\bar{D}}+\mu_{b.uds}) \times \mathcal{G}(\eta_s; \varepsilon_s, \sigma_s)\mathcal{G}(\mu_{tags}; n_{tags}, \sigma_{tags})\mathcal{G}(\mu_{b.D\bar{D}}; n_{b.D\bar{D}}, \sigma_{b.D\bar{D}})\mathcal{P}(\alpha n_{b.uds}; \alpha\mu_{b.uds})$$

where $\mathcal{P}$ represents a Poisson probability distribution:

$$\mathcal{P}(n; \mu) = \frac{\mu^n e^{-\mu}}{n!};$$

and $\mathcal{G}$ represents a Gaussian distribution:

$$G(x;\mu,\sigma^2) = \frac{1}{\sigma\sqrt{2\pi}} exp\left(-\frac{(x-\mu)^2}{2\sigma^2}\right)$$

The constant α is the normalization between the Lund Monte Carlo samples and the $\psi(3770)$ data samples; $\alpha\mu_{b.uds}$ ($\alpha n_{b.uds}$) is the true (estimated) number of Lund Monte Carlo events accepted as the signal. Due to the low statistics, a Poisson distribution is used.

Under the constraint

$$\mu_s = \mu_{tags}\, \eta_s\, B(K^+\pi^-\pi^+)\, C$$

the likelihood function is maximized at different values of $B(K^+\pi^-\pi^+)$ by varying μ_{tags}, η_s, $\mu_{b.D\bar{D}}$ and $\mu_{b.uds}$. The likelihood function is integrated to find the 90% confidence level:

$$\frac{\int_0^{B_\infty} L(B)dB}{\int_0^1 L(B)dB} = 0.9$$

Systematic errors are propagated by changing the mean values for ε_s, n_{tags}, $n_{b.D\bar{D}}$ and $n_{b.uds}$ by the errors which cause the limit to increase, e.g. $\varepsilon_s \to \varepsilon_s - \delta\varepsilon_s$. The joint likelihood function is then maximized using the adjusted values.

The likelihood function is shown in Figure 5.16, treating the three candidate events as non-resonant $K^+\pi^-\pi^+$. The dashed and solid curves show, respectively, the results without and with systematic errors propagated; the arrows indicate the 90% confidence levels. If systematic errors were neglected, $B(D^+ \to K^+\pi^-\pi^+) < 0.57\%$. The systematic errors increase this limit to

$$\boxed{B(D^+ \to K^+\pi^-\pi^+) < 0.77\% \text{ @ } 90\% \text{ CL}}$$

A final test of this result is performed in a separate analysis of doubly Cabibbo suppressed decays where fully reconstructed events are kinematically fitted rather than

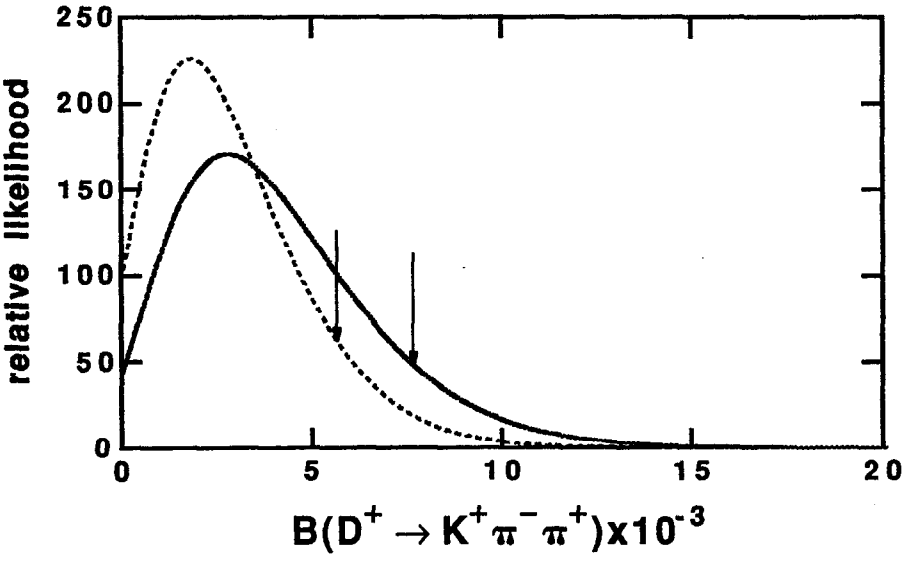

Figure 5.16 The likelihood function relative to $B(D^+ \to K^+\pi^-\pi^+)$.

tagged. The analysis and results are detailed in Appendix 2. The limit for $K^+\pi^-\pi^+$ found in that analysis is $B(D^+ \to K^+\pi^-\pi^+) < 0.77\%$ at 90% confidence level.

5-7 Resonant Substructure Analysis and Upper Limits for $B(D^+ \to K^+\rho^0)$, $B(D^+ \to K^{*0}\pi^+)$, and $B(D^+ \to K^+\pi^-\pi^+[\text{nr}])$

The resonant decay channels of $K^+\pi^-\pi^+$ are $D^+ \to K^+\rho^0 \to K^+(\pi^+\pi^-)$ and $D^+ \to K^{*0}\pi^+ \to (K^+\pi^-)\pi^+$. A substructure analysis has been performed to determine the limits specific to these decay channels and to the nonresonant component.

The analysis begins by introducing cuts to isolate the resonant $K^+\pi^-\pi^+$ modes. Both modes decay as $P \to VP_1$, $V \to P_2 P_3$, where P denotes a pseudoscalar meson and V denotes a vector meson. By conservation of angular momentum, the P, or D^+, must decay to the VP_1 in a relative p-wave, which produces the P_2, or P_3, with an angular distribution of $\cos^2\theta$ in the helicity frame of the V. This property produces the Dalitz plot distributions shown in Figure 5.17, where $M^2_{K\pi}$ is plotted against $M^2_{\pi\pi}$ for Monte Carlo $D^+ \to K^+\rho^0$ and $K^{*0}\pi^+$, $M_{K\pi}$ and $M_{\pi\pi}$ being the $K^+\pi^-$ and $\pi^+\pi^-$ invariant masses, respectively.

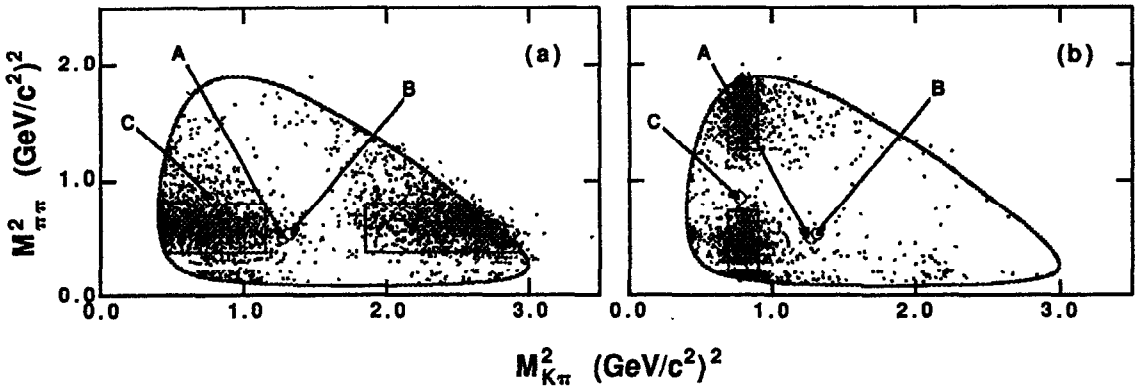

Figure 5.17 The Dalitz plot $M^2_{\pi\pi}$ versus $M^2_{K\pi}$ for the three candidate events and for (a) Monte Carlo $D^+ \to K^+\rho^0$, $\rho^0 \to \pi^+\pi^-$ and (b) $D^+ \to K^{*0}\pi^+$, $K^{*0} \to K^+\pi^-$. The solid lines in the plots indicate the cuts introduced to isolate the respective decay channels. The absence of events about $M^2_{\pi\pi} = 0.248$ (GeV/c^2)^2 is due to the anti-K^0_S cut.

Events are accepted as $K^+\rho^0$ candidates if:

- $0.38 < M^2_{\pi\pi} < 0.80$ (GeV/c^2)^2 $\qquad D^+ \to K^+\rho^0 \to K^+(\pi^+\pi^-)$
- $M^2_{K\pi} > 1.15$ or $M^2_{K\pi} < 1.85$ (GeV/c^2)^2

These cuts isolate the lobes of the ρ^0; in the respective projections, the former cut is a 2σ constraint about the square of the ρ mass, while the latter contains 95% of the $K^+\rho^0$ signal. Events are accepted as $K^{*0}\pi^+$ candidates if:

- $0.74 < M^2_{K\pi} < 1.26$ (GeV/c^2)^2 $\qquad D^+ \to K^{*0}\pi^+ \to (K^+\pi^-)\pi^+$
- $M^2_{\pi\pi} > 0.69$ or $M^2_{\pi\pi} < 0.90$

These cuts isolate the lobes of the K^{*0} in the same manner as the cuts for the $K^+\rho^0$ candidates. Events rejected by both of these cuts are accepted as nonresonant $K^+\pi^+\pi^-$.

Superimposed on the plot in Figure 5.17 are the three candidate events. None of the events are found to be strong candidates for either $D^+ \to K^+\rho^0 \to K^+(\pi^+\pi^-)$ or $D^+ \to K^{*0}\pi^+ \to (K^+\pi^-)\pi^+$, since no events survive after applying either set of Dalitz cuts. In the

Table 5.16 Submasses and submasses squared of the $D^+ \to K^+\pi^-\pi^+$ candidates.

	Event A	Event B	Event C
$M_{\pi\pi}$ (GeV/c^2)	0.707	0.730	0.925
$M_{K\pi}$ (GeV/c^2)	1.127	1.146	0.882
$M^2_{\pi\pi}$ (GeV/c^2)^2	0.500	0.533	0.856
$M^2_{K\pi}$ (GeV/c^2)^2	1.270	1.313	0.778

case of $K^+\rho^0$, Events A and B do have $\pi^+\pi^-$ invariant masses consistent with the ρ mass, but both lie at the edge of the ρ^0 lobe and are removed by the by the $M^2_{K\pi}$ constraints. Similarly in the case of $K^{*0}\pi^+$, Event C has a $K^+\pi^-$ invariant mass consistent with the K^* mass but is removed by the constraints on $M^2_{\pi\pi}$ The invariant mass information for the three events is given in Table 5.16. All three events are consistent with nonresonant $K^+\pi^-\pi^+$.

Before continuing the analysis, a few observations must be made. While the cuts for $K^+\rho^0$, $K^{*0}\pi^+$ and $K^+\pi^-\pi^+$[nr] are designed to isolate the respective decay channels, a cut for one mode does not eliminate the presence of signal events from the other two. Therefore, $K^+\rho^0$ and $K^+\pi^+\pi^-$[nr] contribute background to $K^{*0}\pi^+$, etc. Additionally, the cuts in the Dalitz plots for the $K^+\rho^0$ and $K^{*0}\pi^+$ are not mutually exclusive; they overlap in the lower left region of the Dalitz plot, and a subset of events produced as $K^+\rho^0$, for example, will be detected as both $K^+\rho^0$ and $K^{*0}\pi^+$. To obtain uncorrelated data, e.g. when estimating efficiencies, the overlapping region could be excluded, but this would cause a significant loss in efficiency. Instead for the balance of this analysis, four independent regions of the Dalitz plot are analyzed. If $R_{K\rho}$ and $R_{K^*\pi}$ are the regions cut out by the selection requirements for $K^+\rho^0$ and $K^{*0}\pi^+$, respectively, then the four regions are

- Region 1: $R_{K\rho} - (R_{K\rho} \cap R_{K^*\pi})$

Table 5.17 The $K^+\pi^-\pi^+$ weighted efficiencies in percent.

		Region			
		1	2	3	4
Produced Mode	$K^+\rho^0$	$23.9\pm0.5^{+1.4}_{-3.6}$	$1.0\pm0.1^{+0.1}_{-0.2}$	$3.9\pm0.2^{+0.2}_{-0.6}$	$9.4\pm0.3^{+0.5}_{-1.4}$
	$K^{*0}\pi^+ \to (K^+\pi^-)\pi^+$	$3.2\pm0.2^{+0.2}_{-0.5}$	$18.5\pm0.4^{+1.1}_{-2.8}$	$6.2\pm0.2^{+0.4}_{-0.9}$	$7.4\pm0.3^{+0.4}_{-1.1}$
	$K^+\pi^-\pi^+$[nr]	$7.8\pm0.3^{+0.4}_{-1.2}$	$2.0\pm0.1^{+0.1}_{-0.3}$	$1.1\pm0.1^{+0.1}_{-0.2}$	$29.2\pm0.5^{+1.7}_{-4.4}$

- Region 2: $R_{K^*\pi} - (R_{K\rho} \cap R_{K^*\pi})$
- Region 3: $R_{K\rho} \cap R_{K^*\pi}$
- Region 4: $\overline{\text{Region 1 + Region 2 + Region 3}}$

The number of expected events (n^i_{exp}) from Region i is

$$n^i_{exp} = n_{tags} \sum_j \varepsilon^i{}_j B^j C + n^i_b$$

where n_{tags} is the number of tags, $\varepsilon^i{}_j$ is the efficiency for detecting the produced $K^+\pi^-\pi^+$ decay j in Region i, B^i is the branching fraction for decay i, C is the multiple counting correction factor and n^i_b is the number of events from the other backgrounds.

Detection Efficiencies

As before, efficiencies are determined opposite each of the seven tag modes from Monte Carlo simulations. The weighted efficiencies, $\bar{\varepsilon}^i{}_j$, are given in Table 5.17, with statistical and systematic errors, respectively. The relative systematic errors are the same as before (Section 5-5.7) with the uncertainty from the resonant substructure removed and a $\pm5\%$ error added, in quadrature, to account for the uncertainty introduced by the Dalitz cuts. The reconstruction efficiencies for $D^+ \to K^+\rho^0 \to K^+(\pi^+\pi^-)$, $D^+ \to K^{*0}\pi^+ \to (K^+\pi^-)\pi^+$ and $D^+ \to K^+\pi^-\pi^+$[nr] are, therefore

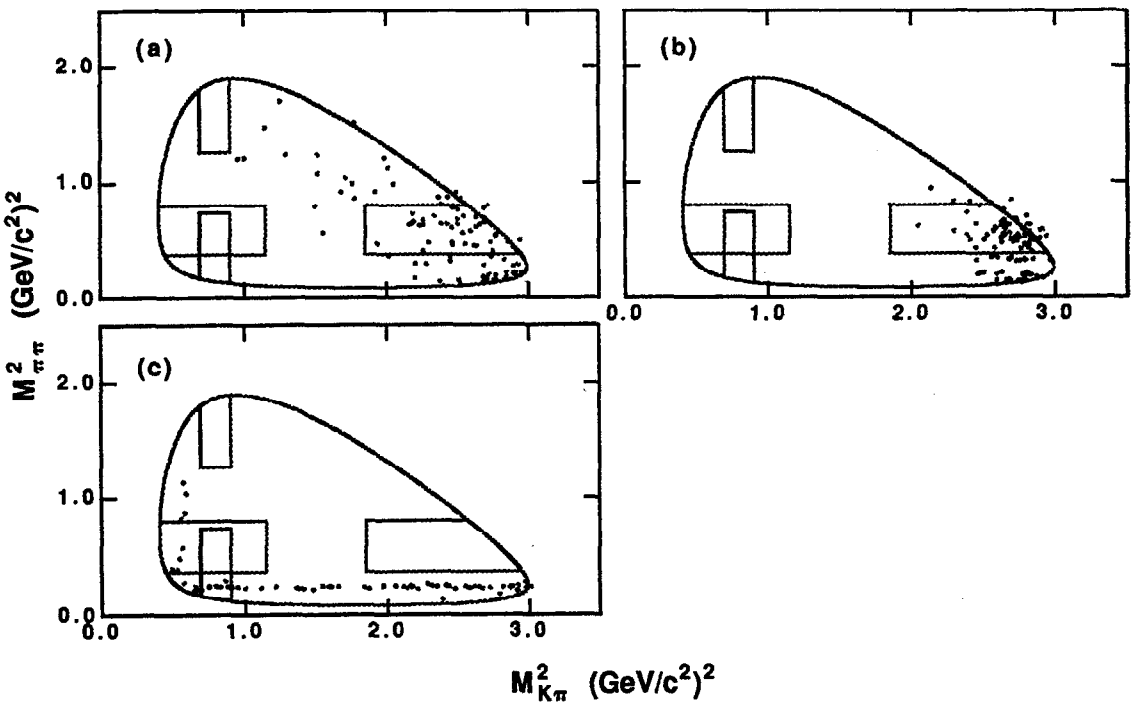

Figure 5.18 Dalitz plots of the major Class I backgrounds: (a) $D^+ \to K^-\pi^+\pi^+$[nr], (b) $D^+ \to \overline{K}^{*0}\pi^+ \to (K^-\pi^+)\pi^+$, and (c) $D^+ \to \overline{K}^0K^+ \to K^0_SK^+ \to (\pi^+\pi^-)K^+$.

$$\varepsilon_{K\rho} = \varepsilon^1_{K\rho} + \varepsilon^2_{K\rho} = 27.8 \pm 0.5^{+1.6}_{-4.2}\%$$

$$\varepsilon_{K^*\pi} = \varepsilon^2_{K^*\pi} + \varepsilon^3_{K^*\pi} = 24.7 \pm 0.4^{+1.4}_{-3.7}\%$$

$$\varepsilon_{nr} = \varepsilon^4_{nr} = 29.2 \pm 0.5^{+1.7}_{-4.4}\%$$

Background Estimates

Dalitz plots of the three Class I backgrounds, $D^+ \to \overline{K}^0K^+ \to K^0_SK^+ \to (\pi^+\pi^-)K^+$, $D^+ \to K^-\pi^+\pi^+$[nr], and $D^+ \to \overline{K}^{*0}\pi^+ \to (K^-\pi^+)\pi^+$, are shown in Figure 5.18. None of the three backgrounds are found to contribute significantly to the overlap region, and only the $\overline{K}^0K^+$ background contributes to Region 2. Numbers of events are estimated as before with the additional cuts for the four Dalitz plot regions. The total numbers of events from $D\overline{D}$ backgrounds are listed in Table 5.18 with statistical and systematic errors, respectively. The relative systematic errors are the same as before (Section 5-5.7) with, again, an

Table 5.18 The expected numbers of background events, and the covariant matrix associated with the numbers of events from $D\overline{D}$ production (see text).

$D\overline{D}$ Background	Region			
	1	2	3	4
$D^+ \to K^-\pi^+\pi^+$[nr]	$0.210\pm0.035\pm0.062$	negligible	negligible	$0.226^{+0.037}_{-0.036}\pm0.067$
$D^+ \to \overline{K}^{*0}\pi^+ \to (K^-\pi^+)\pi^+$	$0.181\pm0.135\pm0.174$	negligible	negligible	$0.106\pm0.080\pm0.102$
$D^+ \to \overline{K}^0K^+$	$0.005^{+0.003}_{-0.002}\pm0.001$	$0.008\pm0.003\pm0.002$	negligible	$0.062\pm0.020^{+0.012}_{-0.015}$
Total $D\overline{D}$ Contribution	$0.396\pm0.135\pm0.144$	$0.008\pm0.003\pm0.002$	–	$0.394\pm0.084^{+0.096}_{-0.101}$
Total u, d, s Contribution	$0.10^{+0.23}_{-0.03}\pm0.02$	$0.10^{+0.23}_{-0.03}\pm0.02$	$0.10^{+0.23}_{-0.03}\pm0.02$	$0.10^{+0.23}_{-0.03}{}^{+0.04}_{-0.03}$
Total Number of Events	$0.50^{+0.27}_{-0.14}\pm0.16$	$0.11^{+0.23}_{-0.03}\pm0.02$	$0.10^{+0.23}_{-0.03}\pm0.02$	$0.49^{+0.25}_{-0.09}\pm0.12$

$D\overline{D}$ Covariances	1	2	3	4
1	0.0182	4.0×10^{-6}	0	0.0096
2	4.0×10^{-6}	9.0×10^{-6}	0	4.9×10^{-6}
3	0	0	0	0
4	0.0096	4.9×10^{-6}	0	0.0071

additional ±5% error included, in quadrature, to account for the uncertainty introduced by the Dalitz cuts. From those numbers, the total expected numbers for the three decay channels are found to be

$$n^{K\rho}_{b.D\bar{D}} = n^1_{b.D\bar{D}} = 0.40\pm0.14\pm0.14$$

$$n^{K^*\pi}_{b.D\bar{D}} = n^2_{b.D\bar{D}} = 0.008\pm0.003\pm0.002$$

$$n^{nr}_{b.D\bar{D}} = n^4_{b.D\bar{D}} = 0.39\pm0.08\pm0.10.$$

Significant correlations exist among these numbers due to the errors in the branching fractions for the background processes. The covariance among the total numbers are included with Table 5.18.

Table 5.18 includes the contributions from *u*, *d*, *s* production. The numbers are determined to be

$$n^{K\rho}_{b.uds} = n^1_{b.uds} + n^3_{b.uds} = 0.20^{+0.33}_{-0.04}\pm0.04$$

$$n^{K^*\pi}_{b.uds} = n^2_{b.uds} + n^3_{b.uds} = 0.20^{+0.33}_{-0.04}\pm0.04$$

$$n^{nr}_{b.uds} = n^4_{b.uds} = 0.10^{+0.23}_{-0.03}\pm0.02.$$

The numbers of expected events from all background sources are $n^{K\rho}_b = 0.60^{+0.35}_{-0.14}$ $n^{K^*\pi}_b = 0.21^{+0.33}_{-0.04}$, $n^{nr}_b = 0.49^{+0.25}_{-0.09}$. The probabilities for 0.60 and 0.21 events to fluctuate to zero are 0.55 and 0.81, respectively, while the probability for 0.49 events to fluctuate to three is 0.01.

Upper Limits for $B(D^+ \to K^+\rho^0)$, $B(D^+ \to K^{*0}\pi^+)$, and $B(D^+ \to K^+\pi^-\pi^+[\text{nr}])$

Upper limits for $D^+ \to K^+\rho^0$, $D^+ \to K^{*0}\pi^+$ and $D^+ \to K^+\pi^-\pi^+$[nr] are obtained by a variation of the maximum likelihood procedure described in Section 5-6. The following notation is used to describe the likelihood functions for this analysis:

- μ^i (n^i_{obs}) ≡ the true (observed) numbers of signal events after the cuts for Region i.
- μ^i_j ≡ the true numbers of events from the $K^+\pi^-\pi^+$ decay j after the cuts for Region i.
- $\mu^i_{b.D\bar{D}}$ ($n^i_{b.D\bar{D}}$) ≡ the true (estimated) number of background events from Region i originating from charm production.
- $\mu^i_{b.uds}$ ($n^i_{b.uds}$) ≡ the true (estimated) number of background events from Region i originating from u, d, s production.
- n^i_{obs} ≡ the observed number of events for Region i.
- η^i_j (ε^i_j) ≡ the true (estimated) reconstruction efficiencies for the $K^+\pi^-\pi^+$ decay j with the cuts for Region i.
- μ_{tags} (n_{tags}) ≡ the true (estimated) number of tags.
- σ^i_j, σ_{tags} ≡ the statistical standard deviations on ε^i_j and n_{tags}, respectively.
- $\vec{\mu}_{b.D\bar{D}}$ ($\vec{n}_{b.D\bar{D}}$) ≡ the vector of the $\mu^i_{b.D\bar{D}}$'s ($n^i_{b.D\bar{D}}$'s).
- V ≡ the covariance matrix of the $n^i_{b.D\bar{D}}$'s.
- $\boldsymbol{p}$ ≡ the set of true quantities $\{\eta^i_j, \mu^i_j, \mu^i_{b.D\bar{D}}, \mu^i_{b.uds}\}$.
- $\hat{\boldsymbol{p}}$ ≡ the set of estimated quantities $\{\varepsilon^i_j, n^i_{b.D\bar{D}}, n^i_{b.uds}, \sigma_s, V_{ij}\}$.

The joint likelihood function is

$$\mathcal{L}(n_{obs}, \boldsymbol{p}; \hat{\boldsymbol{p}}) = \prod_i [\mathcal{P}(n^i_{obs}; \mu^i)] \prod_{i,j} [\mathcal{G}(\eta^i_j; \varepsilon^i_j, \sigma^i_j)] \times$$
$$\mathcal{G}(\mu_{tags}; n_{tags}, \sigma_{tags})\, \mathcal{M}(\vec{\mu}_{b.D\bar{D}}; \vec{n}_{b.D\bar{D}}, V) \prod_i [\mathcal{P}(\alpha\, n^i_{b.uds}; \alpha\mu^i_{b.uds})]$$

where $\mathcal{P}$ represents a Poisson probability distribution, $\mathcal{G}$ a Gaussian probability distribution and $\mathcal{M}$ a multivariate Gaussian distribution:

$$\mathcal{M}(\vec{x}; \vec{\mu}, V) = \frac{1}{(2\pi)^{n/2}} |V|^{-1/2} exp\left(-\frac{1}{2}(\vec{x} - \vec{\mu})^T V^{-1} (\vec{x} - \vec{\mu})\right)$$

The upper limit calculation for a given branching fraction again involves first maximizing the likelihood function at different values of that branching fraction. The other two branching fractions are allowed to vary along with μ_{tags}, the η_j^i's, the $\mu_{b.D\bar{D}}^i$'s, and the $\mu_{b.uds}^i$'s, all under the constraints

$$\mu^i = \mu_{K\rho}^i + \mu_{K^*\pi}^i + \mu_{K\pi\pi[nr]}^i + \mu_{b.D\bar{D}}^i + \mu_{b.uds}^i$$

$$\mu_{K\rho}^i = \mu_{tags}\, \eta_{K\rho}^i\, B(K^+\rho^0)\, C$$

$$\mu_{K^*\pi}^i = \mu_{tags}\, \eta_{K^*\pi}^i\, B(K^{*0}\pi^+)\, (2/3)\, C$$

$$\mu_{K\pi\pi[nr]}^i = \mu_{tags}\, \eta_{K\pi\pi[nr]}^i\, B(K^+\pi^-\pi^+[nr])\, C \qquad i = 1, 2, 3, 4.$$

The likelihood function is then integrated numerically to find the 90% confidence level, and the systematic errors are treated as before.

The likelihood functions for $B(K^+\rho^0)$, $B(K^{*0}\pi^+)$ and $B(K^+\pi^-\pi^+[nr])$ are shown in Figure 5.19. Dashed and solid curves show, respectively the results without and with systematic errors propagated, and the arrows indicate the 90% confidence levels. With the systematic errors neglected, $B(D^+ \to K^+\rho^0) < 0.37\%$, $B(D^+ \to K^{*0}\pi^+) < 0.57\%$ and $B(D^+ \to K^+\pi^+\pi^-[nr]) < 0.61\%$. The systematic errors increase these limits to

$$B(D^+ \to K^+\rho^0) < 0.45\% \text{ @ } 90\% \text{ CL}$$

$$B(D^+ \to K^{*0}\pi^+) < 0.68\% \text{ @ } 90\% \text{ CL}$$

$$B(D^+ \to K^+\pi^+\pi^-[nr]) < 0.76\% \text{ @ } 90\% \text{ CL}$$

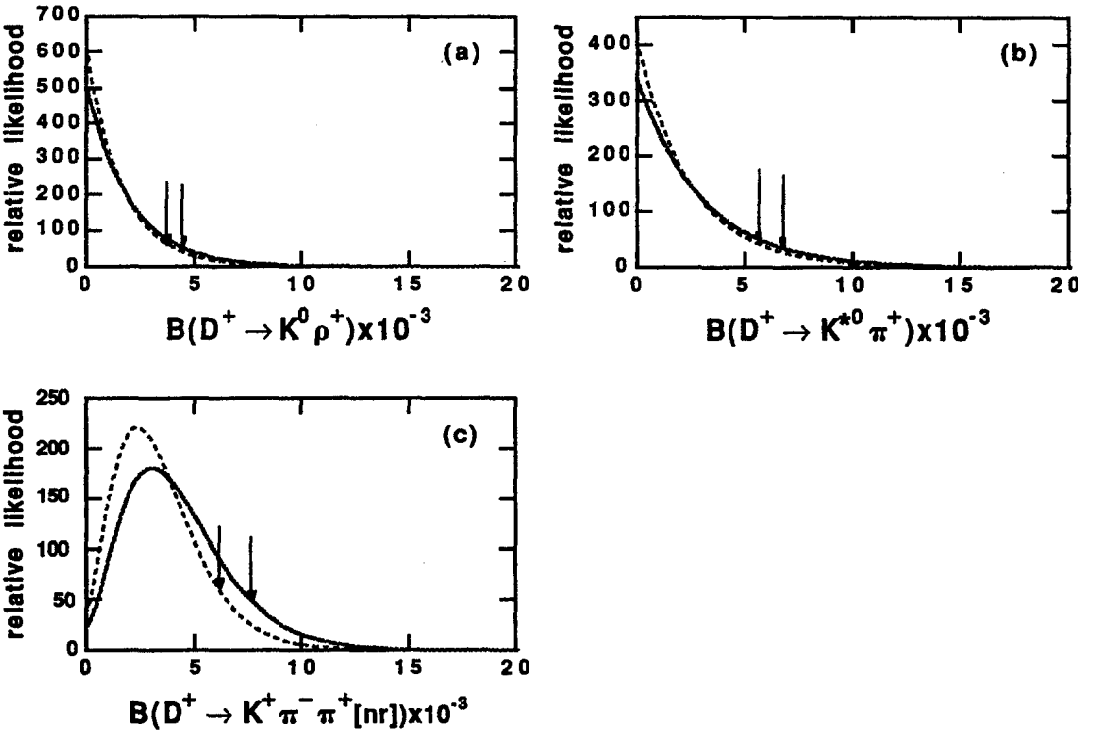

Figure 5.19 The likelihood functions for (a) $D^+ \to K^+\rho^0$, (b) $D^+ \to K^{*0}\pi^+$ and (c) $D^+ \to K^+\pi^+\pi^-$[nr].

Chapter 6

Search for $D^+ \to K^+\pi^0$

6-1 Introduction

This chapter discusses the search for $D^+ \to K^+\pi^0$ and is outlined as follows. Section 6-2 describes the initial event selection for $K^+\pi^0$, and Section 6-3 discusses the contribution of the doubly Cabibbo suppressed decay $D^+ \to K^+\eta$ to the $K^+\pi^0$ signal. Section 6-4 discusses the backgrounds that arise from charm and u, d, s production, and it describes the cuts added to reduce them. Section 6-5 gives the results of the analysis on the data and includes various analysis checks and estimates of the efficiency and level of background. Finally, Section 6-6 gives the upper limit calculation on the branching fraction for $D^+ \to K^+\pi^0$.

6-2 Event Selection

As a first approach to this analysis, the same general procedure used for $D^+ \to K^+\pi^-\pi^+$ was applied, i. e. try to fully reconstruct the $D^+ \to K^+\pi^0$ final state opposite a tag. The difference for this channel is the presence of a π^0, which is reconstructed through the decay $\pi^0 \to \gamma\gamma$; the shower energies are poorly measured by the calorimetry, and the number of spurious track combinations is larger than for the $K^+\pi^-\pi^+$ case. The event selection was as follows: given a tagged event

- Require one charged track and two or more isolated photons in the recoil. The charge of the recoil track must be opposite that of the tag.
- Require the charged track to have a good helix fit, energy loss corrections and a good beam fit.

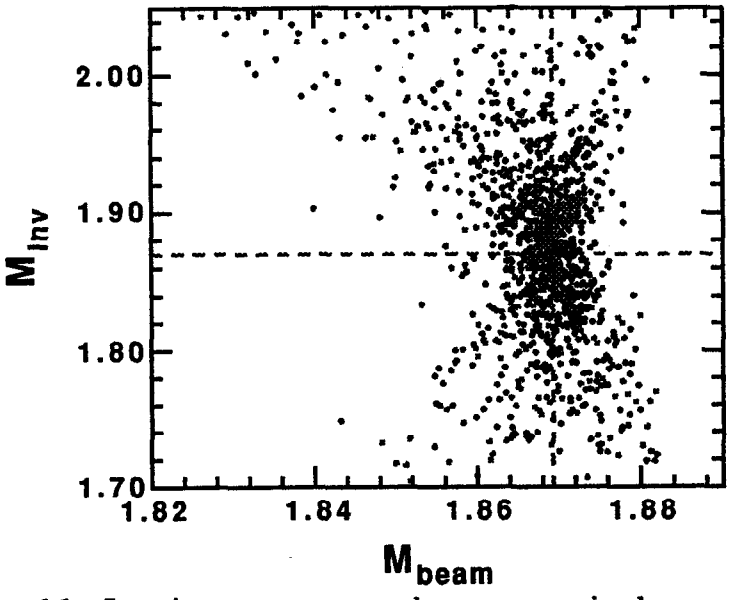

Figure 6.1 Invariant mass versus beam constrained mass for $D^+ \to K^+\pi^0$. The dashed lines denote the expected signal masses

- Require the track to be identified as a kaon according to the particle identification algorithm from the tagging procedure.
- Reconstruct the π^0 by kinematically fitting each pair of isolated photons to the π^0 mass, and require the χ^2 confidence level to be greater than 0.1.

The scatter plot of invariant mass versus beam-constrained mass was then formed from the $K\pi^0$ candidates, as shown in Figure 6.1 for the desired signal.

The efficiency for detecting the signal is ~30% before applying any further cuts on the backgrounds. The poor resolution due to the π^0 reconstruction is evident. This problem presents difficulties when attempting to remove background, for example, from $D^+ \to \pi^+\pi^0$ events; the reflection peaks which occur in M_{inv} from track misidentifications are no longer well resolved from the signal peaks.

To avoid the resolution problems and to try to improve efficiency, another approach was pursued. This approach exploits the unique features of $D^+ \to K^+\pi^0$. This channel has only one charged track. Because it is a two-body decay and the D meson is

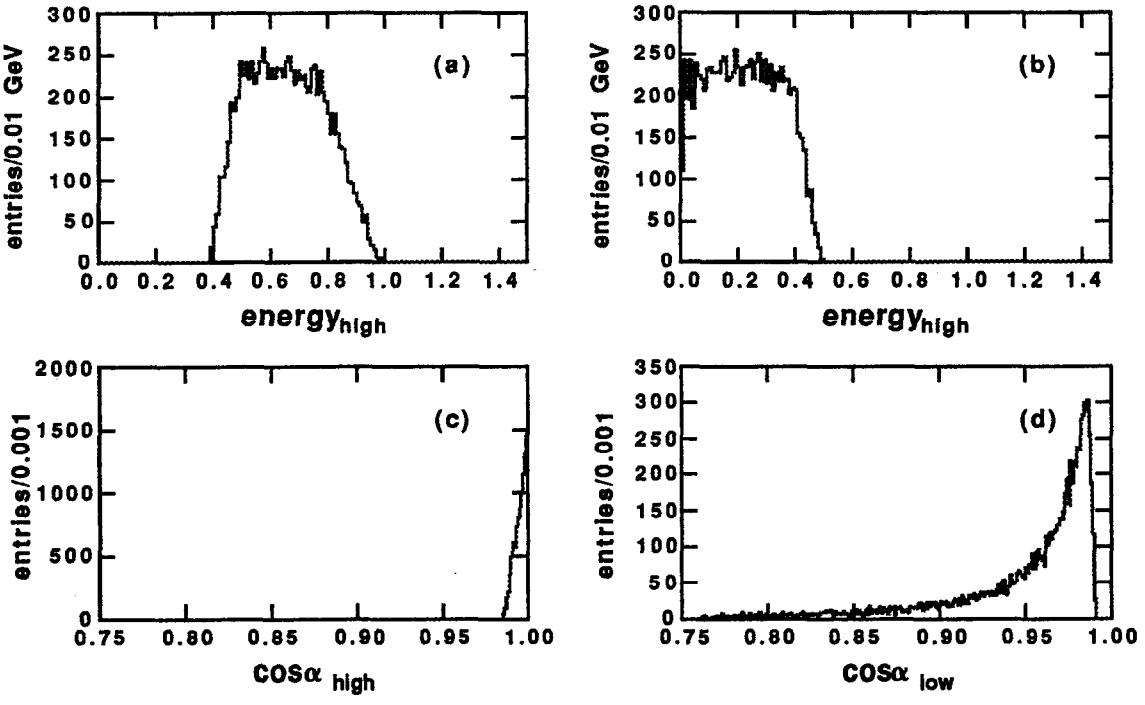

Figure 6.2 Properties of the π^0 from $D^+ \to K^+\pi^0$ before applying the detector resolution: (a) the energy spectrum of the higher energy photon; (b) the energy spectrum of the lower energy photon; (c) the alignment, $\cos\alpha_{high}$, between the momenta of the π^0 and the higher energy photon; (d) the alignment, $\cos\alpha_{low}$, between the momenta of the π^0 and lower energy photon.

nearly at rest, the π^0 is very energetic with a momentum of approximately 800 MeV/c. The π^0 in turn must produce one if not two detected high energy showers, with the higher energy shower at least 400 MeV. The two showers will also tend to be highly collimated opposite the K^+ in the direction of the π^0. These properties are illustrated in Figure 6.2 and Figure 6.3. Figures 5.2(a) and 5.2(b) show the *produced* energies of the high and low energy showers, while Figures 5.2(c) and 5.2(d) show the alignment between the photons and the original π^0 in terms of the cosine of the angle α between their momenta. Figure 6.3 shows the same quantities after detector simulation.

Because the photons are highly collimated, they may not always be distinguished in the shower reconstruction. Therefore, rather than try to reconstruct the π^0, this analysis

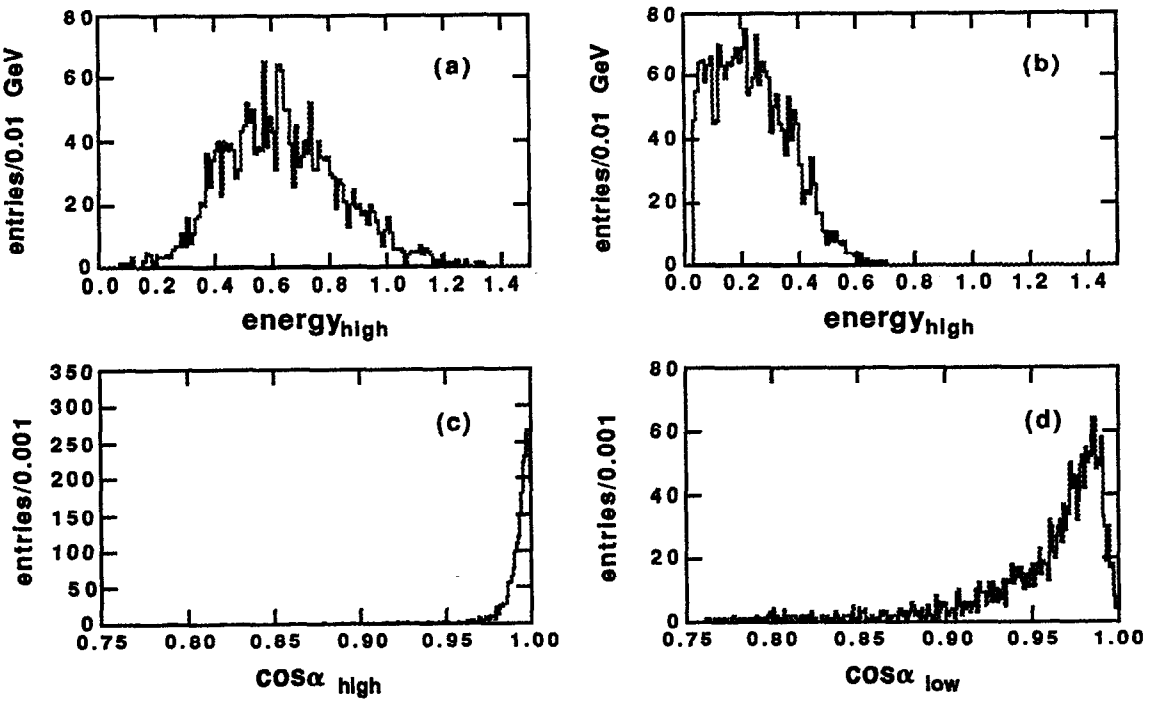

Figure 6.3 Properties of the π^0 from $D^+ \to K^+\pi^0$ after the detector resolution is applied; the plots correspond with those in Figure 6.2.

initially assumes it to be missing. The approach is, given an event with a tag and one recoil track, to search for showers in the direction of the missing π^0 momenta. The tag plays a more active role in this analysis, and good resolution in the tag momentum is required. Since the two tag modes $D^+ \to \bar{K}^0\pi^+\pi^0$ and $D^+ \to K^-\pi^+\pi^+\pi^0$ suffer in resolution due to the poor shower counter energy resolution (see Figure 6.4), these two samples are not used. The initial sample of 2350±33±40 events reduces to a sample of 2062±25±36 events.

A *search* cone around the π^0 direction is established in which to try to observe the photons. Based on Figure 6.3(d) and the fact that the Mark III shower counter has good angular resolution, the cone is defined by $\cos\theta > 0.84$ about the π^0 direction. This cone will contain 96.5% of the low energy photons as well as almost all the high energy photons detected in the calorimeter from $D^+ \to K^+\pi^0$. Some losses occur in the regions of the ribs and barrel/endcap interfaces of the calorimeter.

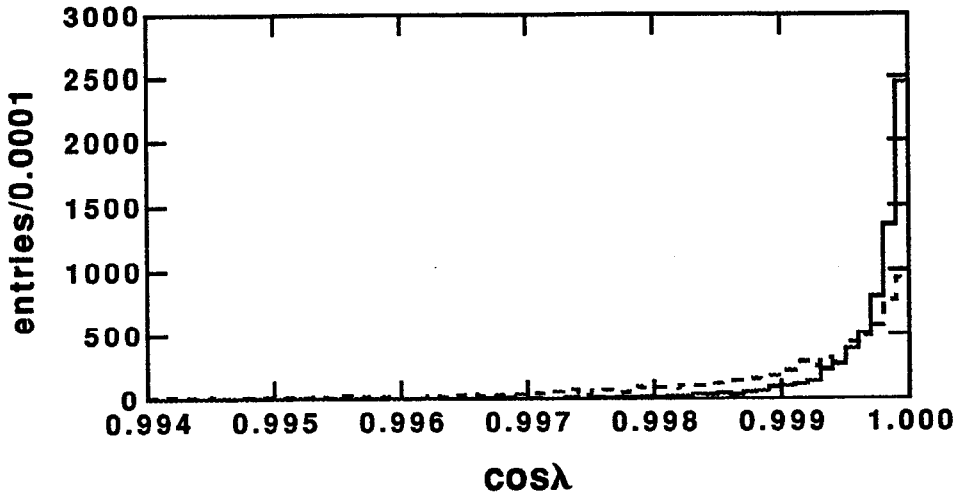

Figure 6.4 Resolution of the missing π^0 momentum in $K^+\pi^0$. The quantity λ is the angle between the true and reconstructed π^0 momenta, where the latter is determined from the momenta of the K^+ and the tag with conservation of momentum. Better resolution is achieved when the π^0 momentum is reconstructed in the presence of a $\bar{K}^0\pi^+$ tag (solid histogram) than when reconstructed in the presence of a $\bar{K}^0\pi^+\pi^0$ tag (dashed histogram).

Since the π^0 is missing, the invariant and beam constrained masses for the recoil cannot be computed. To plot and study a signal, another Lorentz invariant quantity is used:

$$U \equiv \sum_{\mu} P^{\mu}_{\text{recoil}} P_{K\mu} = \sum_{\mu} (P_{\text{event}} - P_{\text{tag}})^{\mu} P_{K\mu}$$

where P^{μ}_{recoil}, P^{μ}_{tag}, P^{μ}_{K}, and P^{μ}_{event} are, respectively, the four momenta of the recoil, tag, the charged kaon and the full event. Note that $P^{\mu}_{\text{event}} = (\sqrt{s}, \mathbf{0})$. Note also that the last expression does not require measurement of the photon momenta. Furthermore, if the tracking had perfect resolution, this U quantity would be equal to the constant 1.8598 $(\text{GeV}/c^2)^2$, derivable from four vector algebra.

The full analysis procedure is summarized as follows. Given a tagged event:

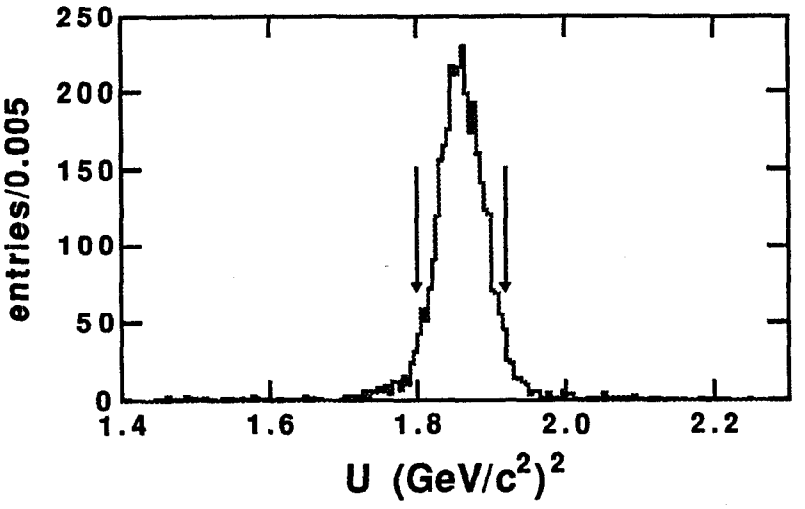

Figure 6.5 The Lorentz invariant quantity U for a Monte Carlo $D^+ \to K^+\pi^0$ signal (generated opposite $K^-\pi^+\pi^+$).

- Require one recoil charged track with a good helix fit, corrections for energy losses and a successful beam fit. The sign of the track must be opposite that of the tag.
- Compute the missing π^0 momentum and tally all isolated photons whose direction with respect to the missing momentum gives $\cos\theta > 0.84$. The number of photons must be > 0.
- Compute U and plot.

To attempt to achieve maximum efficiency and minimize the systematic uncertainties, no TOF identification cuts on the kaon are initially imposed. In the computation of U, the energy of the tag, E_{tag}, is replaced by $\sqrt{s}/2$ to improve the resolution (the same substitution is used in computing a beam-constrained mass).

Figure 6.5 shows a Monte Carlo plot for the expected signal. The signal region is defined by an approximate 2σ cut:

- $1.80 < U < 1.92(\text{GeV/c}^2)^2$.

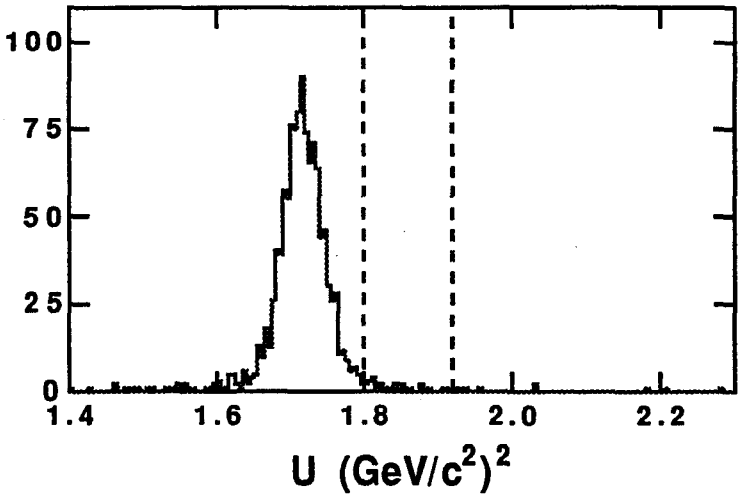

Figure 6.6 The U distribution for Monte Carlo $D^+ \rightarrow K^+\eta$ (generated opposite $K^-\pi^+\pi^+$).

The U variable is dependent upon the kaon mass hypothesis. It will be shown that this quantity separates backgrounds due to single misidentifications--e. g. $D^+ \rightarrow \pi^+\pi^0$--from the signal, and that the major backgrounds to $D^+ \rightarrow K^+\pi^0$ arise from double-misidentifications.

Figure 6.11(a) shows U for the data opposite all the tags after the initial event selection. Thirty-three events lie within the signal region.

6-3 Contribution of $D^+ \rightarrow K^+\eta$

In addition to $D^+ \rightarrow K^+\pi^0$, the initial selection procedure accepts events with the doubly Cabibbo suppressed channel $D^+ \rightarrow K^+\eta$ when $\eta \rightarrow \gamma\gamma$. This decay could therefore confuse the answer for $K^+\pi^0$. However the larger mass from the η (958 MeV/c^2) causes a downward shift in U as indicated in Figure 6.5; the distribution peaks at 1.72 (GeV/c^2)^2. The probability for $K^+\eta$ to be reconstructed as $K^+\pi^0$ is 1.3% after the initial event selection and <0.12% at 90% confidence level after the data reduction cuts, described in Section 6-4.2. Since $B(K^+\eta)$ is expected to be of the order of $B(K^+\pi^0)$, the contribution of $K^+\eta$ is removed from consideration.

6-4 Major Backgrounds to $D^+ \to K^+\pi^0$

As in the analysis for $D^+ \to K^+\pi^-\pi^+$, all major backgrounds investigated appear to involve two errors when identifying them as signal events. The backgrounds are of the Class I category, where only the recoil D is incorrectly reconstructed. This section is divided into two parts: Section 6-4.1 discusses the known background to $K^+\pi^0$, and Section 6-4.2 discusses the cuts which are introduced to remove them. The results of the cuts on the data is postponed until Section 6-5.

6-4.1 The Class I Backgrounds

There are two major Class I backgrounds, both which originate from the same D decay:

- $D^+ \to \bar{K}^0\pi^+$ where the $\bar{K}^0$ decays via $\bar{K}^0 \to K_S^0 \to \pi^0\pi^0$. The π^+ is misidentified as the K^+ and the $\bar{K}^0$ products are misidentified as the π^0 by the observation of photons in the search cone.
- $D^+ \to \bar{K}^0\pi^+$ where the $\bar{K}^0$ decays via $\bar{K}^0 \to K_L^0$. Again the π^+ is misidentified as the K^+, while the K_L^0 showers (hadronically) in the electromagnetic shower counter, and appears as the π^0.

Because of the double misidentification, both of these backgrounds peak in the signal region, as shown in Figure 6.7.

Other D^+ decay modes which contribute background are:

- $D^+ \to \bar{K}^0K^+$ where the $\bar{K}^0$ decays via $\bar{K}^0 \to K_S^0 \to \pi^0\pi^0$. The decay starts out Cabibbo suppressed, and the $\bar{K}^0$ products are misidentified as the π^0. The K^+ is correctly assigned.
- $D^+ \to \bar{K}^0K^+$ where the $\bar{K}^0$ decays via $\bar{K}^0 \to K_L^0$. Again the decay starts out Cabibbo suppressed, while the K_L^0 showers (hadronically) in the electromagnetic shower counter. The K^+ is correctly assigned.
- $D^+ \to \pi^+\pi^0$. The decay starts out Cabibbo suppressed, and the charged pion is misidentified as the K^+.

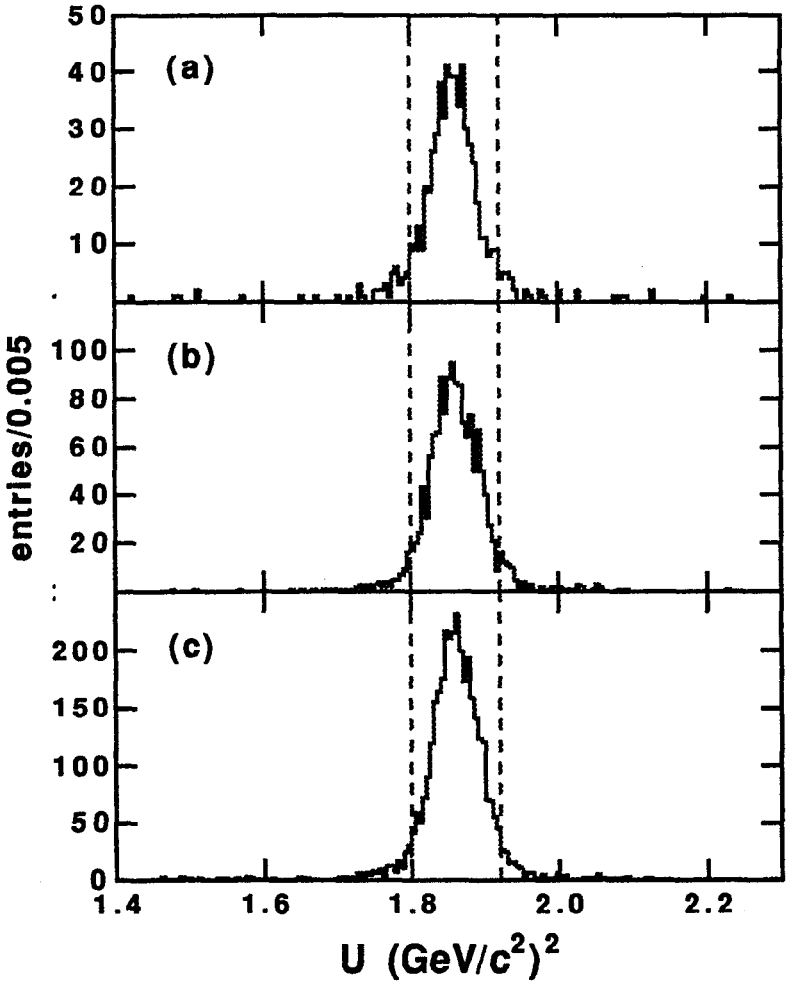

Figure 6.7 The U distributions for (a) $D^+ \to \bar{K}^0\pi^+$, $\bar{K}^0 \to K_S^0 \to \pi^0\pi^0$; (b) $D^+ \to \bar{K}^0\pi^+$, $\bar{K}^0 \to K_L^0$; and (c) the signal, $D^+ \to K^+\pi^0$.

These backgrounds contribute less because they peak outside the signal region; see Figure 6.8. Only the tails in their U distribution feed into the signal region.

The standard detector Monte Carlo simulation for the Mark III does not model K_L^0 interactions. To study the backgrounds $D^+ \to \bar{K}^0\pi^+$ and $D^+ \to \bar{K}^0K^+$ with $\bar{K}^0 \to K_L^0$, a routine was used which inserts K_L^0 showers into the Monte Carlo data, using a sample of real K_L^0 showers obtained from $J/\psi \to K_S^0K_L^0$, $K_S^0 \to \pi^+\pi^-$ and $J/\psi \to \phi\eta$, $\phi \to K_S^0K_L^0$, $K_S^0 \to \pi^+\pi^-$ events. The plots in Figure 6.7(b) and Figure 6.8(b) were developed with this model. Because the momentum of K_L^0 in the $J/\psi \to K_S^0K_L^0$ events is approximately fixed at 1.466

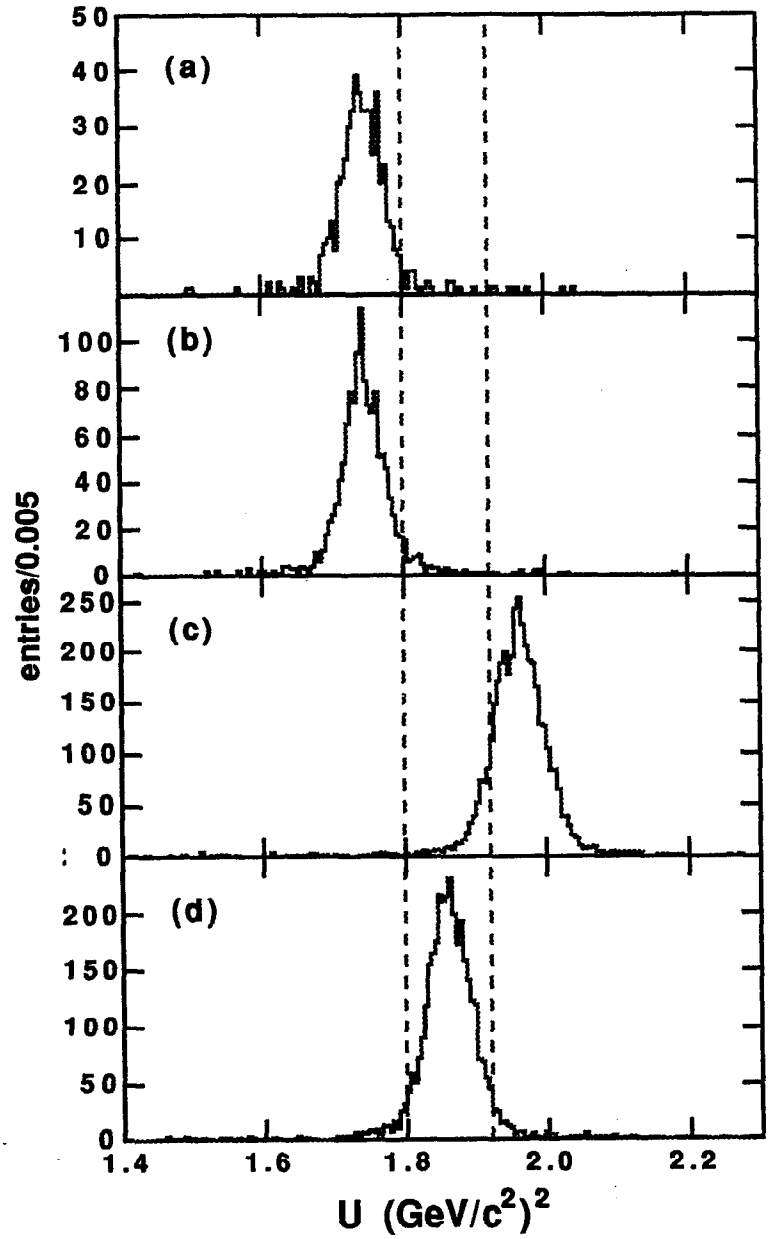

Figure 6.8 The U distributions for (a) $D^+ \to \bar{K}^0K^+$, $\bar{K}^0 \to K_S^0 \to \pi^0\pi^0$; (b) $D^+ \to \bar{K}^0K^+$, $\bar{K}^0 \to K_L^0$; (c) $D^+ \to \pi^+\pi^0$ and (d) the signal, $D^+ \to K^+\pi^0$.

GeV/c, the model is expected to underestimate the true number of hadronic showers at lower momentum where the cross section increases. That uncertainty plus the limited statistics of the K_L^0 sample introduce an estimated 25% systematic uncertainty in the background correction. This routine was developed in a previous Mark III analysis.[63]

6-4.2 Background Cuts

The momentum of the kaon in $K^+\pi^0$ approaches the limit where particle identification in the Mark III is useful. The approach to introducing background cuts was to avoid, therefore, the use of particle identification and to instead impose tighter restrictions on the photon topology. The first two cuts discussed--the veto cut and the $\cos\delta$ cut--were designed for this purpose. However, it will be shown in Section 6-5 that particle identification is required to sufficiently remove all background; hence the third cut discussed is kaon identification.

The Veto Cut

This cut is introduced to reduce the background from $D^+ \to \bar{K}^0K^+$ and $D^+ \to \bar{K}^0K^+$ when $\bar{K}^0 \to K_S^0 \to \pi^0\pi^0$. It imposes tighter requirements on the photons to better distinguish between a background $\bar{K}^0 \to \pi^0\pi^0$ and the single π^0 from $K^+\pi^0$. Since the $\bar{K}^0$ decays to two π^0's, the final state photons tend to be less energetic and more isotropic in the detector than those expected from $K^+\pi^0$. Figure 6.2 shows that $D^+ \to K^+\pi^0$ always produces one photon with an energy greater than 400 MeV and a $\cos\alpha > 0.98$; α, recall, is the angle between the photon and π^0 directions.The veto cut requires finding a high energy photon in the absence of any other energetic photons in the event. For an event to be retained by the cut:

- it must have one or more photons with energy greater than 400 MeV and $\cos\alpha > 0.98$.
- it must not have any photons with energy greater than 300 MeV and $\cos\alpha < 0.98$.
- it must not have more than one photon with energy between 150 MeV and 300 MeV and $\cos\alpha < 0.98$.

The lower energy limit of 150 MeV was chosen to avoid vetoing on noise and spurious photons in the shower counter. The good angular resolution of the shower counters allows

the tight cut on $\cos\alpha$.This criteria removes approximately 85% of the $\bar{K}^0\pi^+$ and $\bar{K}^0K^+$, $\bar{K}^0 \to \pi^0\pi^0$, events which survive the initial event selection and retains 73% of the signal events.

The veto cut is also effective at removing $\bar{K}^0\pi^+$ and $\bar{K}^0K^+$ where $\bar{K}^0 \to K_L^0$. Although the hadronic shower falls within $\cos\alpha > 0.98$, the hadronic showers are not fully contained within the electromagnetic calorimeter, and the energy is measured to be typically lower than 400 MeV. The cut removes approximately 85% of the $\bar{K}^0\pi^+$ and $\bar{K}^0K^+$, $\bar{K}^0 \to K_L^0$ events which survive the initial event selection. The veto cut is not effective against $D^+ \to \pi^+\pi^0$, because of the similar photon topology to $K^+\pi^0$.

The Cosδ Cut

This cut provides additional reduction of the backgrounds from $D^+ \to \bar{K}^0K^+$ and $D^+ \to \bar{K}^0K^+$ when $\bar{K}^0 \to K_S^0 \to \pi^0\pi^0$ by exploiting the photon topology further. All photons detected within the search cone $\cos\theta > 0.84$ are assumed to come from the π^0. The value 0.84 guarantees that when both photons from $K^+\pi^0$ generate separate showers, both will be counted ~96.5% of the time. The photons from $\bar{K}^0\pi^+$ and $\bar{K}^0K^+$ with $\bar{K}^0 \to \pi^0\pi^0$, however are not all expected to fall within the search cone since these photons tend to be more isotropic. Therefore, for $D^+ \to K^+\pi^0$, the total momentum of the photons within the search cone will be sharply peaked in the direction of the missing π^0, while for the two background modes, it will not. The Monte Carlo plots in Figure 6.9 demonstrate this assertion. The quantity plotted is $\cos\delta$ where δ is defined to be the angle between the direction of the π^0 momentum and the direction of the total momentum of all photons found in the search cone. Figure 6.9(a) shows the plot for $D^+ \to \bar{K}^0\pi^+$, $\bar{K}^0 \to \pi^0\pi^0$ opposite $D^- \to K^+\pi^-\pi^-$; Figure 6.9(b) shows the distribution for $D^+ \to K^+\pi^0$ opposite $D^- \to K^+\pi^-\pi^-$. The veto cut has been applied in both cases.

Reducing further the $\bar{K}^0\pi^+$ and $\bar{K}^0K^+$ backgrounds with $\bar{K}^0 \to \pi^0\pi^0$, it is required that:

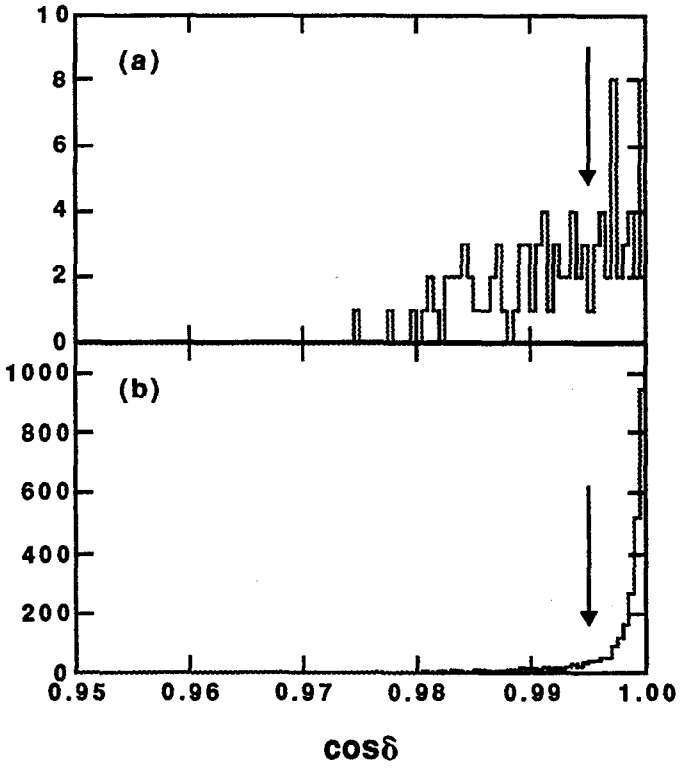

Figure 6.9 The $\cos\delta$ distributions for (a) $D^+ \to \overline{K}^0\pi^+$, $\overline{K}^0 \to \pi^0\pi^0$ and (b) the signal $D^+ \to K^+\pi^0$. The arrows indicate the cut at $\cos\delta > 0.995$.

- $\cos\delta > 0.995$.

This criteria removes about 65% of the $\overline{K}^0\pi^+$ and $\overline{K}^0K^+$, $\overline{K}^0 \to \pi^0\pi^0$, events which survive the veto requirement, while retaining 90% of the signal events.

The $\cos\delta$ cut is not effective against $\overline{K}^0\pi^+$ and $\overline{K}^0K^+$ when $\overline{K}^0 \to K_L^0$ since the hadronic shower is typically well aligned with the direction of the missing momentum. Nor is the cut effective against $D^+ \to \pi^+\pi^0$, because of the similar photon topology to $K^+\pi^0$.

Kaon Identification

For this analysis only time-of-flight information is used to identify the recoil kaon; the momentum of the kaon in the lab is ≥ 700 MeV/c, which prevents reliable use of dE/dx information. Based on the ΔT distributions for the signal and $\overline{K}^0\pi^+$ background, Figure

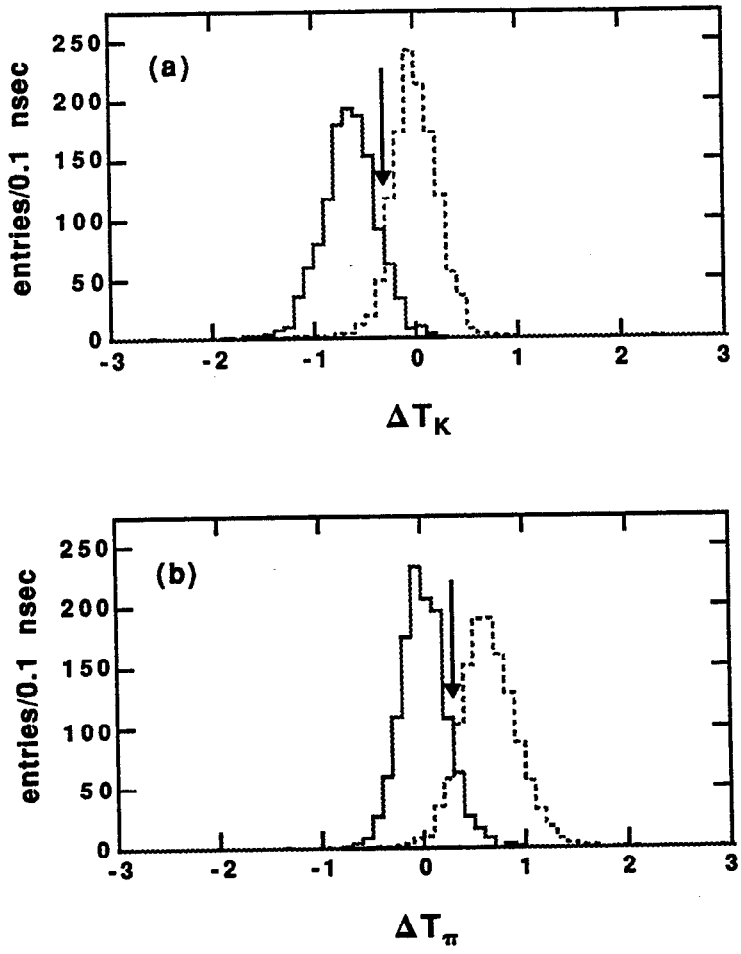

Figure 6.10 Pion misidentification from the $\overline{K}^0\pi^+$ backgrounds. Plotted (solid histograms) are the time-of-flight variables, ΔT_i, for the charged track assuming (a) a kaon hypothesis and (b) a pion hypothesis. Shown also (dashed histograms) are the distributions for the signal. The arrows indicate the kaon identification cuts.

6.10, the recoil charged track is identified as a kaon if it has good time-of-flight information and:

- $\Delta T_K > -0.3$ ns
- $\Delta T_\pi > 0.3$ ns

when the track is assigned, respectively, the kaon and pion hypotheses. This criteria removes 94% of the $\bar{K}^0\pi^+$ backgrounds which survive after the cosδ cuts, while retaining 74% of the signal events

This cut is not effective against the $\bar{K}^0K^+$ backgrounds, since the K^+ is correctly identified. It does remove $\pi^+\pi^0$ background, where the pion is misidentified; 95% of these events are expected to be removed.

6-5 Results

Figure 6.11 shows the application of the cuts to the data. After all cuts are applied no events remain in the signal region.

Analysis Tests

As a check on the analysis, the numbers of events that are expected to be removed by each of the background cuts are calculated and compared to the numbers that are removed. This is done for three regions of the U plot:

Signal Region: $1.80 < U < 1.92$ $(\text{GeV/c}^2)^2$

Region I: $1.69 < U < 1.80$ $(\text{GeV/c}^2)^2$

Region II: $1.92 < U < 2.00$ $(\text{GeV/c}^2)^2$

Region I contains events within about 2σ of a $D^+ \to \bar{K}^0K^+$ peak, while Region II contains events within approximately 1.2σ of a $D^+ \to \pi^+\pi^0$ peak. These regions were chosen to be symmetric, respectively, about the $D^+ \to \bar{K}^0K^+$ and $D^+ \to \pi^+\pi^0$ peaks and to not overlap with the signal region.

Table 6.1 gives the background branching fractions used to estimate the numbers of events from the major D backgrounds. To those numbers a few comments are added. The first comment is that, experimentally, only the an upper limit has been determined for the $\pi^+\pi^0$ branching fraction--$B(\pi^+\pi^0) < 0.53\%$ at 90% CL.[20] The number used for this analysis is the theoretically expected value:

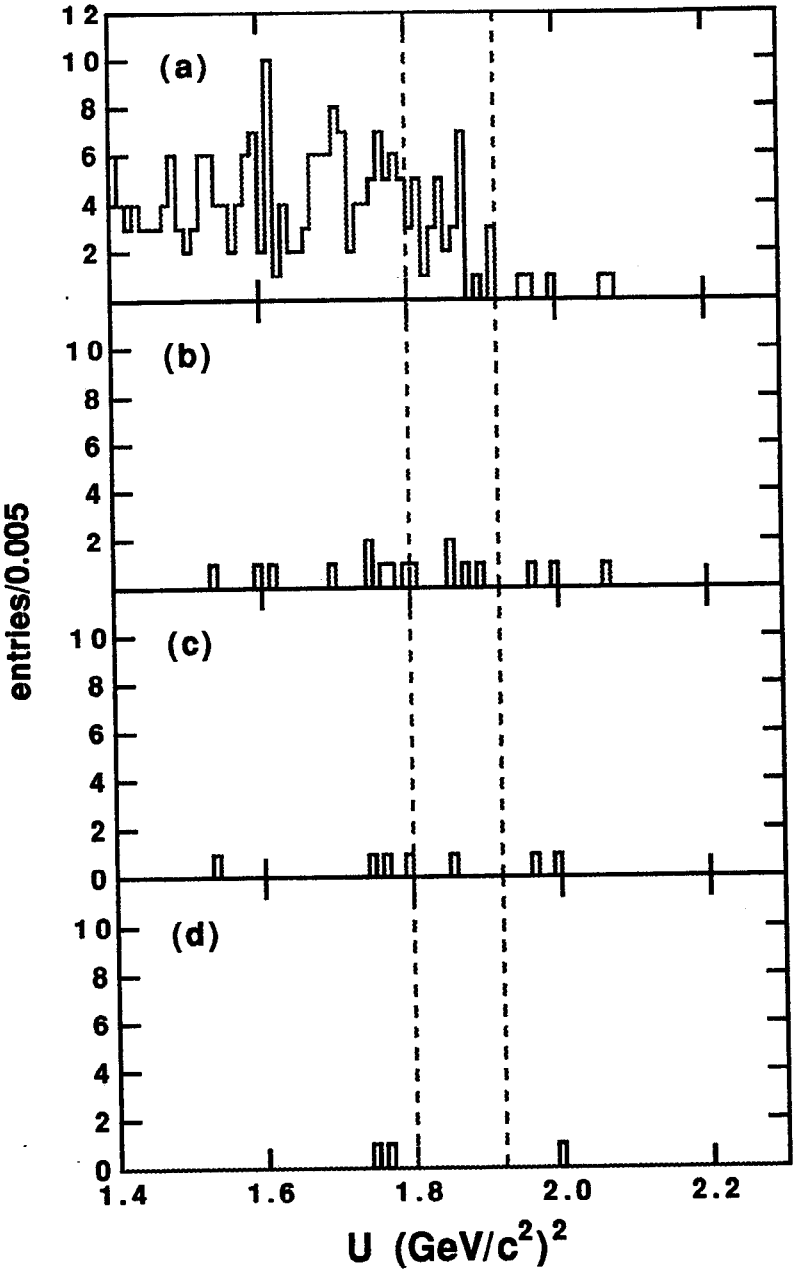

Figure 6.11 Data after (a) the initial event selection, (b) the veto cut, (c) the $\cos\delta$ cut and (d) the particle identification cuts. (See text.)

$$B(\pi^+\pi^0) = 1/2 \tan^2\theta_c \times B(\bar{K}^0\pi^+) = 0.082\pm0.013\pm0.005\%$$

where $\tan\theta_c = 0.0514$ has been used and $B(\bar{K}^0\pi^+)$ is given in Table 6.1; the theoretical uncertainty in $\tan\theta_c$ is not included in the errors. The second comment is that all

Table 6.1 Branching fractions of the Class I backgrounds to $D^+ \to K^+\pi^0$

Mode	Branching Fraction (%)	Reference
$D^+ \to \bar{K}^0\pi^+$	$3.2 \pm 0.5 \pm 0.2$	24
$\bar{K}^0K^+$	1.01±0.32±0.17	24, 20
$\pi^+\pi^0$	0.082±0.013±0.005	(see text)

Table 6.2 Numbers of events observed and expected to be removed by the background cuts.

Cut	Region I		Signal Region		Region II	
	Obs.	Exp.	Obs.	Exp.	Obs.	Exp.
veto	53	12.3±2.3	28	28.2±3.8	1	$2.6^{+0.5}_{-0.4}$
cosδ	3	$0.5^{+0.4}_{-0.1}$	4	$1.8^{+0.4}_{-0.3}$	0	$0.3^{+0.3}_{-0.1}$
kaon identification	1	$0.7^{+0.3}_{-0.1}$	1	$4.0^{+0.7}_{-0.5}$	1	$2.1^{+0.5}_{-0.3}$
Total Number	57	13.5±2.4	33	34.0±4.5	2	5.0±0.4

branching fractions are correlated by a common factor of $B(\bar{K}^0\pi^+)$ (the branching fraction for $\bar{K}^0K^+$ is derived from measurements of the branching fraction ratio, $B(\bar{K}^0K^+)/B(\bar{K}^0\pi^+)$, and of the absolute branching fraction for $B(\bar{K}^0\pi^+)$). This correlation is accounted for when deriving the errors on the numbers of events.

Included in the predicted numbers are the estimated contributions from the continuum u, d, s events, determined from an analysis of Lund Monte Carlo data. The analysis is shown in Figure 6.12.

Table 6.2 gives the total expected numbers of events lost and compares the results against the data. The total number of events expected to be lost from the signal region, 34.0±4.5, agrees well with the observed number lost, 33. An excess is observed in

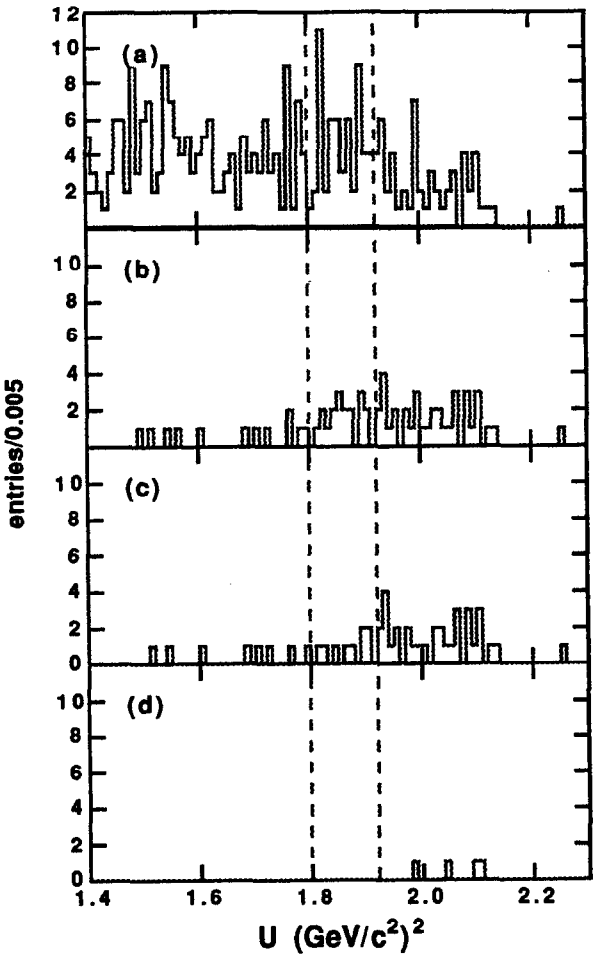

Figure 6.12 Analysis procedure applied to the Lund Monte Carlo: (a) after the initial event selection; (b) after the veto cut; (c) after the cosδ cut; and (d) after kaon identification.

Region I where the observed loss is 57 events and the predict loss is only 13.5±2.4. This discrepancy would indicate that other backgrounds in Region I have not been accounted for. They do not, however, appear to significantly leak into the signal region. The numbers for Region II, 2 events observed and 5.0±0.4 events expected, are in reasonable agreement given the small statistics.

Event Scans

To verify that background was indeed removed, the two events lost by the kaon identification cuts were examined visually; displays of the signal event and the event at the signal boundary are given in Figure 6.13 and Figure 6.14, respectively.

From the tag side, the event in the signal region appears to be a good D^+D^- event. The tag is $K^+\pi^-\pi^-$ reconstructed from tracks 4, 2 and 3 with 4 as the kaon. Both pion tracks are strongly identified by time-of-flight information, while the kaon track is strongly identified by the dE/dx information. It even appears the kaon decayed while in flight through the drift chamber, creating the neutral shower labelled 6. The invariant and beam constrained masses of the tag are 1.873 GeV/c^2 and 1.8681 GeV/c^2, respectively. In the recoil, identification of the charged track is weaker. Track 1 is an assumed K^+. This track has neither good time-of-flight nor dE/dx information because of its high momentum, p_K = 0.933 GeV/c. Neutral track 5 with an energy of 1.064 GeV is the shower which recoils from the charged tracks. In the event display, this track appears more like a hadronic shower than an electromagnetic shower; the transverse profile is broader than that typically observed for showers from actual photons. The computed value for U is 1.8552 $(\text{GeV}/c^2)^2$.

The event on the boundary of the signal region--$U = 1.796\,(\text{GeV}/c^2)^2$--is also tagged by $K^+\pi^-\pi^-$ from tracks 3, 1 and 4 where 3 is the kaon. The invariant and beam constrained masses are 1.887 GeV/c^2 and 1.8637 GeV/c^2, respectively. Tracks 3 and 1 are well identified by TOF, while track 1 has neither good TOF nor dE/dx information and is therefore an assumed pion. In the recoil the charged track is strongly identified as a pion by the TOF information; no dE/dx information exists to corroborate (track 2 hits the same dE/dx wires as track 4). One neutral shower, track 5, is observed in the search cone with an energy of 428 MeV. It also has longitudinal and transverse shower profiles that are more characteristic of hadronic showers than electromagnetic showers.

The three events in the final U plot have also been visually examined. One event lies above the signal region and two below; displays are given in Figure 6.15-17. The event in the high U reflection region looks like a $D^+ \to \pi^+\pi^0$ candidate opposite a $D^+ \to \bar{K}^0\pi^+$. The track identified as a kaon has a high momentum of 0.850 GeV/c and the time--of-flight is consistent with both a pion and kaon hypothesis. Also two energetic photons are observed within the search cone.The value of $U = 1.993$ $(\text{GeV/c}^2)^2$ places the event in the region where $D^+ \to \pi^+\pi^0$ is expected to peak. The other two events below the signal region look like $D^+ \to \bar{K}^0K^+$, $\bar{K}^0 \to K_L^0$ candidates, both opposite a $K^+\pi^-\pi^-$ tag. The recoil track in both events are strongly identified as kaons by time-of-flight information. Both events have only one energetic shower in the direction of missing momentum, and the shower profiles appear more characteristic of hadronic showers than electromagnetic.

Additional Background Checks

Before calculating the final number of background events, a check was made for any less obvious backgrounds which need to be included. This check was done by applying the analysis to the D^+D^- and $D^0\bar{D}^0$ Monte Carlo data sets described in Section 3-3.5. Recall that the number of events in the two sets are 199K for the $D^0\bar{D}^0$ and 157K for the D^+D^- or approximately 7.19 and 7.75× the number of events in the real $\psi(3770)$ data sets.

Figure 6.18 shows the results of the analysis on the D^+D^- Monte Carlo data. After the application of the background cuts, three events remain in the signal region, two fall below in the low U reflection region and one falls above in the high U reflection region. The event records for all six events were examined for unusual topologies. Each of the events in fact contain one of the background channels already discussed. The two events in the low U region and the event in the signal region with the lowest U value all contain the decay $D^+ \to \bar{K}^0K^+$, $\bar{K}^0 \to K_L^0$. The other two events in the signal region contain the decay $D^+ \to \bar{K}^0\pi^+$, $\bar{K}^0 \to K_L^0$. while the event above the signal region contains $D^+ \to$

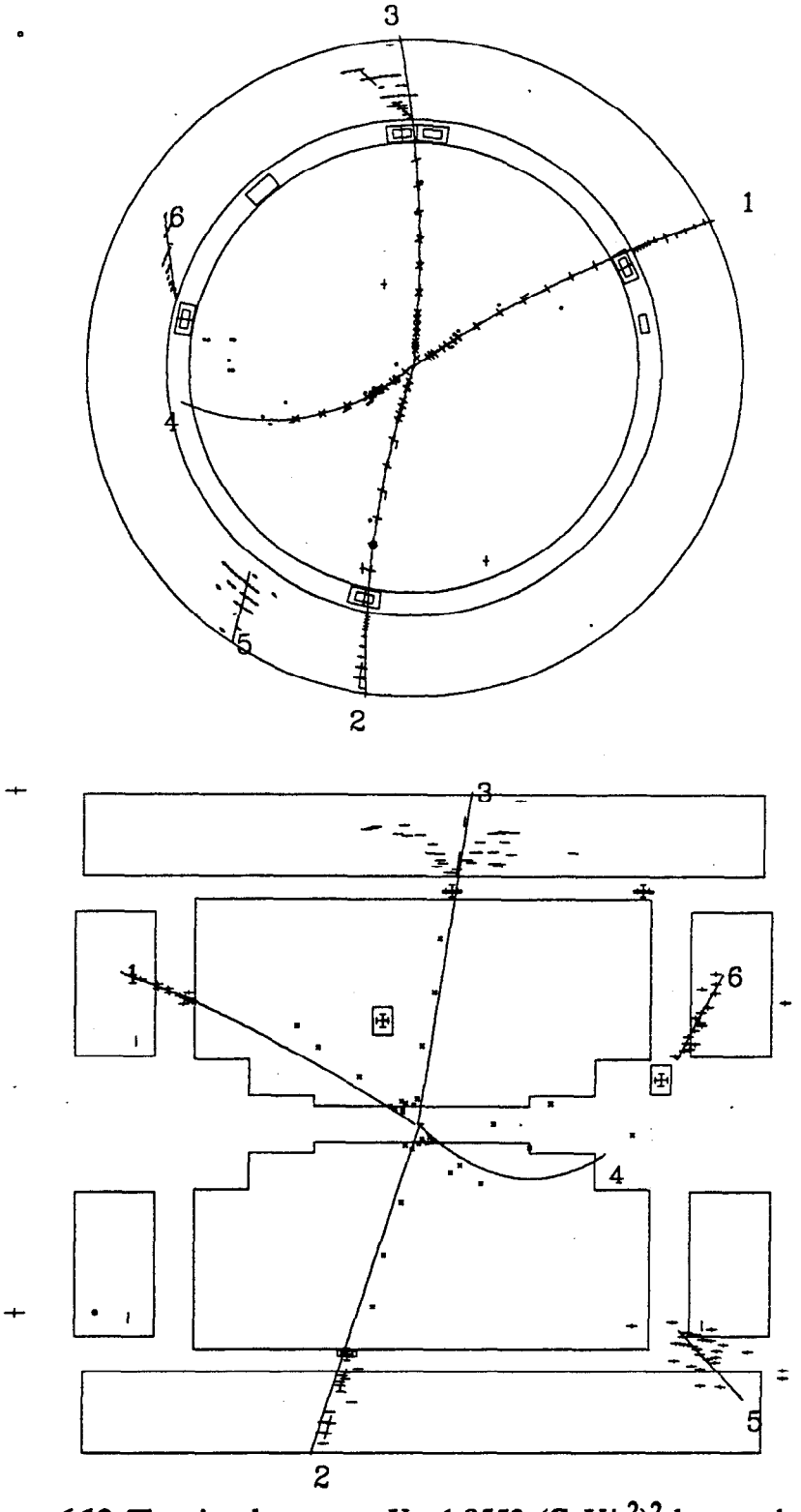

Figure 6.13 The signal event at U= 1.8552 $(GeV/c^2)^2$ lost to the kaon identification.

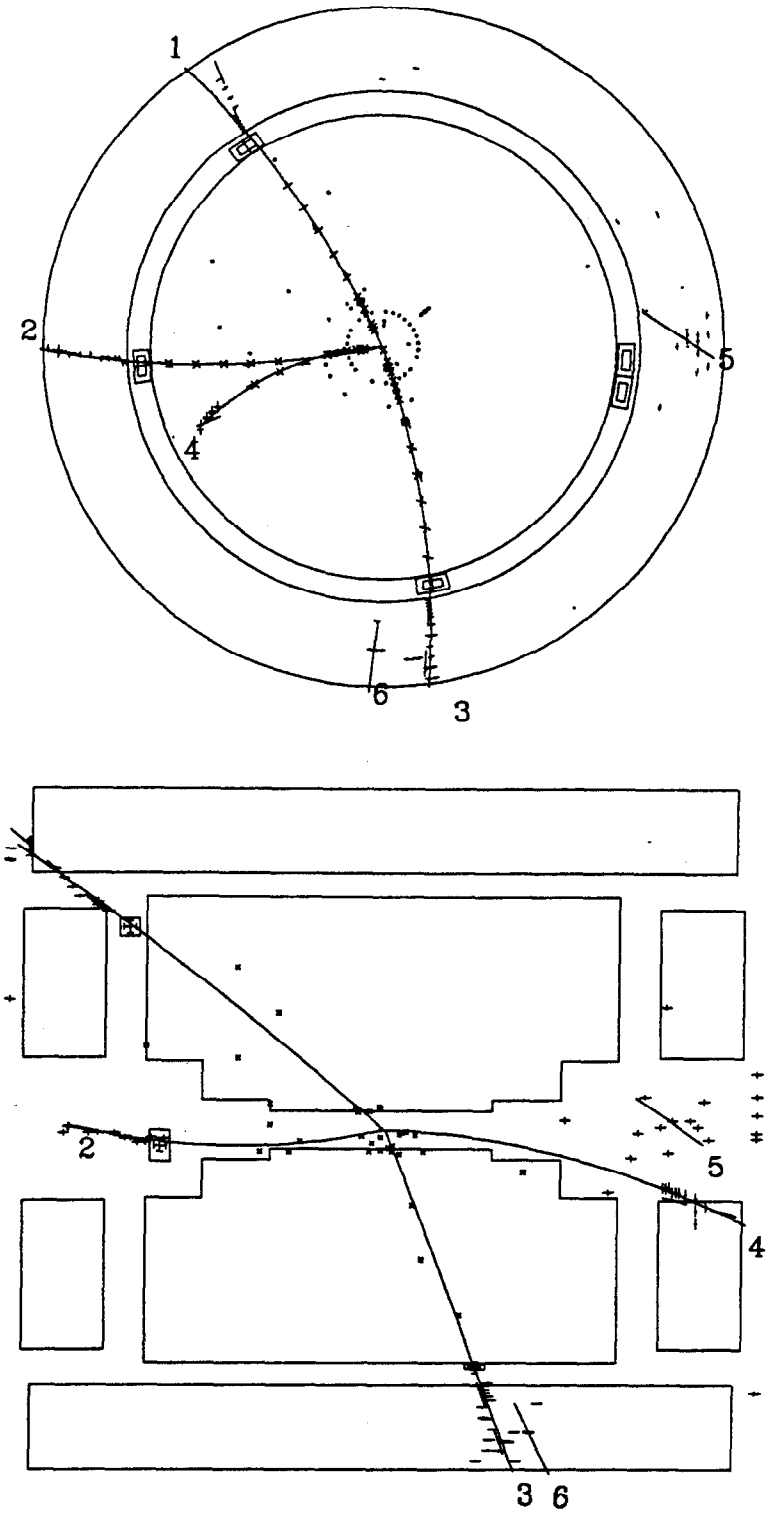

Figure 6.14 The event on the signal boundary lost to the kaon identification.

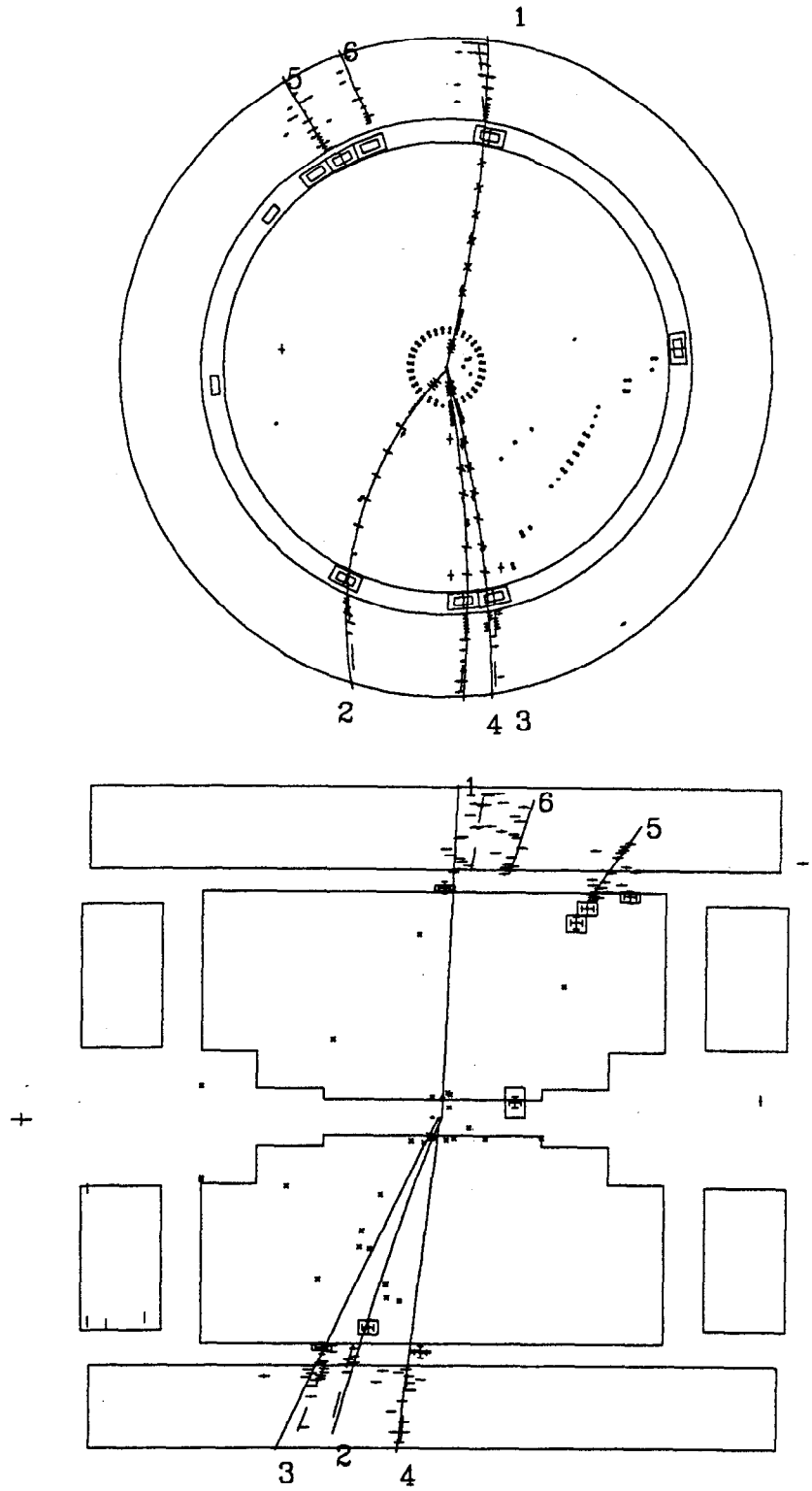

Figure 6.15 The event from Region II at $U = 1.993$ (GeV/c^2)^2.

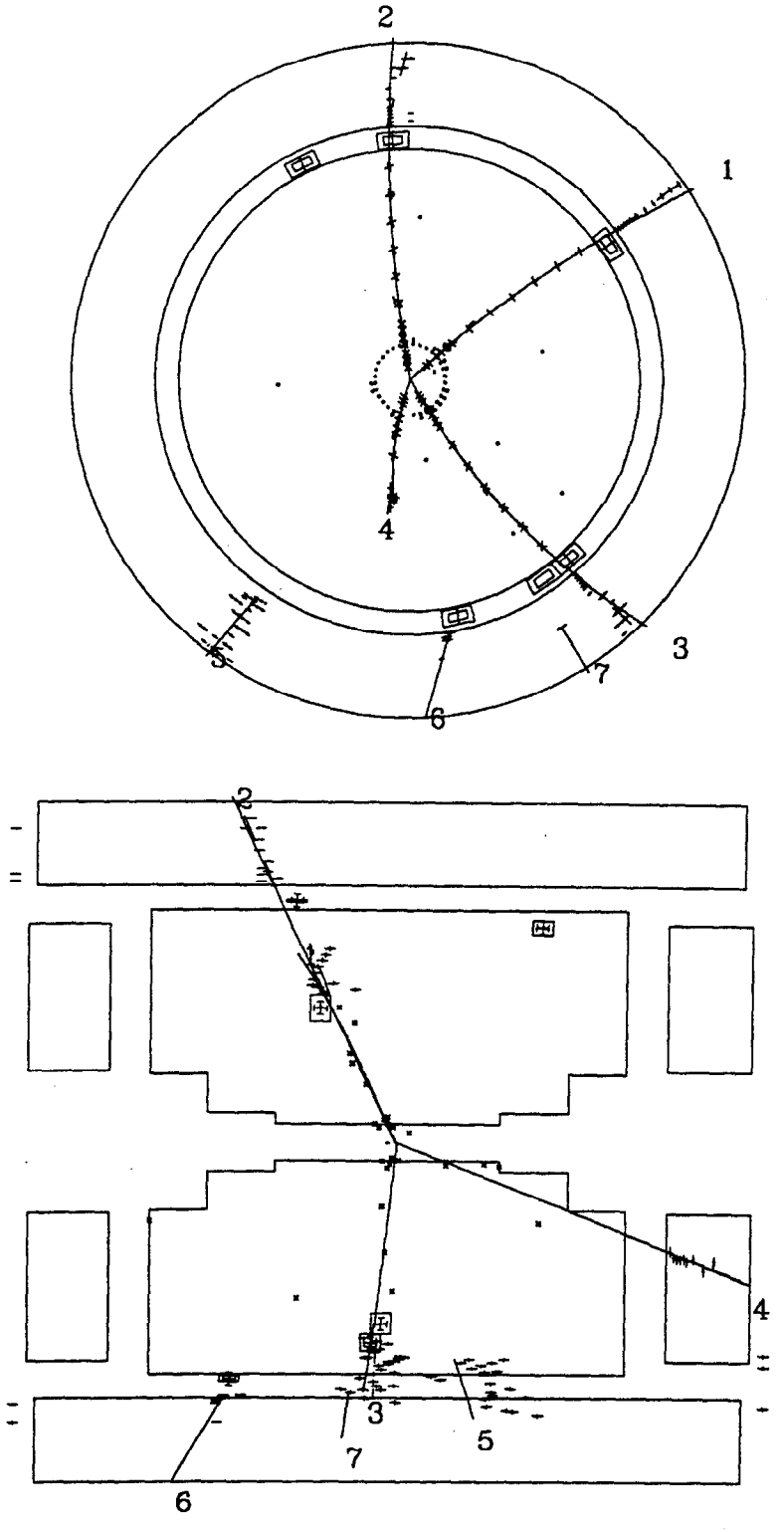

Figure 6.16 The event from Region I at $U = 1.761\,(\mathrm{GeV}/c^2)^2$.

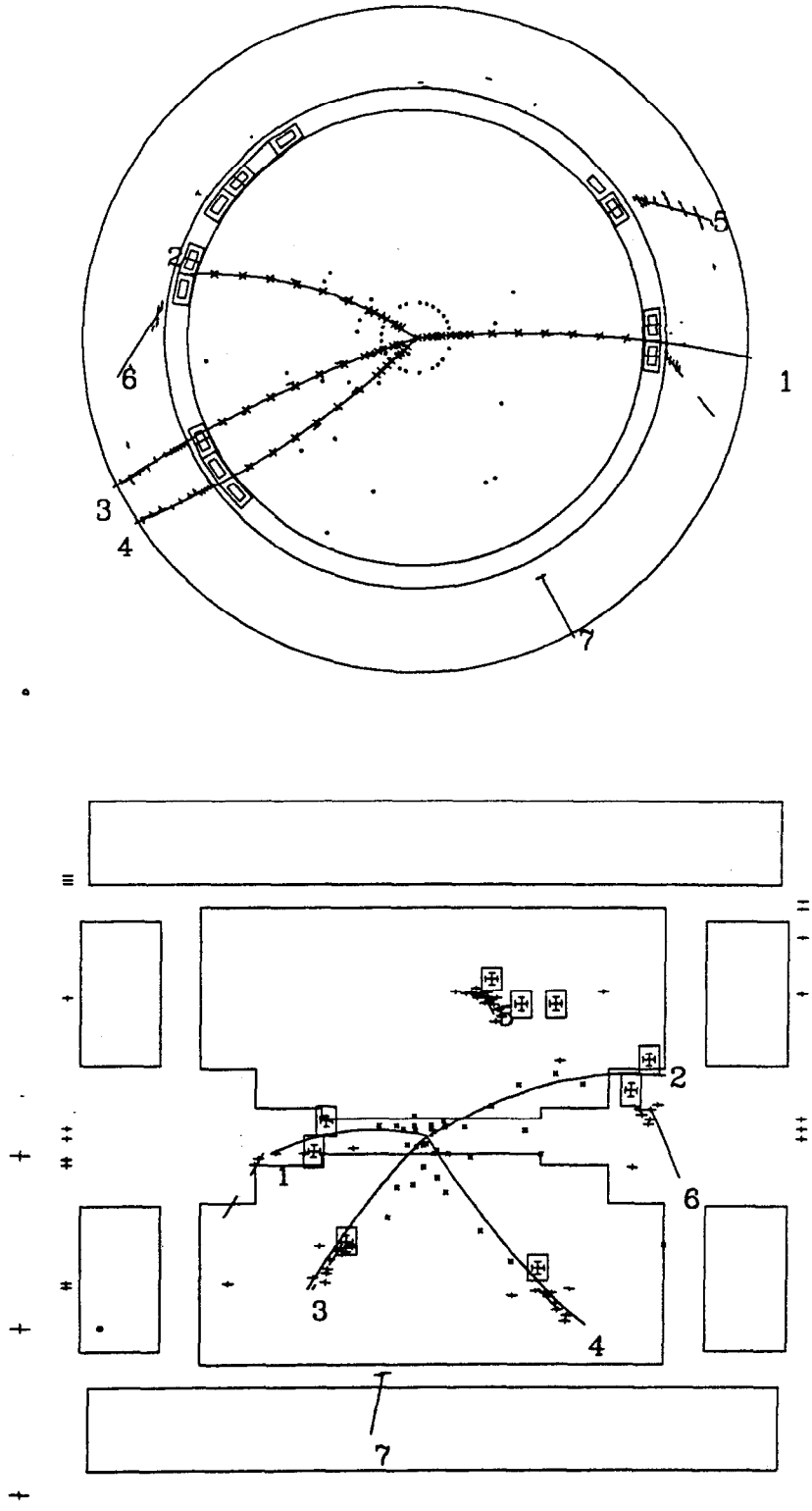

Figure 6.17 The event from Region I at $U = 1.750$ (GeV/c^2)^2.

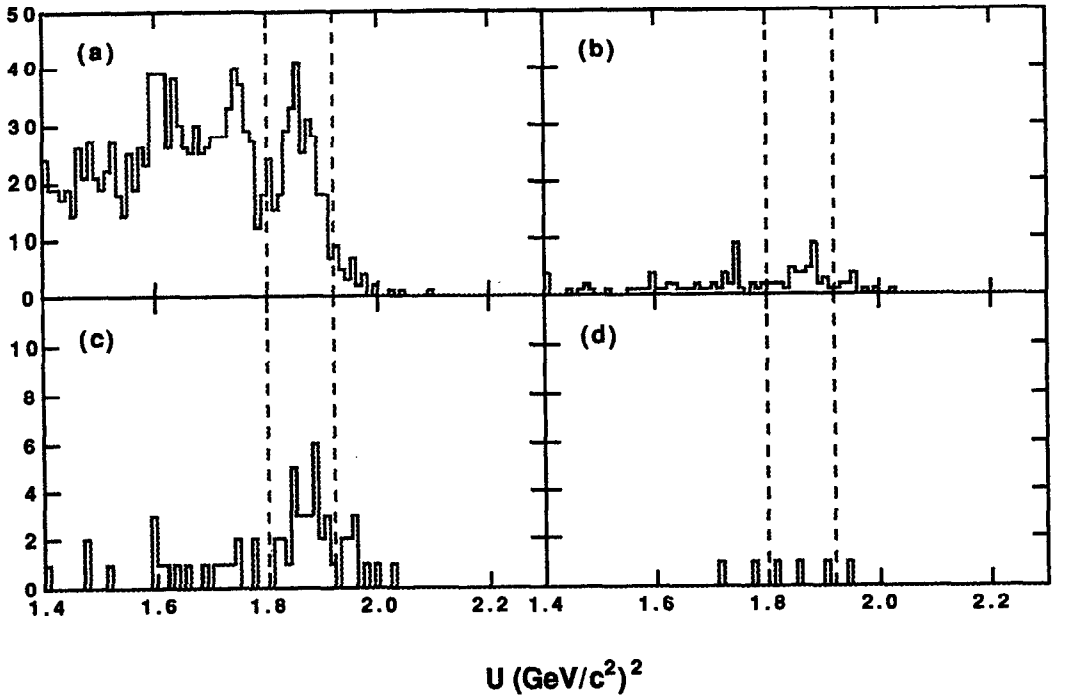

Figure 6.18 The application of the analysis on D^+D^- Monte Carlo events: (a) after the initial event selection; (b) after the veto cut; (c) after the cosδ cut; and (d) after the kaon identification.

$\pi^+\pi^0$. The numbers predicted for the signal region and Regions I and II for the Monte Carlo data are 4.6 , 1.6 and 0.5 events, respectively.

Figure 6.18 shows the results for the analysis on the $D^0\overline{D}^0$ Monte Carlo. After application of all anti-background cuts, no events remain in either the signal or reflection regions.

No unexpected backgrounds have been found. It is therefore concluded that no additional backgrounds from $D\overline{D}$ production need to be accounted for.

6-5.1 Detection Efficiencies

The detection efficiencies for $D^+ \to K^+\pi^0$ are determined opposite each of the five tag modes from Monte Carlo simulations; the numbers are given in Table 6.3. The weighted efficiency is 35.0±0.5.

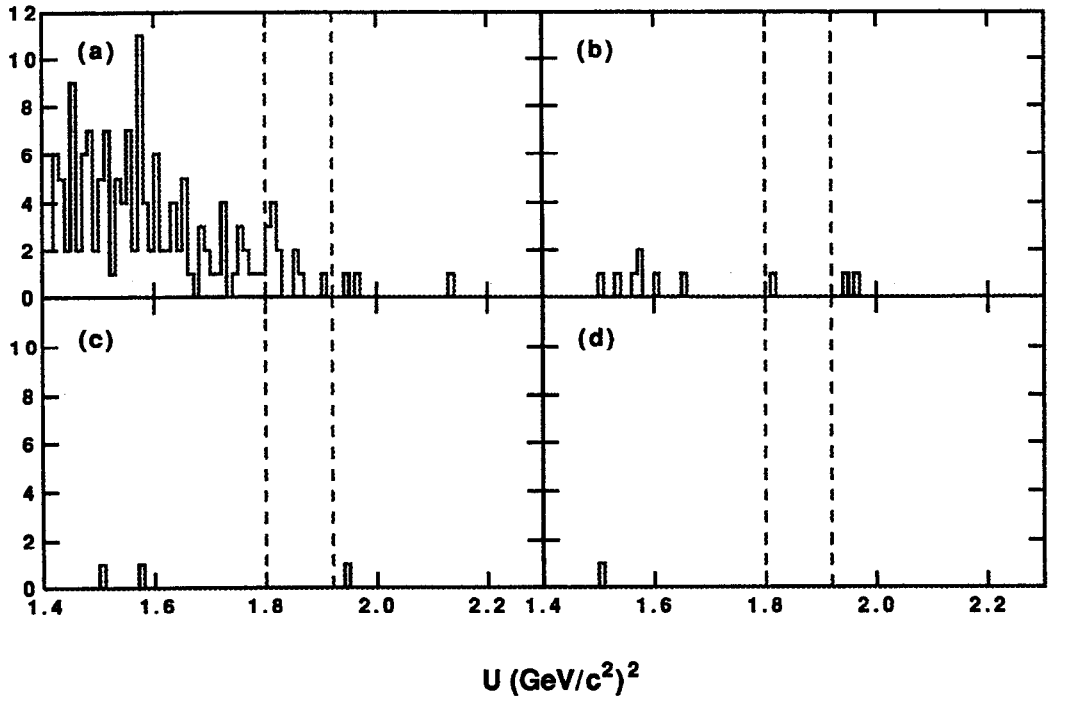

Figure 6.19 The application of the analysis on $D^0\overline{D}^0$ Monte Carlo events: (a) after the initial event selection; (b) after the veto cut; (c) after the $\cos\delta$ cut; and (d) after the kaon identification.

Table 6.3 Efficiencies for $D^+ \to K^+\pi^0$ opposite each tag.

Tag Mode	efficiency(%)
$\overline{K}^0\pi^+$	36.0±0.6
$K^-\pi^+\pi^+$	34.9±0.6
$\overline{K}^0\pi^+\pi^-\pi^+$	34.8±0.8
$\overline{K}^0K^+$	36.5±0.7
$K^-K^+\pi^+$	35.8±0.8
Weighted Efficiency: 35.0±0.5%	

6-5.2 Background Estimates

As opposed to the case for $D^+ \to K^+\pi^-\pi^+$, the selection criteria for $D^+ \to K^+\pi^0$ does not depend strongly on the tag mode. The numbers of D background events are

Table 6.4 The expected numbers of background events in the signal region for $D^+ \to K^+\pi^0$, including the contribution from the continuum. The acceptances for the $D\bar{D}$ backgrounds are also included. All limits are at 90% confidence limit.

$D\bar{D}$ Background	Acceptance(%)	Number of Events
$D^+ \to \bar{K}^0\pi^+ \to (\pi^0\pi^0)\pi^+$	0.319±0.059	0.034±0.008
$D^+ \to \bar{K}^0\pi^+ \to K_L^0\pi^+$	0.460±0.100	0.156±0.042
$D^+ \to \bar{K}^0K^+ \to (\pi^0\pi^0)K^+$	$0.056^{+0.039}_{-0.015}$	0.002±0.001
$D^+ \to \bar{K}^0K^+ \to K_L^0K^+$	$0.068^{+0.066}_{-0.020}$	$0.007^{+0.007}_{-0.003}$
$D^+ \to \pi^+\pi^0$	0.321±0.060	0.006±0.001
Total expected $D\bar{D}$ contribution		0.20±0.05
Total expected u, d, s contribution		<0.23
Total expected number of events		$0.30^{+0.24}_{-0.06}$

therefore not estimated opposite each tag mode. Table 6.4 lists the number of expected events from the background sources in the signal region. The errors are statistical only, derived from the errors on the number of Monte Carlo events, the statistical error on the number of tags, and the statistical error on the background branching fractions. The total number of events from the D background is $n_{b,D\bar{D}} = 0.20\pm0.05$

The number of events expected from u, d, s production is determined to be $n_{b,uds}$ <0.23 at 90% confidence level. This number is included in Table 6.4.

The number of expected events from all background sources is $n_b = 0.30^{+0.24}_{-0.06}$, where the 63.8% confidence level upper limit for $n_{b,uds}$--0.10 events--has been used. Assuming Poisson statistics, the probability for 0.30 events to fluctuate to no events is 0.74.

Table 6.4 and Table 6.4 gives the number of events for Regions I and II, respectively. For the totals, the 63.8% confidence level upper limits are used for those backgrounds where no Monte Carlo events were observed. The number of events expected in

Table 6.5 The expected numbers of background events for Region I, including the contribution from the continuum. The acceptances for the $D\bar{D}$ backgrounds are also included. All limits are at 90% confidence limit.

$D\bar{D}$ Background	Acceptance(%)	Number of Events
$D^+ \to \bar{K}^0\pi^+ \to (\pi^0\pi^0)\pi^+$	<0.025	<0.003
$D^+ \to \bar{K}^0\pi^+ \to K_L^0\pi^+$	<0.050	<0.017
$D^+ \to \bar{K}^0K^+ \to (\pi^0\pi^0)K^+$	3.20±0.19	0.108±0.035
$D^+ \to \bar{K}^0K^+ \to K_L^0K^+$	4.44±0.32	0.477±0.153
$D^+ \to \pi^+\pi^0$	<0.026	$<4\times10^{-4}$
Total expected $D\bar{D}$ contribution		0.59±0.19
Total expected u, d, s contribution		<0.23
Total expected number of events		$0.70^{+0.30}_{-0.19}$

Table 6.6 The expected numbers of background events for Region II, including the contribution from the continuum. The acceptances for the $D\bar{D}$ backgrounds are also included. All limits are at 90% confidence limit.

$D\bar{D}$ Background	Acceptance(%)	Number of Events
$D^+ \to \bar{K}^0\pi^+ \to (\pi^0\pi^0)\pi^+$	<0.025	<0.003
$D^+ \to \bar{K}^0\pi^+ \to K_L^0\pi^+$	$0.022^{+0.050}_{-0.006}$	$0.007^{+0.017}_{-0.002}$
$D^+ \to \bar{K}^0K^+ \to (\pi^0\pi^0)K^+$	$0.011^{+0.026}_{-0.003}$	$(4^{+9}_{-2})\times10^{-4}$
$D^+ \to \bar{K}^0K^+ \to K_L^0K^+$	<0.052	<0.006
$D^+ \to \pi^+\pi^0$	3.00±0.18	0.052±0.009
Total expected $D\bar{D}$ contribution		$0.07^{+0.02}_{-0.01}$
Total expected u, d, s contribution		$0.10^{+0.23}_{-0.03}$
Total expected number of events		$0.17^{+0.24}_{-0.03}$

Region I is $0.70^{+0.30}_{-0.19}$, while in fact two events are observed, both which appear to contain $D^+ \to \overline{K}^0 K^+$, $\overline{K}^0 \to K^0_L$. In Region II, $0.07^{+0.02}_{-0.01}$ events are expected for $D^+ \to \pi^+\pi^0$ while one candidate event is seen; a total of $0.17^{+0.24}_{-0.03}$ events are expected for this region.

6-5.3 Systematic Errors

Systematic errors are estimated for the detection efficiency of the signal, the number of $D\overline{D}$ background events and the number of u, d, s background events. Sources of error and their level of contribution are described below. Several of the effects have also been discussed in the $K^+\pi^-\pi^+$ analysis.

Systematic Errors on $\bar{\varepsilon}_s$

The following sources are considered to contribute to the systematic error on the reconstruction efficiency. The errors are given in terms of the relative uncertainty.

1) Charged track reconstruction efficiency. A -1% error is attributed for detecting one charged track.

2) The effect of no cuts for the fiducial regions of the detector. For one charged track, a -1% uncertainty is attributed.

3) Monte Carlo modelling of photons in the shower counter, and the shower angle cuts. The standard Mark III Monte Carlo shower generator uses a dictionary of real showers from $J/\psi \to \rho\pi$ decays to simulate photon showers in the calorimeter. To estimate the uncertainty on the modelling and on the shower angle cuts used in the initial event selection, the veto criteria and the $\cos\delta$ cut, events are also produced using a shower generator which simulates the showers using the model by Rossi.[64] A comparison of analysis results finds a $\pm 9\%$ uncertainty in the efficiency.

4) Photon detection efficiency. The effects of the calorimeter ribs and barrel/endcap interface regions introduce a -2.5% uncertainty per photon. Both the initial event selection and the veto cut require the observation of only one of the two photons from the π^0 in $D^+ \to K^+\pi^0$. Therefore

Table 6.7 The systematic errors on the $K^+\pi^0$ detection efficiency.

Source	Systematic Error (%)
Charged track efficiency	−0.4
Absence of fiducial cuts	−0.4
Shower modelling	±3.2
Photon detection efficiency	−0.9
Kaon identification	±0.4
Mass and signal region cuts	±0.4
Total Error	+3.2 / −3.7

only one factor of −2.5% is given for this source.The photon detection uncertainty is based on previous studies of the $\psi(3770)$ data.[62]

5) Kaon identification. The effects of the particle identification cuts on charged kaons in Monte Carlo data and real data were compared through a method similar that for the $K^+\pi^-\pi^+$analysis (see Section 5-5.7). To better match the kinematic topology of the charged kaon in $K^+\pi^0$, samples of $D^0 \to K^-\pi^+$ were used for this study. Differences in the efficiencies between the Monte Carlo and data were found to be less ±1.0%.

6) Definition of the U signal region. A ±1 % error is given to account for possible tails in the signal distribution.

These errors are summarized in Table 6.7 in terms of the absolute error on the reconstruction efficiency. The total errors are obtained by adding the biased errors linearly and the remaining errors in quadrature. Quoting both statistical and systematic errors, the weighted efficiency for the signal is

$$\bar{\varepsilon}_s = 35.0 \pm 0.5^{+3.2}_{-3.7}\,\%$$

Systematic Errors on $n_{b.D\bar{D}}$

Several effects which contribute to the systematic uncertainty of the signal efficiency also introduce uncertainties to the number of D (Class I) background events. Discussion of these effects on the backgrounds follows, with the errors given in terms of the relative uncertainty.

1) Charged track reconstruction efficiency. All backgrounds are detected with one track in the recoil; therefore a -1% error is attributed.

2) The effect of no cuts for the fiducial regions of the detector. For one charged track, a -1% uncertainty is attributed.

3) Monte Carlo modelling of photons in the shower counter, and the shower angle cuts. Using the differing shower generators shows also an uncertainty of about $\pm 9\%$ for the $\bar{K}^0\pi^+$ and $\bar{K}^0K^+$ backgrounds with $\bar{K}^0 \to \pi^0\pi^0$. The uncertainty for the $\pi^+\pi^0$ is assumed to be the same as for the $K^+\pi^0$ signal. The relative uncertainty on the total number of background events is therefore $\pm 1.9\%$.

4) Photon detection efficiency. For a background event to pass the initial event selection, only one shower needs to be observed within the search cone. This gives a factor of -2.5%. An additional factor of -0.5% accounts for 25% of the $\bar{K}^0\pi^+$ and $\bar{K}^0K^+$, $\bar{K}^0 \to \pi^0\pi^0$ backgrounds removed by the veto cut, when at least one other shower is observed in the event. The total is therefore -3.0%.

5) Particle identification. For the $\bar{K}^0\pi^+$ and $\pi^+\pi^0$ backgrounds, a $+16\%$ uncertainty is estimated for the pion misidentification, while for the $\bar{K}^0K^+$ backgrounds, a $\pm 1\%$ uncertainty is given for correct kaon identification. Since the $\bar{K}^0\pi^+$ backgrounds dominate, the uncertainty on the total number of background events is $+16\%$.

6) Modelling of K_L^0 hadronic showers in the calorimeter. The $\pm 25\%$ uncertainty in the K_L^0 model, used for the $\bar{K}^0\pi^+$ and $\bar{K}^0K^+$ backgrounds with $\bar{K}^0 \to K_L^0$, is derived to a $\pm 20\%$ error in the total number of background events.

7) Definition of the U signal region. A $\pm 5\%$ error is given to account for the uncertainty in modelling the tails from the background distributions.

The following additional sources have been considered in the systematic error on $n_{b.D\bar{D}}$.

8) The branching fractions for the background processes. The relative systematic errors in the branching fractions for $\bar{K}^0\pi^+$ (6.3%), $\bar{K}^0K^+$ (16.8%), and $\pi^+\pi^0$ (6.3%) propagate to a $\pm 6.3\%$ error in the number of background events, where the correlations and common systematic errors have been taken into account. The systematic errors for the resonance decays are either negligible or zero.

9) The error on the number of tags. These systematic errors contribute a $\pm 1.7\%$ uncertainty on the total number of background events (refer to Table 4.2).

These errors are summarized in Table 6.8 in terms of the absolute error on $n_{b.D\bar{D}}$. The total errors are obtained by adding the biased errors linearly and the remaining errors in quadrature. Quoting both statistical and systematic errors, the number of D background events is:

$$n_{b.D\bar{D}} = 0.20 \pm 0.05^{+0.05}_{-0.04}$$

Systematic Errors on $n_{b.uds}$

Because of the limited statistics from the Lund Monte Carlo data, the various u, d, s event topologies which can leak into the signal are not well understood. To estimate the systematic errors for $n_{b.uds}$, some assumptions are made about the topologies and the misidentification mechanisms: for the majority of the topologies (1) the charged track multiplicity is four; (2) the track identified as the recoil K^+ is a pion which has been misidentified; and (3) the showers are from photons. With these assumptions the relative systematic errors on the number of u, d, s background events follows.

Table 6.8 The systematic errors on the number of $D\bar{D}$ background events.

Source	Error (#events)
Charged track efficiency	–0.002
Absence of fiducial cuts	–0.002
Shower modelling	±0.004
Photon detection efficiency	–0.006
Particle identification	+0.032
K_L^0 modelling	±0.040
U signal cut	±0.010
Branching fractions	±0.013
Number of tags	±0.003
Total uncertainty	+0.054 / –0.044

1) Charged track reconstruction efficiency. For four charged tracks, a –4% error is attributed.

2) The effect of no cuts for the fiducial regions of the detector. For four charged tracks, a –4% uncertainty is attributed.

3) Monte Carlo modelling of photons in the shower counter, and the shower angle cuts. A ±9% error is given based on the studies for the $\bar{K}^0\pi^+$ and $\bar{K}^0K^+$ backgrounds with $\bar{K}^0 \to \pi^0\pi^0$.

4) Photon detection efficiency. A –2.5% error accounts for the one shower that must be observed within the search cone. Another –1.0% is added to account conservatively for background topologies which are removed by the veto cut when at least one other shower is observed in the event. The total is therefore –3.5%.

5) Particle identification. Misidentification in the recoil contributes a +16% error. Assuming the other tracks to be correctly identified contributes an additional ±2.4% uncertainty. Adding the errors in

Table 6.9 The systematic errors on the number of u, d, s background events.

Source	Error (#events)
Charged track efficiency	–0.009
Absence of fiducial cuts	–0.009
Shower angle cuts	±0.021
Photon detection efficiency	–0.008
Particle identification	+0.038 / –0.006
U signal cut	±0.012
Integrated Luminosity	±0.012
Total uncertainty	+0.047 / –0.042

quadrature gives a total uncertainty of $^{+16}_{-2}\%$ from particle identification.

6) Definition of the U signal region. A ±5% error is given to account for the possible tails in the background distributions.

7) Integrated Luminosity for the $\psi(3770)$ data set. This number contains a ±5% error which directly contributes to the systematic error on the number background events.

These errors are summarized in Table 6.8 in terms of the absolute error on the (upper limit) number of u, d, s background events. The total errors are obtained by adding the biased errors linearly and the remaining errors in quadrature. The limit on the number of u, d, s background events is enlarged by the adding the positive error, becoming:

$$n_{b.uds} < 0.28 \text{ @ } 90\% \text{ CL}$$

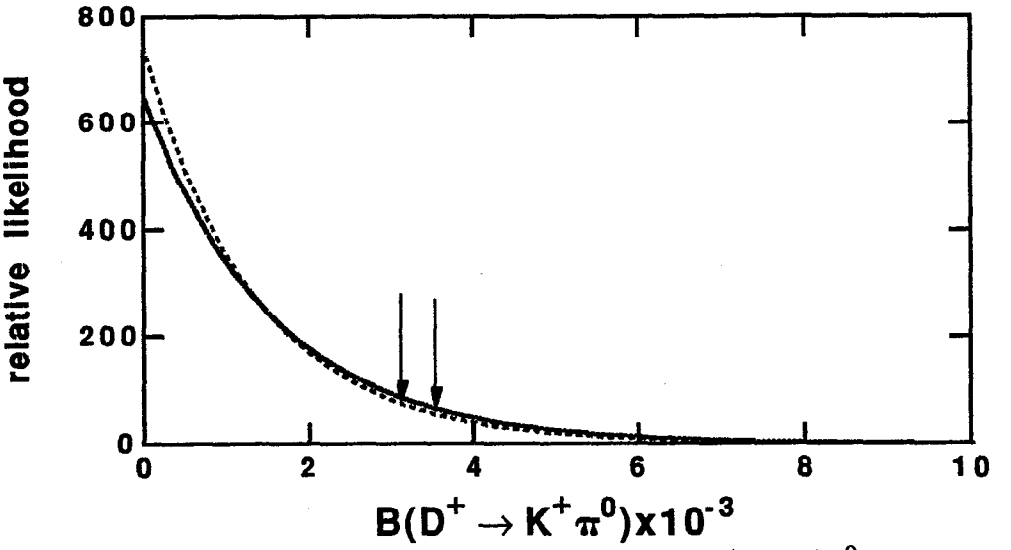

Figure 6.20 The likelihood function relative to $B(D^+ \to K^+\pi^0)$.

6-6 Upper Limit for $B(D^+ \to K^+\pi^0)$

An upper limit on $B(D^+ \to K^+\pi^0)$ is obtained by the maximum likelihood procedure prescribed in Section 5-6. The likelihood function for this analysis is shown in Figure 6.20, maximized for different values of $B(D^+ \to K^+\pi^0)$. The dashed and solid curves show, respectively, the results without and with systematic errors propagated; the arrows indicate the 90% confidence levels. If systematic errors were neglected, $B(D^+ \to K^+\pi^0) <$ 0.31%. The systematic errors increase this limit to

$$B(D^+ \to K^+\pi^0) < 0.35\% \text{ @ } 90\% \text{ CL}$$

The separate analysis (Appendix 2) where fully reconstructed doubly Cabibbo suppressed events are kinematically fitted rather than tagged yields $B(D^+ \to K^+\pi^0) < 0.51\%$ at 90% confidence level.

Chapter 7

Search for $D^+ \rightarrow K^{*+}\pi^0$

7-1 Introduction

The doubly Cabibbo suppressed decay $D^+ \rightarrow K^{*+}\pi^0$ is of particular interest since it has been predicted to have the largest $\bar{\rho}$ parameter:$|\ \bar{\rho}_{K^{*+}\pi^0}|^2 = \frac{B(K^{*+}\pi^0)}{B(\bar{K}^{*0}\pi^+)} \times \frac{1}{\tan^4\theta_c} =$ 12-25. To maximize the efficiency for $D^+ \rightarrow K^{*+}\pi^0$ this mode is searched for in both decay channels of the K^{*+}: $K^{*+} \rightarrow K^0\pi^+$ (with $K^0 \rightarrow K^0_S \rightarrow \pi^+\pi^-$) and $K^{*+} \rightarrow K^+\pi^0$. Section 7-2 and Section 7-3 describe these two searches, respectively. The results of the searches are combined to calculate a limit on $B(D^+ \rightarrow K^{*+}\pi^0)$, as covered in Section 7-4.

7-2 Search for $D^+ \rightarrow K^{*+}\pi^0, K^{*+} \rightarrow K^0\pi^+$

This section describes the search for $D^+ \rightarrow K^{*+}\pi^0$ in the $K^0\pi^+$ channel of K^{*+}. The analysis discussions are organized as follows. Section 7-2.1 covers the initial event selection. Section 7-2.2 discusses all the known backgrounds and the cuts that are added to remove them. Section 7-2.3 presents the results of the analysis on the data and includes analysis checks and estimates of the efficiencies and level of background. Section 7-2.4 gives a *preliminary* upper limit calculation on $B(D^+ \rightarrow K^{*+}\pi^0)$.

7-2.1 Event Selection

The analysis technique for $D^+ \rightarrow K^{*+}\pi^0 \rightarrow (K^0\pi^+)\pi^0$ is analogous to that for $D^+ \rightarrow K^+\pi^0$, due to the similar kinematic properties. The decay $D^+ \rightarrow K^{*+}\pi^0$ is a quasi-two--body decay, which produces a high momentum π^0 with $P_{\pi^0} \cong 700$ MeV/c in the rest frame of the D meson. When boosted to the lab frame P_{π^0} is no less than 600 MeV/c, and at least one high energy photon is produced highly collimated in the π^0 direction. Figure 7.1 and

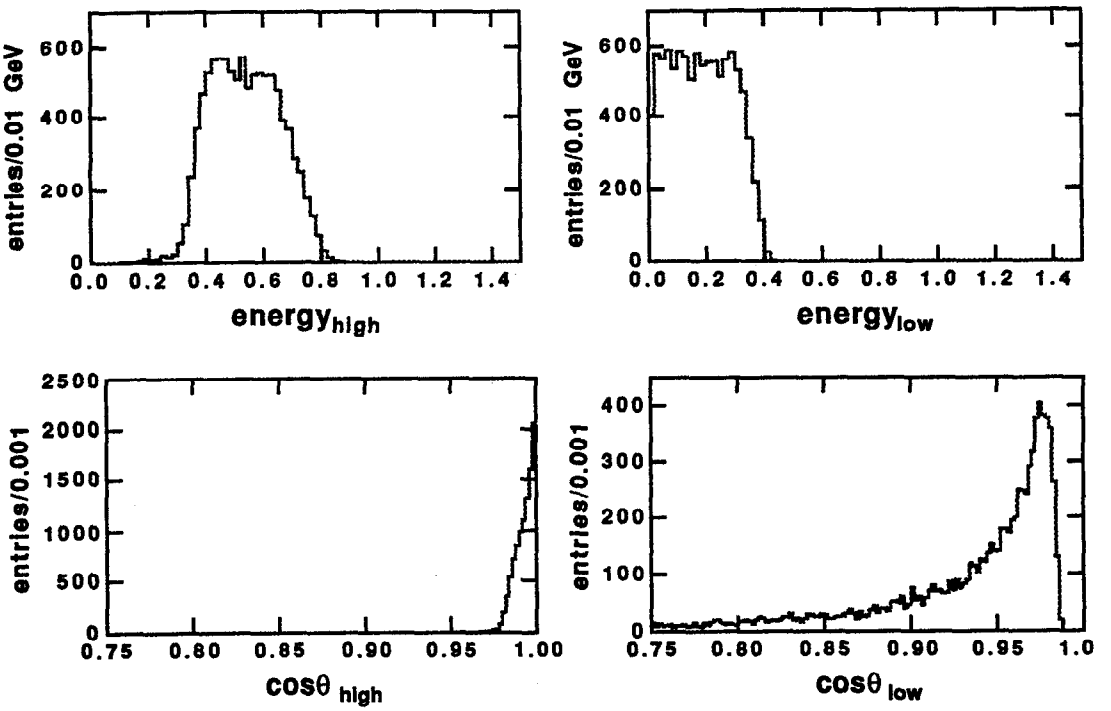

Figure 7.1 Properties of the π^0 from $D^+ \to K^{*+}\pi^0$ before applying the detector resolution: (a) the energy spectrum of the higher energy photon; (b) the energy spectrum of the lower energy photon; (c) the collinearity, $\cos\theta_{high}$, between the momenta of the π^0 and the higher energy photon; (d) the collinearity, $\cos\theta_{low}$, between the momenta of the π^0 and lower energy photon.

Figure 7.2 illustrate the properties of the two photons from the π^0 before and after applying the detector resolution.

Again the approach employed avoids reconstruction of the π^0 and the poor resolution in the mass distribution that results. Instead all charged track momenta in an event are summed to determine the π^0 flight direction, and showers attributed to isolated photons are required to be seen in the π^0 direction. The fiducial region in which to look for the photons is defined by the cone $\cos\theta > 0.8$. This search cone retains 92.1% of the low energy photons and effectively all the high energy photons, detected in the shower counter solid angle.

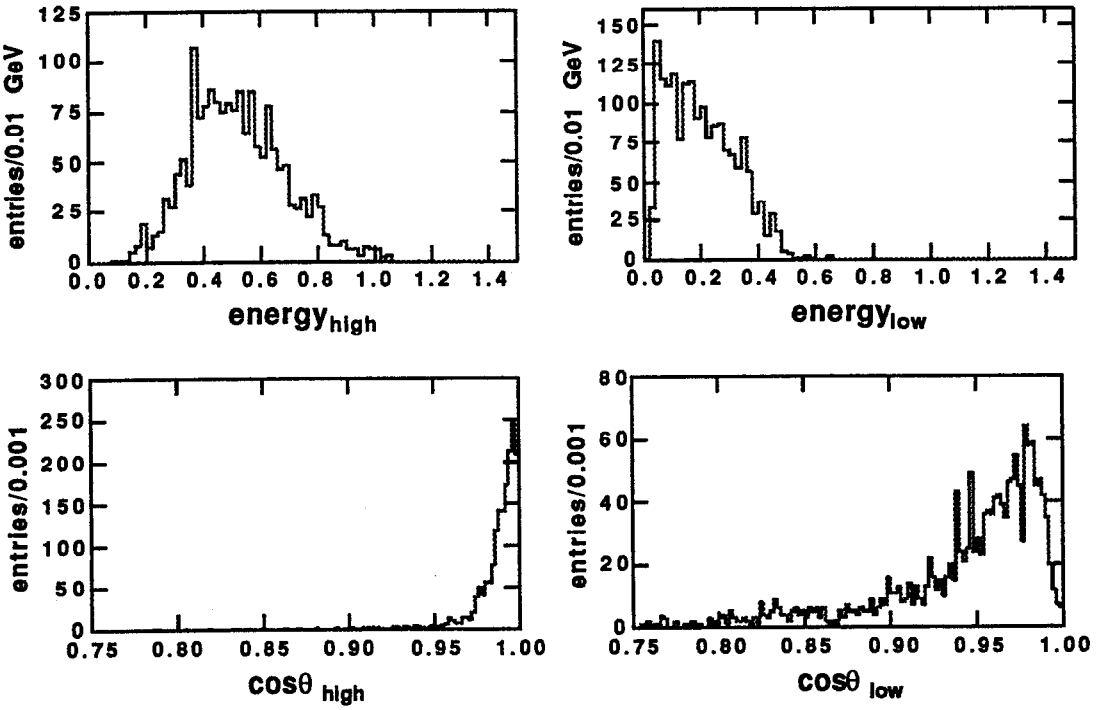

Figure 7.2 Properties of the π^0 from $D^+ \to K^{*+}\pi^0$ after the detector resolution is applied; the plots correspond with those in Figure 7.1.

Corresponding to the U quantity for the $K^+\pi^0$ analysis, the Lorentz invariant quantity used to study a signal in this analysis is:

$$V \equiv \sum_{\mu} P^{\mu}_{\text{recoil}} P_{K^*\mu} = \sum_{\mu} (P_{\text{event}} - P_{\text{tag}})^{\mu} P_{K^*\mu}$$

where P^{μ}_{recoil}, P^{μ}_{tag}, $P^{\mu}_{K^*}$, and P^{μ}_{event}, are, respectively the four momenta of the recoil, the tag, the K^{*+} and the full event. Note that V is effectively the same as U from the $K^+\pi^0$ analysis, with the substitution of $P^{\mu}_{K^*}$ for P^{μ}_{K}. From the four-vector algebra, $V = 2.136$ $(\text{GeV}/c^2)^2$ for a precisely measured $D^+ \to K^{*+}\pi^0$ signal.

The details of the initial event selection are as follows. Given a tagged event:

- Require three charged tracks with good helix fits. The net charge of the three tracks must be opposite that of the tag.

- For charged tracks not used in the K^0_S reconstruction, require energy loss corrections and a successful beam fit.

- For the K^0_S reconstruction, obtain the $\pi^+\pi^-$ pairs (two combinations are possible per event), and for each combination apply the same method used to reconstruct K^0_S's in the tagging procedure:

- recalculate the track parameters at the decay vertex

- require $l_{xy} > 2$mm

- require $P(\chi^2_{xy}) > 0.01\%$

- require $|M_{\pi^+\pi^-} - M_{K0}| < 30$ MeV/c^2

  Use the adjusted track parameters in the balance of the analysis.

- From all the charged tracks in the event, compute the π^0 momentum, assuming conservation of energy and momentum, and require one or more photons to lie within the search cone, $\cos\theta > 0.8$.

- Compute V and plot.

The major backgrounds to $D^+ \to K^{*+}\pi^0 \to (K^0\pi^+)\pi^0$ involve no particle misidentifications. Therefore to minimize the systematic uncertainties no requirements are made with the time-of-flight or dE/dx information on the tracks found in the recoil. To improve resolution in V, E_{tag} is again replaced by $\sqrt{s}/2$. No cuts have been applied to isolate the K^{*+}; the K^{*+} signature will be extracted by the data reduction cuts in Section 7-2.2.

Figure 7.3 displays a Monte Carlo plot of the expected signal. The signal region is defined as

- $2.00 < V < 2.26$ (GeV/c^2)^2

which extends to approximately $\pm 2\sigma$ about the central value. Figure 7.6(a) shows V for the data opposite the five tags. Thirty-nine events lie within the signal region after the initial event selection.

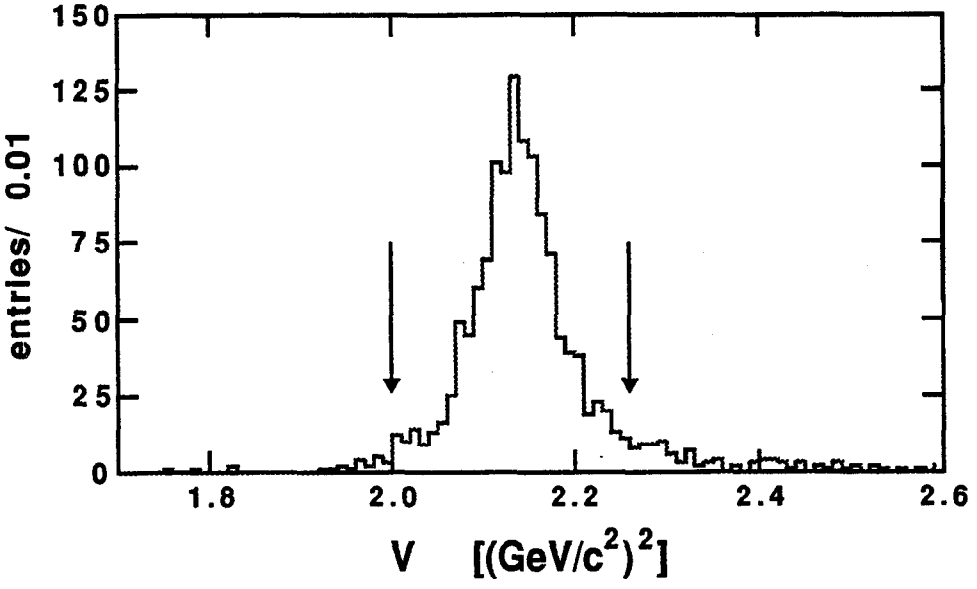

Figure 7.3 The Lorentz invariant quantity V for a Monte Carlo $D^+ \to K^{*+}\pi^0 \to (K^0\pi^+)\pi^0$ signal (generated opposite $D^- \to K^+\pi^-\pi^-$).

7-2.2 Major Backgrounds to $D^+ \to K^{*+}\pi^0, K^{*+} \to K^0\pi^+$

The major backgrounds for $D^+ \to K^{*+}\pi^0 \to (K^0\pi^+)\pi^0$ were determined by applying the event selection procedure to the full D^+D^- and $D^0\overline{D}^0$ Monte Carlo data sets discussed in Section 3-3.5. The major contributions are found to be only the Class I category, where only the recoil D^+ is incorrectly reconstructed. It was observed in the analyses for $D^+ \to K^+\pi^-\pi^+$ and $D^+ \to K^+\pi^0$ that the major backgrounds to doubly Cabibbo suppressed decays usually involve at least two errors in misidentifying an event as a signal. This property is also observed in this analysis.

This section is divided into two parts. Section 7-2.2.1 discusses the known backgrounds to and $D^+ \to K^{*+}\pi^0 \to (K^0\pi^+)\pi^0$, and Section 7-2.2.2 discuss the cuts which are introduced to remove them. The results of the cuts on the data is postponed until Section 7-2.3.

7-2.2.1 The Class I backgrounds

The major Class I backgrounds arise from two hadronic Cabibbo allowed channels, two semileptonic Cabibbo allowed channels and one hadronic Cabibbo suppressed channel:

- $D^+ \to \bar{K}^0\pi^+\pi^0$, $\bar{K}^0 \to K_S^0 \to \pi^+\pi^-$. The K_S^0 is assumed to originate from a K^0, not a $\bar{K}^0$, and the $K_S^0\pi^+$ combination is assumed to form a K^{*+}.
- $D^+ \to \bar{K}^0\pi^+\pi^0\pi^0$, $\bar{K}^0 \to K_S^0 \to \pi^+\pi^-$. The same reconstruction errors occur. In addition, the photons from the extra π^0's are either mistakenly grouped as the products of the single π^0 from $K^{*+}\pi^0$ or ignored altogether.
- $D^+ \to \bar{K}^{*0}e^+\nu_e$ and $\bar{K}^{*0}\mu^+\nu_\mu$, $\bar{K}^{*0} \to \bar{K}^0\pi^0$, $\bar{K}^0 \to K_S^0 \to \pi^+\pi^-$. The neutrino is not detected and the charged lepton is misidentified as a pion to compensate the missing energy and momentum.
- $D^+ \to \phi\pi^+$, $\phi \to K_S^0K_L^0$, $K_S^0 \to \pi^+\pi^-$. The K_S^0 is assumed to originate from a K^0, while the K_L^0 showers (hadronically) in the electromagnetic calorimeter and appears as the π^0.

The $\bar{K}^0\pi^+\pi^0$ background has been studied through the resonant modes $D^+ \to \bar{K}^0\rho^+ \to \bar{K}^0(\pi^+\pi^0)$ and $D^+ \to \bar{K}^{*0}\pi^+ \to (\bar{K}^0\pi^0)\pi^+$ and the nonresonant $D^+ \to \bar{K}^0\pi^+\pi^0$. The $\bar{K}^0\pi^+\pi^0\pi^0$, however, has been largely studied as nonresonant. Figure 7.4 compares the V distributions for these backgrounds and the $D^+ \to K^{*+}\pi^0 \to (K^0\pi^+)\pi^0$ signal.

7-2.2.2 Background Cuts

The Dalitz Cuts

These cuts are introduced to reduce the backgrounds from $D^+ \to \bar{K}^0\pi^+\pi^0$. The event selection for $D^+ \to K^{*+}\pi^0 \to (K^0\pi^+)\pi^0$ has involved only the reconstruction of the final state $D^+ \to K_S^0\pi^+\pi^0$, with no attempt made to identify the resonant $\bar{K}^{*0}$ substructure. To reduce the backgrounds and isolate the $K^{*+}\pi^0$ signal, a Dalitz plot analysis is performed. The signal and each of the resonant channels of the $\bar{K}^0\pi^+\pi^0$ background decay as

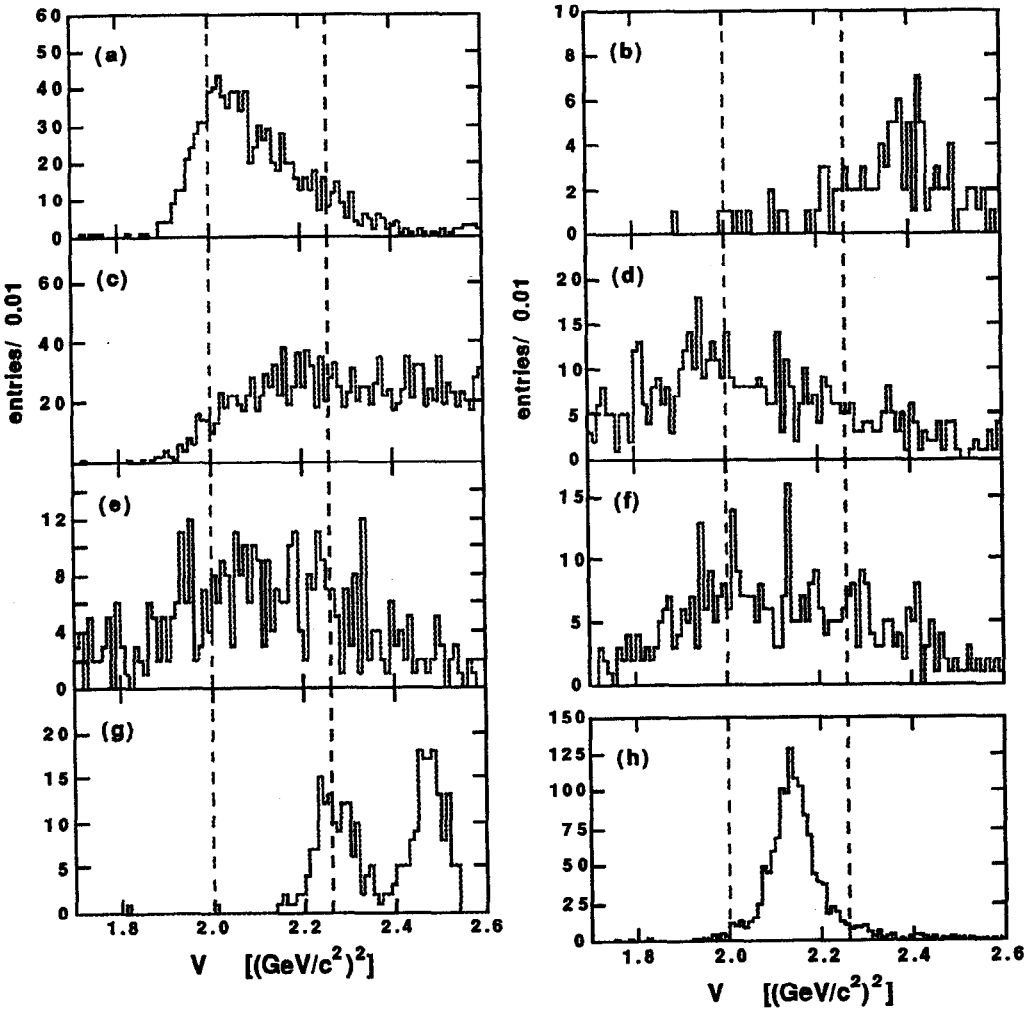

Figure 7.4 The V distributions for the backgrounds (a) $D^+ \to \bar{K}^0\rho^+$, (b) $D^+ \to \bar{K}^{*0}\pi^+$, $\bar{K}^{*0} \to \bar{K}^0\pi^0$, (c) $D^+ \to \bar{K}^0\pi^+\pi^0$ [nr], (d) $D^+ \to \bar{K}^0\pi^+\pi^0\pi^0$, (e) $D^+ \to \bar{K}^{*0}e^+\nu_e \to (\bar{K}^0\pi^0)e^+\nu_e$, (f) $\bar{K}^{*0}\mu^+\nu_\mu \to (\bar{K}^0\pi^0)\mu^+\nu_\mu$ and (g) $D^+ \to \phi\pi^+$, $\phi \to K_S^0K_L^0$ and for (h) the DCSD signal $D^+ \to K^{*+}\pi^0$, $K^{*+} \to K^0\pi^+$. All neutral kaons decay via $\bar{K}^0 \to K_S^0 \to \pi^+\pi^-$.

$P \to VP_1 \to (P_2 P_3) P_1$, where P denotes a pseudoscalar meson and V denotes a vector meson. Their expected distributions in $M^2_{\pi\pi}$ versus $M^2_{K\pi}$ are shown in Figure 7.5, where $M_{\pi\pi}$ and $M_{K\pi}$ are the $\pi^+\pi^0$ and $K_S^0\pi^+$ invariant masses, respectively. Since the π^0 is not reconstructed in this analysis, $M^2_{\pi\pi}$ is obtained from the π^+ momentum and the missing π^0 momentum, as calculated in the initial event selection. Interference effects, which can cause

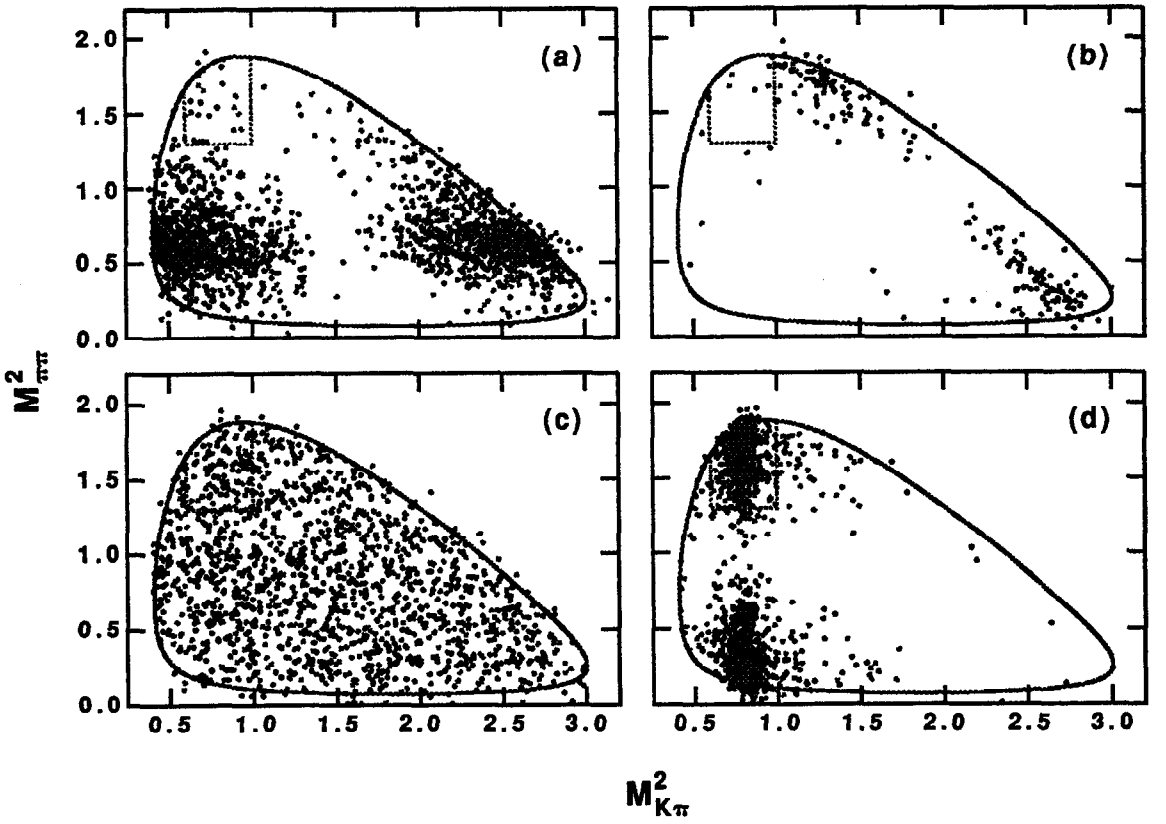

Figure 7.5 Monte Carlo Dalitz plots of $M^2_{\pi\pi}$ versus $M^2_{K\pi}$ for (a) $D^+ \to \overline{K}^0\rho^+ \to \overline{K}^0(\pi^+\pi^0)$, (b) $D^+ \to \overline{K}^{*0}\pi^+ \to (\overline{K}^0\pi^0)\pi^+$, (c) $D^+ \to \overline{K}^0\pi^+\pi^0$[nr] and (d) $D^+ \to K^{*+}\pi^0 \to (K^0\pi^+)\pi^0$. The dotted line designates the background reduction cuts.

small shifts in the mass peaks for the $\overline{K}^0\pi^+\pi^0$ channels, are ignored; the uncertainties this approach introduces will be discussed below in the systematic errors.

Figure 7.5 shows a significant overlap between the low $M^2_{K\pi}$ lobe in the $\overline{K}^0\rho^+$ plot and the low $M^2_{\pi\pi}$ lobe in the $K^{*+}\pi^0$ plot. A cut only in $M^2_{K\pi}$ to enhance the $K^{*+}\pi^0$ signal would still allow approximately 70% of the $\overline{K}^0\rho^+$ background to feed in. Cuts are therefore applied in both $M^2_{K\pi}$ and $M^2_{\pi\pi}$:

- $0.6 < M^2_{K\pi} < 1.0\ (\mathrm{GeV/c^2})^2$
- $M^2_{\pi\pi} > 1.3\ (\mathrm{GeV/c^2})^2$

as determined by the Monte Carlo. This criteria removes approximately 96% of the $\bar{K}^0\rho^+$ events, 70% of the $\bar{K}^{*0}\pi^+$ events and 75% of the $\bar{K}^0\pi^+\pi^0$[nr] events which survive the initial event selection and retains 42% of the signal events.

The Dalitz cuts are also effective at removing the other backgrounds. They remove 85% of the $\bar{K}^0\pi^+\pi^0\pi^0$ events, 66% of the $\bar{K}^{*0}e^+\nu_e$ and $\bar{K}^{*0}\mu^+\nu_\mu$ and 98% of the $\phi\pi^+$ events which survive the initial event selection.

The Veto Cut

This cut is introduced to reduce the background from $D^+ \to \bar{K}^0\pi^+\pi^0\pi^0$. It is effectively the same cut as the veto cut for the $K^+\pi^0$ search (Section 6-4.2) with modifications accounting for the different π^0 momenta and charged track multiplicity of $K^{*+}\pi^0$. Since the π^0 in this analysis is ~100 MeV lower in momentum, the cuts are:

- one or more photons with energy > 300 MeV must lie within $|\cos\alpha| > 0.96$
- no photons with energy > 300 MeV may lie outside $|\cos\alpha| < 0.96$.
- no more than 1 photon with energy between 150 MeV and 250 MeV may lie outside $|\cos\alpha| < 0.96$.

This criteria removes approximately 80% of the $\bar{K}^0\pi^+\pi^0\pi^0$ background which survives the Dalitz cuts, while retaining 78% of the signal.

The veto cut is also effective at removing the backgrounds from $D^+ \to \bar{K}^{*0}e^+\nu_e$ and $\bar{K}^{*0}\mu^+\nu_\mu$, $\bar{K}^{*0} \to \bar{K}^0\pi^0$ because of the different kinematic topology of the π^0 in the final state. About 92% of these backgrounds are removed by the cut.

7-2.3 Results

Figure 7.6 shows the application of the cuts to the data. After all cuts are applied no events remain in the signal region. For reference, Figure 7.7 gives the Dalitz plot of the events which passed the initial event selection. One event, displayed in Figure 7.8, is

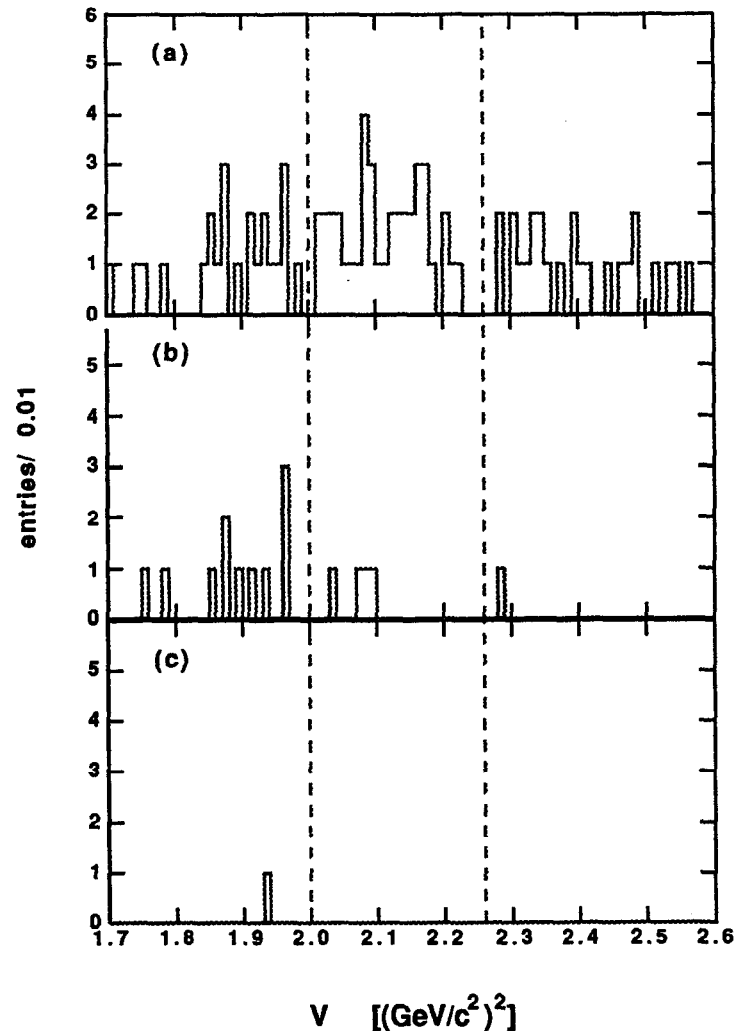

Figure 7.6 Data from all tags (a) after the initial event selection, (b) after the Dalitz-plot cuts, and (c) after the veto cut (see text).

observed at $V = 1.930$ $(\mathrm{GeV/c^2})^2$, below the signal region where 0.13 ± 0.05 events are expected from the known backgrounds.

7-2.3.1 Analysis Tests

As a test of the analysis procedure, the numbers of events that are expected to be removed from the signal region by each of the background cuts are calculated and compared to the numbers that are removed.

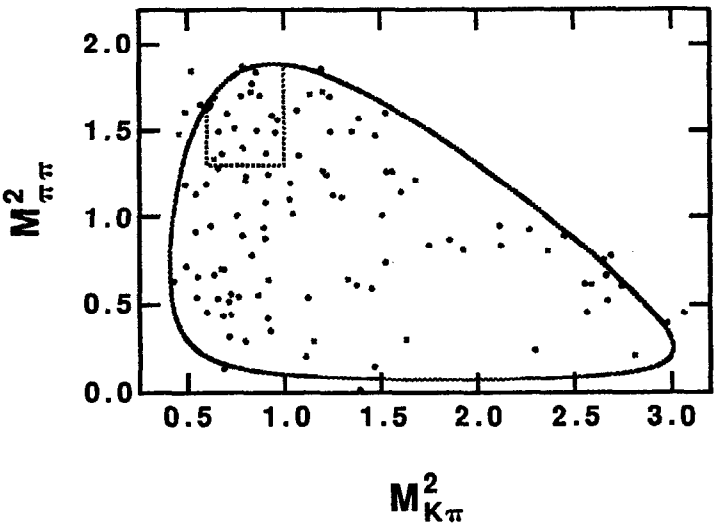

Figure 7.7 Dalitz plot of $M^2_{\pi\pi}$ versus $M^2_{K\pi}$ for the events that survived the initial event selection.

Table 7.1 gives the background branching fractions used to estimate the numbers of background events. No experimental measurements currently exists for either $B(D^+ \to \bar{K}^0\pi^+\pi^0\pi^0)$ or $B(\bar{K}^{*0}\mu^+\nu_\mu)$. For $B(D^+ \to \bar{K}^0\pi^+\pi^0\pi^0)$ the number quoted in Table 7.1 is obtained from $B(D^+ \to K^-\pi^+\pi^+\pi^0) = 5.8\pm0.9\pm1.5\%$[23] and isospin: $B(D^+ \to \bar{K}^0\pi^+\pi^0\pi^0)$ $= B(D^+ \to K^-\pi^+\pi^+\pi^0) \times 1/2 = 2.9\pm0.5\pm1.5\%$, where a systematic error of 50% is added, in quadrature, to account for the uncertainty in this result. This formula assumes that $D^+ \to \bar{K}^0\pi^+\pi^0\pi^0$ and $D^+ \to K^-\pi^+\pi^+\pi^0$ are dominated by $D^+ \to \bar{K}^{*0}\pi^+\pi^0$. This assumption is supported by a resonant substructure analysis of $D^+ \to K^-\pi^+\pi^+\pi^0$[23] where large event fractions were found for $\bar{K}^{*0}\rho^+$ and $\bar{K}_1(1400)^0\pi^+$ (which goes 1/3 of the time to $(\bar{K}^{*0}\pi^0)\pi^+$). For $B(\bar{K}^{*0}\mu^+\nu_\mu)$, the number in Table 7.1 assumes lepton universality: $B(\bar{K}^{*0}\mu^+\nu_\mu) = B(\bar{K}^{*0}e^+\nu_e) = 5.3^{+1.9}_{-1.1}\pm0.6\%$.

Included in the predicted numbers are the estimated contributions from u, d, s events in the continuum, determined from an analysis of Lund Monte Carlo data. The results of the analysis is shown in Figure 7.9.

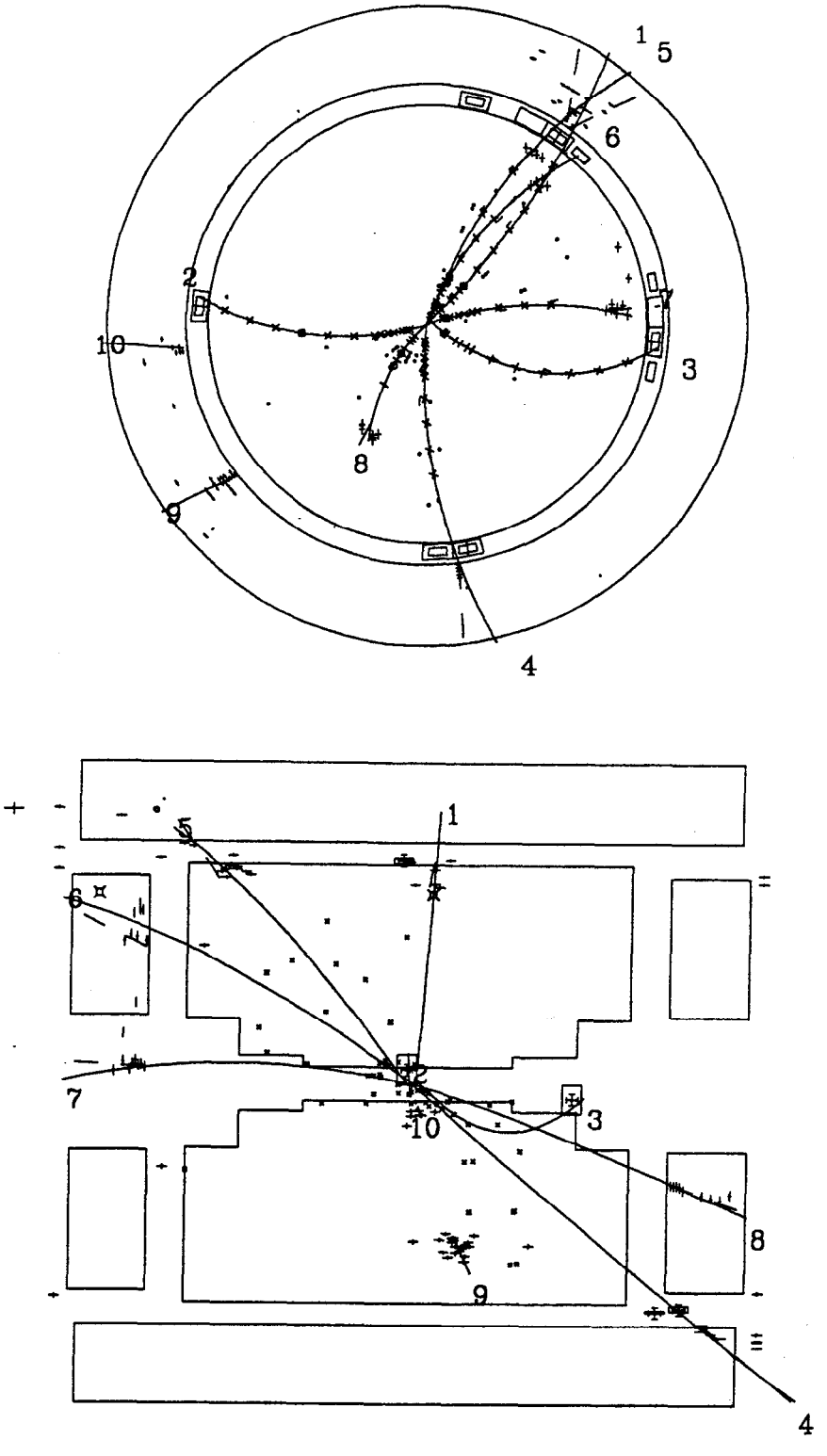

Figure 7.8 The event at $V = 1.930$ (GeV/c^2)^2. The tag is $\bar{K}^0\pi^+\pi^-\pi^+$.

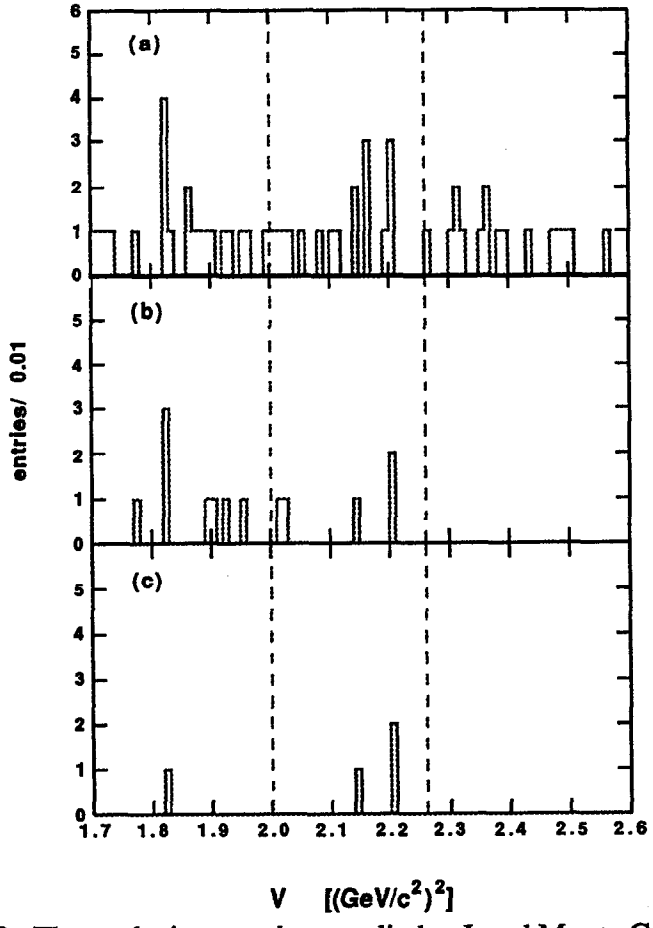

Figure 7.9 The analysis procedure applied to Lund Monte Carlo: (a) after initial event selection; (b) after cuts in the Dalitz plot and (c) after the veto cut.

Table 7.2 gives the results of the test by comparing the total expected numbers of events lost against the observed numbers lost. The total number of events expected to be lost from the signal region, $13.9^{+1.3}_{-1.2}$, deviates by approximately 4σ from the observed number lost, 39, assuming Poisson statistics. Most of this discrepancy occurs at the Dalitz cuts, where $12.9^{+1.3}_{-1.2}$ events are expected to be lost versus four events observed to be lost. Further studies to understand the discrepancy were made, including tests for potential Class II background topologies (e.g. $D^0 \to K^-\pi^+\pi^0$ vs. $\overline{D}^0 \to K^0\pi^+\pi^-$ for $D^+ \to K^-\pi^+\pi^+$ vs. $D^- \to K^{*-}\pi^0 \to \overline{K}^0\pi^-\pi^0$) and visual scans of the events (which involved checking the

Table 7.1 Branching fractions of the Class I backgrounds to $D^+ \to K^{*+}\pi^0 \to (K^0\pi^+)\pi^0$

Mode	Branching Fraction (%)	Reference
$D^+ \to \bar{K}^0\rho^+$	6.9±0.8±2.3	22
$\bar{K}^{*0}\pi^+$	5.9±1.9±2.5	22
$\bar{K}^0\pi^+\pi^0$[nr]	1.3±0.7±0.9	22
$\bar{K}^0\pi^+\pi^0\pi^0$	2.9±0.5±1.5	(see text)
$\bar{K}^{*0}e^+\nu_e$	$5.3^{+1.9}_{-1.1}$±0.6	25
$\bar{K}^{*0}\mu^+\nu_\mu$	$5.3^{+1.9}_{-1.1}$±0.6	(see text)
$\phi\pi^+$	0.77±0.22±0.11	24, 20

Table 7.2 The application of the background rejection cuts as a comparison of the observed numbers of events removed against the expected numbers (from known backgrounds).

Cut	Observed Loss	Expected Loss
Dalitz	35	$12.9^{+1.3}_{-1.2}$
Veto	4	$1.0^{+0.3}_{-0.1}$
Total	39	$13.9^{+1.3}_{-1.2}$

events for extra showers, indicative of backgrounds with extra π^0's). However, no other known backgrounds have been identified.

7-2.3.2 Detection Efficiencies

The detection efficiencies for $D^+ \to K^{*+}\pi^0 \to (K^0\pi^+)\pi^0$ are determined opposite each of the five tag modes from the Monte Carlo simulations; the numbers are given in Table 7.3. The weighted efficiency is $\bar{\varepsilon}_s = 14.1 \pm 0.4\%$.

The efficiency found opposite the $\bar{K}^0\pi^+\pi^-\pi^+$ tag is larger than the efficiencies found opposite the other tags. This increase is caused by the effect that events tagged by that channel have higher track multiplicities, which make those events more prone to multiple counting. Since only one tag is counted per event by the tagging procedure, but all tag candidates are considered in the full event analysis, a larger efficiency is obtained for the signal opposite $\bar{K}^0\pi^+\pi^-\pi^+$.

7-2.3.3 Background Estimates

Table 7.4 lists the number of expected events from each of the Class I backgrounds after all cuts have been applied. The errors are statistical only, derived from the errors on the number of Monte Carlo events, the statistical error on the number of tags, and the statistical error on the branching fractions for the background processes.The uncertainty in multiple counting events which contain the $\bar{K}^0\pi^+\pi^-\pi^+$ tag will be accounted for in the systematic errors. The total number of $D\bar{D}$ background events expected is $n_{b,D\bar{D}} = 0.6\pm0.1$.

The number of events expected from u, d, s production is determined to be $n_{b,uds} = 0.31^{+0.30}_{-0.09}$ This number is included in Table 7.4.

The number of expected events from all background sources is $n_b = 1.0^{+0.3}_{-0.2}$. Assuming Poisson statistics, the probability for 1.0 events to fluctuate to no events is 0.37.

7-2.3.4 Systematic Errors

Systematic errors are estimated for the detection efficiency for the signal, and the number of $D\bar{D}$ (Class I) background events, and the number of u, d, s background events. Sources of error and their level of contribution are described below. Several of the effects have been described in the previous analyses.

Table 7.3 Efficiencies for $D^+ \to K^{*+}\pi^0 \to (K^0\pi^+)\pi^0$ opposite each tag.

Tag Mode	efficiency(%)
$\bar{K}^0\pi^+$	13.3±0.5
$K^-\pi^+\pi^+$	13.5±0.5
$\bar{K}^0\pi^+\pi^-\pi^+$	19.7±1.0
$\bar{K}^0K^+$	13.3±0.6
$K^-K^+\pi^+$	14.5±0.7
Weighted Efficiency: 14.1±0.4%	

Table 7.4 The expected numbers of background events for $D^+ \to K^{*+}\pi^0 \to (K^0\pi^+)\pi^0$, including the contribution from the continuum. The acceptances for the $D\bar{D}$ backgrounds are also included.

$D\bar{D}$ Background	Acceptance(%)	Number of Events
$D^+ \to \bar{K}^0\rho^+ \to \bar{K}^0(\pi^+\pi^0)$	0.40±0.07	0.20±0.05
$D^+ \to \bar{K}^{*0}\pi^+ \to (\bar{K}^0\pi^0)\pi^+$	0.78±0.18	0.11±0.05
$D^+ \to \bar{K}^0\pi^+\pi^0$[nr]	2.37±0.18	0.20±0.10
$D^+ \to \bar{K}^0\pi^+\pi^0\pi^0$	0.47±0.08	0.10±0.02
$D^+ \to \bar{K}^{*0}e^+\nu_e \to (\bar{K}^0\pi^0)e^+\nu_e$	0.11±0.06	0.01±0.01
$D^+ \to \bar{K}^{*0}\mu^+\nu_\mu \to (\bar{K}^0\pi^0)\mu^+\nu_\mu$	0.17±0.07	0.02±0.01
$D^+ \to \phi\pi^+ \to (K^0_SK^0_L)\pi^+$	0.03±0.02	$(6\pm4)\times10^{-4}$
Total expected $D\bar{D}$ contribution		0.64±0.13
Total expected u, d, s contribution		$0.31^{+0.30}_{-0.09}$
Total expected number of events		$1.0^{+0.3}_{-0.2}$

Systematic Errors on $\bar{\varepsilon}_S$

The following sources are considered to contribute to the systematic error on $\bar{\varepsilon}_S$.

The errors are given in terms of the relative uncertainty.

1) Charged track reconstruction efficiency. A −3% error is attributed for detecting three charged tracks.

2) The effect of no cuts for the fiducial regions of the detector. For the three charged tracks, a −3% uncertainty is attributed.

3) The K_S^0 vertex requirements. Previous studies of the $\psi(3770)$ data found that the cuts on l_{xy} and $P(\chi^2_{xy})$ introduce a ±5% uncertainty in the reconstruction efficiency of K_S^0's![62]

4) Monte Carlo modelling of photons in the shower counter, and the shower angle cuts. A comparison of analysis results using different shower simulators (confer Section 6-5.3) finds discrepancies of no more than 10%. Therefore, a ±5% uncertainty is attributed to this effect.

5) Photon detection efficiency. Both the initial event selection and the veto cut require the observation of only one of the two photons from the π^0 in $D^+ \to K^{*+}\pi^0$. Therefore only one factor of −2.5% is given for this source.

6) Invariant mass cuts, and definition of the V signal region. Loose cuts are applied to the Dalitz plot, and loose cuts define the signal region in the V distribution. A ±1% error is given to account for possible tails in the signal distribution.

These errors are summarized in Table 7.5 in terms of the absolute error on the reconstruction efficiency. The total errors are $^{+1.0}_{-1.6}$%, obtained by adding the biased errors linearly and then the result to the remaining errors in quadrature. Quoting both statistical and systematic errors, the weighted efficiency for the signal is

$$\bar{\varepsilon}_s = 14.1 \pm 0.4^{+1.0}_{-1.6}\%$$

Table 7.5 The systematic errors on the detection efficiency for $D^+ \to K^{*+}\pi^0 \to (K^0\pi^+)\pi^0$.

Source	Absolute Error (%)
Charged track efficiency	–0.42
Absence of fiducial cuts	–0.42
K_S^0 vertex requirements	±0.71
Shower modelling and angle cuts	±0.71
Photon detection efficiency	–0.35
Mass and V signal cuts	±0.14
Total Error	+1.0 / –1.6

Systematic Errors on $n_{b.D\bar{D}}$

Several effects which contribute systematic errors to the signal also introduce uncertainties on the number of D background events. Discussion of these effects on the background follows, with errors given in terms of the relative uncertainty.

1) Charged track reconstruction efficiency. All backgrounds channels are detected with charged tracks in the recoil; therefore a –3 % error is attributed.

2) The effect of no cuts for the fiducial regions of the detector. A –3 % uncertainty is attributed for three charged tracks.

3) The K_S^0 vertex requirements. All backgrounds include the reconstruction of a K_S^0, and therefore an overall ±5 % uncertainty is included.

4) Monte Carlo modelling of photons in the shower counter, and the shower angle cuts. For the backgrounds, ±5 % uncertainty is attributed for this effect.

5) Photon detection efficiency. For a background event to pass the initial event selection, only one shower needs to be observed within the search

cone. This gives a factor of –2.5%. An additional factor of –0.1% accounts for 25% of the $\bar{K}^0\pi^+\pi^0\pi^0$ background which is removed by the veto cut when at least one other shower is observed in the event. The total is therefore –2.6%.

6) Invariant mass cuts, and definition of the V signal region. The mass cuts in the Dalitz plot lie outside the lobes from the resonant background channels. The uncertainty from those cuts are, therefore, considered negligible. A ±5% uncertainty is given to account for the background in the V signal region.

The following additional sources have been considered in the systematic error for $n_{b.D\bar{D}}$:

7) Multiple counting events. The number of events which have been tagged by $\bar{K}^0\pi^+\pi^-\pi^+$ is given a +25% uncertainty due to the effect of multiple counting. This contributes a +2% uncertainty on the total number of background events.

8) The branching fractions for the background processes. The relative systematic errors in the branching fractions for $\bar{K}^0\rho^+$ (33%), $\bar{K}^{*0}\pi^+$ (42%), $\bar{K}^0\pi^+\pi^0$[nr] (69%) and $\bar{K}^0\pi^+\pi^0\pi^0$ (50%) propagate to a ±28% error in the number of background events, accounting for common systematic errors. The systematic errors from the branching fractions for the other background modes and for the resonances are either negligible or zero.

9) The error on the number of tags. These errors are quoted in Table 4.2. They contribute a ±1.7% uncertainty on the total number of background events.

These errors are summarized in Table 7.5 in terms of the absolute error $n_{b.D\bar{D}}$. The total errors, $^{+0.19}_{-0.20}$ events, are obtained by adding the biased errors linearly and the remaining errors in quadrature. Quoting both statistical and systematic errors, the number of $D\bar{D}$ background events is:

Table 7.6 The systematic errors on the number of $D\bar{D}$ background events.

Source	Error (#events)
Charged track efficiency	–0.019
Absence of fiducial cuts	–0.019
K_S^0 vertex requirements	±0.032
shower angle cuts	±0.032
Photon detection efficiency	–0.017
Mass and V signal cuts	±0.032
Multiple counting events	+0.013
Branching Fractions	±0.180
Number of tags	±0.011
Total uncertainty	+0.19 / –0.20

$$n_{b.D\bar{D}} = 0.64 \pm 0.13^{+0.19}_{-0.20}$$

Systematic Errors on $n_{b.uds}$

To estimate the systematic errors for $n_{b.uds}$, it is assumed the dominant u, d, s event topology is similar to $D^+ \to K^-\pi^+\pi^+$, $D^- \to K^0\pi^-\pi^0(\pi^0)$, $K^0 \to \pi^+\pi^-$ in terms of the final state particle topology. With this assumption the relative systematic errors on the number of u, d, s background events follows.

1) Charged track reconstruction efficiency. For six charged tracks, a –6% error is attributed.

2) The effect of no cuts for the fiducial regions of the detector. For six charged tracks, a –6% uncertainty is attributed.

3) The K_S^0 vertex requirements. A ±5% is attributed to this effect, assuming only one K_S^0 is reconstructed.

Table 7.7 The systematic errors on the number of u, d, s background events.

Source	Error (#events)
Charged track efficiency	–0.019
Absence of fiducial cuts	–0.019
K_S^0 vertex requirements	±0.016
Shower angle cuts	±0.016
Photon detection efficiency	–0.011
Mass and V signal cuts	±0.016
Integrated Luminosity	±0.016
Total uncertainty	+0.032 / –0.059

4) Monte Carlo modelling of photons in the shower counter, and the shower angle cuts. Based on the studies for the signal efficiency, a ±5% error is given.

5) Photon detection efficiency. A –2.5% error accounts for the one shower that must be observed within the search cone. Another –1.0% is added to account conservatively for background topologies which are removed by the veto cut when at least one other shower is observed in the event. The total is therefore –3.5%

6) Invariant mass cuts, and definition of the V signal region. A ±5% is given to account for the uncertainty in the background distribution.

7) Integrated Luminosity for the $\psi(3770)$ data set. This number contains a ±5% error which directly contributes to the systematic error on the number of background events.

These errors are summarized in Table 7.5 in terms of the absolute error on the number of u, d, s background events; the total errors are $^{+0.03}_{-0.06}$. Quoting both statistical and systematic errors, the number of u, d, s background events is

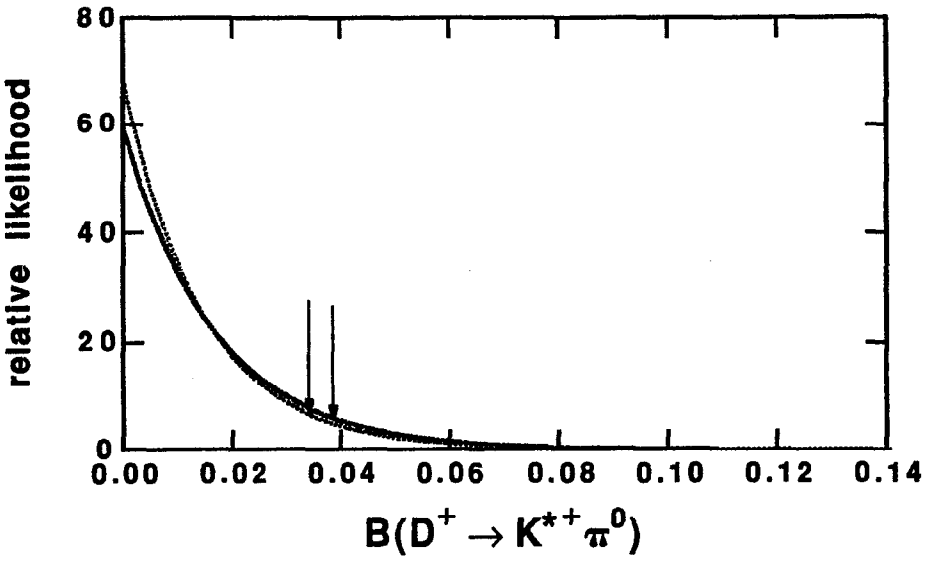

Figure 7.10 The likelihood function relative to $B(D^+ \to K^{*+}\pi^0)$.using the results of the search for $D^+ \to K^{*+}\pi^0 \to (K^0\pi^+)\pi^0$.

$$n_{b.uds} = 0.31^{+0.30+0.03}_{-0.09-0.06}$$

7-2.4 Preliminary Upper Limit for $B(D^+ \to K^{*+}\pi^0)$

An upper limit calculation can be performed for $B(D^+ \to K^{*+}\pi^0)$ (with the Clebsch-Gordon coefficient for $K^{*+} \to K^0\pi^+$ taken into account), following the maximum likelihood procedure in Section 5-6. The likelihood function for this analysis is shown in Figure 7.10, maximized for different values of $B(D^+ \to K^{*+}\pi^0)$. The dashed and solid curves show, respectively, the results without and with systematic errors propagated; the arrows indicate the 90% confidence levels. If systematic errors were neglected, $B(D^+ \to K^{*+}\pi^0) < 3.4\%$. The systematic errors increase this limit to

$$B(D^+ \to K^{*+}\pi^0) < 3.9\% \text{ @ } 90\% \text{ CL}$$

7-3 Search for $D^+ \to K^{*+}\pi^0, K^{*+} \to K^+\pi^0$

This section discusses the search for $D^+ \to K^{*+}\pi^0$ in the $K^+\pi^0$ channel of K^{*+}. Section 7-3.1 covers the initial event selection. Section 7-3.2 discusses all the known

backgrounds and the cuts that are added to remove them. Section 7-3.3 presents the results of the analysis on the data and includes analysis checks and estimates of the efficiencies and level of background. Section 7-2.4 gives a second, preliminary upper limit calculation on $B(D^+ \to K^{*+}\pi^0)$.

7-3.1 Event Selection

In the decay chain $D^+ \to K^{*+}\pi^0 \to (K^+\pi^0)\pi^0$, two π^0's are produced: a *primary* π^0 from the direct decay of the D^+ and a *secondary* π^0 from the decay of the K^{*+}. To achieve better efficiency and resolutions, this analysis avoids full reconstruction of the final state by requiring that only one of the two π^0's be reconstructed along with the kaon track. To reduce the large backgrounds, it is also required that the charged track be identified as a kaon with the "wrong-sign" strangeness and that the neutral showers have the correct multiplicities and topologies. The procedure is detailed as follows:

- require one track with the correct charge opposite a tag. The track is required to have a good helix fit, energy loss corrections and a successful beam fit. Again tags with only charged tracks are used to obtain the best resolutions.
- require three or more isolated showers.
- require particle identification for the recoil charged track. Strict particle identification is applied to reduce the high backgrounds; the track must have a good quality time-of-flight measurement with

$$|T_{\text{meas}} - T_K| \leq 1 \text{ ns } (\sim 5\sigma)$$

and

$$|T_{\text{meas}} - T_K| < |T_{\text{meas}} - T_\pi|$$

- Reconstruct a π^0 by kinematically fitting all pairs of isolated showers to the π^0 mass (a one-constraint fit). A shower pair is considered a π^0 candidate if the χ^2 confidence level is larger than 0.01. To reduce the combinatoric background in the asymmetric π^0 decays where fake showers or

incorrect photons replace the real, low energy photon, the fitted-photon energies are required to be greater than 100 MeV. Events with more than one π^0 candidate are counted once by selecting only the combination with the lowest χ^2.

- Require one shower, which is not used in the π^0 fit, to have an energy greater than 100 MeV. This requirement further reduces the backgrounds arising from low energy fake showers.

- Require one shower to have an energy greater than 300 MeV. This shower may or may not have been used in the π^0 fit. This requirement accounts for the high energy photon produced in the decay of the primary π^0.

A signal is studied with the Lorentz invariant quantity:

$$W \equiv \sum_{\mu}[P^{\mu}_{\text{recoil}}(P_{\text{K}} + P_{\pi})_{\mu} - P^{\mu}_{\text{K}} P_{\pi\mu}]$$

$$= \sum_{\mu}[(P_{\text{event}} - P_{\text{tag}})^{\mu}(P_{\text{K}} + P_{\pi})_{\mu} - P^{\mu}_{\text{K}} P_{\pi\mu}]$$

where P^{μ}_{recoil}, P^{μ}_{K}, P^{μ}_{π}, P^{μ}_{event}, and P^{μ}_{tag} are the four momentum of the recoil, the charged kaon, the reconstructed π^0, the full event and the tag, respectively. This quantity makes no assumption on whether the reconstructed π^0 is the primary or secondary π^0. If all tracks were precisely measured, W would equal 1.8690 $(\text{GeV}/c^2)^2$. To achieve the best resolution for W, E_{tag} is replace by $\sqrt{s}/2$, and the fitted photon energies and momenta are used for P^{μ}_{π}.

Figure 7.11 shows the expected W distribution for $D^+ \to K^{*+}\pi^0 \to (K^+\pi^0)\pi^0$. The non-Gaussian distribution arises from the difference in energy resolutions of showers from low and high momentum π^0's. The signal region is defined by

- $1.75 < W < 1.99\ (\text{GeV}/c^2)^2$

which contains 95% of the Monte Carlo signal.

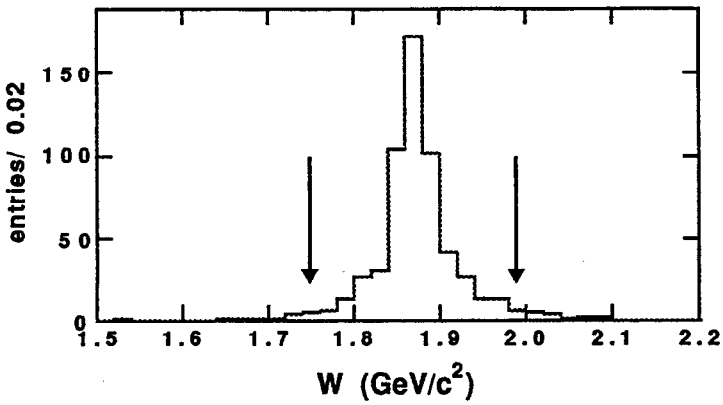

Figure 7.11 The W distribution for the desired process $D^+ \rightarrow K^{*+}\pi^0 \rightarrow (K^+\pi^0)\pi^0$. Arrows indicate the limits of the signal region.

Figure 7.16(a) shows the W distribution for the actual data. Eight candidate events are observed in the signal region.

7-3.2 Major Backgrounds to $D^+ \rightarrow K^{*+}\pi^0, K^{*+} \rightarrow K^+\pi^0$

Several sources of background to $D^+ \rightarrow K^{*+}\pi^0 \rightarrow (K^+\pi^0)\pi^0$ were determined by applying the event selection procedure to the D^+D^- and $D^0\overline{D}^0$ Monte Carlo cocktails. Major contributions come from both the Class I and Class II backgrounds. Again at least two errors are involved in misidentifying a background process as the desired signal.

This section is broken down into three parts: Section 7-3.2.1 describes the Class I backgrounds, Section 7-3.2.2 discusses the Class II backgrounds, and Section 7-3.2.3 discusses the cut introduced remove both Classes of backgrounds.

7-3.2.1 The Class I Backgrounds

The Class I backgrounds arise from the following modes:

- $D^+ \rightarrow \overline{K}^0\pi^+$, $\overline{K}^0 \rightarrow K^0_S \rightarrow \pi^0\pi^0$. The charged pion is misidentified and the K^0_S is not recognized.
- $D^+ \rightarrow \overline{K}^0K^+$, $\overline{K}^0 \rightarrow K^0_S \rightarrow \pi^0\pi^0$. The decay starts out Cabibbo suppressed and the K^0_S is not recognized.

- $D^+ \to \bar{K}^0\pi^+\pi^0$, $\bar{K}^0 \to K_S^0 \to \pi^0\pi^0$. The charged pion is misidentified and the K_S^0 and extra π^0 are not recognized.

- $D^+ \to \bar{K}^0 e^+\nu_e$ and $\bar{K}^0\mu^+\nu_\mu$, $\bar{K}^0 \to K_S^0 \to \pi^0\pi^0$. The lepton is misidentified, the neutrino is not observed and the K_S^0 is not recognized.

The third channel has been studied in the resonant modes $D^+ \to \bar{K}^0\rho^+$, $\rho^+ \to \pi^+\pi^0$ and $D^+ \to \bar{K}^{*0}\pi^+$, $\bar{K}^{*0} \to \bar{K}^0\pi^0$ and the nonresonant $D^+ \to \bar{K}^0\pi^+\pi^0$. As shown in Figure 7.12, all backgrounds are observed to peak in the signal region.

7-3.2.2 The Class II Backgrounds

In this analysis the Class II backgrounds are found to arise from $D^0\bar{D}^0$ events, with one of the two neutral D's decaying either through $D^0 \to K^-\pi^+\pi^0$ or $D^0 \to K^-\pi^+\pi^0\pi^0$. The backgrounds are listed below under the tag-versus-recoil topology to which they contribute.

1) $D^+ \to K^+\pi^0\pi^0$ vs. $D^- \to K^+\pi^-\pi^-$:

   - $D^0 \to K^-\pi^+\pi^0$ vs. $\bar{D}^0 \to K^+\pi^-\pi^0$. The tag is formed by a double misidentification between a charged kaon and a charged pion and by a misassociation of the charged tracks. All neutral tracks are misassociated with the recoil (the charged kaon in the recoil is correctly identified).
   - $D^0 \to K^-\pi^+\pi^0\pi^0$ vs. $\bar{D}^0 \to K^+\pi^-\pi^0$. The same errors occur as in the previous background along with the additional error of not recognizing the extra π^0.

2) $D^+ \to K^+\pi^0\pi^0$ vs. $D^- \to K^0\pi^-\pi^+\pi^-$:

   - $D^0 \to K^-\pi^+\pi^0$ vs. $\bar{D}^0 \to K^0\pi^-\pi^+\pi^0$, when $K^0 \to K_S^0 \to \pi^+\pi^-$. No charged track misidentification occurs, but the K^0 is misidentified as a $\bar{K}^0$. Charged and neutral tracks are again misassociated to form the tag and recoil.
   - $D^0 \to K^-\pi^+\pi^0\pi^0$ vs. $\bar{D}^0 \to K^0\pi^-\pi^+\pi^0$. The same errors occur as for the previous background with the additional error of not recognizing the extra π^0.

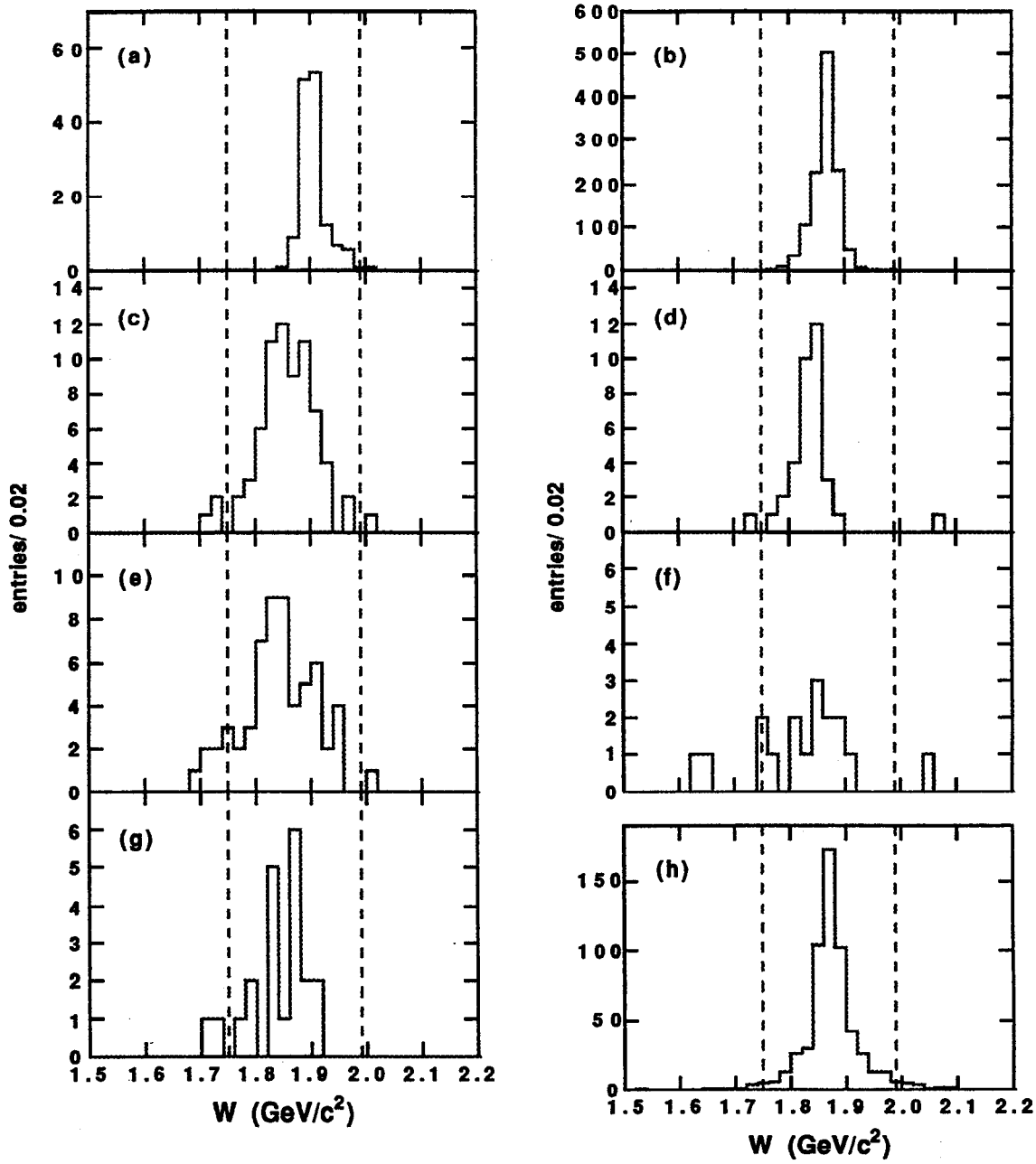

Figure 7.12 The W distributions for the Class I backgrounds (a) $D^+ \to \bar{K}^0\pi^+$; (b) $D^+ \to \bar{K}^0K^+$; (c) $D^+ \to \bar{K}^0\rho^+$, $\rho^+ \to \pi^+\pi^0$; (d) $D^+ \to \bar{K}^{*0}\pi^+$, $\bar{K}^{*0} \to \bar{K}^0\pi^0$; (e) $D^+ \to \bar{K}^0\pi^+\pi^0$[nr]; (f) $D^+ \to \bar{K}^0e^+\nu_e$; (g) $D^+ \to \bar{K}^0\mu^+\nu_\mu$; and for the signal (h) $D^+ \to K^{*+}\pi^0$, $K^{*+} \to K^+\pi^0$. For all backgrounds the neutral kaon decays through the chain $\bar{K}^0 \to K_S^0 \to \pi^0\pi^0$.

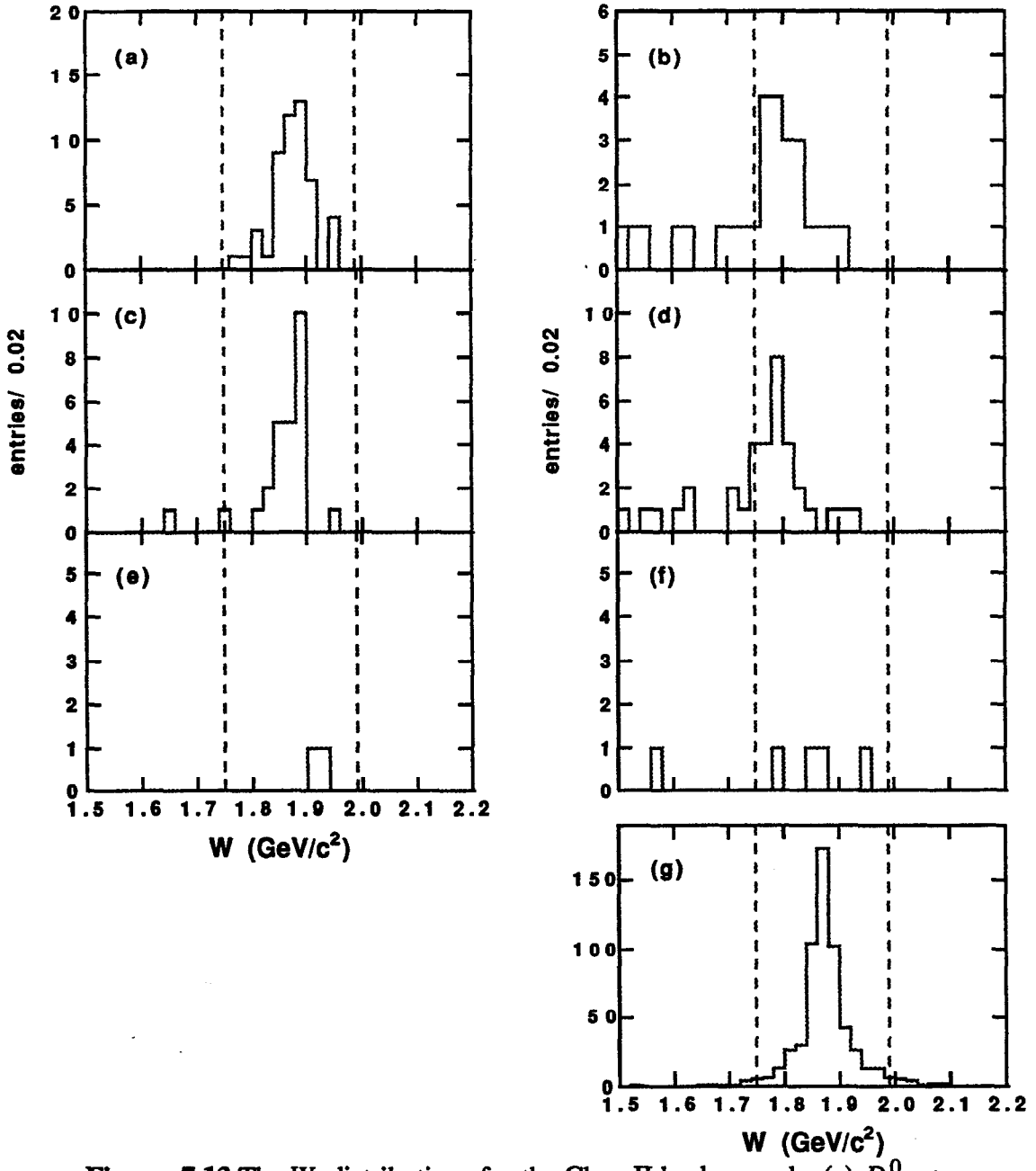

Figure 7.13 The W distributions for the Class II backgrounds: (a) $D^0 \to K^-\pi^+\pi^0$ vs. $\overline{D}^0 \to K^+\pi^-\pi^0$ when reconstructed as $D^+ \to K^+\pi^0\pi^0$ vs. $D^- \to K^+\pi^-\pi^-$; (b) $D^0 \to K^-\pi^+\pi^0\pi^0$ vs. $\overline{D}^0 \to K^+\pi^-\pi^0$ when reconstructed as $D^+ \to K^+\pi^0\pi^0$ vs. $D^- \to K^+\pi^-\pi^-$; (c) $D^0 \to K^-\pi^+\pi^0$ vs. $\overline{D}^0 \to K^0\pi^-\pi^+\pi^0$ when reconstructed as $D^+ \to K^+\pi^0\pi^0$ vs. $D^- \to K^0\pi^-\pi^+\pi^-$; (d) $D^0 \to K^-\pi^+\pi^0\pi^0$ vs. $\overline{D}^0 \to K^0\pi^-\pi^+\pi^0$; when reconstructed as $D^+ \to K^+\pi^0\pi^0$ vs. $D^- \to K^0\pi^-\pi^+\pi^-$; (e) $D^0 \to K^-\pi^+\pi^0$ vs. $\overline{D}^0 \to K^+\pi^-\pi^0$ when reconstructed as $D^+ \to K^+\pi^0\pi^0$ vs. $D^- \to K^+K^-\pi^-$; (f) $D^0 \to K^-\pi^+\pi^0\pi^0$ vs. $\overline{D}^0 \to K^+\pi^-\pi^0$ when reconstructed as $D^+ \to K^+\pi^0\pi^0$ vs. $D^- \to K^+K^-\pi^-$. The distribution for the desired signal is shown in (g).

3) $D^+ \to K^+\pi^0\pi^0$ vs. $D^- \to K^+K^-\pi^-$ (backgrounds same as those for $D^+ \to K^+\pi^0\pi^0$ vs. $D^- \to K^+\pi^-\pi^-$):

- $D^0 \to K^-\pi^+\pi^0$ vs. $\bar{D}^0 \to K^+\pi^-\pi^0$. A charged pion is misidentified in the tag, while charged and neutral tracks are misassociated to from the tag and recoil.
- $D^0 \to K^-\pi^+\pi^0\pi^0$ vs. $\bar{D}^0 \to K^+\pi^-\pi^0$. The same errors occur as in the previous background along with the additional error of not recognizing the extra π^0.

No significant backgrounds are observed for the signal opposite the $\bar{K}^0\pi^+$ and $\bar{K}^0K^+$ tags.

The W distributions for each of the Class II backgrounds are shown in Figure 7.12. Again all backgrounds are observed to peek in the signal region. Background topologies with $D^0 \to K^-\pi^+\pi^0$ have been studied with the decay proceeding through the resonant channel $D^0 \to K^-\rho^+ \to K^-(\pi^+\pi^0)$, which dominates the $K^-\pi^+\pi^0$ mode. All the other D^0 modes were decayed with the momenta distributed uniformly over the allowed phase space.

7-3.2.3 The Background Cut

The backgrounds are reduced through a Dalitz analysis of the $K^+\pi^0\pi^0$ final state. A plot of $M^2_{\pi\pi}$ versus $M^2_{K\pi}$ is formed, where $M_{\pi\pi}$ is the $\pi^0\pi^0$ invariant mass and $M_{K\pi}$ is the $K^+\pi^0$ invariant mass. To obtain $M^2_{K\pi}$, the charged kaon momenta and the fitted photon momenta are used, while to obtain $M^2_{\pi\pi}$ conservation of four momenta is employed:

$$M^2_{\pi\pi} = (P_{\pi_1} + P_{\pi_2})^2$$
$$= (P_{\text{recoil}} - P_K)^2$$
$$= (P_{\text{event}} - P_{\text{tag}} - P_K)^2$$

This relation yields a value for $M^2_{\pi\pi}$ which does not depend upon poor shower counter energy measurements. The expected distributions for the backgrounds and the signal are compared in Figure 7.14 and Figure 7.15. The distribution for the signal, $D^+ \to K^{*+}\pi^0 \to$

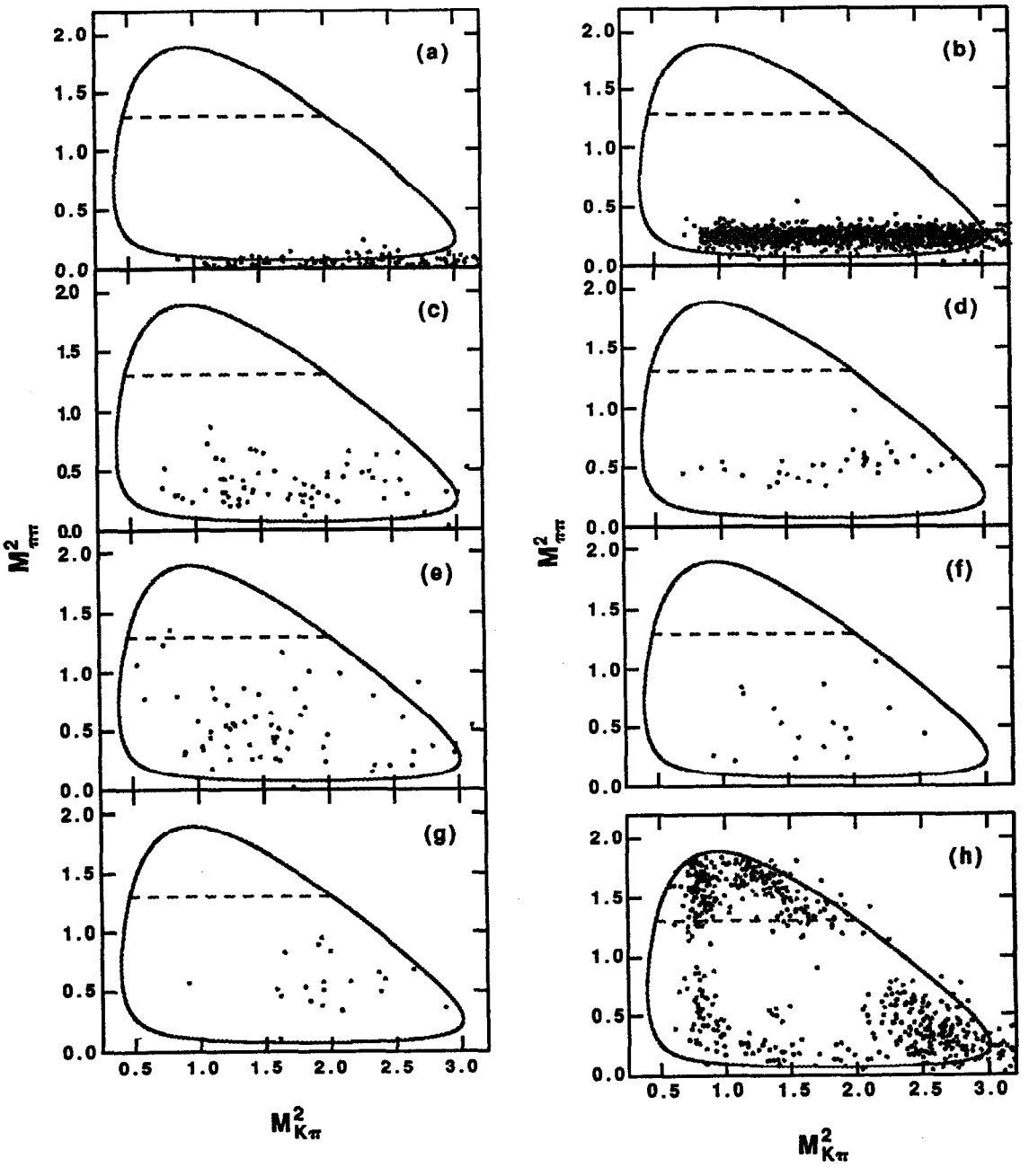

Figure 7.14 Dalitz plots of the Class I backgrounds (a) $D^+ \to \bar{K}^0\pi^+$, (b) $D^+ \to \bar{K}^0K^+$, (c) $D^+ \to \bar{K}^0\rho^+$, $\rho^+ \to \pi^+\pi^0$, (d) $D^+ \to \bar{K}^{*0}\pi^+$, $\bar{K}^{*0} \to \bar{K}^0\pi^0$, (e) $D^+ \to \bar{K}^0\pi^+\pi^0$[nr], (f) $D^+ \to \bar{K}^0e^+\nu_e$, (g) $D^+ \to \bar{K}^0\mu^+\nu_\mu$, and the signal (h) $D^+ \to K^{*+}\pi^0 \to (K^+\pi^0)\pi^0$. All neutral kaons decay through the chain $\bar{K}^0 \to K^0_S \to \pi^0\pi^0$.

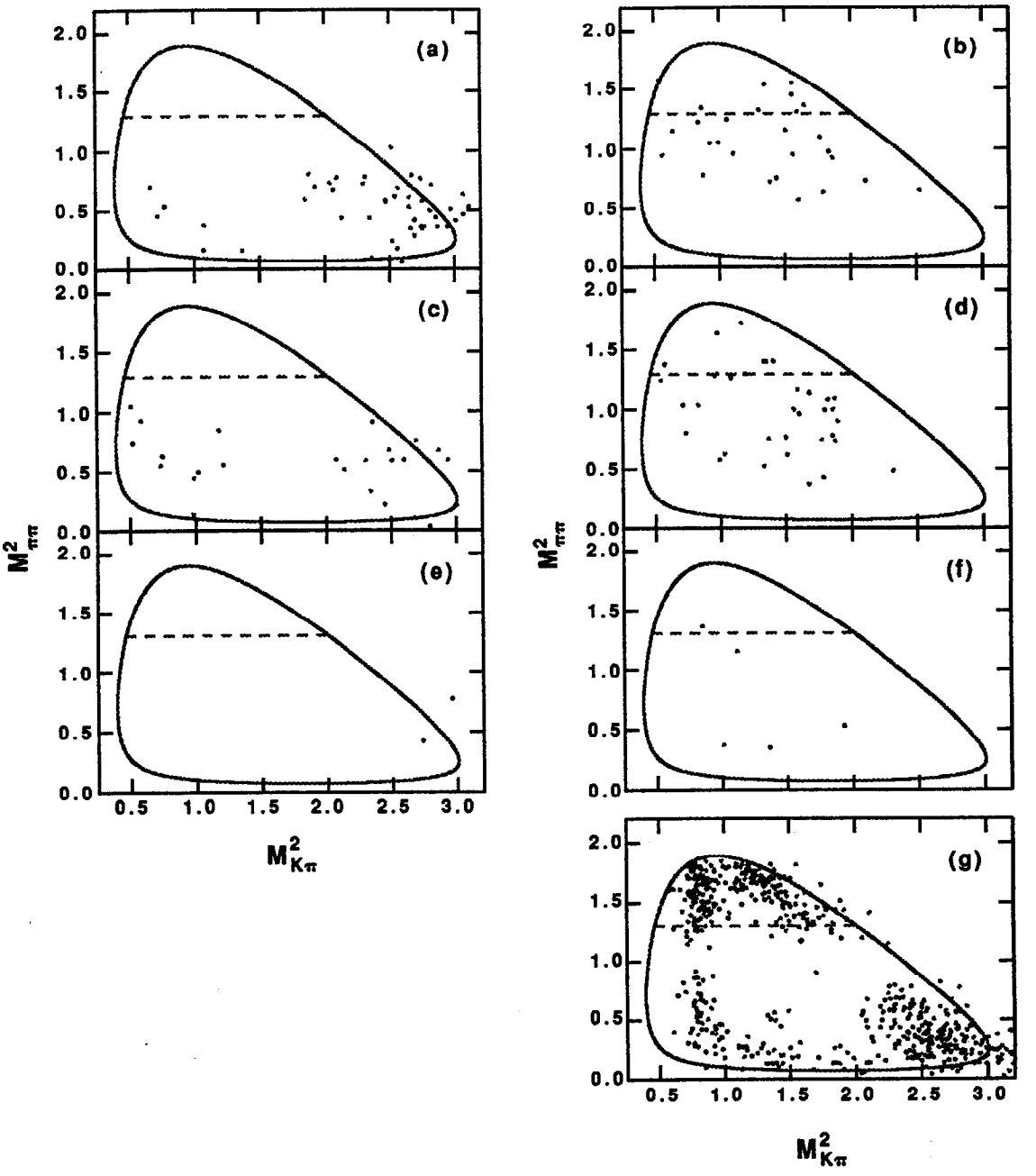

Figure 7.15 Dalitz plots for the Class II backgrounds. The labels correspond to those in Figure 7.12

$(K^+\pi^U)\pi^U$, reflects the properties of a $P \to VP_1 \to (P_2\, P_3)\, P_1$ decay, where P denotes a pseudoscalar meson and V denotes a vector meson. The two pairs of lobes correspond to the two cases where the primary and secondary π^0 have been reconstructed.

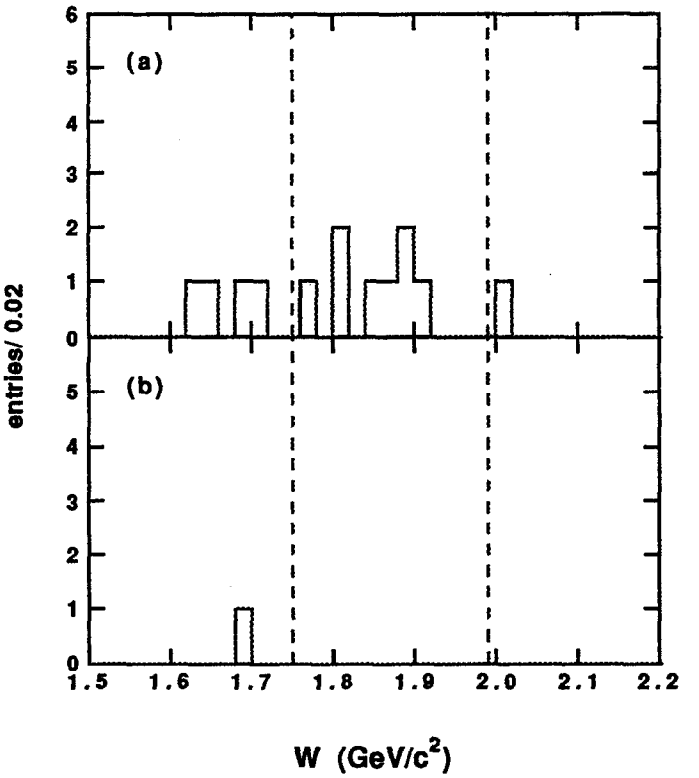

Figure 7.16 Data after: (a) the initial event selection and (b) the Dalitz cut.

All backgrounds overlap with the signal in the low $M^2_{\pi\pi}$ region, motivating the following cut:

- $M^2_{\pi\pi} > 1.3$ (GeV/c^2)^2

This cut removes 63% of the signal but also effectively all Class I backgrounds and the Class II backgrounds with $D^0 \to K^-\pi^+\pi^0$. Approximately 80% of the background topologies with $D^0 \to K^-\pi^+\pi^0\pi^0$ are also removed.

7-3.3 Results

Figure 7.16 shows the application of the cuts to the data. After all cuts are applied no events remain in the signal region. For reference, Figure 7.17 gives the Dalitz plot of the events which passed the initial event selection. One event is observed at $W = 1.695$

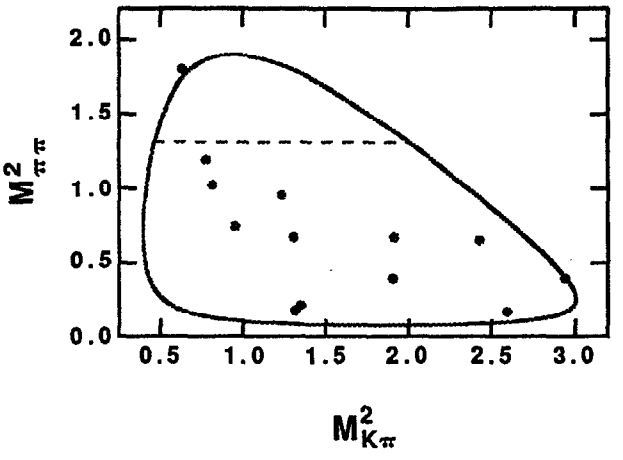

Figure 7.17 Dalitz plot of the candidate events for $D^+ \to K^{*+}\pi^0 \to (K^+\pi^0)\pi^0$.

$(GeV/c^2)^2$, below the signal region where $0.18^{+0.24}_{-0.05}$ events are expected from the known backgrounds; Figure 7.18 displays the event.

7-3.3.1 Analysis Test

The number of events that are expected to be moved from the signal region by the Dalitz cut is calculated and compared to the number that is removed. Table 7.1 lists the background branching fractions used to estimate the numbers of events from the Class I and Class II backgrounds. The contribution from continuum *u*, *d*, *s* production is determined from the an analysis of Lund Monte Carlo data (Figure 7.19). The calculations yield an estimated 2.0±0.4 events from the Class I backgrounds, 4.7±0.9 events from the Class II backgrounds, and $0.7^{+0.4}_{-0.2}$ events from the continuum, summing to a total of $7.4^{+0.4}_{-0.2}$ events. This number is in good agreement with the observed loss of eight events.

7-3.3.2 Detection Efficiencies

The detection efficiencies for $D^+ \to K^{*+}\pi^0 \to (K^+\pi^0)\pi^0$ are determined as before. Table 7.3 gives the efficiency opposite each tag mode. The weighted efficiency is $\bar{\varepsilon}_s$ = 8.2±0.5%.

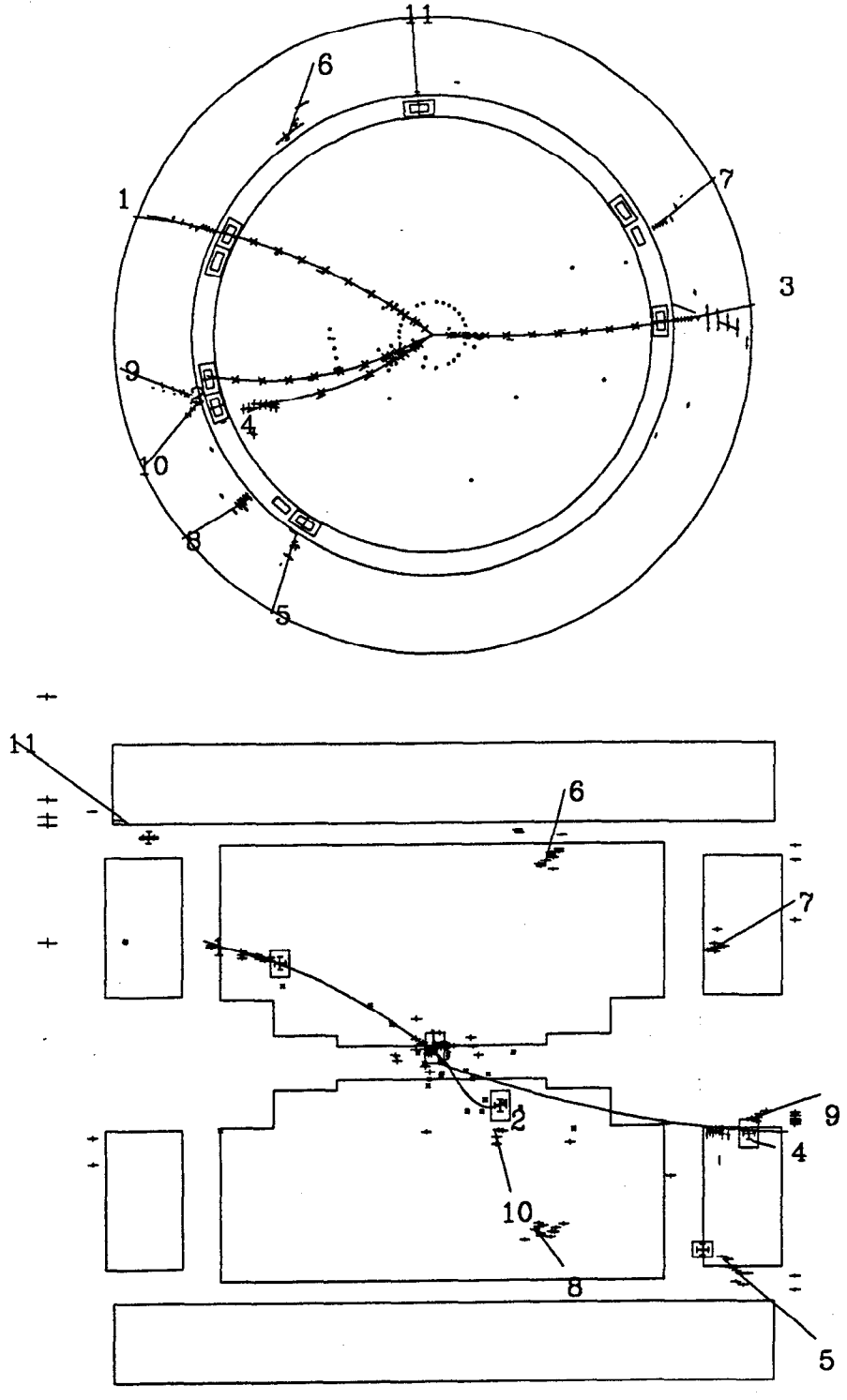

Figure 7.18 The event at $W = 1.695$ (GeV/c^2)^2.

Table 7.8 Branching fractions of the Class I and Class II backgrounds to $D^+ \to K^{*+}\pi^0 \to (K^+\pi^0)\pi^0$

Mode	Branching Fraction (%)	Reference
$D^+ \to \bar{K}^0\pi^+$	3.2±0.5±0.2	24
$\bar{K}^0K^+$	1.01±0.32±0.17	24, 20
$\bar{K}^0\rho^+$	6.9±0.8±2.3	22
$\bar{K}^{*0}\pi^+$	5.9±1.9±2.5	22
$\bar{K}^0\pi^+\pi^0$[nr]	1.3±0.7±0.9	22
$\bar{K}^0e^+\nu_e$	$6.0^{+2.2}_{-1.3}$±0.7	25
$\bar{K}^0\mu^+\nu_\mu$	$7.0^{+2.8}_{-1.6}$±1.2	25
$D^0 \to K^-\pi^+\pi^0$	13.3±1.2±1.3	24
$K^-\pi^+\pi^0\pi^0$	14.9±3.7±3.0	24
$\bar{K}^0\pi^+\pi^-\pi^0$	10.3±2.2±2.5	23

7-3.3.3 Background Estimates

After the cut on $M^2_{\pi\pi}$ no Class I backgrounds are still considered significant. Of the Class II backgrounds, only those processes with $D^0 \to K^-\pi^+\pi^0\pi^0$ are still found to make a non-negligible contribution to the signal. To simplify the discussions here and in the section on systematic errors, these backgrounds are labelled as follows:

- Background I--$K^-\pi^+\pi^0\pi^0$ vs. $K^+\pi^-\pi^0$ when reconstructed as $K^+\pi^0\pi^0$ vs. $K^+\pi^-\pi^-$
- Background II--$K^-\pi^+\pi^0\pi^0$ vs. $K^0\pi^-\pi^+\pi^0$ when reconstructed as $K^+\pi^0\pi^0$ vs. $K^0\pi^-\pi^+\pi^-$
- Background III--$K^-\pi^+\pi^0\pi^0$ vs. $K^+\pi^-\pi^0$ when reconstructed as $K^+\pi^0\pi^0$ vs. $K^+K^-\pi^-$

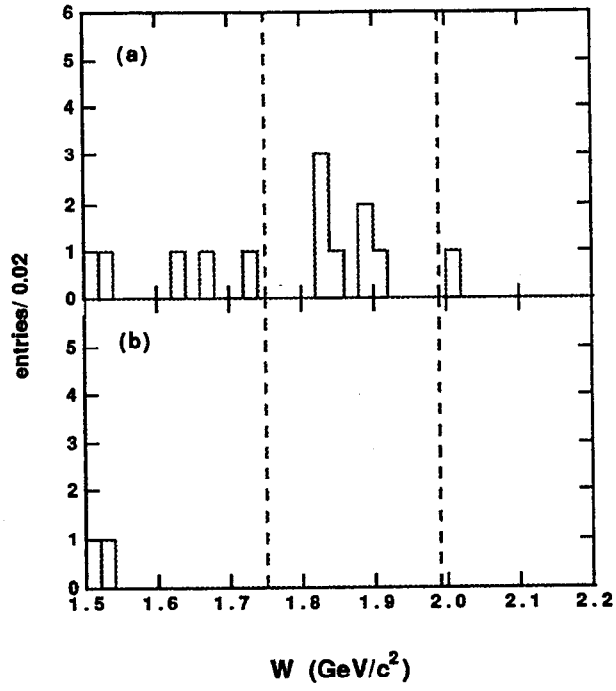

Figure 7.19 Analysis of Lund Monte Carlo data: (a) after the initial event selection and (b) after the cut on $M^2_{\pi\pi}$.

Table 7.9 Efficiencies for $D^+ \to K^{*+}\pi^0 \to (K^0\pi^+)\pi^0$ opposite each tag.

Tag Mode	efficiency (%)
$\bar{K}^0\pi^+$	7.6 ± 0.6
$K^-\pi^+\pi^+$	8.5 ± 0.6
$\bar{K}^0\pi^+\pi^-\pi^+$	6.7 ± 0.7
$\bar{K}^0K^+$	8.6 ± 0.7
$K^-K^+\pi^+$	7.6 ± 0.7
Weighted Efficiency: $8.2 \pm 0.5\%$	

Table 7.10 lists the three backgrounds with the acceptances and number of events expected in the signal, with statistical errors only. The total number of background events expected from $D\bar{D}$ production is $n_{b.D\bar{D}} = 0.21 \pm 0.07$.

Table 7.10 The expected numbers for the backgrounds to $D^+ \to K^{*+}\pi^0 \to (K^+\pi^0)\pi^0$, including the contribution from the continuum. Backgrounds I, II and III are labelled in the text.

$D\bar{D}$ Background	Acceptance (%)	Number of Events
I	0.013 ± 0.003	0.14 ± 0.05
II	0.015 ± 0.005	0.04 ± 0.02
III	0.003 ± 0.002	0.03 ± 0.02
Total Expected $D\bar{D}$ Contribution		0.21 ± 0.07
Expected Continuum Contribution		< 0.23
Total Expected Background		0.3 ± 0.1

The number of events expected from u, d, s production is determined to be $n_{b.uds} < 0.23$ at 90% confidence level. This number is included in Table 7.10.

The total number of background events is $n_b = 0.3 \pm 0.1$, where the 63.8% confidence level upper limit for $n_{b.uds}$--0.1 events--has been used. Assuming Poisson statistics, the probability for 0.3 events to fluctuate to no events is 0.74.

7-3.3.4 Systematic Errors

Systematic errors are estimated for the detection efficiency of the signal, the number of $D\bar{D}$ background events, and the number of u, d, s background events. Sources of error and their level of contribution are described below. Several of these effects have been discussed in the previous analyses.

Systematic Errors on $\bar{\varepsilon}_s$

The following sources are considered to contribute to the systematic error on the reconstruction efficiency. The errors are given in terms of the relative uncertainty.

1) Charged track reconstruction efficiency. A −1% error is attributed for detecting one charged track.

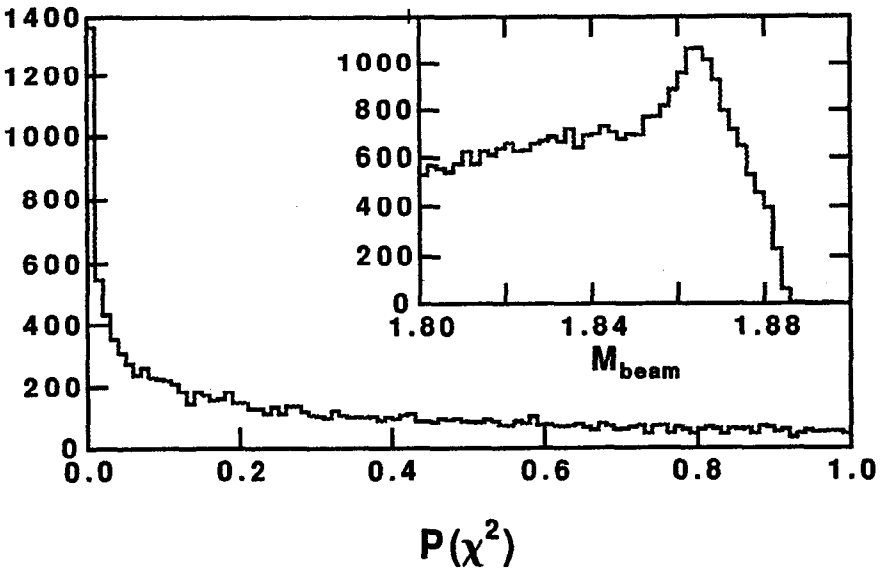

Figure 7.20 The $D^0 \to K^-\pi^+\pi^0$ sample used to estimate the systematic uncertainty of the χ^2 cut for the π^0 fit.

2) The effect of no cuts for the fiducial regions of the detector. For one charged track, a −1% uncertainty is attributed.

3) Monte Carlo modelling of photons in the shower counter. A comparison of analysis results using different shower simulators (confer Section 6-5.3) finds discrepancies of no more than 10%. Therefore, a ±5% uncertainty is attributed to this effect.

4) Photon detection efficiency. The uncertainty of −2.5% per photon leads to a −7.5% uncertainty in requiring three photons to be observed.

5) The χ^2 requirement for the kinematic fit to the π^0 mass. The uncertainty due to this requirement is estimated by analyzing $D^0 \to K^-\pi^+\pi^0$ candidates from real and simulated data. In both samples, π^0 candidates were obtained by kinematically fitting all pairs of isolated showers. The π^0 candidates were subsequently combined with pairs of oppositely charged tracks to form $K^-\pi^+\pi^0$ candidates. The beam constrained mass distribution of the $K^-\pi^+\pi^0$ candidates and the χ^2 distribution of the π^0 fits are shown in Figure 7.20. After the χ^2 cut the

Table 7.11 The systematic errors on the detection efficiency for $D^+ \to K^{*+}\pi^0 \to (K^+\pi^0)\pi^0$.

Source	Systematic Error (%)
Charged track efficiency	–0.082
Absence of fiducial cuts	–0.082
Shower modelling	±0.410
Photon detection efficiency	–0.615
χ^2 requirement for π^0 fit	–0.205
Kaon identification	–0.492
Mass and signal region cuts	±0.082
Total Error	+0.4 / –1.5

efficiency in the Monte Carlo was found to be 5% greater than that in the real data. Therefore a –2.5% error is attributed to this effect.

6) Kaon identification. The effects of the particle identification cuts on charged kaons in Monte Carlo data and real data were compared using $K^-\pi^+\pi^+$ data samples (see Section 5-5.7). Since the kinematic topology of the charged kaon in $K^+\pi^0\pi^0$ is constrained by the $M^2_{\pi\pi}$ requirement, this kaon identification study included a requirement that the invariant mass squared of the $\pi^+\pi^+$ system be greater than 1.3 $(GeV^2)^2$. The study found the Monte Carlo to be to more efficient by 12%, and therefore a –6% error is given for this effect.

7) Invariant mass cuts, and definition of the W signal region. A ±1% error is given to account for the uncertainty in the $M^2_{\pi\pi}$ requirement and possible tails in the signal distribution.

In Table 7.5, these errors are summarized in terms of the absolute error on the reconstruction efficiency. The total errors, $^{+0.4}_{-2.2}$%, is obtained by adding the biased errors linearly and the remaining errors in quadrature. Quoting both statistical and systematic errors, the weighted efficiency for the signal is

$$\bar{\varepsilon}_s = 8.2 \pm 0.5^{+0.4}_{-2.2}\%$$

Systematic Errors on $n_{b\text{-}D\bar{D}}$

Several effects which contribute to the systematic uncertainty of the signal efficiency also introduce uncertainties to the number of $D\bar{D}$ (Class II) background events. Discussion of these effects on the backgrounds follows, with the errors given in terms of the relative uncertainty.

1) Charged track reconstruction efficiency. A relative uncertainty of –4% is attributed to the uncertainty in the number of events from Backgrounds I and III, and –6% is attributed to the uncertainty in the number of events from Background II. This results in a total error of –4.4%.

2) No cuts for the fiducial regions of the detector. Errors of –4% in the number of Background I and III events and –6% in the number of Background II events propagate to a total error of –4.4%.

3) Monte Carlo modelling of photons in the shower counter. A ±5% error is given to account for the uncertainty due to this effect.

4) Photon detection efficiency. A –7.5% error is attributed for requiring three photons to be observed.

5) The χ^2 requirement for the kinematic fit to the π^0 mass. Since the backgrounds also contain a reconstructed π^0, a –2.5% error is given to account for this effect.

6) Particle identification. In the number of Background I events, the kaon identification criteria for the recoil and the double misidentification in the tag contribute an error of $^{+9}_{-18}$%. In the number of Background II events, the kaon identification for the recoil and the pion identification for the tag contribute an error of $^{+2}_{-6}$%. In the number of Background III events, the kaon identification for the recoil and the single misidentification in the tag contribute an error of $^{+9}_{-6}$%. Treating these errors linearly, the relative systematic error for the total number of background events is $^{+6}_{-12}$%.

7) Invariant mass cuts, and definition of the W signal region. A $\pm 5\%$ error is given to account for the uncertainty arising from possible tales in the mass and W distributions.

The following additional sources have been considered in the systematic error on $n_{b\_D\overline{D}}$.

8) Branching fractions for $D^0 \to K^-\pi^+\pi^0\pi^0$, $K^-\pi^+\pi^0$ and $\overline{K}^0\pi^+\pi^-\pi^0$. The relative systematic errors of these branching fractions (20%, 10%, and 24%, respectively) propagate to a $\pm 22\%$ error in the number of background events.

9) Number of produced $D^0\overline{D}^0$ events. The systematic uncertainty on this number (± 2600 events out of 27,700) gives a $\pm 9\%$ error.

Table 7.12 The systematic errors on the number of $D\bar{D}$ background events.

Source	Error (#events)
Charged track efficiency	–0.009
Absence of fiducial cuts	–0.009
Shower modelling	±0.011
Photon detection efficiency	–0.016
χ^2 requirement for π^0 fit	–0.005
Particle identification	+0.013 / –0.025
Mass and signal region cuts	±0.011
Branching fractions	±0.046
Number of $D^0\bar{D}^0$ events	±0.019
Total uncertainty	+0.05 / –0.08

These errors are summarized in Table 7.5 in terms of the absolute error on $n_{b.D\bar{D}}$. The total errors, $^{+0.05}_{-0.08}$ events. Quoting both statistical and systematic errors, the number of $D\bar{D}$ background events is:

$$n_{b.D\bar{D}} = 0.21 \pm 0.07^{+0.05}_{-0.08}$$

Systematic Errors on $n_{b.uds}$

To estimate the systematic errors for $n_{b.uds}$, it is assumed the dominant u, d, s event topology is similar to Background I--$D^0 \to K^-\pi^+\pi^0\pi^0$, $\bar{D}^0 \to K^+\pi^-\pi^0$--in terms of the final state topology. With this assumption the relative systematic errors on the number of u, d, s background events follows.

1) Charged track reconstruction efficiency. A relative uncertainty of –4% is attributed for four charged tracks.

2) No cuts for the fiducial regions of the detector. A –4% error is given for four charged tracks.

3) Monte Carlo modelling of photons in the shower counter. A ±5% error is given to account for the uncertainty due to this effect.

4) Photon detection efficiency. A –7.5% error is attributed for requiring three photons to be observed.

5) The χ^2 requirement for the kinematic fit to the π^0 mass. A –2.5% error is given to account for the requirement that a π^0 be reconstructed.

6) Particle identification. Assuming the same misidentification mechanisms occur as for Background I, a $^{+9}_{-18}$% uncertainty is given for particle identification.

7) Invariant mass cuts, and definition of the W signal region. A ±5% error is given to account for possible tales in the mass and W distributions.

8) Integrated Luminosity for the $\psi(3770)$ data set. This number contains a ±5% error which directly contributes to the systematic error on the number of background events.

These errors are summarized in Table 7.5 in terms of the absolute error on the (upper limit) number of u, d, s background events; the total errors are $^{+0.03}_{-0.08}$. The limit on the number of u, d, s background events is enlarged by adding the positive error, becoming:

$$n_{b.uds} < 0.26$$

7-3.4 Preliminary Upper Limit for $B(D^+ \to K^{*+}\pi^0)$

A second upper limit calculation is performed for $B(D^+ \to K^{*+}\pi^0)$ using the results of the search for $K^+\pi^0\pi^0$. The likelihood function is shown in Figure 7.10, maximized for different values of $B(D^+ \to K^{*+}\pi^0)$. If systematic errors were neglected, $B(D^+ \to K^{*+}\pi^0) < 4.0\%$. The systematic errors increase this limit to

$$B(D^+ \to K^{*+}\pi^0) < 5.6\% \text{ @ } 90\% \text{ CL}$$

Table 7.13 The systematic errors on the number of u, d, s background events.

Source	Error (#events)
Charged track efficiency	–0.009
Absence of fiducial cuts	–0.009
Shower modelling	±0.012
Photon detection efficiency	–0.017
χ^2 requirement for π^0 fit	–0.006
Particle identification	+0.021 / –0.041
Integrated Luminosity	±0.012
Total uncertainty	+0.027 / –0.084

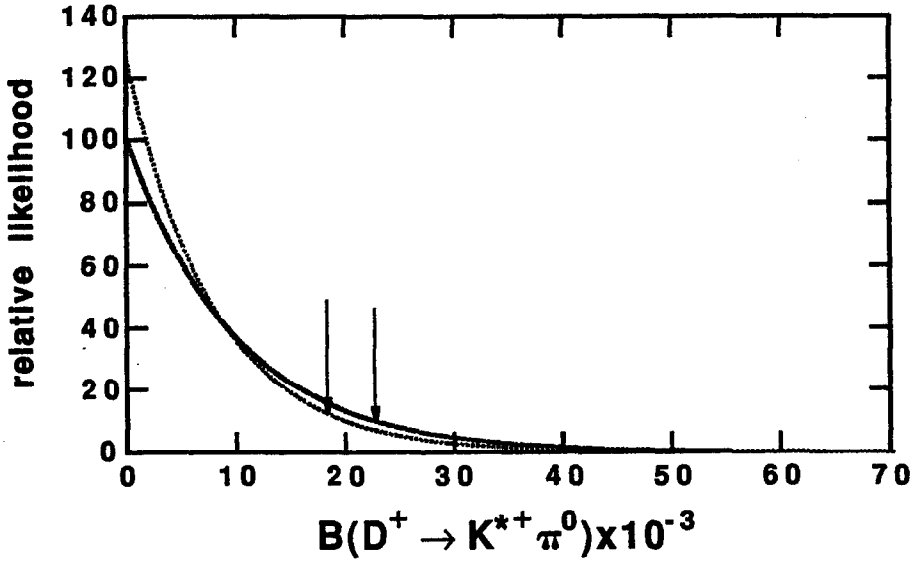

Figure 7.21 The likelihood function relative to $B(D^+ \to K^{*+}\pi^0)$, using the results of the search for $D^+ \to K^{*+}\pi^0 \to (K^+\pi^0)\pi^0$.

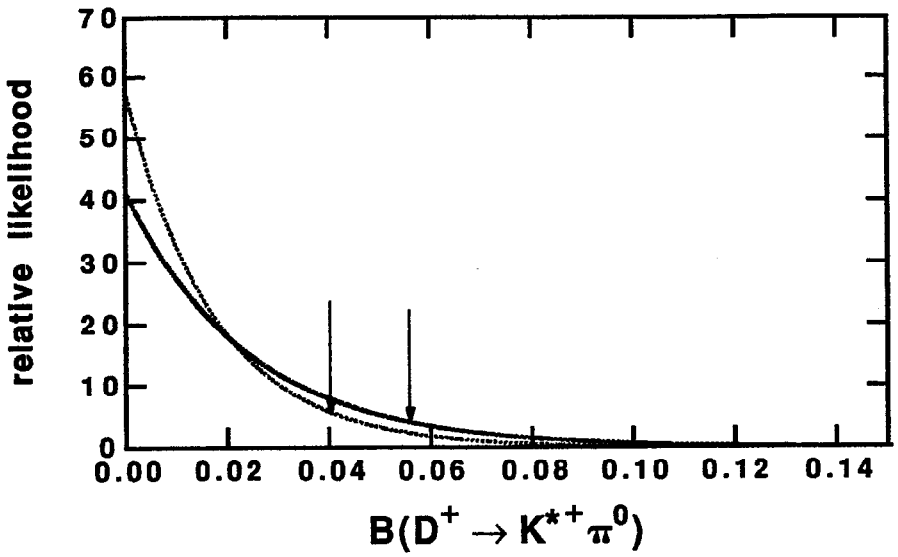

Figure 7.22 The likelihood function relative to $B(D^+ \to K^{*+}\pi^0)$ with the results of the searches for $D^+ \to K^{*+}\pi^0 \to (K^0\pi^+)\pi^0$ and $D^+ \to K^{*+}\pi^0 \to (K^+\pi^0)\pi^0$ combined.

7-4 Upper Limit for $B(D^+ \to K^{*+}\pi^0)$

The limits for $B(D^+ \to K^{*+}\pi^0)$ are improved when the results of the searches for $D^+ \to K^{*+}\pi^0 \to (K^0\pi^+)\pi^0$ and $D^+ \to K^{*+}\pi^0 \to (K^+\pi^0)\pi^0$ are combined. The calculation is performed with the joint likelihood function:

$$\mathcal{L}_{K^{*+}\pi^0} = \mathcal{L}(n_{K^0\pi^+\pi^0}, p_{K^0\pi^+\pi^0}; \hat{p}_{K^0\pi^+\pi^0})\, \mathcal{L}(n_{K^+\pi^0\pi^0}, p_{K^+\pi^0\pi^0}; \hat{p}_{K^+\pi^0\pi^0})$$

where $\mathcal{L}(n_i, p_i; \hat{p}_i)$ are the likelihood functions used to obtain the preliminary limits in Section 7-2.4 and Section 7-2.4. The likelihood function is shown graphically in Figure 7.22, maximized as a function of $B(D^+ \to K^{*+}\pi^0)$. The dashed and solid curves respectively show the results without and with systematic errors propagated, and the arrows indicate the 90% confidence levels. If the systematic errors were negligible, $B(D^+ \to K^{*+}\pi^0) <$ 1.8% With systematic errors this limit increases to

$$B(D^+ \to K^{*+}\pi^0) < 2.3\% \text{ @ } 90\% \text{ CL}$$

The separate analysis (Appendix 2), where fully reconstructed doubly Cabibbo suppressed events are kinematically fitted rather than tagged, yields $B(D^+ \to K^{*+}\pi^0) < 11.6\%$ at 90% confidence level. That analysis however, only searched for $D^+ \to K^{*+}\pi^0$ through $K^{*+} \to K^0\pi^+$.

Chapter 8

Conclusions

In a sample of 9.56±0.48 pb^{-1}, containing 20300±2900±1100 D^+D^- pairs, the doubly Cabibbo suppressed decays $D^+ \to K^+\pi^-\pi^+$ (including $D^+ \to K^+\rho^0$, $D^+ \to K^{*0}\pi^+$ and $D^+ \to K^+\pi^-\pi^+$[nr]), $D^+ \to K^+\pi^0$ and $D^+ \to K^{*+}\pi^0$ have been searched for by tagging $\psi(3770) \to D^+D^-$ events. Three candidate events have been found for $D^+ \to K^+\pi^-\pi^+$ with an expected background of $1.2^{+0.4}_{-0.2}\pm0.4$ events. None of the three events favor a two-body resonant interpretation. No candidate events have been found for either $D^+ \to K^+\pi^0$ or $D^+ \to K^{*+}\pi^0$. The upper limits calculated for the branching fractions are summarized in Table 8.1. The limit on $B(D^+ \to K^+\pi^-\pi^+)$ is found to be consistent with a measured value of $B(D^+ \to K^+\pi^-\pi^+) = 0.39^{+0.09}_{-0.08}{}^{+0.09}_{-0.08}\%$, which is obtained through an untagged analysis of $K^+\pi^-\pi^+$ presented in Appendix 1. Table 8.1 also contains the results for upper limits on $B(D^+ \to K^+\pi^-\pi^+)$, $B(D^+ \to K^+\pi^0)$ and $B(D^+ \to K^{*+}\pi^0)$ obtained through independent analyses presented in Appendix 2, wherein the doubly Cabibbo suppressed decays are searched for by kinematically fitting, rather than explicitly tagging, the final states. This second analysis makes no improvement on the branching fraction limits but does provide a crosscheck of the analysis techniques and background calculations. In this chapter the limits on the $|\bar{\rho}|^2$ parameters are calculated and compared to theoretical predictions, and the conclusions are drawn.

8-1 Upper Limit Calculations of the $|\bar{\rho}|^2$ Parameters and Comparison with Theory

The $|\bar{\rho}|^2$ parameters whose limits are calculated are defined

Table 8.1 Summary of doubly Cabibbo suppressed branching fractions obtained in this thesis. All limits are at 90% confidence level.

Mode	Tagging B. F. (%)	Fitting B. F. (%)	Inclusive B. F. (%)
$K^+\pi^-\pi^+$	<0.77	<0.78	$0.39^{+0.09+0.09}_{-0.08-0.08}$ (> 0.22)
$K^+\rho^0$	<0.45	–	–
$K^{*0}\pi^+$	<0.68	–	–
$K^+\pi^-\pi^+$[nr]	<0.76	–	–
$K^+\pi^0$	<0.35	<0.51	–
$K^{*+}\pi^0$	<2.3	<11.6	–

$$|\bar{\rho}_{K\pi\pi}|^2 \equiv \frac{B(D^+ \to K^+\pi^-\pi^+)}{B(D^+ \to K^-\pi^+\pi^+)} \times \frac{1}{\tan^4\theta_c}$$

$$|\bar{\rho}_{K\rho^0}|^2 \equiv \frac{B(D^+ \to K^+\rho^0)}{B(D^+ \to \bar{K}^0\rho^+)} \times \frac{1}{\tan^4\theta_c}$$

$$|\bar{\rho}_{K^{*0}\pi}|^2 \equiv \frac{B(D^+ \to K^{*0}\pi^+)}{B(D^+ \to \bar{K}^{*0}\pi^+)} \times \frac{1}{\tan^4\theta_c}$$

$$|\bar{\rho}_{K\pi\pi[\mathrm{nr}]}|^2 \equiv \frac{B(D^+ \to K^+\pi^-\pi^+[\mathrm{nr}])}{B(D^+ \to K^-\pi^+\pi^+[\mathrm{nr}])} \times \frac{1}{\tan^4\theta_c}$$

$$|\bar{\rho}_{K\pi^0}|^2 \equiv \frac{B(D^+ \to K^+\pi^0)}{B(D^+ \to \bar{K}^0\pi^+)} \times \frac{1}{\tan^4\theta_c}$$

$$|\bar{\rho}_{K^{*}\pi^0}|^2 \equiv \frac{B(D^+ \to K^{*+}\pi^0)}{B(D^+ \to \bar{K}^{*0}\pi^+)} \times \frac{1}{\tan^4\theta_c}$$

Upper limits on these parameters are calculated by maximum likelihood procedures similar to those used to obtain the doubly Cabibbo suppressed branching fractions.

In the case of $|\bar{\rho}_{K\pi\pi}|^2$, for example, the joint likelihood function is

Table 8.2 The Cabibbo Allowed branching fractions used in the calculations of the $|\bar{\rho}|^2$ parameters.

Channel	Branching Fraction (%)	Reference
$D^+ \to K^-\pi^+\pi^+$	9.1±1.3±0.4	24
$D^+ \to \bar{K}^0\rho^+$	6.9 ± 0.8 ± 2.3	22
$D^+ \to \bar{K}^{*0}\pi^+$	5.9 ± 1.9 ± 2.5	22
$D^+ \to K^-\pi^+\pi^+$[nr]	7.2 ± 0.6 ± 1.8	22
$D^+ \to \bar{K}^0\pi^+$	3.2 ± 0.5 ± 0.2	24

$$\mathcal{L}(n_{obs}, \boldsymbol{p}; \hat{\boldsymbol{p}}) = \mathcal{P}(n_{obs}; \mu_s+\mu_{b.D\bar{D}}+\mu_{b.uds}) \times$$
$$\mathcal{G}(\eta_s; \varepsilon_s, \sigma_s)\mathcal{G}(\mu_{tags}; n_{tags}, \sigma_{tags})\mathcal{M}(\vec{\mu}; \vec{b}, V)\mathcal{P}(\alpha n_{b.uds}; \alpha\mu_{b.uds})$$

where the notation from Section 5-6 has been followed. The constraint is

$$\mu_s = \mu_{tags}\, \eta_s\, |\bar{\rho}_{K\pi\pi}|^2\, \beta(K^-\pi^+\pi^+) \tan^4\theta_c C$$

where $\beta(K^-\pi^+\pi^+)$ is the true branching fraction for $D^+ \to K^-\pi^+\pi^+$. Here the multivariate Gaussian distribution $\mathcal{M}(\vec{\mu}; \vec{b}, V)$ accounts for the correlations between $n_{b.uds}$ and $B(K^-\pi^+\pi^+)$. The likelihood function is maximized at different values of $|\bar{\rho}_{K\pi\pi}|^2$ and then integrated numerically to find the 90% confidence level. Systematic errors are treated as in the branching fraction calculations.

The limits on the other $|\bar{\rho}|^2$ parameters are obtained analogously. Table 8.2 lists the Cabibbo allowed branching fractions used in the likelihood functions, and $\tan\theta_c$ = 0.2267 is used in the constraint. The likelihood functions for the six $|\bar{\rho}|^2$ parameters are indicated in Figure 8.1. The resulting upper limits with systematic errors are listed in Table 8.1.

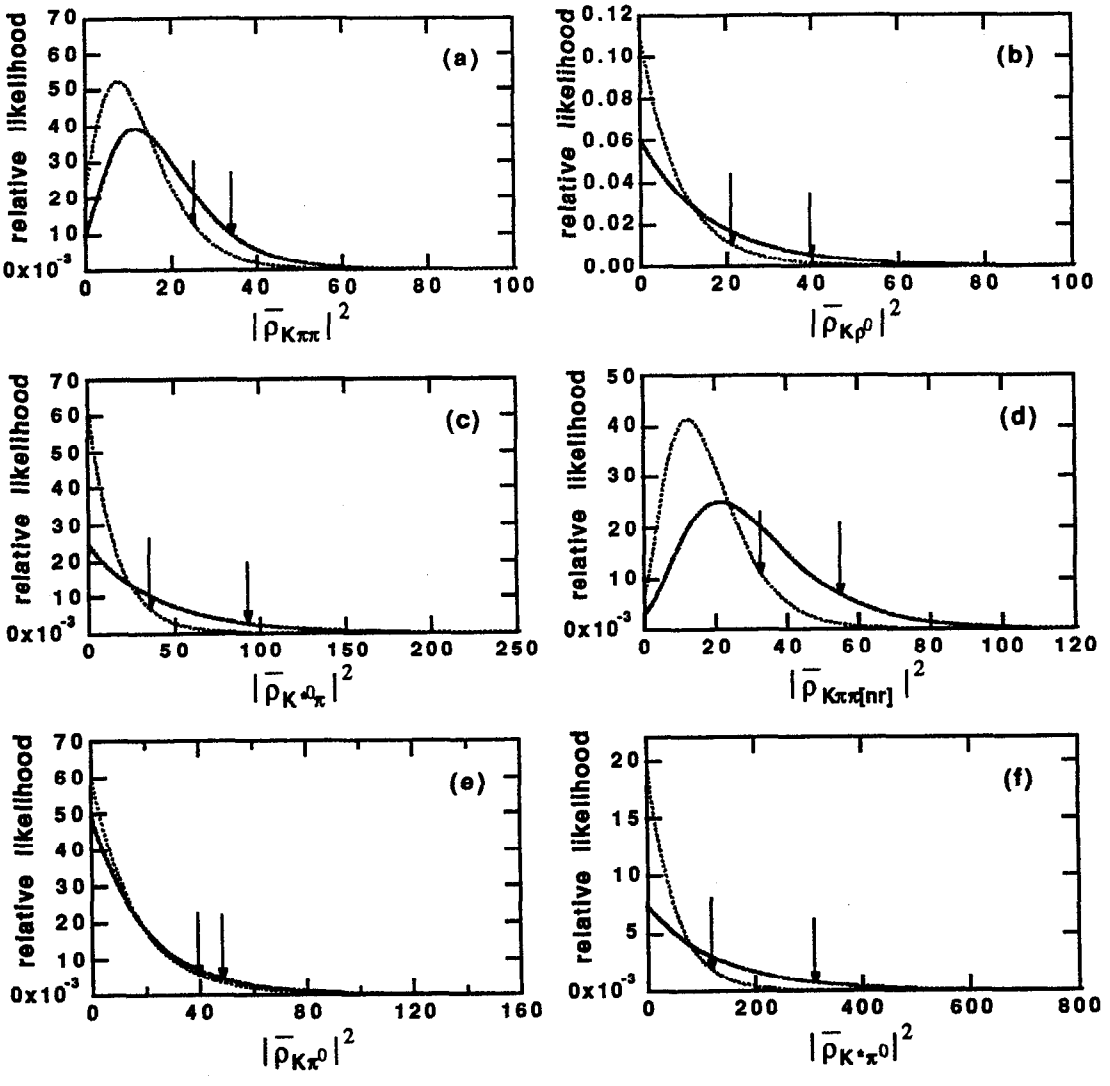

Figure 8.1 The likelihood functions for (a) $|\bar{\rho}_{K\pi\pi}|^2$, (b) $|\bar{\rho}_{K\rho^0}|^2$, (c) $|\bar{\rho}_{K^{*0}\pi}|^2$, (d) $|\bar{\rho}_{K\pi\pi[nr]}|^2$, (e) $|\bar{\rho}_{K\pi^0}|^2$ and (f) $|\bar{\rho}_{K^*\pi^0}|^2$.

The measurement $|\bar{\rho}_{K\pi\pi}|^2 = 18.3^{+3.6}_{-3.2}\pm4.0$ and limit $|\bar{\rho}_{K\pi\pi}|^2 < 34.1$ are consistent. Included also for comparison are upper limits for $|\bar{\rho}_{K\pi\pi}|^2$, $|\bar{\rho}_{K\pi^0}|^2$ and $|\bar{\rho}_{K^*\pi^0}|^2$, obtained by the kinematic fitting analysis in Appendix 2.

Table 8.4 compares the best experimental numbers obtained for the six $|\bar{\rho}|^2$ parameters against the numbers predicted by Bigi.[38] The limit on $|\bar{\rho}_{K\pi^0}|^2$ does not test the

Table 8.3 The $|\bar{\rho}|^2$ obtained in this thesis. All limits are at 90% confidence level, and the limits in parentheses are without systematic errors.

Parameter	Tagging $\|\bar{\rho}\|^2$	Fitting $\|\bar{\rho}\|^2$	Inclusive $\|\bar{\rho}\|^2$
$\|\bar{\rho}_{K\pi\pi}\|^2$	<34.1	<36.0	$18.3^{+3.6}_{-3.2}\pm4.0$ (> 9.1)
$\|\bar{\rho}_{K\rho^0}\|^2$	<39.9	–	–
$\|\bar{\rho}_{K^{*0}\pi}\|^2$	<92.9[a]	–	–
$\|\bar{\rho}_{K\pi\pi[\mathrm{nr}]}\|^2$	<55.3	–	–
$\|\bar{\rho}_{K\pi^0}\|^2$	<48.4	<68.2	–
$\|\bar{\rho}_{K^*\pi^0}\|^2$	<312[a]	<1610	–

a. The large errors in $B(\bar{K}^{*0}\pi^+)$ necessitated that the limits on these parameters be obtained by fixing $\beta(\bar{K}^{*0}\pi^+)$ to $B(\bar{K}^{*0}\pi^+)$ and to $B(\bar{K}^{*0}\pi^+) - \delta B(\bar{K}^{*0}\pi^+)$, in the absence and presence, respectively, of systematic errors; $\delta B(\bar{K}^{*0}\pi^+)$ is the statistical and systematic errors on $B(\bar{K}^{*0}\pi^+)$ added in quadrature.

Table 8.4 Comparison of the $|\bar{\rho}|^2$ numbers with theory. Values in parentheses are 90% confidence level lower limits.

Parameter	Experiment	Bigi[a]
$\|\bar{\rho}_{K\pi\pi}\|^2$	$18.3^{+3.6}_{-3.2}\pm4.0$ (> 9.1)	–
$\|\bar{\rho}_{K\rho^0}\|^2$	<39.9	0.35
$\|\bar{\rho}_{K^{*0}\pi}\|^2$	<92.9	5-11
$\|\bar{\rho}_{K\pi\pi[\mathrm{nr}]}\|^2$	<55.3	–
$\|\bar{\rho}_{K\pi^0}\|^2$	<48.4	3
$\|\bar{\rho}_{K^*\pi^0}\|^2$	<312	12-25

a. Reference [34].

small values predicted for it by the model. The limit is also sufficiently poor on $|\bar{\rho}_{K^*\pi^0}|^2$ in that it does not address even the large value predicted by Bigi. For $|\bar{\rho}_{K\pi\pi[\mathrm{nr}]}|^2$ no predictions exist, due to the inability of the model to estimate three-body decays. The limits on

the $|\bar{\rho}|^2$ parameters for the $K^+\pi^-\pi^+$ resonant modes are consistent, but generally larger, than the model predictions. The surprising result is the measured central value for $|\bar{\rho}_{K\pi\pi}|^2$ $= 18.3^{+3.6}_{-3.2}\pm4.0$, with a lower limit of $|\bar{\rho}_{K\pi\pi}|^2 > 9.1$ at 90% confidence level. This is larger than the predicted values both for $|\bar{\rho}_{K\rho^0}|^2$ and for $(2/3)\times|\bar{\rho}_{K^{*0}\pi}|^2$ (the 2/3 arises from the Clebsch-Gordon coefficient in the decay of the K^{*0}).

8-2 Comparisons of the Branching Fractions with Theory

8-2.1 BSW Predictions

Further understanding of the apparent discrepancy between experiment and theory for $D^+ \to K^+\pi^-\pi^+$ must be obtained by examining individually the numerator and denominator of the $|\bar{\rho}|^2$ parameters, i. e. to study how successfully theory can predict the branching fractions for the doubly Cabibbo suppressed decays and the corresponding Cabibbo allowed decays. To do this study, this author has calculated the branching fractions using the BSW model. A check finds the predictions for the Cabibbo allowed modes to agree with those given in Reference [18]. The branching fractions for both the Cabibbo allowed and doubly Cabibbo suppressed decay modes are expressed, respectively, in Table 8.5 and Table 8.6 in terms of the a_1 and a_2 parameters, showing explicitly how interference enters into the latter class of decays and not the former. The predicted numbers are evaluated using $a_1 = 1.2$ and $a_2 = -0.5$.

The choice of form factors is crucial in the model, and those dependencies are also made explicit in Table 8.5 and Table 8.6. Therefore, some study is also made regarding the choice of form factors. The first column of predicted numbers given in each of the tables is obtained using the BSW form factors. The second column of predicted numbers instead uses experimentally measured form factors, in a fashion similar to what was done for the branching fractions in Table 2.4 of Section 2-2.6. The experimentally measured form factors, obtained from studies of $D^0 \to K^-e^+\nu_e$,[65] and $D^+ \to \bar{K}^{*0}e^+\nu_e$,[26] are given in Table

Table 8.5 Comparison of the theoretical D^+ Cabibbo allowed branching fractions (%) with measurement.

Mode	Formula	BSW1[a]	BSW2[b]	Experiment
$\bar{K}^0\rho^+$	$24.3\left[F_1^{D\to K}(q^2=m_\rho^2)a_1 + 0.73\,A_0^{D\to\rho}(q^2=m_K^2)a_2\right]^2$	15.1	16.1	$6.9\pm0.8\pm2.3$
$\bar{K}^{*0}\pi^+$	$10.1\left[A_0^{D\to K^*}(q^2=m_\pi^2)a_1 + 1.66\,F_1^{D\to\pi}(q^2=m_{K^*}^2)a_2\right]^2$	0.3	0.01	$5.9\pm1.9\pm2.5$
$\bar{K}^0\pi^+$	$18.2\left[F_0^{D\to K}(q^2=m_\pi^2)a_1 + 1.31\,F_0^{D\to\pi}(q^2=m_K^2)a_2\right]^2$	3.6	3.1	$3.2\pm0.5\pm0.2$

a. Using the form factors in the BSW model, Reference [18].
b. Using the experimentally measured form factors, Table 8.7

Table 8.6 Comparison of the BSW theoretical doubly Cabibbo suppressed branching fractions (%) with measurement.

Mode	Formula	BSW1[a]	BSW2[b]	Experiment
$K^+\pi^-\pi^+$	–	–	–	$0.39^{+0.09+0.09}_{-0.08-0.08}$ (>0.22)
$K^+\rho^0$	$0.017\left[A_0^{D\to\rho}(q^2=m_K^2)\right]^2a_1^2$	0.013	0.014	<0.45
$K^{*0}\pi^+$	$0.074\left[F_1^{D\to\pi}(q^2=m_{K^*}^2)\right]^2a_2^2$	0.014	0.018	<0.68
$K^+\pi^-\pi^+$[nr]	–	–	–	<0.76
$K^+\pi^0$	$0.041\left[F_0^{D\to\pi}(q^2=m_K^2)\right]^2a_1^2$	0.031	0.040	<0.35
$K^{*+}\pi^0$	$0.037\left[F_1^{D\to\pi}(q^2=m_{K^{*+}}^2)\right]^2a_1^2$	0.040	0.052	<2.3

a. Using the form factors in the BSW model, Reference [18].
b. Using the experimentally measured form factors, Table 8.7

Table 8.7 Form factors from $D^0 \to K^- e^+ \nu_e$ and $D^+ \to \bar{K}^{*0} e^+ \nu_e$.

Form Factor	E691	ISGW[a]	BSW[b]	GS[c]	KS[d]
$F_1(0)$	0.79±0.05±0.06[e]		0.762		0.7
$F_0(0)$	0.79±0.05±0.06[e]		0.762		0.7
$A_2(0)$	0.0±0.2±0.1[f]	0.8	1.147	0.6	1.0
$A_1(0)$	0.46±0.05±0.05[f]	0.8	0.880	0.8	1.0
$A_0(0)$	0.71±0.13±0.09[f]	0.8	0.734	0.9	1.0

a. Reference [66].
b. Reference [18]
c. Reference [67]
d. Reference [68]
e. Reference [65].
f. Reference [26].

8.7, where they are also compared with some model predictions. The form factors for $D \to \pi$ and ρ are set respectively equal to those for $D \to K$ and K^*, i. e. $SU(3)$ symmetry is assumed.

Examining first the Cabibbo allowed modes, one finds:

1) the theoretical branching fraction for $D^+ \to \bar{K}^0 \rho^+$ is larger than the measured branching fraction by approximately a factor of two. This suggests that the theoretical prediction for $|\bar{\rho}_{K^{*0}\pi}|^2$ is too small, making it somewhat more consistent with the $|\bar{\rho}_{K\pi\pi}|^2 > 9.1$ limit.

2) the theoretical branching fraction for $D^+ \to \bar{K}^{*0} \pi^+$ is smaller than the measured branching fraction by at least a factor of ten. The reason for this is destructive interference for $D^+ \to \bar{K}^{*0} \pi^+$ is strong. When the measured form factors are used the interference is almost complete; the errors in fact make the branching fraction consistent with zero. These results suggest that the theoretical prediction for $|\bar{\rho}_{K^{*0}\pi}|^2$ is too large, making it less consistent with the limit $|\bar{\rho}_{K\pi\pi}|^2 > 9.1$. These results also suggest that $|\bar{\rho}_{K^*\pi^0}|^2$ is too large.

3) the theoretical branching fraction for $D^+ \rightarrow \bar{K}^0\pi^+$ is approximately equal to the measured branching fraction. This result is expected since $D^+ \rightarrow \bar{K}^0\pi^+$ was one of the channels used to fit the a_1 and a_2 parameters. Due to the denominator, therefore, one therefore expects no discrepancies with $|\rho_{K\pi^0}|^2$ values.

For the doubly Cabibbo suppressed modes, one finds:

1) the experimental limits for $D^+ \rightarrow K^+\rho^0$ and $K^{*0}\pi^+$ are sufficiently poor to test the predictions for the branching fractions. The same is true for $D^+ \rightarrow K^+\pi^0$ and $K^{*+}\pi^0$.

2) no predictions exist for $D^+ \rightarrow K^+\pi^-\pi^+$[nr].

3) the sum of the predictions for $D^+ \rightarrow K^+\rho^0$ and $K^{*0}\pi^+$ is approximately a factor of ten smaller than the measured branching fraction for $B(D^+ \rightarrow K^+\pi^-\pi^+) = 0.39^{+0.09+0.09}_{-0.08-0.08}$.

This last effect appears to be the main factor in the large experimental values for $|\bar{\rho}_{K\pi\pi}|^2$.

8-2.2 Other Models

For contrast and to be complete, the doubly Cabibbo suppressed branching fractions predicted by two less widely accepted models have also been studied. These models have had less success in describing the full body of charm data.

Verma and Kamal[69] (VK) have applied a phenomenological nonet-symmetry scheme to weak charmed decays. Transition amplitudes are calculated from linear combinations of matrix elements which are categorized according their representation of $SU(3)$ flavor symmetry. The contributions of the matrix elements to a given amplitude are parametrized by coefficients whose values are determined by fitting to measured branching ratios. Final state interactions are accounted for in the $K^+\pi^0$ mode by including isospin phases in the parametrization, and sextet dominance is assumed in the predictions for $D^+ \rightarrow K^+\rho^0$ and $K^{*0}\pi^+$.

Table 8.8 Comparison of the VK and CC theoretical doubly Cabibbo suppressed branching fractions (%) and with measurement.

Mode	VK[a]	CC[b]	Experiment
$K^+\pi^-\pi^+$	–	–	$0.39^{+0.09+0.09}_{-0.08-0.08}$
$K^+\rho^0$	0.007	0.010	<0.45
$K^{*0}\pi^+$	0.022	0.011	<0.68
$K^+\pi^-\pi^+$[nr]	–	–	<0.76
$K^+\pi^0$	0.016	0.037	<0.35
$K^{*+}\pi^0$	0.015	0.022	<2.3

a. Reference [69].
b. Reference [70].

Chau and Cheng[70] (CC) take a similar approach to the VK model, except the matrix elements are classified according to a quark diagram scheme. Six matrix elements represent the external and internal W-emission spectator diagrams, the W-exchange and W-annihilation diagrams and the two Penguin diagrams. Final state interactions are also accounted for via isospin phases.

The prediction from these modes are given in Table 8.6 with the experimental results. Here again the upper limits are sufficiently poor to test the models, while the large measured branching fraction for $B(D^+ \to K^+\pi^-\pi^+)$ is not predicted.

8-3 Conclusions

The central value of the branching fraction for $D^+ \to K^+\pi^-\pi^+$ has been measured to be more than a factor of ten larger than the theoretical predicted values, and this largely accounts for a large value for $|\bar{\rho}_{K\pi\pi}|^2$. Five possible phenomena have been considered which could enhance $D^+ \to K^+\pi^-\pi^+$, assuming the measurements are correct:

1) The theoretical form factors may not be correct. The effect of the form factors have been examined in Table 8.5 and Table 8.6. It is unlikely, however, the form factors are inaccurate by a factor of ten.

2) Decay modes other than $D^+ \rightarrow K^+\rho^0$ and $K^{*0}\pi^+$ are contributing to the $K^+\pi^-\pi^+$ final state. These additional modes would involve higher $K^+\pi^-$ or $\pi^-\pi^+$ resonances. The Dalitz plot analysis in Section 5-7 provides some support for this hypothesis; none of the three tagged candidate $K^+\pi^-\pi^+$ events are found to be likely either $K^+\rho^0$ or $K^{*0}\pi^+$.

3) There may be some unexpected effects in three-body nonresonant $K^+\pi^-\pi^+$, where the models fail to provide any predictions.

4) Final state interactions may be rescattering other decay mode states into the $K^+\rho^0$, $K^{*0}\pi^+$ and $K^+\pi^-\pi^+$[nr] channels.[71] Cabibbo allowed decays produce final states with only an isospin 3/2 amplitude. Phase shifts, therefore do not affect these decays (confer Section 2-2.4), and inelastic scattering would have to occur through a 3/2 resonance, which is considered to be an exotic state. Doubly Cabibbo suppressed final states, however, have isospin 1/2 and 3/2 amplitudes. This allows phase shifts to change the net amplitudes for these decays, and inelastic scattering to feed in through a 1/2 resonance. Final state interactions could thus increase $B(D^+ \rightarrow K^+\pi^-\pi^+)$ while leaving $B(D^+ \rightarrow K^-\pi^+\pi^+)$ unaffected, thereby enhancing $|\bar{\rho}_{K\pi\pi}|^2$. Recall that in the $1/n_c$ expansion employed by Bigi, final state interactions are non-leading order effects, and are thus not included in the leading term calculations. Also, in the BSW predictions calculated by this author, no corrections are made for isospin phases since they are unknown.

5) Quark annihilation may be contributing. As shown by the diagram in Figure 8.2, doubly Cabibbo suppressed decays can also occur through a *W*-annihilation transition. The amplitude for this process adds to the usual *W*-emission process and could therefore enhance the doubly Cabibbo suppressed decays. As discussed in Section 2-2.4, however, there has been no compelling evidence for large *W*-annihilation in the D^0 or the D_s^+; QCD sum rules suggest that annihilation contributes to only ~20% of D^0 hadronic width.

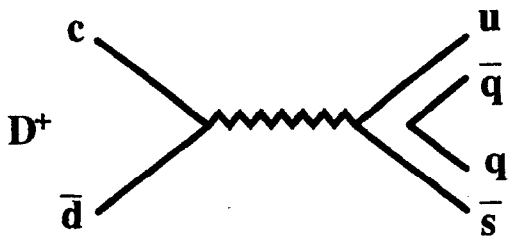

Figure 8.2 *W*-annihilation in doubly Cabibbo suppressed decays.

One or some combination of these effects may increase the widths of doubly Cabibbo suppressed decays relative to the Cabibbo allowed decays.

There is also a chance that the large $B(D^+ \to K^+\pi^-\pi^+)$ and $|\bar{\rho}_{K\pi\pi}|^2$ are reflecting physics outside the Standard Model.[34] Before making such claims, however, it is important to understand the final state interactions and other long range QCD effects which may be important for understanding doubly Cabibbo suppressed decays. For this it would be desirable to obtain predictions based on QCD sum rules, which have been developed specifically to estimate the long range non-factorizable effects.

In conclusion evidence has been found for the doubly Cabibbo suppressed decay of the D^+ meson in the $K^+\pi^-\pi^+$ final state. The branching fraction to this state is larger than anticipated within a range of models which describe these weak decays. In particular, it was found that $B(D^+ \to K^+\pi^-\pi^+) = 0.39^{+0.09}_{-0.08}{}^{+0.09}_{-0.08}\%$, with a lower limit of $B(D^+ \to K^+\pi^-\pi^+) > 0.22$ at 90% confidence level. This corresponds to $|\bar{\rho}_{K\pi\pi}|^2 = 18.3^{+3.6}_{-3.2}\pm 4.0$, with a lower limit of $|\bar{\rho}_{K\pi\pi}|^2 > 9.1$ at 90% confidence level.

The significance of this result is similar to that observed for the D^0 decays to the final state $K^\pm\pi^\mp\pi^0$ in the D^0-$\bar{D}^0$ mixing analysis of this experiment, discussed in Section 2-3.3. Namely, if $r < 3.7\times10^{-3}$ as quoted by E691, then the three $S = \pm 2$ events observed by this experiment leads to $|\bar{\rho}_{K\pi\pi^0}|^2 > 1.9$ at 90% confidence level. The D^+ measurement

presented here lends further support that those three events are doubly Cabibbo suppressed as well.

In more general terms, this analysis should point to the beauty and challenge of charmed meson decays. Lying between the perturbative and nonperturbative regimes in QCD, the major subprocesses appear to play significant roles in influencing and complicating the decay patterns. Any detailed progress in this field will clearly require three to four orders of magnitude increases in data, and only those experiments able to measure the full pattern of decays will succeed in understanding the very elegant and fundamental underlying physics.

Appendix 1

Inclusive Search for $D^+ \to K^+\pi^-\pi^+$

A1-1 Introduction

This appendix discusses the inclusive search performed for $D^+ \to K^+\pi^-\pi^+$. Section A1-2 describes the event selection procedure, including the cuts to reduce the major backgrounds $D^+ \to \bar{K}^0K^+ \to K^0_SK^+ \to (\pi^+\pi^-)K^+$ and $D^+ \to K^-\pi^+\pi^+$. Section A1-3 yields the results including the estimated efficiencies and background levels. Section A1-4 produces the maximum likelihood calculation for $B(D^+ \to K^+\pi^-\pi^+)$, and Section A1-5 presents the maximum likelihood calculation for $|\bar{\rho}_{K\pi\pi}|^2$.

A1-2 Event Selection

Given an event from the full $\psi(3770)$ data set, the reconstruction of $D^+ \to K^+\pi^-\pi^+$ proceeds as follows:

- At least three charged tracks with a good helix fit must be found in the event. The tracks must also be corrected for energy losses and have a good beam fit.

- All tracks must have good time-of-flight information and lie within the well-modelled region of the time-of-flight system:

$$|\cos\theta| < 0.76$$

where θ is the polar angle of the detector. A track is given the kaon mass assignment if

$$|\Delta T_K| < 1 \text{ ns } (\sim 5\sigma) \qquad |\Delta T_K| < |\Delta T_\pi|.$$

Analogous relations must hold for a track to be given the pion assignment.

- Tracks are combined to form $D^+ \to K^+\pi^-\pi^+$ candidates. To reduce the combinatoric background, the beam-constrained mass (M_{beam}) is subjected to a 3σ cut about the signal peak:

$$1.8643 < M_{beam} < 1.8743 \text{ GeV/c}^2$$

as determined from Monte Carlo.

- To remove the background from $D^+ \to \bar{K}^0 K^+$, $\bar{K}^0 \to K^0_S \to \pi^+\pi^-$, the $\pi^+\pi^-$ invariant mass must satisfy

$$|M_{\pi^+\pi^-} - M_{K^0}| > 30 \text{ MeV/c}^2$$

The invariant mass (M_{inv}) is then used to study a signal; the signal region is defined by the 2σ mass cut

$$1.836 < M_{inv} < 1.902 \text{ GeV/c}^2.$$

A1-3 Results

Figure A1.1 shows the M_{inv} plot from the data. A small excess of events is observed above the combinatoric background about the D^+ mass. A test is made to insure that the excess is not dominantly due to double misidentification of $D^+ \to K^-\pi^+\pi^+$. For a given track combination, each track is reassigned its mass hypothesis simply according to its charge; e.g. if the tracks have charge (−++) then the (−) track is given the kaon assignment and the two (+) tracks are given the pion assignments. The invariant mass of the combination is then recalculated and plotted. The resulting distribution is shown in Figure A1.1 where the excess of events is no longer observed.

The number of signal events is determined by a binned log likelihood fit to a Gaussian function plus a third order polynomial. The fit is performed with the mean of the Gaussian fixed at the D^+ mass, 1.8693 GeV/c^2, and the width fixed at 0.0166 GeV, as determined by Monte Carlo simulation. So obtained, the number of observed events (n_{obs}) is

$$n_{obs} = 37.1 \pm 12.4 \pm 5.5 \qquad \text{(A1.1)}$$

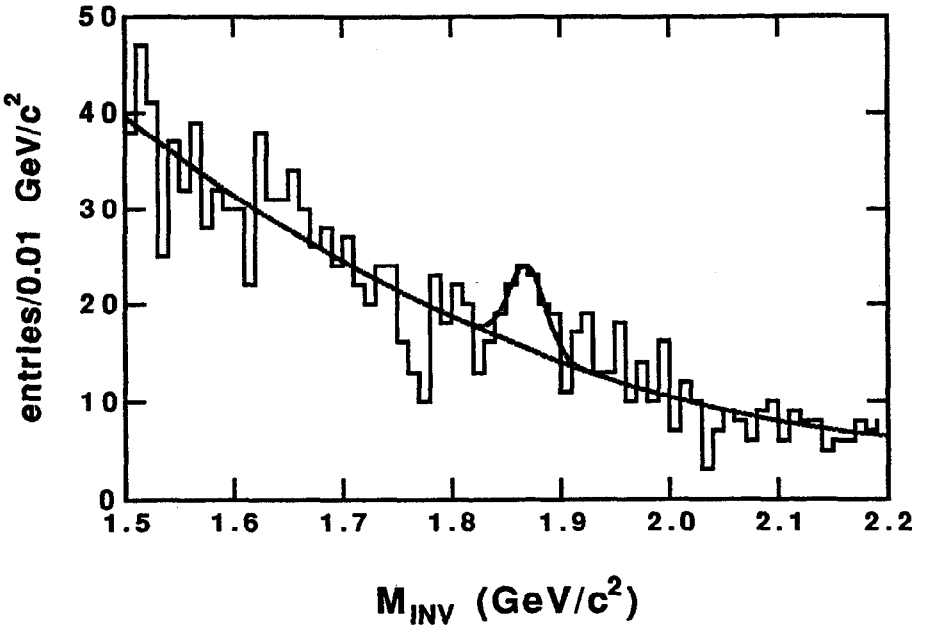

Figure A1.1 Invariant mass distribution for inclusive $K^+\pi^-\pi^+$.

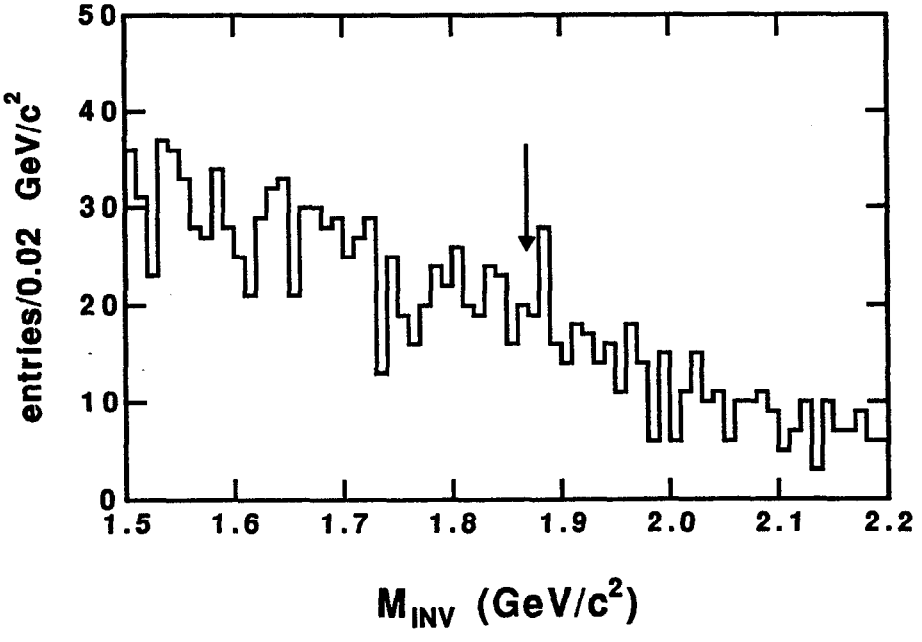

Figure A1.2 Invariant mass distribution after reassigning track hypotheses according to $K^-\pi^+\pi^+$. The arrow points to the D^+ mass.

where the errors are statistical and systematic respectively. The statistical errors are derived from the parameter fit errors. The systematic error contains the uncertainty in the background shape, the uncertainties arising from varying the fit region and the bin size,

Table A1.1 The systematic errors on the number of observed $K^+\pi^-\pi^+$ events.

Source	Error (#events)
Fixed Gaussian mean and width	±1.3
Background shape	±5.3
Bin Size	±0.3
Fit region	±0.6
Total uncertainty	±5.5

Table A1.2 The systematic errors on the detection efficiency for inclusive $K^+\pi^-\pi^+$.

Source	Absolute Error (%)
Charged track efficiency	–0.7
Particle Identification	–1.8
Mass and signal region cuts	±1.1
Resonant substructure	±1.8
Total Error	+2.1 / –3.3

and the uncertainties due to fixing the mean and width of the Gaussian function; these errors are broken down in Table A1.1.

A1-3.1 Detection Efficiency

The efficiency (ε_s) for detecting $D^+ \to K^+\pi^-\pi^+$ is estimated to be

$$\varepsilon_s = 22.0 \pm 0.3^{+2.1}_{-3.3}\% \qquad \text{(A1.2)}$$

The statistical error reflects the Monte Carlo statistics, and the contributing factors to the systematic error are listed in Table A1.2.

A1-3.2 Background Estimates

Above the combinatoric background, the decays $D^+ \to \bar{K}^0K^+ \to K^0_SK^+ \to (\pi^+\pi^-)K^+$, $D^+ \to K^-\pi^+\pi^+$[nr], and $D^+ \to \bar{K}^{*0}\pi^+ \to (K^-\pi^+)\pi^+$ are expected to contribute to the signal. The numbers of events from each decay channel i, $n_{b.i}$, are calculated according to

$$n_{b.i} = n_D B_i \varepsilon_{b.i} \tag{A1.3}$$

where n_D is the number of produced charged D mesons (= 40600±5800±2200), B_i is the branching fraction for the background process i (given in Table 5.6), and $\varepsilon_{b.i}$ is the acceptance. Table A1.3 lists the acceptances and the expected numbers of events for the three channels. The total number of events expected is

$$n_b = 2.5 \pm 0.9^{+1.0}_{-0.9}. \tag{A1.4}$$

The statistical error is derived from the statistical errors on n_D, B_i, and $\varepsilon_{b.i}$. The contributing factors to the systematic error on the total number are listed in Table A1.4.

The statistical significance of the signal is determined by subtracting n_b from n_{obs} and dividing the result by the sum in quadrature of the errors on n_b and n_{obs}. So obtained, the statistical significance of the signal is 2.5σ.

A1-4 Measurement of $B(D^+ \to K^+\pi^-\pi^+)$

A maximum likelihood procedure is performed to obtain a measurement for $B(D^+ \to K^+\pi^-\pi^+)$. The joint likelihood function is

$$\mathcal{L} = \mathcal{P}(n_{obs};\, \mu_s+\mu_b)\mathcal{G}(\eta_s;\, \varepsilon_s,\, \sigma_s)\mathcal{M}(\vec{\mu};\, \vec{b},\, V)$$

where $\mathcal{P}$ represents a Poisson distribution, $\mathcal{G}$ a Gaussian distribution $\mathcal{M}$ a multivariate Gaussian distribution and

- $n_{obs} \equiv$ the number of observed events for $K^+\pi^-\pi^+$.

Table A1.3 The expected numbers of background events in the signal region for inclusive $D^+ \to K^+\pi^-\pi^+$. Acceptances are included.

Background	Acceptance(%)	Number of Events
$D^+ \to K^-\pi^+\pi^+$[nr]	$0.027\pm0.016^{+0.004}_{-0.002}$	$0.80^{+0.52+0.24}_{-0.44-0.21}$
$D^+ \to \bar{K}^{*0}\pi^+ \to (K^-\pi^+)\pi^+$	$0.149\pm0.023^{+0.024}_{-0.008}$	$1.15\pm0.88^{+1.11}_{-1.09}$
$D^+ \to \bar{K}^0K^+ \to (\pi^+\pi^-)K^+$	$0.363\pm0.052^{+0.004}_{-0.023}$	$0.52\pm0.19^{+0.09}_{-1.09}$
Total expected number of events		$2.5\pm0.9^{+1.0}_{-0.9}$

Table A1.4 The systematic errors on the total number of background events for inclusive $K^+\pi^-\pi^+$.

Source	Absolute Error (#events)
Charged track efficiency	−0.07
Particle Identification	+0.31 / −0.08
Mass and signal region cuts	±0.02
Branching fractions	±0.90
Number of produced D^+'s	±0.13
Total Error	+1.0 / −0.9

- $\mu_s \equiv$ the true number of $D^+ \to K^+\pi^-\pi^+$ events.
- η_s (ε_s) $\equiv$ the true (estimated) reconstruction efficiency for $K^+\pi^-\pi^+$.
- μ_b (n_b) $\equiv$ the true (estimated) number of background events for $K^+\pi^-\pi^+$.
- μ_D (n_D) $\equiv$ the true (estimated) number of produced D^+ mesons.
- $\vec{\mu}$ ($\vec{b}$) $\equiv$ the two-component vector of μ_D and μ_b (n_D and n_b).
- V $\equiv$ the covariance matrix (Table A1.5) of n_D and n_b.
- $\sigma_s \equiv$ the statistical standard deviation on ε_s.

Table A1.5 The covariance matrix for n_D and n_b.

	n_D	n_b
n_D	33.6×10^6	–3660.0
n_b	–3660.0	0.78

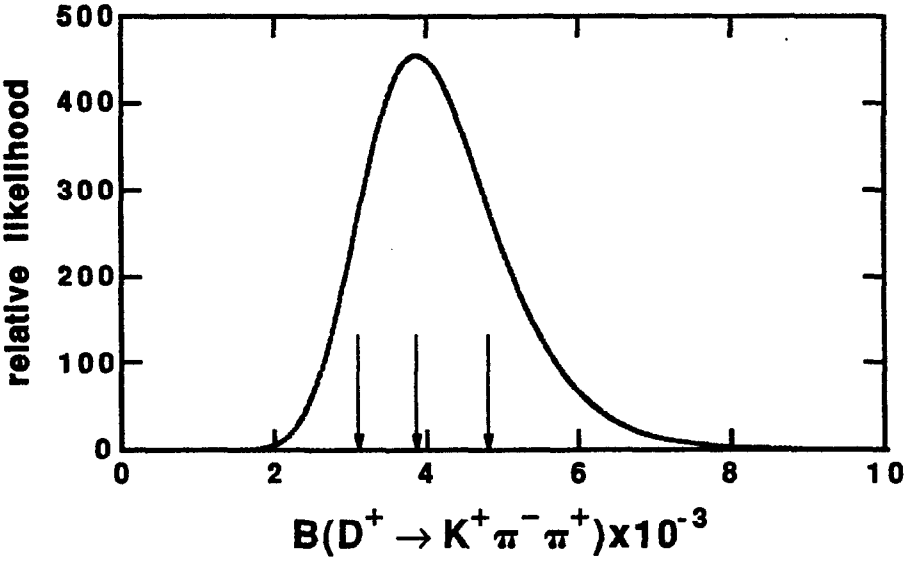

Figure A1.3 The likelihood function relative to $B(D^+ \to K^+\pi^-\pi^+)$.

The multivariate Gaussian treats the correlation between n_D and n_b arising from Equation A1.3. The constraint is

$$\mu_s = \mu_D\, B(K^+\pi^-\pi^+)\, \eta_s$$

through which the limit on $B(K^+\pi^-\pi^+)$ is obtained. The numbers from Equations A1.1, A1.2 and A1.4 produce the likelihood function in Figure A1.3, maximized as a function of $B(K^+\pi^-\pi^+)$.

The measured value for $B(D^+ \to K^+\pi^-\pi^+)$ is that value with the largest likelihood, and the statistical errors are those values where the likelihood has dropped by $e^{-0.5}$ of the maximum. These points are shown by the arrows in Figure A1.3. The systematic errors on

$B(D^+ \to K^+\pi^-\pi^+)$ are obtained from the systematic errors on n_{obs}, ε_s, n_b and n_D propagated in quadrature. So obtained,

$$B(D^+ \to K^+\pi^-\pi^+) = 0.39^{+0.09+0.09}_{-0.08-0.08}\%$$

A lower limit calculation, using the likelihood function, finds $B(D^+ \to K^+\pi^-\pi^+) > 0.22\%$ at 90% confidence level.

A1-5 Measurement of $|\bar{\rho}_{K\pi\pi}|^2$

To measure $|\rho_{K\pi\pi}|^2 \equiv B(D^+ \to K^+\pi^-\pi^+)/B(D^+ \to K^-\pi^+\pi^+)\tan^4\theta_c$, one could simply divide the result for $B(D^+ \to K^+\pi^-\pi^+)$, given above, by the published measurement for $B(D^+ \to K^-\pi^+\pi^+)$ ($=9.1\pm1.3\pm0.4\%$[24]) and $\tan^4\theta_c$. In doing so, however, the statistical significance for $|\rho_{K\pi\pi}|^2$ will suffer not only from the approximately $\pm25\%$ error on $B(D^+ \to K^+\pi^-\pi^+)$ but also the $\pm14\%$ error from $B(D^+ \to K^-\pi^+\pi^+)$. The error on the latter branching fraction arises from the limited statistics in the double tag procedure used in the determination of the absolute branching fraction.[24] An improvement is made by exploiting the similarities between the two decay modes. Since both decays produce an all charged final state with one kaon and two pions, the inclusive $K^+\pi^-\pi^+$ analysis procedure, with modifications made for the charge assignments, can also be used to search for $K^-\pi^+\pi^+$. This approach significantly improves the statistics since events are not fully reconstructed. Furthermore, since $|\rho_{K\pi\pi}|^2$ only involves the ratio of the two branching fractions, then

$$|\rho_{K\pi\pi}|^2 = \frac{B(K^+\pi^-\pi^+)}{B(K^-\pi^+\pi^+)} \times \frac{1}{\tan^4\theta_c}$$

$$= \frac{n_{K^+\pi^-\pi^+}/n_D\,\varepsilon_{K^+\pi^-\pi^+}}{n_{K^-\pi^+\pi^+}/n_D\,\varepsilon_{K^-\pi^+\pi^+}} \times \frac{1}{\tan^4\theta_c}$$

$$= \frac{n_{K^+\pi^-\pi^+}\varepsilon_{K^-\pi^+\pi^+}}{n_{K^-\pi^+\pi^+}\varepsilon_{K^+\pi^-\pi^+}} \times \frac{1}{\tan^4\theta_c}$$

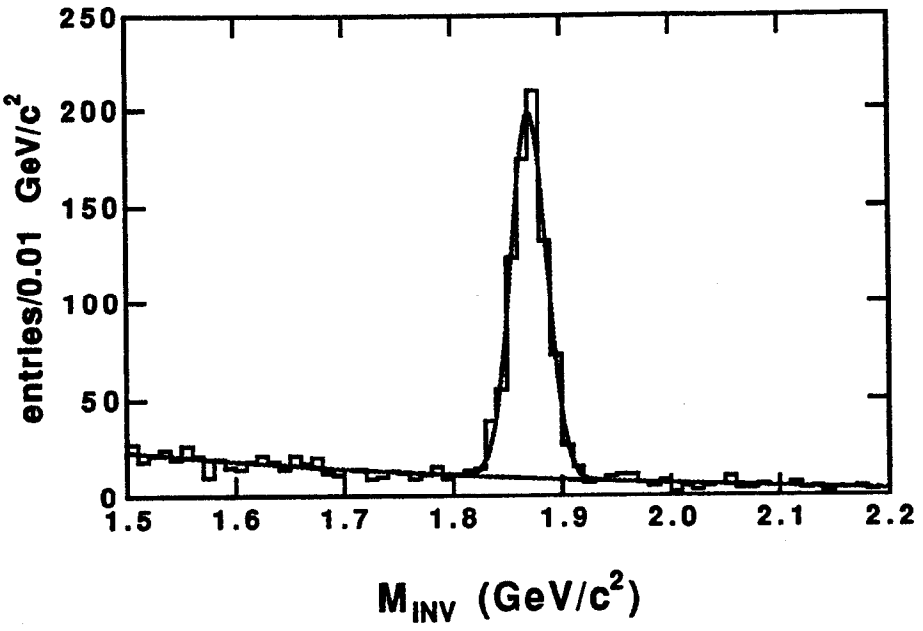

Figure A1.4 Invariant mass distribution for inclusive $K^-\pi^+\pi^+$.

which avoids the systematic errors from n_D and several common systematic errors from the efficiencies.

The results of the $K^-\pi^+\pi^+$ analysis is shown in Figure A1.4. For this analysis the anti-K^0_S cut is not necessary and therefore removed. The number of events found above background is 734±22±5, where the effects contributing to the systematic errors are the uncertainties from varying the bin size (±1 event) and fit region (±4 events) and the uncertainty in the shape of the background (±3 events). The number of background events contributing to the peak is found to be negligible. The reconstruction efficiency is estimated to be $22.5\pm0.7^{+2.4}_{-3.1}$%, where the effects contributing to these systematic errors are charged track efficiency (–0.7%), particle identification (–1.8%), signal region cuts (±1.1%) and efficiency variations according to resonant substructure (±2.2%).

A maximum likelihood procedure, separate from that used to calculate $B(D^+ \to K^+\pi^-\pi^+)$, is performed to obtain a measurement for $|\rho_{K\pi\pi}|^2$. Keeping with the notation from Section A1-4, the joint likelihood function is

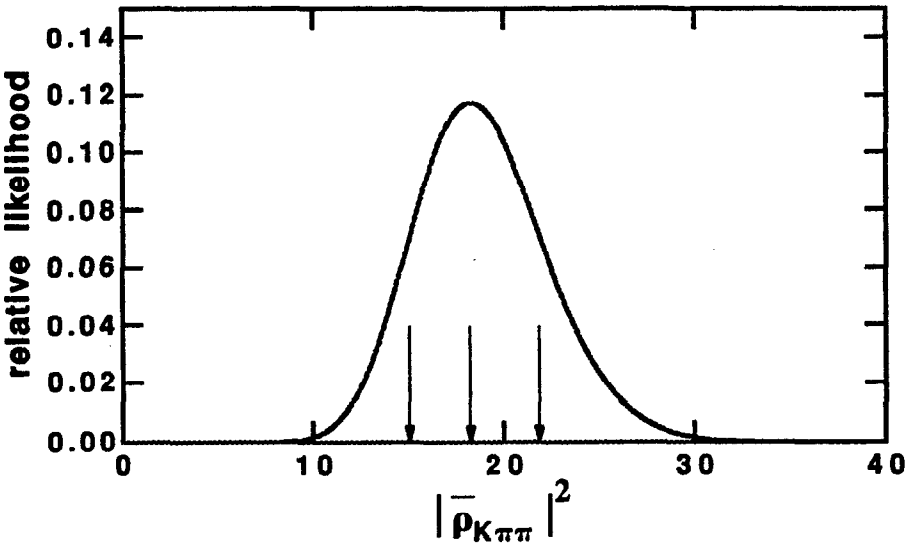

Figure A1.5 The likelihood function relative to $|\bar{\rho}_{K\pi\pi}|^2$.

$$\mathcal{L} = \mathcal{L}_{K^+\pi^-\pi^+}\mathcal{L}_{K^-\pi^+\pi^+}$$

where

$$\mathcal{L}_{K^+\pi^-\pi^+} = \mathcal{P}(n_{obs}^{K^-\pi^+\pi^+};\ \mu_s^{K^-\pi^+\pi^+} + \mu_b^{K^+\pi^-\pi^+}) \times \mathcal{G}(\eta_s^{K^-\pi^+\pi^+};\ \varepsilon_s^{K^-\pi^+\pi^+},\ \sigma_s^{K^-\pi^+\pi^+})\,\mathcal{G}(\mu_b^{K^+\pi^-\pi^+};\ n_b^{K^+\pi^-\pi^+},\ \sigma_b^{K^+\pi^-\pi^+})$$

$$\mathcal{L}_{K^-\pi^+\pi^+} = \mathcal{P}(n_{obs}^{K^-\pi^+\pi^+};\ \mu_s^{K^-\pi^+\pi^+})\,\mathcal{G}(\eta_s^{K^-\pi^+\pi^+};\ \varepsilon_s^{K^-\pi^+\pi^+},\ \sigma_s^{K^-\pi^+\pi^+})$$

which are subjected to the constraint

$$\left|\rho_{K\pi\pi}\right|^2 = \frac{\mu_{K^+\pi^-\pi^+}\eta_{K^-\pi^+\pi^+}}{\mu_{K^-\pi^+\pi^+}\eta_{K^+\pi^-\pi^+}} \times \frac{1}{\tan^4\theta_c}$$

where $\tan^2\theta_c = 0.0514$ is used.

The likelihood is maximized as a function of $|\rho_{K\pi\pi}|^2$ is shown in Figure A1.5; the arrows indicate the most likely value for $|\rho_{K\pi\pi}|^2$ and the points where the likelihood has dropped to $e^{-0.5}$ of the maximum likelihood. The systematic effects which contribute to $|\rho_{K\pi\pi}|^2$ are listed in Section Table A1.4. with their associated errors. The value obtained is

Table A1.6 The systematic errors on $|\bar{\rho}_{K\pi\pi}|^2$.

Source	Absolute Error
Number of $K^+\pi^-\pi^+$ events	±2.9
Number of $K^-\pi^+\pi^+$ events	±0.1
Level of $K^+\pi^-\pi^+$ background	±0.5
$K^+\pi^-\pi^+$ mass and signal region cuts	±0.9
$K^-\pi^+\pi^+$ mass and signal region cuts	±0.9
$K^+\pi^-\pi^+$ resonant substructure	±1.5
$K^-\pi^+\pi^+$ resonant substructure	±1.8
Total Error	±4.0

$$|\bar{\rho}_{K\pi\pi}|^2 = 18.3^{+3.6}_{-3.2}\pm 4.0$$

A lower limit calculation, using the likelihood function, finds $|\bar{\rho}_{K\pi\pi}|^2 > 9.1\,\%$ at 90 % confidence level.

Appendix 2

Kinematically Fitting Doubly Cabibbo Suppressed Decays

A2-1 Introduction

Separate to the tagging analyses described in Chapters 4 through 7, an analysis has been performed for doubly Cabibbo suppressed decays to serve as an additional test of the prior results. In this analysis, full event reconstruction is again performed to reduce the combinatoric backgrounds for the doubly Cabibbo suppressed decays. However, instead of tagging the events, the event reconstruction is done by kinematically fitting track combinations to a set of constraints which describe the topology of a given event hypothesis. One of the constraints is an equal-mass constraint where events are assumed to be produced through the reaction

$$e^+e^- \rightarrow X\overline{X} \rightarrow \text{final state}$$

but M(X), the mass of resonance X, is not required to equal the mass of the D^+ meson. In kinematically fitting events, the χ^2 which compares the fitted track parameters to the measured parameters can be used to further determine the quality of a candidate event.

This appendix is organized as follows. Section A2-2 discusses the initial event selection procedure. Section A2-3 discusses the method used in this analysis to estimate signal and backgrounds. Section A2-4 discusses the cuts introduced to reduce the known backgrounds. Section A2-5 shows the results of the selection criteria on the data and discusses the analysis tests that were performed. Finally, Section A2-6 gives the upper limit calculations for $B(D^+ \rightarrow K^+\pi^-\pi^+)$, $B(D^+ \rightarrow K^+\pi^0)$ and $B(D^+ \rightarrow K^{*+}\pi^0)$ based on this analysis.

A2-2 Event Selection

In this analysis the D^+ doubly Cabibbo suppressed decays searched for are

- $K^+\pi^-\pi^+$
- $K^+\pi^0$
- $K^{*+}\pi^0, K^{*+} \rightarrow K^0\pi^+$

each reconstructed opposite seven dominant modes of the D^+:

- $\overline{K}^0\pi^+$
- $K^-\pi^+\pi^+$
- $\overline{K}^0\pi^+\pi^-\pi^+$
- $\overline{K}^0\pi^+\pi^0$
- $\overline{K}^0K^+$
- $K^-K^+\pi^+$
- $K^-\pi^+\pi^+\pi^0$

where $K^0(\overline{K}^0) \rightarrow K^0_S \rightarrow \pi^+\pi^-$ and $\pi^0 \rightarrow \gamma\gamma$. The channel $K^{*+}\pi^0, K^{*+} \rightarrow K^+\pi^0$ has been omitted due the high combinatoric background anticipated from having to reconstruct two neutral pions. The decays pair to form 21 different final states. The seven dominant modes are the same as those used to obtain the D^+ tags (confer Table 4.1).

The initial event selection is performed at two levels, each including a separate series of fits. The first level uses loose selection criteria to reduce the event sample size:

- obtain an event with the correct number of charge tracks with an overall charge sign of zero. The tracks are required to have a good helix fit and to be corrected for energy losses.

- require the event to contain at least the same number of isolated photons as the desired final state. No initial restriction is made on the number of extra showers since real events with spurious showers could be rejected.

- combine the charged and neutral tracks to obtain all possible event combinations. No particle identification is imposed, and therefore all charged tracks are given both π and K hypotheses. All oppositely charged tracks are tried as K_S^0 candidates, and all isolated photon pairs are tried as π^0 candidates.

- kinematically fit the event combinations, imposing the four constraints of energy and momentum conservation. Combinations are retained for further consideration if $\chi^2 < 50$. No mass cuts are applied.

This selection criteria reduces the number of events considered for the 21 topologies from 668,100 to approximately 56,800 events.

The second level selection criteria imposes particle identification, stricter K_S^0 and π^0 candidate criteria, and additional constraints to the kinematic fit:

- charged track mass hypotheses must be consistent with available TOF or dE/dx information. A track is identified as a pion by TOF if the measurement has a good quality flag, and

$$|\Delta T_\pi| < 1.0 \text{ ns} \qquad |\Delta T_\pi| < |\Delta T_K|.$$

  If not identified by TOF, a track is identified as a pion by dE/dx if the measurement was obtained from six or more track hits, the track momentum is less than 0.650 GeV/c, and

$$|\Delta E_\pi| < 3\sigma \qquad |\Delta E_\pi| < |\Delta E_K|.$$

  Kaon identification is the same but with the π and K indices switched in the above relations. To maximize efficiency one track in an event is allowed to be not identified; single misidentifications which can result are largely eliminated by the fitting procedure.

- require the tracks selected as K_S^0 candidates to have

$$|M_{\pi^+\pi^-} - M_{K^0}| < 30 \text{ MeV/c}^2$$

after recalculating the track parameters for a secondary vertex. Reconstructing the states $K^0_S\pi^+\pi^-\pi^+$ and $K^0_S\pi^+\pi^0$ must additionally have $l_{xy} >$ 2mm and $P(\chi^2_{xy}) > 0.01\%$.

- refit the event combinations. The constraint $M(X) = M(\bar{X})$ is added, assuming the reaction $e^+e^- \rightarrow X\bar{X} \rightarrow$ final state. Events containing K^0_S's and/or π^0's are subjected to mass constraints for those resonances. The event is retained if $P(\chi^2_{fit};\, n_c) > 0.02\%$ where n_c is the number of constraints ($\geq$5).

- following the second level fit, shower tracks selected as π^0 candidates are required to have

$$|\cos\theta_{\pi^0}| < 0.95$$

where θ_{π^0} is the π^0 decay angle in the π^0 rest frame. This cut rejects events where a low energy, spurious shower combines with a shower from a high energy photon to form an asymmetric π^0. Since π^0's are pseudoscalar mesons, they decay uniformly in $\cos\theta_{\pi^0}$, making the cut 95% efficient for real π^0's.

Real events peak at the D^+ mass in the fitted mass distribution for M(X). The signal region is defined to be:

- $1.862 < M(X) < 1.876$ GeV/c^2

These cuts delimit a $\pm 3\sigma$ region about the D^+ mass peak resulting from the reconstruction of the Cabibbo allowed final state $K^-\pi^+\pi^+$ vs. $K^+\pi^-\pi^-$ (discussed in Section A2-5.1).

A2-3 Estimating Efficiencies and Numbers of Events

Unlike the tagging approach, the fitting approach couples the kinematic topologies of the two D decays in a $D\bar{D}$ event and therefore requires that efficiencies be determined individually for the 21 signal topologies and the backgrounds. The number of expected events, n^{exp}_{ij}, for mode i opposite mode j is calculated according to

$$n_{ij}^{exp} = (2 - \delta_{ij}) n_{D\bar{D}} B_i B_j \varepsilon_{ij}$$

where δ_{ij} is a Kronecker delta function, $n_{D\bar{D}}$ is the number of produced $D\bar{D}$ events (=20,300±2900±1100), B_i is the branching fraction for mode i, and ε_{ij} is the efficiency for reconstructing mode i opposite mode j. The factor of $2 - \delta_{ij}$ prevents double counting events when mode i is also mode j. The formula is used when calculating signals and backgrounds.

A2-4 Background Cuts

A2-4.1 Cuts for $D^+ \to K^+\pi^-\pi^+$

The M(X) distribution for the seven topologies with $D^+ \to K^+\pi^-\pi^+$ after the initial event selection is shown in Figure A2.3. To reduce the known backgrounds--the Class I backgrounds $D^+ \to K^-\pi^+\pi^+$, $D^+ \to \bar{K}^{*0}\pi^+ \to (K^-\pi^+)\pi^+$ and $D^+ \to \bar{K}^0 K^+$; and the Class II backgrounds (refer to Table 5.1 and Table 5.2)--the following cuts have been added.

The Anti-K_S^0 Cut

This cut is the same as the anti-K_S^0 cut used in the tagging analysis (Section 5-4.3.). An event is retained if

- $|M_{\pi^+\pi^-} - M_{K^0}| > 30$ MeV/c^2

thereby reducing the $\bar{K}^0 K^+$ background. For this analysis this criteria removes > 96% of the $\bar{K}^0 K^+$ which survives the initial event selection, while retaining approximately 95% of the signal.

The Second Level Particle Identification Cuts

Since the particle identification criteria differ between the tagging analysis and this analysis, a different set of second level particle identification cuts are introduced to suppress the $K^-\pi^+\pi^+$ backgrounds. In reconstructing $K^+\pi^-\pi^+$, a K^+ must be identified by TOF and satisfy

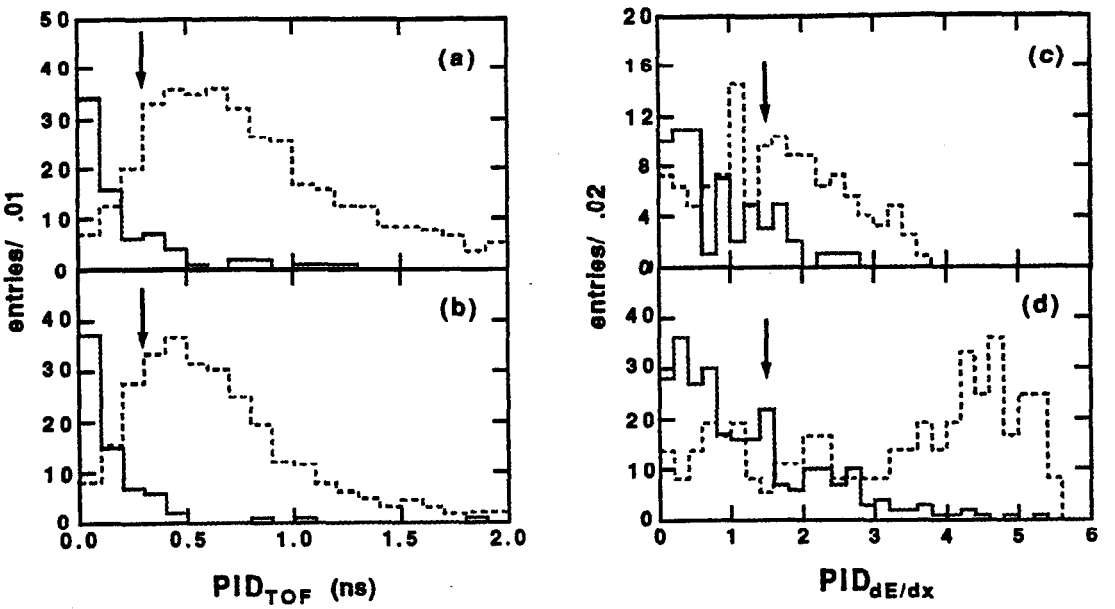

Figure A2.1 Double misidentification of $D^+ \rightarrow K^-\pi^+\pi^+$ when reconstructed as $K^+\pi^-\pi^+$. Plots (a) and (b) are PID_{TOF} (see text) distributions, respectively, for the K^+ and π^- tracks identified by TOF, while plots (c) and (d) are $PID_{\mathrm{dE/dx}}$ distributions for the K^+ and π^- tracks identified by dE/dx. The solid histograms show the distributions for Monte Carlo $K^-\pi^+\pi^+$ and the dashed histograms show the distributions for the desired $K^+\pi^-\pi^+$ signal. The arrows indicate the second level particle identification cuts.

- $PID_{\mathrm{TOF}K} \equiv (\Delta T_K + \Delta T_\pi)/2 > 0.3$ ns

or be identified by dE/dx and satisfy

- $PID_{\mathrm{dE/dx}K} \equiv (\Delta E_K + \Delta E_\pi)/2\sigma > 1.5$

Analogous relations must hold for a track to be given the pion assignment. (Note that a track with $PID_{\mathrm{TOF}K} = 0$ ns or $PID_{\mathrm{dE/dx}K} = 0$ is equally likely to be a kaon or a pion.) The effectiveness of these criteria are demonstrated in Figure A2.1. These cuts remove > 93% of the $K^-\pi^+\pi^+$ background which survives the anti-K^0_S cut, while retaining approximately 62% of the signal.

The Topology Cuts

As in the tagging analysis, the major Class II backgrounds are identified by reanalyzing the events for the alternate $D\overline{D}$ hypotheses. An event is discarded if any of the combinations fits to a background topology with

- $P(\chi^2_{\text{fit}}; n_c) > 0.02\%$
- $1.862 < \text{M}(X) < 1.876\ \text{GeV}/c^2$

Effectively all of the Class II backgrounds are found to be removed by these cuts. These cuts retain >99% of the signal when reconstructed opposite a $K^0_S\pi^+$ tag, 96% when opposite $K^0_S\pi^+\pi^-\pi^-$, 98% when opposite $K^0_S\pi^+\pi^0$, >99% when opposite $K^0_SK^+$, and 99% when opposite $K^+K^-\pi^+$.

A2-4.2 Cuts for $D^+ \to K^+\pi^0$

The fitted mass distribution for the topologies with $D^+ \to K^+\pi^0$ after the initial event selection is shown in Figure A2.4. Of the five Class I backgrounds found in the tagging analysis for this channel, $D^+ \to \overline{K}^0\pi^+$ and $D^+ \to \overline{K}^0K^+$ with $\overline{K}^0 \to K^0_L$ are eliminated in this analysis by directly reconstructing the π^0. To remove the remaining backgrounds--$D^+ \to \overline{K}^0\pi^+$ and $D^+ \to \overline{K}^0K^+$ with $\overline{K}^0 \to K^0_S \to \pi^0\pi^0$, and $D^+ \to \pi^+\pi^0$--two additional cuts are introduced.

The ΔM Cut

This kinematic cut is introduced to suppress all three backgrounds by comparing the unfitted invariant mass (M_{inv}) with the beam constrained mass (M_{beam}) for the $K^+\pi^0$ candidate. Distributions of $\Delta\text{M} \equiv \text{M}_{\text{inv}} - \text{M}_{\text{beam}}$ are shown in Figure A2.2for the three backgrounds and the signal. The requirement

- $100 < \Delta\text{M} < 120\ \text{MeV}/c^2$

is found to remove > 35% of the $\overline{K}^0\pi^+$, > 60% of the $\overline{K}^0K^+$ and > 51% of the $\pi^+\pi^0$ backgrounds while retaining typically 74% of the signal.

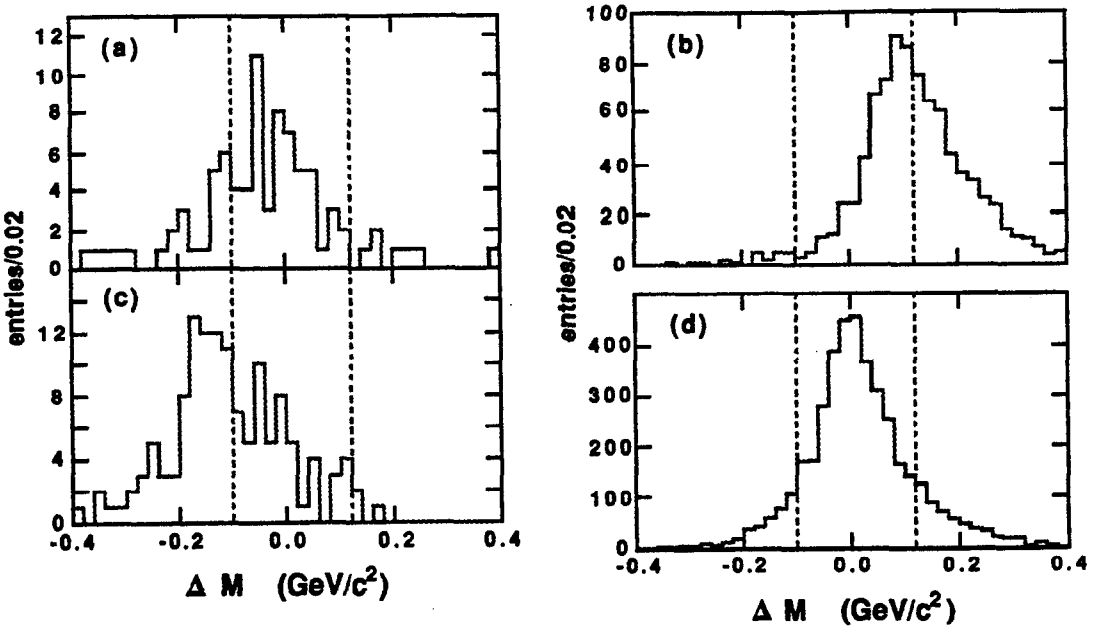

Figure A2.2 Distributions of $\Delta M \equiv M_{inv} - M_{beam}$ for the $K^+\pi^0$ backgrounds (a) $D^+ \to \bar{K}^0\pi^+$, $\bar{K}^0 \to K_S^0 \to \pi^0\pi^0$; (b) $D^+ \to \pi^+\pi^0$; and (c) $D^+ \to \bar{K}^0K^+$, $\bar{K}^0 \to K_S^0 \to \pi^0\pi^0$ and for (d) the signal (with all modes generated and reconstructed opposite $D^- \to K^+\pi^-\pi^-$). The dashed lines indicate the ΔM cuts.

The Second Level Particle Identification Cuts

These cuts are essentially the same as those for $K^+\pi^-\pi^+$ and are introduced to remove the $\bar{K}^0\pi^+$ and $\pi^+\pi^0$ backgrounds. In reconstructing $K^+\pi^0$, the K^+ must be identified by TOF and satisfy

- $PID_{TOF,K} > 0.2$ ns

Again the high momentum of the kaon prevents reliable use of dE/dx information. This cut removes, respectively, > 80% and > 91% of the $\bar{K}^0\pi^+$ and $\pi^+\pi^0$ backgrounds which survive the initial event selection, while retaining approximately 65% of the signal.

A2-4.3 Cuts for $D^+ \to K^{*+}\pi^0 \to (K^0\pi^+)\pi^0$

The fitted mass distribution for the topologies with $D^+ \to K^{*+}\pi^0 \to (K^0\pi^+)\pi^0$ after the initial event selection is shown in Figure A2.5. Of the seven Class I backgrounds found in the tagging analysis for this channel, $D^+ \to \phi\pi^+$, $\phi \to K_S^0K_L^0$ is eliminated in this

analysis by reconstructing the π^0. To reduce the remaining backgrounds--$D^+ \to \bar{K}^0\rho^+ \to \bar{K}^0(\pi^+\pi^0)$, $D^+ \to \bar{K}^{*0}\pi^+ \to (\bar{K}^0\pi^0)\pi^+$, $D^+ \to \bar{K}^0\pi^+\pi^0$[nr], $D^+ \to \bar{K}^0\pi^+\pi^0\pi^0$, $D^+ \to \bar{K}^{*0}e^+\nu_e \to (\bar{K}^0\pi^0)e^+\nu_e$ and $\bar{K}^{*0}\mu^+\nu_\mu \to (\bar{K}^0\pi^0)\mu^+\nu_\mu$--the following cuts have been added.

The Dalitz Cuts

These are the same cuts as those for the tagging analysis. In reconstructing $K^0\pi^+\pi^0$, the $K^0\pi^+$ and $\pi^+\pi^0$ invariant masses, formed from the fitted track momenta, must satisfy

- $0.6 < M^2_{K\pi} < 1.0$ $(GeV/c^2)^2$
- $M^2_{\pi\pi} > 1.3$ $(GeV/c^2)^2$

In terms of the backgrounds, these cuts remove > 97 % of $\bar{K}^0\rho^+$, > 94 % of $\bar{K}^{*0}\pi^+$, > 91 % of $\bar{K}^0\pi^+\pi^0$[nr], > 60 % of $\bar{K}^0\pi^+\pi^0\pi^0$, and effectively all of $\bar{K}^{*0}e^+\nu_e$ and $\bar{K}^{*0}\mu^+\nu_\mu$, and retains typically 40 % of the signal.

The ΔM Cut

This is the same cut as that for $K^+\pi^0$, targeted for the $\bar{K}^0\pi^+\pi^0\pi^0$ background. It removes > 75 % of the $\bar{K}^0\pi^+\pi^0\pi^0$ events which survive the Dalitz cut and retains approximately 77 % of the signal.

A2-5 Results

$D^+ \to K^+\pi^-\pi^+$

Figure A2.3 shows the application of the cuts to the data for $K^+\pi^-\pi^+$. After all cuts are applied two candidate events remain in the signal region--one with the topology $K^-\pi^+\pi^-$ versus $K^0_S\pi^+$ the other with the topology $K^+\pi^-\pi^+$ versus $K^0_S\pi^-\pi^+\pi^-$. The former event is Event B found from the tagging analysis, reconstructed in this analysis with the same track combinations and mass assignments; M(X) = 1.8700 GeV/c^2 and $P(\chi^2_{fit})$ = 35.1 % for the event. The second event, displayed in Figure A2.6, was not found in the

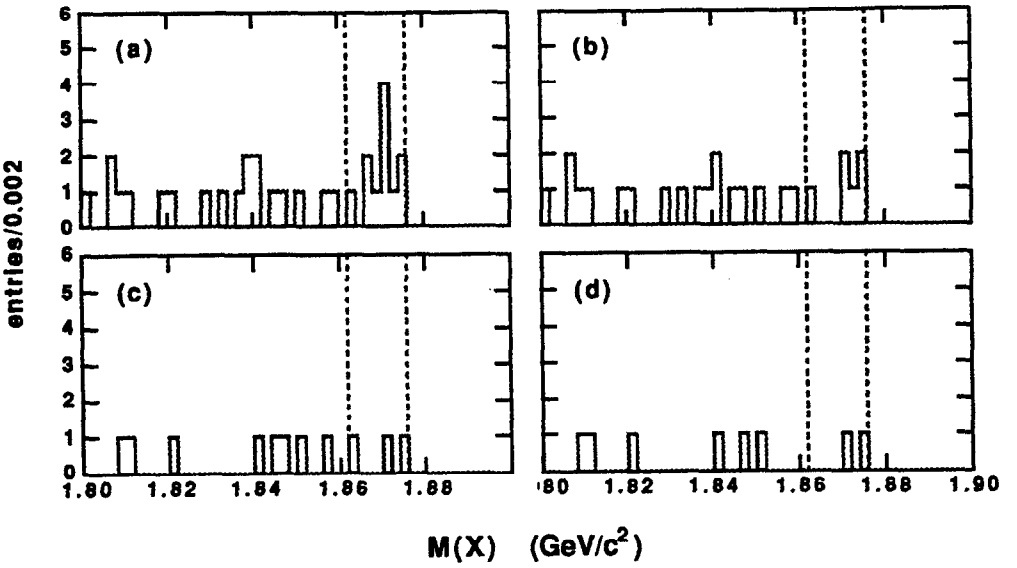

Figure A2.3 The summed M(X) distributions for $K^+\pi^-\pi^+$ after (a) the initial event selection, (b) the anti-K^0_S cut, (c) the second level particle identification cuts and (d) the topology cuts.

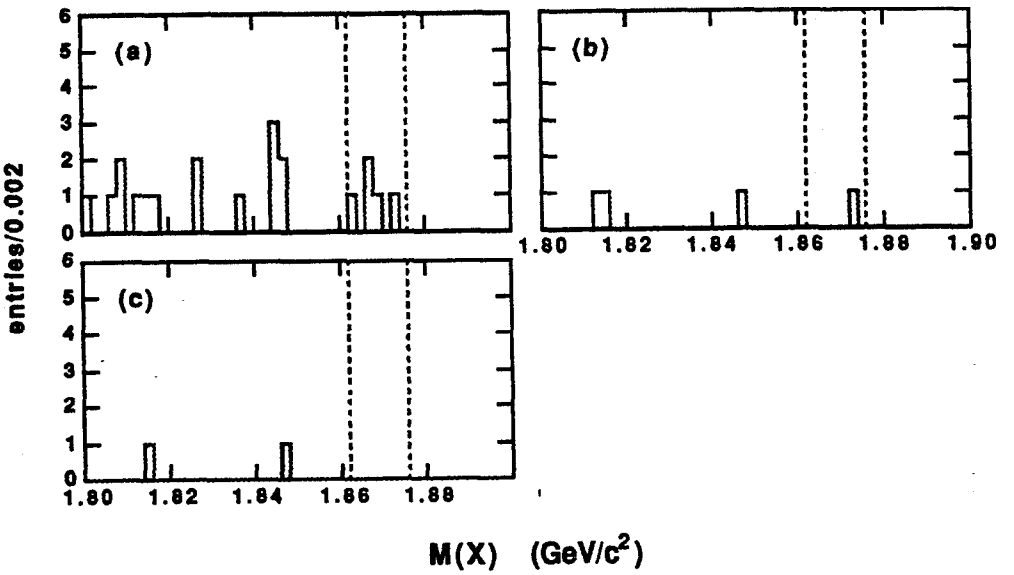

Figure A2.4 The summed M(X) distributions for $K^+\pi^0$ after (a) the initial event selection, (b) the ΔM cut and (c) the second level particle identification cuts.

tagging analysis, where it had been removed by the $D^0\overline{D}^0$ topology cut and would have otherwise fallen outside the signal region with M_{beam} = 1.8761 GeV/c^2 for the recoil;

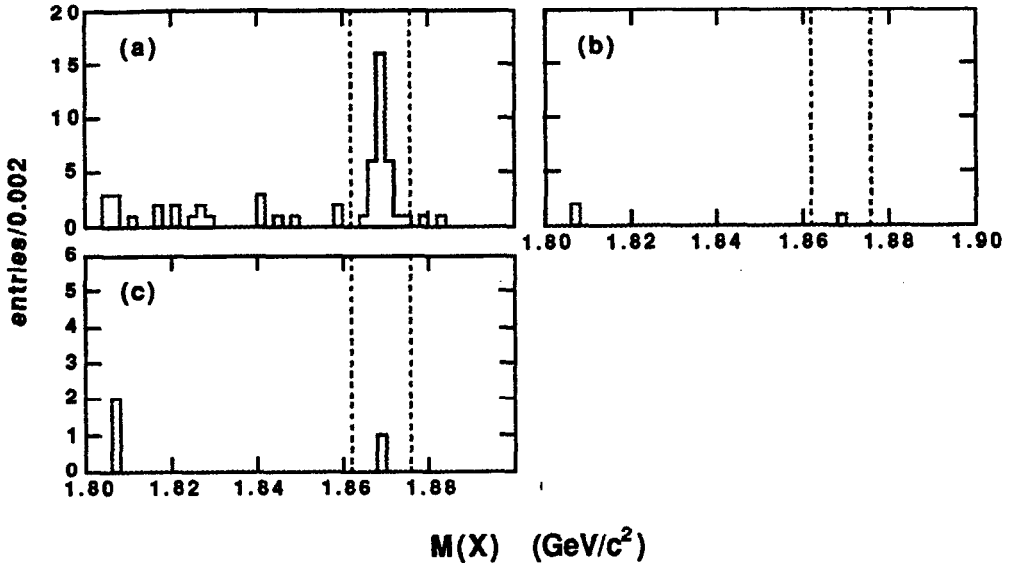

Figure A2.5 The summed M(X) distributions for $K^{*+}\pi^0$ after (a) the initial event selection, (b) the ΔM cut and (c) the second level particle identification cuts.

M(X) = 1.8746 GeV/c^2 and $P(\chi^2_{fit}) = 0.5\%$ for this event. Event A from the tagging analysis is not recovered here due to the more stringent particle identification requirements used in the initial event selection, and Event B is lost after failing the kinematic fits with a χ^2 exceeding 50.

$D^+ \to K^+\pi^0$

Figure A2.4 shows the application of the cuts to the data for $K^+\pi^0$. After all cuts are applied no candidate events remain in the signal region. One event, with the topology $K^+\pi^0$ versus $K^+\pi^-\pi^-$, is lost from the signal region by the second level particle identification cuts; that event is displayed in Figure A2.7. The particle identification cuts removed the event on the basis that it had no time-of-flight (or dE/dx) information for the K^+ track. The tagging analysis removed this event when the veto cut was applied; no showers were found greater than 400 MeV within $\cos\alpha > 0.98$. For this event M(X) = 1.8730 GeV/c^2 and $P(\chi^2_{fit}) = 54.8\%$.

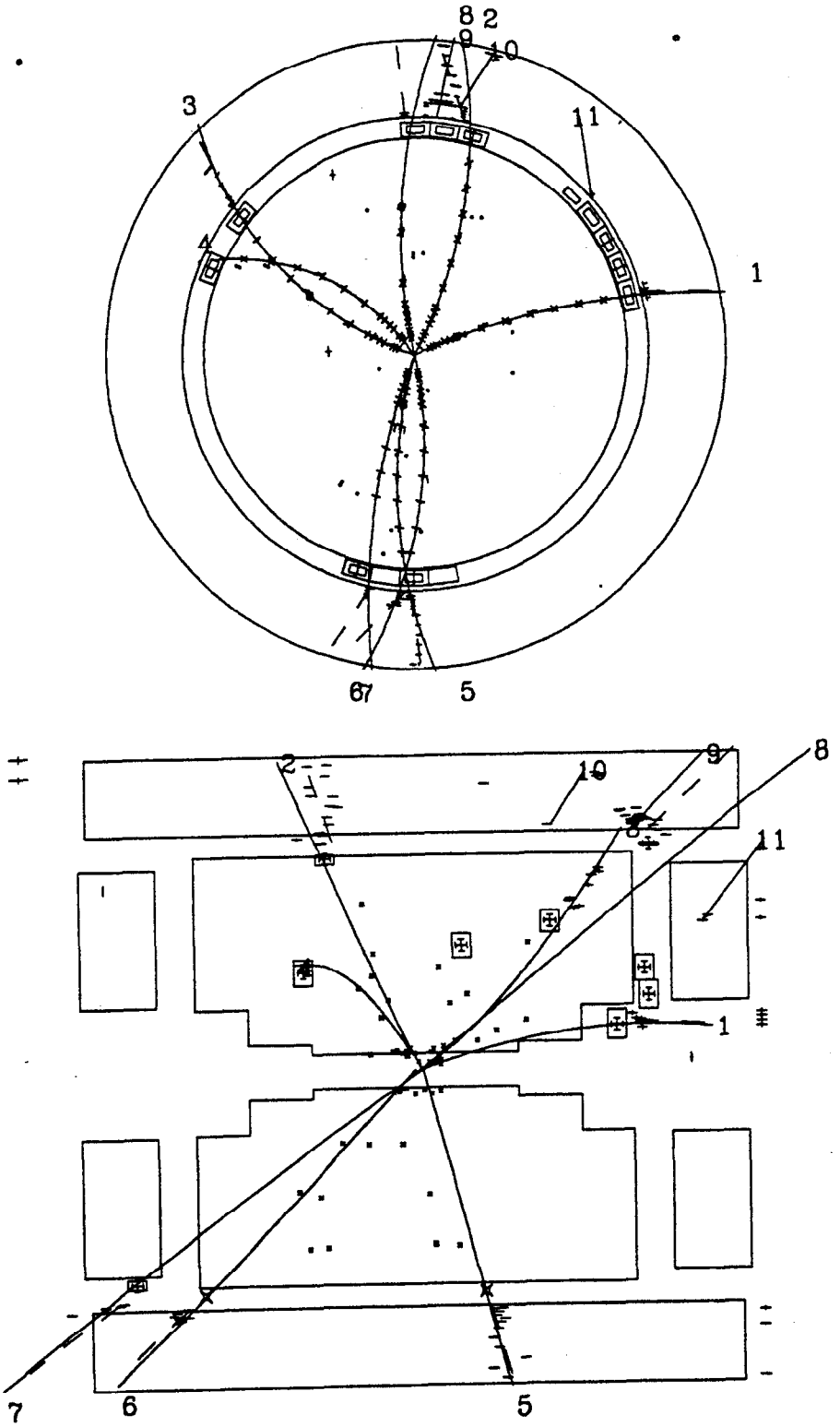

Figure A2.6 The $K^+\pi^-\pi^+$ versus $K^0_S\pi^-\pi^+\pi^-$ candidate event.

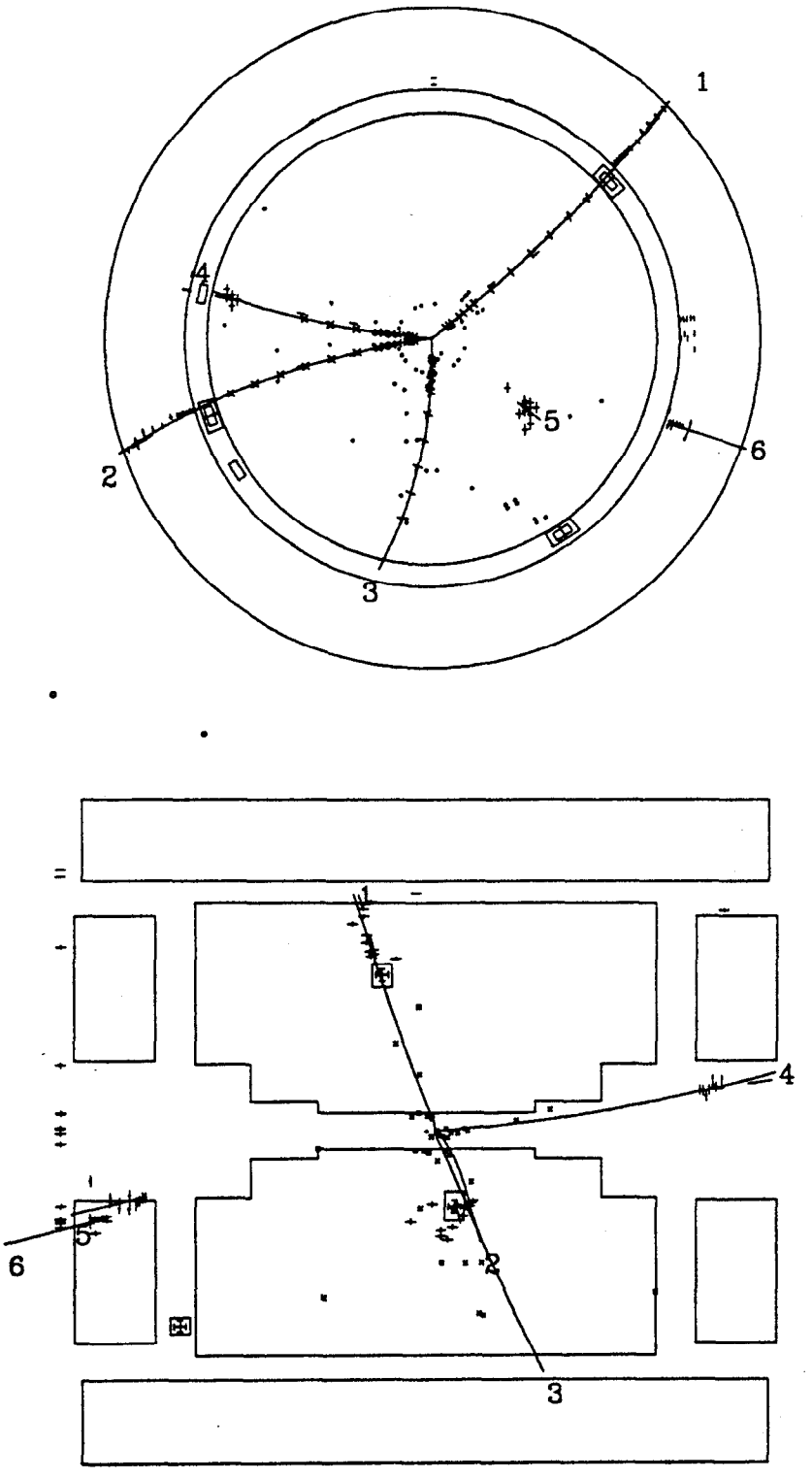

Figure A2.7 The $K^+\pi^0$ signal event (versus $K^+\pi^-\pi^-$) lost to the kaon identification.

$D^+ \to K^{*+}\pi^0$

Figure A2.5 shows the application of the cuts to the data for $K^{*+}\pi^0 \to (K^0\pi^+)\pi^0$. After all cuts are applied one candidate event, displayed in Figure A2.8, remains in the signal region. The topology for this event is $K^0_S\pi^+\pi^0$ versus $K^+\pi^-\pi^-$. The tagging analysis did not find the event because the invariant mass of the $K^+\pi^-\pi^-$ combination is 1.811 GeV/c^2, below the lower 1.819 GeV/c^2 cut applied by the tagging procedure (the corresponding beam constrained mass is 1.8672 GeV/c^2, which does pass the tagging criteria). For this event M(X) = 1.8690 GeV/c^2 and $P(\chi^2_{\rm fit}) = 32.9\,\%$.

A2-5.1 Analysis Tests

Two series of tests were made of the analysis procedures. The first series studies the fitting procedure and the initial event selection criteria by searching for the Cabibbo-allowed channel $D^+ \to K^-\pi^+\pi^+$ opposite the seven dominant modes of the D^+. The second series studies the data reduction cuts by comparing the number of expected events lost against the observed number lost.

Search for $D^+ \to K^-\pi^+\pi^+$

Figure A2.9 shows the sum of the M(X) distributions for $K^-\pi^+\pi^+$ opposite $K^0\pi^-$, $K^+\pi^-\pi^-$, $K^0\pi^-\pi^+\pi^-$, $K^0\pi^-\pi^0$, K^0K^-, $K^+K^-\pi^-$, and $K^+\pi^-\pi^-\pi^0$. Table A2.1 lists the efficiencies for the seven final state topologies and the number of expected events. The total number expected, 127±14, is in good agreement with 115 observed events. Errors are statistical only, reflecting the statistical uncertainties from (and correlations among) the number of D^+D^- events, the branching fractions, and the Monte Carlo statistics. No significant background from charm production is found. The number of u, d, s events expected is $0.31^{+0.30}_{-0.09}$.

Test of the Background Cuts

Tables A2.2 through A2.4 list the three tests of the background cuts for $K^+\pi^-\pi^+$, $K^+\pi^0$ and $K^{*+}\pi^0 \to (K^0\pi^+)\pi^0$ with the total numbers of events predicted and observed to

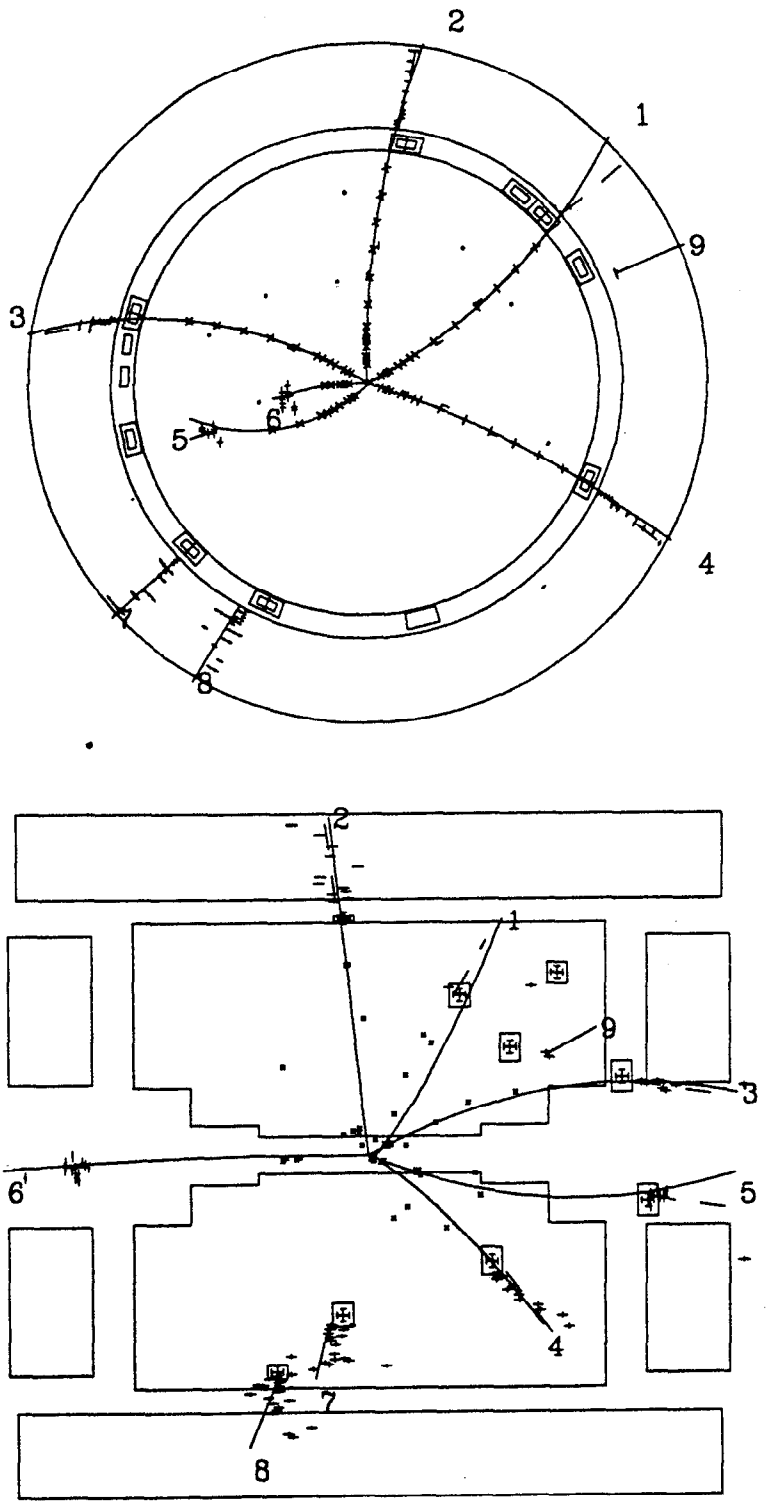

Figure A2.8 The $K^{*+}\pi^0$, $K^{*+} \to K^0\pi^+$ versus $K^+\pi^-\pi^-$ candidate event.

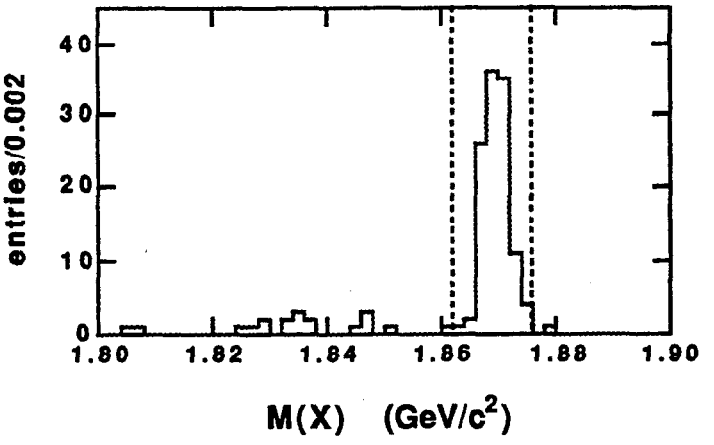

Figure A2.9 Sum of the M(X) distributions for $K^-\pi^+\pi^+$ opposite $K^0\pi^-$, $K^+\pi^-\pi^-$, $K^0\pi^-\pi^+\pi^-$, $K^0\pi^-\pi^0$, K^0K^-, $K^+K^-\pi^-$, and $K^+\pi^-\pi^-\pi^0$, with $K^0 \to \pi^+\pi^-$.

Table A2.1 Analysis test of $D^+ \to K^-\pi^+\pi^+$. The efficiencies are averages of the efficiencies for $D^+ \to K^-\pi^+\pi^+$[nr] and $D^+ \to \bar{K}^{*0}\pi^+ \to (K^-\pi^+)\pi^+$, weighted by the branching fractions for the two channels.

Topology	Efficiency (%)	Expected Number	Observed Number
$K^-\pi^+\pi^+$ vs. $K^0\pi^-$	20.5±0.5	8.3±1.2	8
$K^+\pi^-\pi^-$	41.8±0.1	70.3±13.5	64
$K^0\pi^-\pi^+\pi^-$	11.1±0.3	9.3±2.1	10
$K^0\pi^-\pi^0$	8.7±0.2	11.3±2.7	17
K^0K^-	18.6±0.4	2.4±0.7	0
$K^+K^-\pi^-$	17.1±0.4	7.6±3.5	7
$K^+\pi^-\pi^-\pi^0$	8.4±0.2	18.0±2.6	9
Total $K^-\pi^+\pi^+$ Events		127±14	115

be lost for a given cut. For the $K^+\pi^-\pi^+$ analysis, good agreement is found between an expected total number of 8.3±1.6 events versus an observed number of 9 events. For the $K^+\pi^0$ and $K^{*+}\pi^0$ analyses, however, excesses are found with the total observed numbers;

for $K^+\pi^0$ a total of $1.0^{+0.4}_{-0.2}$ events are expected while 5 events are observed, and for $K^{*+}\pi^0$ 21.1 ± 1.6 events are expected while 31 events are observed. Some or all of this excess may be backgrounds originating from shower split-offs, albedo, and other processes not modelled by the shower simulation. For both analyses the excesses occur largely at the first cut, suggesting that these backgrounds are no longer significant after the full analyses.

A2-5.2 Detection Efficiencies

Table A2.5 gives the 21 detection efficiencies for $K^+\pi^-\pi^+$, $K^+\pi^0$ and $K^{*+}\pi^0 \rightarrow (K^0\pi^+)\pi^0$ opposite the seven dominant D^+ decay channels. In determining the numbers, the decays $D^+ \rightarrow \bar{K}^0\pi^+\pi^-\pi^+$, $D^+ \rightarrow K^-K^+\pi^+$ and $D^+ \rightarrow K^-\pi^+\pi^+\pi^0$ were generated according to phase space. The decay $D^+ \rightarrow K^-\pi^+\pi^+$ was generated according to $D^+ \rightarrow \bar{K}^{*0}\pi^+ \rightarrow (K^-\pi^+)\pi^+$ and $D^+ \rightarrow K^-\pi^+\pi^+$[nr], since that channel is the dominant D^+ decay mode; the efficiencies are weight by the respective branching fractions to obtain the number in the table. Also, $D^+ \rightarrow \bar{K}^0\pi^+\pi^0$ was generated according to phase space when paired with $D^+ \rightarrow K^+\pi^-\pi^+$ and $D^+ \rightarrow K^+\pi^0$ but generated as $D^+ \rightarrow \bar{K}^{*0}\pi^+ \rightarrow (\bar{K}^0\pi^+)\pi^0$, $D^+ \rightarrow \bar{K}^0\rho^+ \rightarrow \bar{K}^0(\pi^+\pi^0)$, $D^+ \rightarrow \bar{K}^0\pi^+\pi^0$[nr] when paired with $D^+ \rightarrow K^{*+}\pi^0 \rightarrow (K^0\pi^+)\pi^0$, due to the similarity in the final states of those decays. The errors given in the table are statistical and systematic respectively. Discussion of the latter is postponed until Section A2-5.4.

A2-5.3 Background Estimates

Tables A2.6 through A2.8 give the sums of the background levels for the three sets of doubly Cabibbo suppressed topologies. Included are the contributions from the u, d, s background. The total number of events expected are $1.09\pm0.32^{+0.17}_{-0.25}$, $0.25^{+0.27}_{-0.07}\pm0.05$ and $0.46^{+0.25}_{-0.09}{}^{+0.14}_{-0.16}$ for $K^+\pi^-\pi^+$, $K^+\pi^0$ and $K^{*+}\pi^0$, respectively.

Table A2.2 The application of the background reduction cuts for $K^+\pi^-\pi^+$ as a comparison of the observed numbers of events removed against the expected numbers.

Cut	Expected Loss	Observed Loss
Anti-K^0_S	$5.0^{+1.5}_{-1.4}$	5
Second level particle id.	$2.5^{+0.4}_{-0.3}$	3
Topology	0.8±0.1	1
Total Number	8.3±1.6	9

Table A2.3 The application of the background reduction cuts for $K^+\pi^0$ as a comparison of the observed numbers of events removed against the expected numbers.

Cut	Expected Loss	Observed Loss
ΔM	$0.4^{+0.2}_{-0.1}$	4
Second level particle id.	$0.6^{+0.3}_{-0.1}$	1
Total Number	$1.0^{+0.4}_{-0.2}$	5

Table A2.4 The application of the background reduction cuts for $K^{*+}\pi^0 \rightarrow (K^0\pi^+)\pi^0$ as a comparison of the observed numbers of events removed against the expected numbers.

Cut	Expected Loss	Observed Loss
Dalitz	20.9±1.6	31
ΔM	$0.24^{+0.24}_{-0.04}$	0
Total Number	21.1±1.6	31

Table A2.5 Detection efficiencies (in percent) for the doubly Cabibbo suppressed topologies.

Mode j \ Mode i	$K^+\pi^-\pi^+$	$K^+\pi^0$	$K^{*+}\pi^0$, $K^{*+}\to K^0\pi^+$, $K^0\to\pi^+\pi^-$
$K^0\pi^-, K^0\to\pi^+\pi^-$	$12.7\pm0.3^{+2.0}_{-2.7}$	$9.9\pm0.2^{+1.7}_{-1.9}$	$3.2\pm0.1^{+0.4}_{-0.8}$
$K^+\pi^-\pi^-$	$13.3\pm0.3^{+2.1}_{-2.4}$	$9.8\pm0.3\pm1.7$	$3.2\pm0.1^{+0.4}_{-0.7}$
$K^0\pi^-\pi^+\pi^-, K^0\to\pi^+\pi^-$	$6.5\pm0.2^{+1.1}_{-1.5}$	$5.1\pm0.2^{+0.9}_{-1.1}$	$1.4\pm0.1^{+0.2}_{-0.4}$
$K^0\pi^-\pi^0, K^0\to\pi^+\pi^-$	$5.2\pm0.2^{+1.0}_{-1.6}$	$4.1\pm0.1^{+0.8}_{-1.2}$	$1.7\pm0.1^{+0.3}_{-0.5}$
$K^0K^-, K^0\to\pi^+\pi^-$	$11.6\pm0.3^{+2.5}_{-2.1}$	$8.9\pm0.2^{+2.1}_{-1.5}$	$2.6\pm0.1^{+0.4}_{-0.6}$
$K^+K^-\pi^-$	$10.4\pm0.3^{+1.6}_{-1.9}$	$8.2\pm0.2\pm1.4$	$2.4\pm0.1^{+0.3}_{-0.5}$
$K^+\pi^-\pi^-\pi^0$	$5.1\pm0.2^{+1.0}_{-1.5}$	$4.5\pm0.2^{+0.9}_{-1.2}$	$1.2\pm0.1^{+0.2}_{-0.4}$

Table A2.6 Sums of the expected numbers of background events for $D^+\to K^+\pi^-\pi^+$ opposite $K^0\pi^-$, $K^+\pi^-\pi^-$, $K^0\pi^-\pi^+\pi^-$, $K^0\pi^-\pi^0$, K^0K^-, $K^+K^-\pi^-$, and $K^+\pi^-\pi^-\pi^0$, including the contribution from the continuum.

D Background	Number of Events
$D^+\to\bar{K}^{*0}\pi^+\to(K^-\pi^+)\pi^+$	$0.008\pm0.007^{+0.003}_{-0.001}$
$D^+\to K^-\pi^+\pi^+$[nr]	$0.021^{+0.007+0.009}_{-0.005-0.004}$
$D^+\to\bar{K}^0K^+\to(\pi^+\pi^-)K^+$	$0.045\pm0.015^{+0.007}_{-0.009}$
Total expected D contribution	$0.074\pm0.018^{+0.022}_{-0.018}$
Total expected u, d, s contribution	$1.02\pm0.32^{+0.17}_{-0.25}$
Total expected number of events	$1.09\pm0.32^{+0.17}_{-0.25}$

A2-5.4 Systematic Errors

The following sources are considered to contribute to the systematic errors given for the reconstruction efficiencies and numbers of background events. The errors are quoted in terms of relative uncertainty.

Table A2.7 Sums of the expected numbers of background events for $D^+ \to K^+\pi^0$ opposite $K^0\pi^-$, $K^+\pi^-\pi^-$, $K^0\pi^-\pi^+\pi^-$, $K^0\pi^-\pi^0$, K^0K^-, $K^+K^-\pi^-$, and $K^+\pi^-\pi^-\pi^0$, including the contribution from the continuum.

D Background	Number of Events
$D^+ \to \bar{K}^0\pi^+ \to (\pi^0\pi^0)\pi^+$	$0.011\pm0.002\pm0.003$
$D^+ \to \bar{K}^0K^+ \to (\pi^0\pi^0)K^+$	$0.025\pm0.008\pm0.007$
$D^+ \to \pi^+\pi^0$	$0.008^{+0.002}_{-0.001}\pm0.002$
Total expected D contribution	$0.044\pm0.010\pm0.012$
Total expected u, d, s contribution	$0.20^{+0.27}_{-0.06}\pm0.05$
Total expected number of events	$0.25^{+0.27}_{-0.07}\pm0.05$

Table A2.8 Sums of the expected numbers of background events for $D^+ \to K^{*+}\pi^0 \to (K^0\pi^+)\pi^0$ opposite $K^0\pi^-$, $K^+\pi^-\pi^-$, $K^0\pi^-\pi^+\pi^-$, $K^0\pi^-\pi^0$, K^0K^-, $K^+K^-\pi^-$, and $K^+\pi^-\pi^-\pi^0$, including the contribution from the continuum.

D Background	Number of Events
$D^+ \to \bar{K}^0\rho^+ \to \bar{K}^0(\pi^+\pi^0)$	$0.13^{+0.03+0.05}_{-0.02-0.06}$
$D^+ \to \bar{K}^{*0}\pi^+ \to (\bar{K}^0\pi^0)\pi^+$	$0.09\pm0.03\pm0.05$
$D^+ \to \bar{K}^0\pi^+\pi^0$[nr]	$0.14\pm0.07^{+0.10}_{-0.11}$
Total expected D contribution	$0.37\pm0.09^{+0.14}_{-0.16}$
Total expected u, d, s contribution	<0.28
Total expected number of events	$0.46^{+0.25+0.14}_{-0.09-0.16}$

1) Charged track reconstruction efficiency. A −1% error is attributed for each charged track.

2) The lack of cuts for the fiducial regions of the detector. A −1% error is attributed for each charged track.

3) K_S^0 vertex requirements. A ±5% error is attributed to topologies with a $K_S^0\pi^+\pi^-\pi^+$ or $K_S^0\pi^+\pi^0$ final state.

4) Photon detection efficiency. A –2.5% error is given for each reconstructed photon. The decay channels $D^+ \to K^-\pi^+\pi^+\pi^0$, $D^+ \to \bar{K}^0\rho^+ \to \bar{K}^0(\pi^+\pi^0)$, $D^+ \to \bar{K}^{*0}\pi^+ \to (\bar{K}^0\pi^0)\pi^+$, and $D^+ \to \bar{K}^0\pi^+\pi^0$[nr] produce a significant proportion of photons with energy below 100 MeV. To topologies with these decays, an additional –2.5% is attributed, except when the $\bar{K}^0\pi^+\pi^0$ decays are reconstructed as background to $D^+ \to K^{*+}\pi^0 \to (K^0\pi^+)\pi^0$.

5) Monte Carlo modelling of photons. A ±7% error is given for each photon.

6) Particle identification. Tracks correctly identified by the first level particle identification criteria are given a ±1% error, except those resulting from two body decays such as $D^+ \to \bar{K}^0\pi^+$. Because of the higher momentum, studies suggest a +7% error for kaon identification and a –3% error for pion identification. The second level particle identification criteria introduces an estimated +13% for kaon identification and a –4% for pion identification. For the backgrounds, misidentified tracks are assigned +20% error.

7) Mass cuts and definition of the signal regions. Errors of ±1% and ±5% are given to account for possible tails in the signal and background distributions, respectively.

8) Fit χ^2 confidence level cut. A ±5% error is attributed, based on studies of the cut with the $K^-\pi^+\pi^+$ test.

The following source applies only to the $K^+\pi^-\pi^+$ efficiencies.

9) $K^+\pi^-\pi^+$ resonant substructure. Variations in the efficiencies for $K^+\pi^-\pi^+$ due to the possible resonant decays $D^+ \to K^+\rho^0 \to K^+(\pi^-\pi^+)$ and $D^+ \to K^{*0}\pi^+ \to (K^+\pi^-)\pi^+$ are approximately ±7%

The following additional sources have been considered for the errors on the number of D background events.

10) Branching fractions for the decay processes. Confer Table 4.1, Table 5.6, Table 6.1, and Table 7.1. for relative errors.

11) Number of produced D^+D^- events. The error from this number--20300±2900±1100 events--is ±5.4%.

The following source contributes to the systematic error on the number of u, d, s background events.

12) Integrated Luminosity for the $\psi(3770)$ data set. This contributes a ±5% error.

The total errors quoted in Tables A2.5 through A2.8 are obtained by propagating biased errors linearly and the remaining errors in quadrature.

A2-6 Upper Limits for $B(D^+ \to K^+\pi^-\pi^+)$, $B(D^+ \to K^+\pi^0)$ and $B(D^+ \to K^{*+}\pi^0)$

Again a maximum likelihood procedure is performed to obtain upper limits for $B(D^+ \to K^+\pi^-\pi^+)$, $B(D^+ \to K^+\pi^0)$ and $B(D^+ \to K^{*+}\pi^0)$. The following notation is used to describe likelihood function for this analysis:

- $\mu_s \equiv$ the true number of doubly Cabibbo suppressed signal events.
- $\mu_{b.D\bar{D}}$ ($n_{b.D\bar{D}}$) $\equiv$ the true (estimated) total number of background events from charm production.
- $\mu_{b.uds}$($n_{b.uds}$) $\equiv$ the true (estimated) total number of background events from u, d, s production.
- $n_{obs} \equiv$ the observed number of signal events.
- $\mu_{D\bar{D}}$ ($n_{D\bar{D}}$) $\equiv$ the true (estimated) number of produced D^+D^- events.
- β_i (b_i) $\equiv$ the true (estimated) branching fractions for decay mode i (i = "$\bar{K}^0\pi^+$", "$K^-\pi^+\pi^+$", "$\bar{K}^0\pi^+\pi^-\pi^+$", "$\bar{K}^0\pi^+\pi^0$", "$\bar{K}^0K^+$", "$K^-K^+\pi^+$", and "$K^-\pi^+\pi^+\pi^0$").

- $\vec{\mu}$, ($\hat{\vec{b}}$) ≡ the vector of $\mu_{D\bar{D}}$, the β_i's, and $\mu_{b.D\bar{D}}$ ($n_{D\bar{D}}$, the b_i's, and $n_{b.D\bar{D}}$).
- V ≡ the covariance matrix of the $n_{D\bar{D}}$, the b_i's, and $n_{b.D\bar{D}}$.
- $\eta_{si}(\varepsilon_{si})$ ≡ the true (estimated) reconstruction efficiency of the doubly Cabibbo suppressed decay mode opposite decay mode i.
- σ_{si} ≡ the statistical standard deviations on the ε_{si}'s.
- $\boldsymbol{p}$ ≡ the set of true quantities.
- $\hat{\boldsymbol{p}}$ ≡ the set of estimated quantities.

The joint likelihood functions used in the calculation of the three limits have the form

$$\mathcal{L}(n_{obs}, \boldsymbol{p}; \hat{\boldsymbol{p}}) = \mathcal{P}(n_{obs}; \mu_s + \mu_{b.D\bar{D}} + \mu_{b.uds}) \times [\prod_i \mathcal{G}(\eta_{si}; \varepsilon_{si}, \sigma_{si})]\, \mathcal{M}(\vec{\mu}; \hat{\vec{b}}, V)\, \mathcal{P}(\alpha n_{b.uds}; \alpha\mu_{b.uds})$$

where $\mathcal{P}$, $\mathcal{G}$, and $\mathcal{M}$ represent Poisson, Gaussian and multivariate Gaussian distributions, respectively. The multivariate distribution accounts for the correlations that exist among the number of D background events, the number of produced D^+D^- events and the branching fractions for the seven dominant D^+ decay modes.[24][61] The data for the three covariant matrices are provided in Table A2.9

The maximum likelihood fit for a given doubly Cabibbo suppressed mode is subjected to the constraint

$$\mu_s = 2\mu_{D\bar{D}} B_s \sum_i \beta_i \eta_{si}$$

where B_s is the branching fraction for the signal channel. The likelihood function is integrated numerically to find the 90% confidence level, and systematic errors are treated as before.

Table A2.9 The covariances among the number of produced D^+D^-, the Mark III branching fractions for the seven dominant D^+ decays and the numbers of background D events.

	$n_{D\bar{D}}$	$B(\bar{K}^0\pi^+)$	$B(K^-\pi^+\pi^+)$	$B(\bar{K}^0\pi^+\pi^-\pi^+)$	$B(\bar{K}^0\pi^+\pi^0)$	$B(\bar{K}^0K^+)$	$B(K^-K^+\pi^+)$	$B(K^-\pi^+\pi^+\pi^0)$
$B(\bar{K}^0\pi^+)$	−13.4							
$B(K^-\pi^+\pi^+)$	−36.7	5.82×10^{-5}						
$B(\bar{K}^0\pi^+\pi^-\pi^+)$	−25.0	3.97×10^{-5}	1.09×10^{-4}					
$B(\bar{K}^0\pi^+\pi^0)$	−41.9	6.80×10^{-5}	1.81×10^{-4}	1.25×10^{-4}				
$B(\bar{K}^0K^+)$	−4.25	7.93×10^{-6}	1.85×10^{-5}	1.26×10^{-5}	2.16×10^{-5}			
$B(K^-K^+\pi^+)$	−2.16	3.44×10^{-6}	9.97×10^{-6}	6.45×10^{-6}	1.07×10^{-5}	1.09×10^{-6}		
$B(K^-\pi^+\pi^+\pi^0)$	0	0	0	0	0	0	0	
$n_{b\bar{D}D}$ $(K^+\pi^-\pi^+)$	−26.0	4.70×10^{-5}	1.20×10^{-4}	9.62×10^{-5}	1.53×10^{-4}	4.95×10^{-5}	1.29×10^{-5}	1.48×10^{-5}
$n_{b\bar{D}D}$ $(K^+\pi^0)$	−14.0	2.75×10^{-5}	6.27×10^{-5}	4.56×10^{-5}	9.82×10^{-5}	2.80×10^{-5}	6.00×10^{-6}	1.95×10^{-5}
$n_{b\bar{D}D}$ $(K^{*+}\pi^0)$	−112.1	1.86×10^{-4}	5.04×10^{-4}	4.00×10^{-4}	2.18×10^{-3}	6.34×10^{-5}	5.00×10^{-5}	6.91×10^{-5}

Upper Limit for $B(D^+ \to K^+\pi^-\pi^+)$

Figure A2.10(a) displays the likelihood function for $B(D^+ \to K^+\pi^-\pi^+)$ without (dashed curve) and with (solid curve) systematic errors included; the arrows indicate the 90% confidence levels. With systematic errors neglected, $B(D^+ \to K^+\pi^-\pi^+) < 0.51\%$. The systematic errors increase this limit to

$$B(D^+ \to K^+\pi^-\pi^+) < 0.78\% \text{ @ } 90\% \text{ CL}$$

Upper Limit for $B(D^+ \to K^+\pi^0)$

Figure A2.10(b) displays the likelihood function for $B(D^+ \to K^+\pi^0)$. With systematic errors neglected, $B(D^+ \to K^+\pi^0) < 0.35\%$. The systematic errors increase this limit to

$$B(D^+ \to K^+\pi^0) < 0.51\% \text{ @ } 90\% \text{ CL}$$

Upper Limit for $B(D^+ \to K^{*+}\pi^0)$

Figure A2.10(c) displays the likelihood function for $B(D^+ \to K^{*+}\pi^0)$. With systematic errors neglected, $B(D^+ \to K^{*+}\pi^0) < 7.4\%$. The systematic errors increase this limit to

$$B(D^+ \to K^{*+}\pi^0) < 11.6\% \text{ @ } 90\% \text{ CL}$$

A2-7 Upper Limits for $|\bar{\rho}_{K\pi\pi}|^2$, $|\bar{\rho}_{K\pi^0}|^2$ and $|\bar{\rho}_{K^*\pi^0}|^2$

The maximum likelihood procedure performed to obtain upper limits for the branching fractions is also used to obtain limits on $|\bar{\rho}_{K\pi\pi}|^2$, $|\bar{\rho}_{K\pi^0}|^2$ and $|\bar{\rho}_{K^*\pi^0}|^2$. The constraint for a given doubly Cabibbo suppressed mode is modified to

$$\mu_s = 2\mu_{D\bar{D}}|\bar{\rho}_{K\pi\pi}|^2 \beta_{CAD} \tan^4\theta_c \sum_i \beta_i \eta_{si}$$

where β_{CAD} is the true branching fraction for the corresponding Cabibbo Allowed mode.

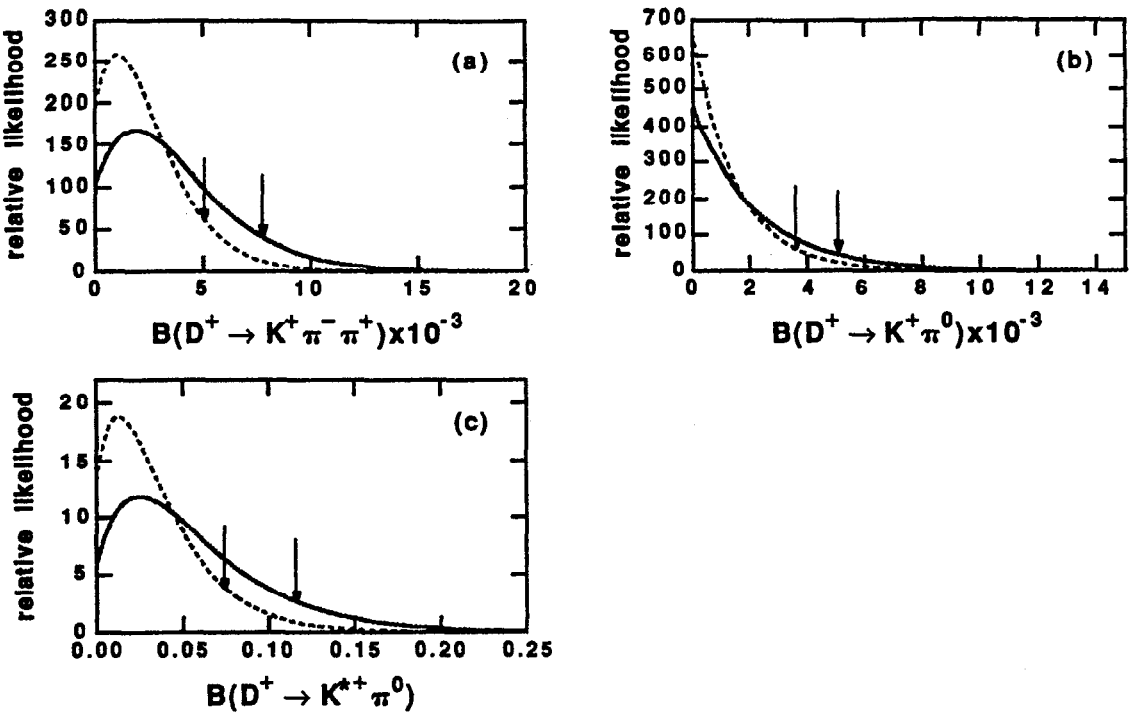

Figure A2.10 The likelihood functions for (a) $B(D^+ \rightarrow K^+\pi^-\pi^+)$, (b) $B(D^+ \rightarrow K^+\pi^0)$ and (c) $B(D^+ \rightarrow K^{*+}\pi^0)$.

Upper Limit for $|\rho_{K\pi\pi}|^2$

Figure A2.10(a) displays the likelihood function for $|\bar{\rho}_{K\pi\pi}|^2$. With systematic errors neglected, $|\bar{\rho}_{K\pi\pi}|^2 < 22.2$. The systematic errors increase this limit to

$$|\bar{\rho}_{K\pi\pi}|^2 < 36.0 \text{ @ } 90\% \text{ CL}$$

Upper Limit for $|\bar{\rho}_{K\pi^0}|^2$

Figure A2.10(b) displays the likelihood function for $|\bar{\rho}_{K\pi^0}|^2$. With systematic errors neglected, $|\bar{\rho}_{K\pi^0}|^2 < 43.2$. The systematic errors increase this limit to

$$|\bar{\rho}_{K\pi^0}|^2 < 68.2 \text{ @ } 90\% \text{ CL}$$

Upper Limit for $|\bar{\rho}_{K^*\pi^0}|^2$

Figure A2.10(c) displays the likelihood function for $|\bar{\rho}_{K^*\pi^0}|^2$. With systematic errors neglected, $|\bar{\rho}_{K^*\pi^0}|^2 < 109$. The systematic errors increase this limit to

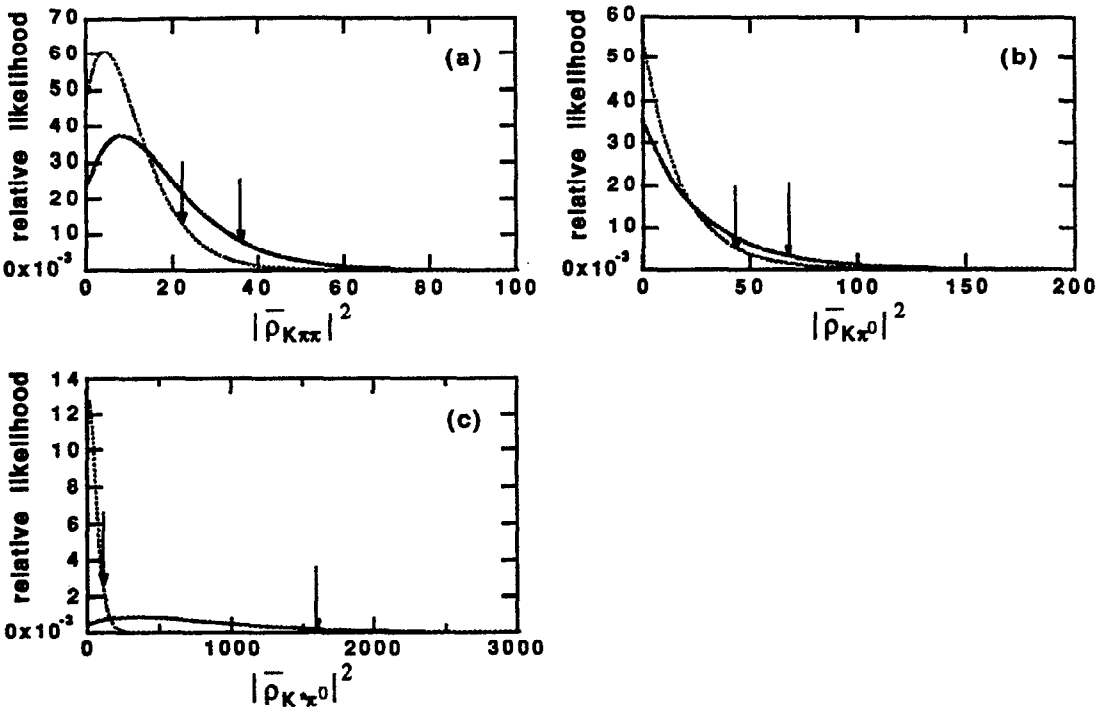

Figure A2.11 The likelihood functions for (a) $|\rho_{K\pi\pi}|^2$, (b) $|\rho_{K\pi^0}|^2$ and (c) $|\rho_{K^*\pi^0}|^2$.

$|\bar{\rho}_{K^*\pi^0}|^2 < 1610$ @ 90% CL

Appendix 3

The SLD Liquid Argon Calorimeter†

A3-1 Introduction

The SLAC Large Detector (SLD)[72], shown in Figure A3.1 and Figure A3.2, is the second high energy physics detector to study the physics of the Z^0 vector boson at the Stanford Linear Collider (SLC) (the Mark II being the first). Designed specifically for the SLC physics program, the SLD is comprised of five major detector subsystems: an inner CCD vertex detector, a conventional wire drift chamber, a Cherenkov Ring Imaging Detector (CRID), a lead liquid argon calorimeter (LAC), and a warm iron calorimeter (WIC).

The LAC and WIC systems provide calorimetry over 95% solid angle with fine segmentation, good energy resolution and uniformity of detector response. Together the two systems are designed to fully contain the energy of a Z^0 hadronic jet, with 85% of the energy in the LAC alone. This chapter discusses the overall design of the LAC, including the readout electronics and data acquisition system.

A3-2 The Design of the LAC

To optimize electromagnetic and pion-electron separation, the LAC has been designed to fit inside the 0.6-λ-thick aluminum solenoid coil. The LAC is divided mechanically into a barrel section, which extends radially from 1.77 meters to 2.91 meters from the beam axis, and two endcap sections, which close the ends of the barrel at ±2.76 meters from the interaction point to ±3.61 meters. Together the barrel and endcaps cover 95% of the solid angle with electromagnetic and hadronic calorimetry.

---

† This appendix largely follows a paper in preparation for publication in Nuclear Instruments and Methods by the Liquid Argon Calorimeter Group in the SLD Collaboration.

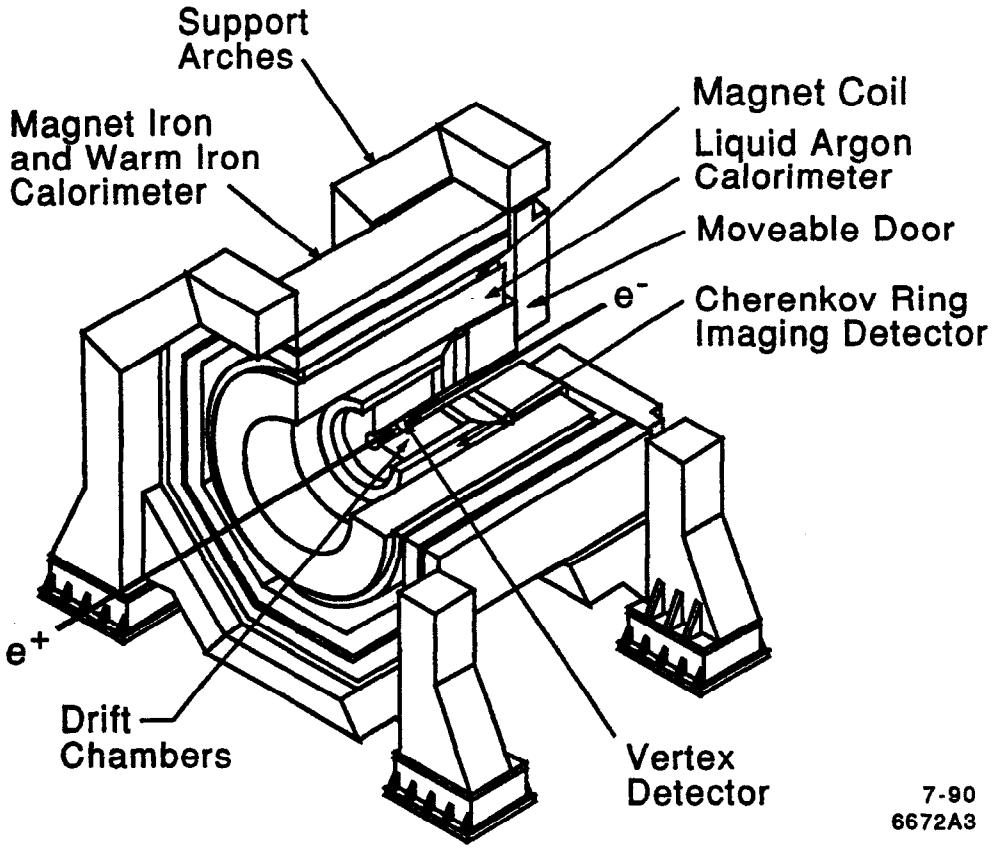

Figure A3.1 Isometric view of the SLD.

A3-2.1 The Lead-Liquid Argon Design

Situating the calorimeter inside the magnet coil was made possible by designing it as a liquid ionization sampling detector. Liquid ionization detectors (LID's) were pioneered in 1974 by Willis and Radeka at Brookhaven.[73] LID's generally consist of high Z material (the radiator) sandwiched between a liquid ionizing medium (the sampling medium). Particle showers develop largely in the high Z material and deposit a fraction of their energy by ionization in the liquid, from which the deposited charge is collected and read out. The advantages of liquid ionization devices are[74]: (1) a liquid sampling medium allows for a compact device; (2) ionization chambers can be finely segmented arbitrarily to provide good position resolution and information on shower development; (3) sensitivity is uniform over the whole detector volume; (4) simple high-precision charge-sensitivity calibration is possible; (5) calibration is stable.

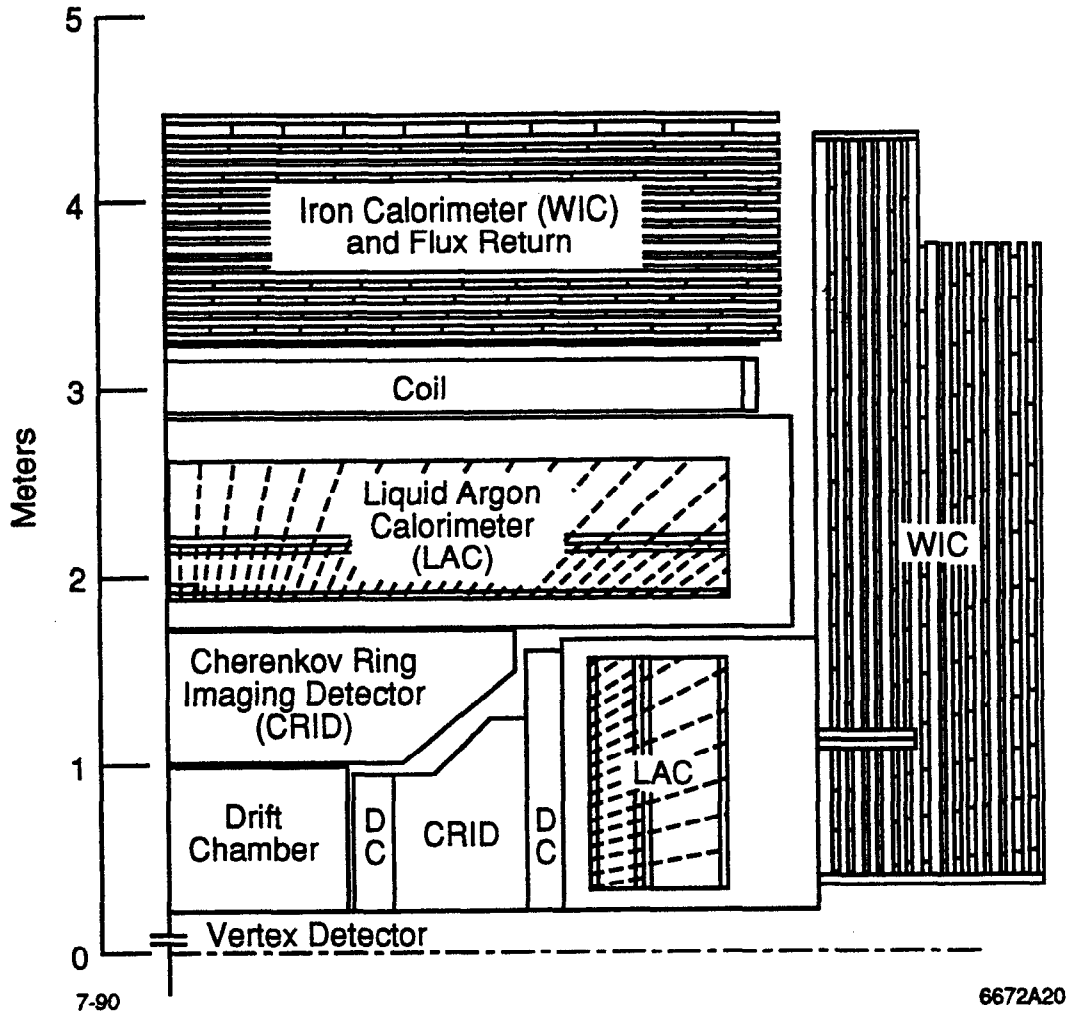

Figure A3.2 Sectional view of the SLD

The sampling medium chosen for the LAC is liquid argon. Several properties make liquid argon a good material for the liquid sampling medium: (1) it is chemically inert; (2) it is dense ($1.4\,g/cm^2$) and radiation resistant; and (3) it does not attach electrons. The disadvantage with liquid argon is that it must be maintained in a liquid state and, therefore must be contained in a dewar insulated at the liquid argon temperature of 86°K and at a few psi in pressure.

The choice of radiator was made with the design goals for an electromagnetic energy resolution of $8\%/\sqrt{E}$ and for the best hadronic resolution obtainable within approximately three interaction lengths. A series of prototype tests[75] were performed to find the

Table A3.1 Results of the energy resolutions on the four prototype devices as determined from test beams of 11 GeV/c and from the Oak Ridge Calor simulation (HETC/EGS/MORSE).

Test Devices	σ_π / E_π (data)	σ_π / E_π (Monte Carlo)	e/h (data)	e/h (Monte Carlo)
Pb	0.187	0.21	1.24	1.28
U-Fe-G10	0.184	0.19	1.26	1.27
U-Pb	0.214	0.20	1.17	1.30
U-U	0.182	0.18	1.10	1.14

best high Z radiator material and sampling dimensions. The performance of four prototype devices were studied at SLAC with 3 to 11 GeV/c electron and pion test beams, where emphasis was placed on the issues of compensation, energy resolution and e/π response. The radiator material used in the prototypes and a comparison of the test results with detailed Monte Carlo simulations are given in Table A3.1. Based on CERN studies by Willis and Fabjan on uranium-scintillater devices,[76] the original intention was to use a mixture of lead and uranium for the radiator in the LAC. It was hypothesized that, with uranium, energy normally lost to nuclear breakup can be "compensated" by the presence of nuclear fission products redepositing energy in the sensitive medium; the detection of otherwise lost neutrons amplifies the signal for hadronic showers. However the results from both the simulation and beam tests show that the U-Pb radiator does not perform significantly better than pure lead. The simulation tests suggested that compensation with uranium only works effectively with scintillating devices, where the presence of hydrogen allows fission neutron energy to be efficiently converted to measurable ionization by elastic scattering reactions. Similar processes are not available in liquid argon. The other aspect of "compensated" calorimetry is suppression of the electromagnetic shower fluctuations in a hadronic shower. High Z materials are best suited for this as well. These studies and test results therefore prompted the choice of lead for the LAC radiator.

Table A3.2 The longitudinal structure of the LAC. An EM cell is defined as: 2.0mm Pb, 2.75mm Ar, 2.0mm Pb, 2.75mm Ar; a HAD cell is defined as: 6.0mm Pb, 2.75mm Ar, 2.0mm Pb, 2.75mm Ar

Barrel and Endcaps	χ_0 per cell	λ per cell	Number of cells	Integral χ_0	Integral λ
EM Section 1	0.75	0.030	8	6.0	0.24
EM Section 2	0.75	0.030	20	21.0	0.84
HAD Section 1	-	0.077	13	-	1.84
HAD Section 2	-	0.077	13	-	2.84

A3-2.2 The Tower Design

The LAC provides approximately 21 radiations lengths (χ_0) of electromagnetic calorimetry and 3 interaction lengths (λ) of hadronic calorimetry. In both the barrel and endcaps the radiator-sampling structures of the electromagnetic (EM) and hadronic (HAD) sections are similar. In the EM sections, planes of 2mm thick lead sheets are alternated with smaller, 2mm thick lead tiles. The sheets and tiles are separated by 2.75mm gaps, which provide the volume for the liquid argon. Connected electrically in parallel, the lead tiles define a tower geometry that projects to the interaction point (see Figure A3.2). For the HAD section, the tower structure is longitudinally the same as that for the EM, except for an increase to 6mm in the tile and plate thicknesses. Both EM and HAD sections are subdivided in depth to supply information on longitudinal shower development. These subdivisions are referred to as EM1, EM2, HAD1 and HAD2. Table A3.2 details the longitudinal structure of the towers. The EM section has a sampling fraction of about 18% of the deposited energy and an expected intrinsic energy resolution of about $8\%/\sqrt{E}$. The HAD section has about a 7% sampling fraction and, when combined with the WIC, is expected to achieve an average resolution of about $60\%/\sqrt{E}$. The readout structure of the towers is discussed in Section A3-2.6.

Towers are segmented transversely to provide a constant projective area with respect to the interaction point. This scheme was chosen so that the energy collected would be the same for each tower, providing z-independent resolutions in shower position. The barrel is segmented azimuthally into 192 electromagnetic towers, with opening angle $\delta\phi =$ 33mr, and 96 hadronic towers, with opening angle $\delta\phi = 66$mr. In the polar angle, 78 divisions in the barrel electromagnetic section vary in angular size to provide constant projected area; the opening angle decreases from $\delta\theta = 36$mr at $\theta = 90^0$ to $\delta\theta = 18$mr at $\theta \approx \pm 35^0$ at the ends of the barrel. In the hadronic section, tower opening angles are twice as large. In the endcaps the azimuth is divided into 192 segments at the outer radius, but the segmentation decreases to 96 and then to 48 at smaller radii to maintain an approximate constant projective area. Seventeen segments in θ continue the constant area projection down to 8^0.

A3-2.3 The LAC Modules

Assembly and testing of the calorimeter was simplified by constructing it in subunits or modules. The division of the barrel is three modules in z (one central module and two end modules) by two modules, radially (one EM and one HAD module) by 48 modules in ϕ. The endcaps are each divided into 16 modules in ϕ, with the EM and HAD sections together in each module. Table A3.3 summarizes the number of modules and towers for all parts of the LAC.

Figure A3.3 shows the general designs of the barrel EM and HAD modules. An EM module has an aluminum base plate at the inner surface followed by the alternating layers of lead tiles and plates. Plastic spacers separate the plates and tiles. After the last plate is a copper clad G10 PC board, which provides the passive elements for carrying charge from the module towers to the front-end electronics (Section A3-2.6). On top of the PC board is an aluminum plate with regions cut out to provide space for the PC board circuit components. Stainless steel bands, 1.25 cm wide, strap the assembly together. The

Table A3.3 Module and tower counts for the LAC

Barrel and Endcaps	Number of Modules	EM1 Channels per Module	EM2 Channels per Module	HAD1 Channels per Module	HAD2 Channels per Module	Sum
Central Barrel	48	112	112	24	24	13056
End Barrel	96	84	80	20	18	19392
Total Barrel	288	13440	13056	3072	2880	32448
EndCap	16	117	105	27	21	4320
Total Endcaps	32	3744	3360	864	672	8640

tension is distributed throughout the stack by spring bars on the aluminum plate above the PC board and by the plastic spacers throughout the stack.

The structure of a barrel hadronic module is similar. Starting from the outer surface, an aluminum strongback is followed by a PC board, then alternating layers of tiles and planes separated by spacers. Stainless steel bands strap the stack together.

Figure A3.4 shows the general design of the LAC endcap modules. These modules contain both the EM and HAD radiator structures. An endcap module begins at the outer z surface with an aluminum strongback, referred to as the "shoe". Alternating layers of lead tiles and plates follow, and a 1/4″ thick aluminum "top plate" ends the structure at the inner surface. Located after each of the four longitudinal readout sections, EM1, EM2, HAD1, and HAD2, are the endcap PC boards. The entire assembly is strapped together by steel bands. At the inner and outer radial surfaces, two straight aluminum support bars align the tiles and plates along Z.

A3-2.4 The Mechanical Support Structures

To maintain the liquid argon temperature of 86 °K, the barrel and endcap calorimeters are housed in separate dewars consisting of an inner argon vessel and an outer vacuum

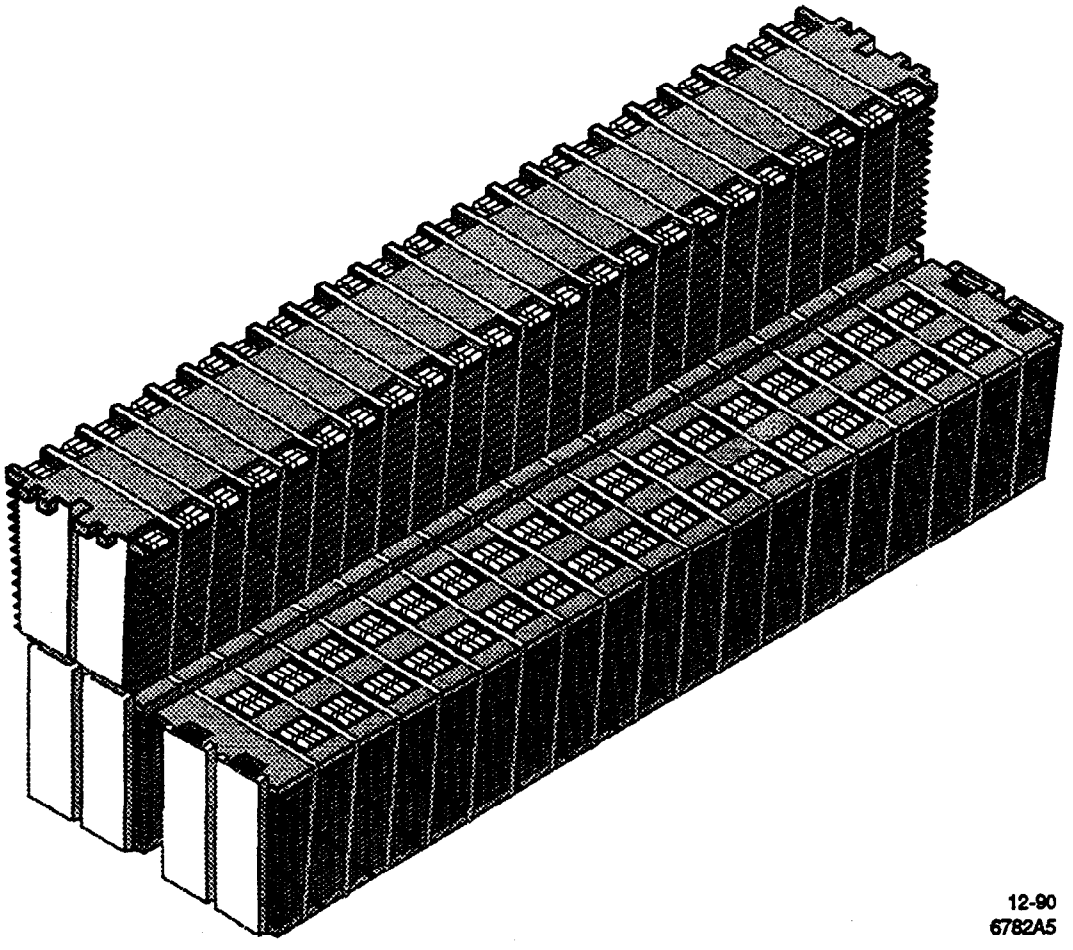

Figure A3.3 The barrel LAC modules.

vessel. Both vessels are constructed from aluminum. The argon vessel contains and supports the liquid argon and lead radiator structure (a total of ~750 tons), while the vacuum vessel provides the insulation. The vacuum vessel is designed to handle not only the normal vacuum load but also the weight of the liquid argon in the event of a spill from the inner vessel. The barrel dewar is suspended at the ends by slings from the support arches of the SLD, while the endcap dewars are mounted to the detector end-doors.

The barrel argon vessel, about eight meters long, is divided in three equal sections along Z: one central and two end sections. The sections are separated by two aluminum annular rings, or washers, which are welded to the inner wall of the argon vessel. These washers serve as stiffeners for the vessel and mounting supports for the barrel modules

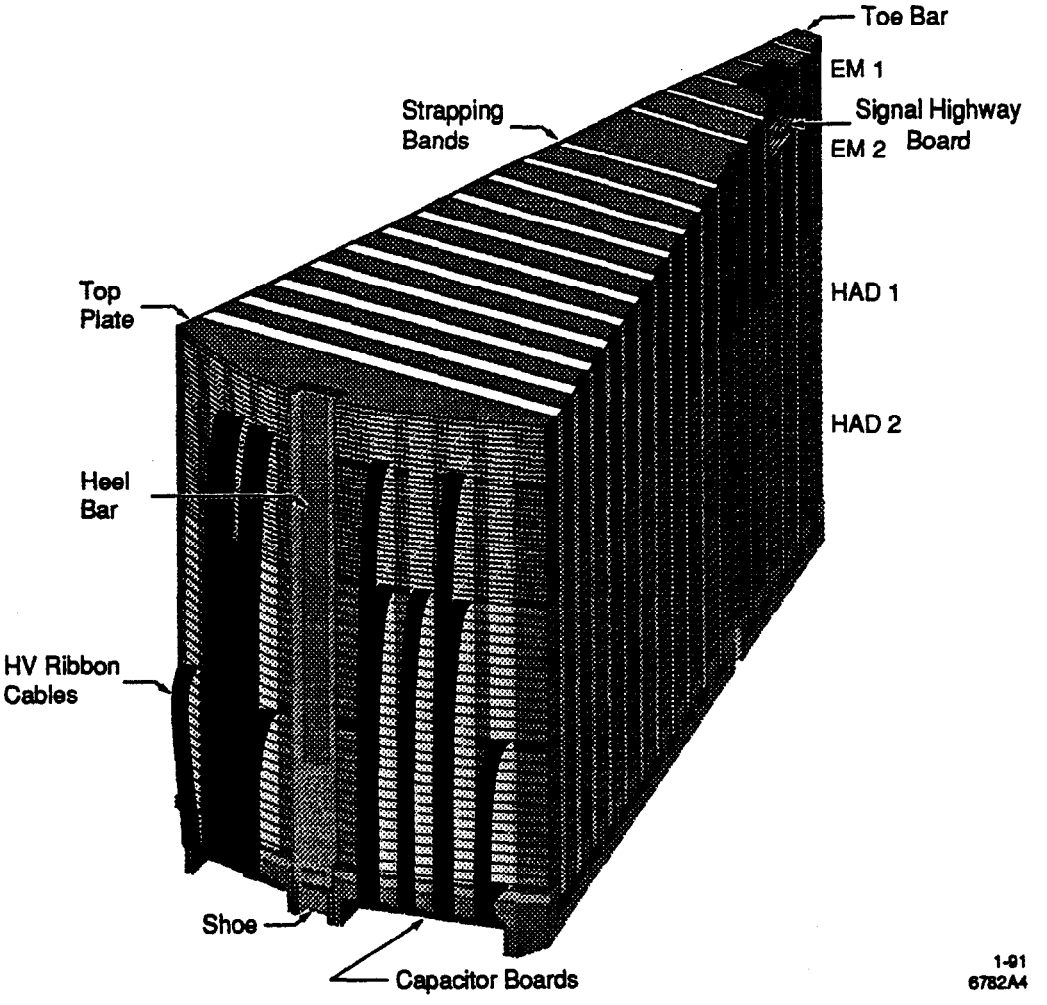

Figure A3.4 The endcap LAC modules.

described above. On the washers and the vessel endplates are equally spaced radially oriented guide rails which aligned the modules during insertion and provide some of the support. The electromagnetic modules are bolted by their endplates to the washers and dewar walls. Each electromagnetic module is also fastened to the inner vessel wall by a bolt at the center of its base plate. The hadronic modules are bolted to the washers and dewar endplates by finger on the strongbacks which extend over the outer edges of the washers and endplates.

The endcap argon vessels can be thinned by the additional support provided by sixteen, 2cm aluminum rods arranged azimuthally. The rods tie the inner and outer faces

of the vessel, together. The endcap modules themselves are doweled inside the argon vessel, to carry the shear load.

A3-2.5 The Cryogenic System

The refrigerant for the LAC is liquid nitrogen. A detailed schematic of the cryogenic system is shown in Figure A3.5. The barrel and endcap sections form three distinct units to facilitate the control and distribution. Separate distribution systems are provided for the liquid argon and the liquid nitrogen.

The outer argon vessel wall of the barrel contains 60 KW ceramic heaters and 11 series of tubes and manifolds for the LN_2 cooling system. The cryogenic lines for the liquid argon penetrate the barrel vacuum vessel radially at the ends of the cylinder and continue into the argon vessel through the endplates. In the endcaps the lines penetrate the vessels through the backplates.

The argon distribution system consists of a 50,000 liter storage dewar with an associated liquid nitrogen condenser system for temperature and pressure regulation. A smaller 300 liter tank (the Argon Head Tank in Figure A3.5) supplies the detector with a reference pressure for the gas phase of the argon.

The nitrogen distribution system consists of a 100,000 liter storage dewar, which supplies LN_2 to the cooling loops welded to the outside surface of the argon vessels. The temperature of the LN_2 in the loops is regulated by the nitrogen pressure via liquid hydrostatic head or exhaust valve back pressure.

The process of cooling down the LAC involves injecting cold liquid nitrogen into the argon vessel cooling loops while also having the argon volume filled with helium gas to provide good heat transfer. To minimize thermal stresses, the nitrogen is pulsed through the loops every fifteen minutes and allowed to vaporize.From room temperature, cooling typically takes seven days to reach 100°K. The helium is then pumped out, and argon gas is introduced. The condensation and vaporization of the gas further cools the internal

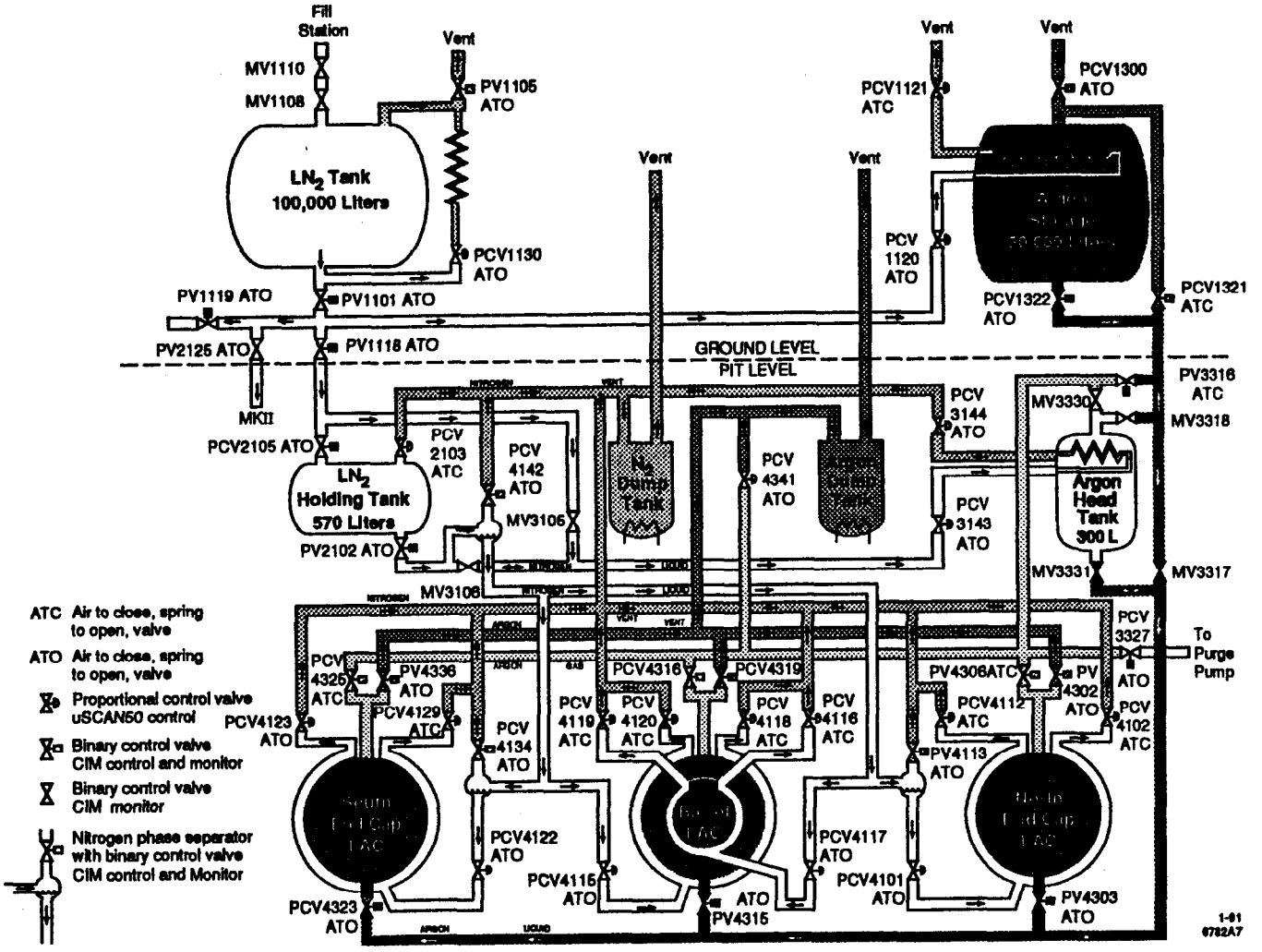

Figure A3.5 Schematic of the LAC cryogenic system.

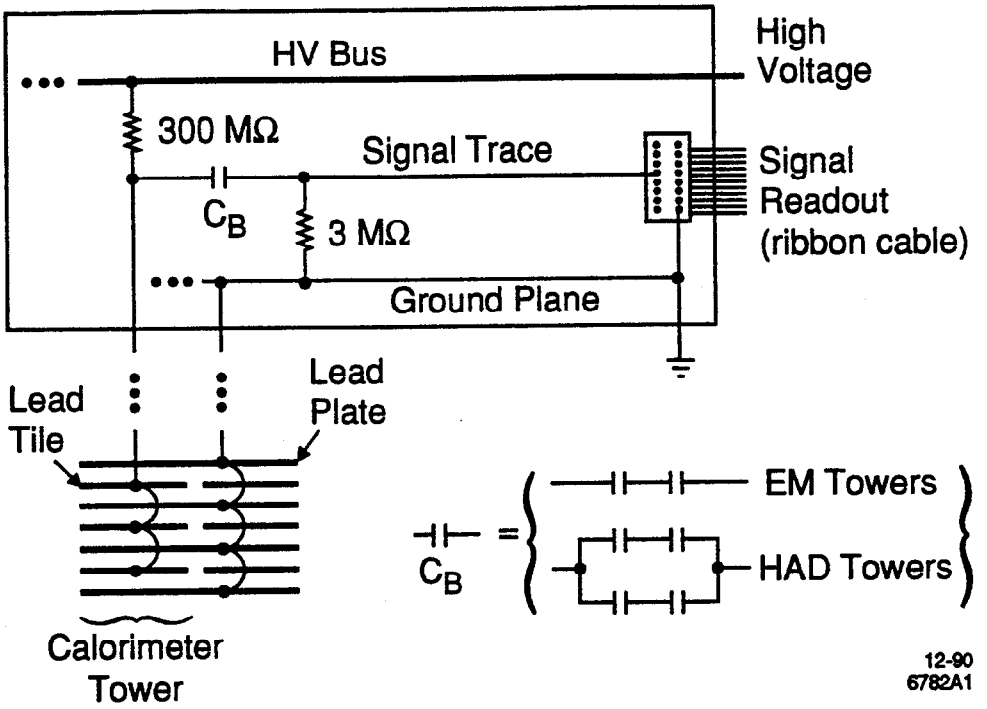

Figure A3.6 The circuit of a signal highway board for a LAC module.

structure down to ~86°K. When the liquid argon temperature has been reached, the vessel is filled with the liquid argon, and the cooling loops are filled less frequently with the liquid nitrogen. Refrigeration is then ideally maintained by the removal of heat through the vaporization of the liquid nitrogen. The total thermal load is approximately 1000 watts.

A3-2.6 Electrical Interconnections

Signal Connections

In the barrel, EM tower tiles are ganged together electrically by printed traces on a Kapton substrate, with pigtail wires soldered between the tiles and the traces. The traces carry the signals up the sides of the tower to the PC signal highway boards. The HAD towers are wired directly.

The basic circuit of the PC signal highway boards is shown in Figure A3.6. These boards transfer the signal from a LAC tower to the cabling which leads to the front-end electronics outside the cryostat. A highway board has a high voltage bus which provides

the towers with the 1.5KV DC bias voltage. A board also has traces to transfer the signal from each connected tower to the teflon ribbon cables which carry the signal to the frontend electronics. The signal traces are ac coupled to the frontend preamps by a set of two or four blocking capacitors. These capacitors isolate the preamps from the high voltage, which gets applied to the tower tiles. The capacitors have values ranging from 1.5nf to 28nf to provide at least four times the tower capacitance at 86°K. Each trace also has a 300MΩ high voltage resistor and a 3MΩ bleeder resistor.

From the PC board the signals are transported by 26 and 34 conductor PTFE Teflon ribbon cables with alternating signal and ground wires. The cables run along the top of the module to printed adapter circuit boards ("transition boards"), which are mounted to flanges on the inner wall of the dewar endplates. The transition boards transfer the signals outside the dewar via 55-pin connectors plugged into hermetic feedthroughs in the flanges on the dewar walls. Through the vacuum space between the inner argon vessel and the outer vacuum vessel, the signals are carried by 1m of 0.0126 Nickel Alloy 180 wire with polyurethane coating. These wires are connected to D-style feedthroughs which transfer the signals directly to the front-end electronics mounted on the opposite side of the wall.

In the endcaps, tower tiles are connected via a wire that runs perpendicular through the tiles and ground planes. The wires are soldered to the tiles but insulated from the ground planes by nylon insulators. These wires transfer the tower signals to the signal highway boards, which are functionally the same as the barrel highway boards. Beldon Teflon ribbon cables carry the signals from the highway boards to transition boards located on flanges on the dewar wall next to the shoe. The transition boards route the signals to 55-pin connectors plugged into feedthroughs in the flanges on the argon wall. The balance of the signal path is the same as that for the barrel.

High Voltage Connections

In the barrel and endcaps, a two layer composite of Teflon-insulated wire is used to transfer high voltage to the towers through the vacuum space and the argon. The high voltage is transferred through additional feedthroughs in the vacuum and argon dewars and is distributed to the towers via the signal highway boards. In the barrel, one HV line supplies high voltage to $2\times(1\frac{1}{2}$ modules) while in the endcaps, one line supplies high voltage to two. To prevent total module failures, connections inside the argon are made redundant.

The Argon and Vacuum Flanges

In the barrel the argon and vacuum vessel endplates have 24 flanges, each containing fifteen feedthroughs for the electrical signals, two feedthroughs for the high voltage and one feedthrough for thermocouple and RTD instrumentation--a total of 18 feedthroughs. Signals from the central modules are divided in half between the opposite ends of the detector, so each flange serves effectively 6 modules--two end electromagnetic, two end hadronic, two half central electromagnetic and two half central hadronic. The 12" argon flanges are made of the same aluminum alloy as the vessel, while the 16" vacuum flanges are made from stainless steel.

In the endcaps the vessel backplates have 16 flanges, 6" in diameter. The endcap flanges contain only four feedthroughs each but are grouped in units of four to correspond functionally to a barrel flange.

A3-3 The LAC Front-end Electronics

This section discusses the architecture of the electronics which receives the signals from the LAC towers and performs the initial on-line data processing. Also described are results from performance tests of the electronics in the lab and on the detector.

Table A3.4 Tower capacitances and preamplifier electronic noise values.

	Tower Capacitance		Electronic Noise		Minimum Ionizing Signal	S/N Minimum Ionizing	
	C_{min} (pF)	C_{max} (pF)	C_{min} (e^-)	C_{max} (e^-)	(e^-)	C_{min}	C_{max}
EM1	250	450	3000	3200	150000	50	48
EM2	1000	1800	3900	5400	450000	117	84
HAD1	3200	4900	8500	12500	300000	35	24
HAD2	4400	6300	11300	16000	300000	27	19

A3-3.1 The Architecture of the Front-end Electronics

General Considerations

Because the liquid argon medium provides no gain, the charge signals from the towers must be amplified. Amplification, however, introduces electronic noise which can effect the energy measurement resolution. Conventionally,[73][74] the signal-to-noise ratio (S/N) is improved by introducing an n:1 transformer which matches amplifier input capacitance to tower capacitance. The noise in such devices goes as $\sqrt{c_d}$, and S/N improves by a factor of 1/n. Disadvantages in using transformers, however, are: (1) they are large and expensive; (2) they can also contribute noise; and (3) they cannot operate in a magnetic field, therefore requiring more cabling which can lead to additional capacitance and noise. Since tower capacitances are small, it was therefore decided not to use transformers in the preamplification circuits for the LAC. Sufficient S/N values were obtained with charge sensitive preamplifiers providing 0.1V/pC gain. Table A3.4 summarizes the capacitance of eight different calorimeter towers and the associated noise.

The LAC electronics contain some unique architectural designs features. Without transformers the electronics are able to be mounted directly onto dewar and operate within the magnetic field, avoiding the problem of extra cabling. The control and readout signals are multiplexed, further reducing cabling requirements. The preamplifiers are turned off

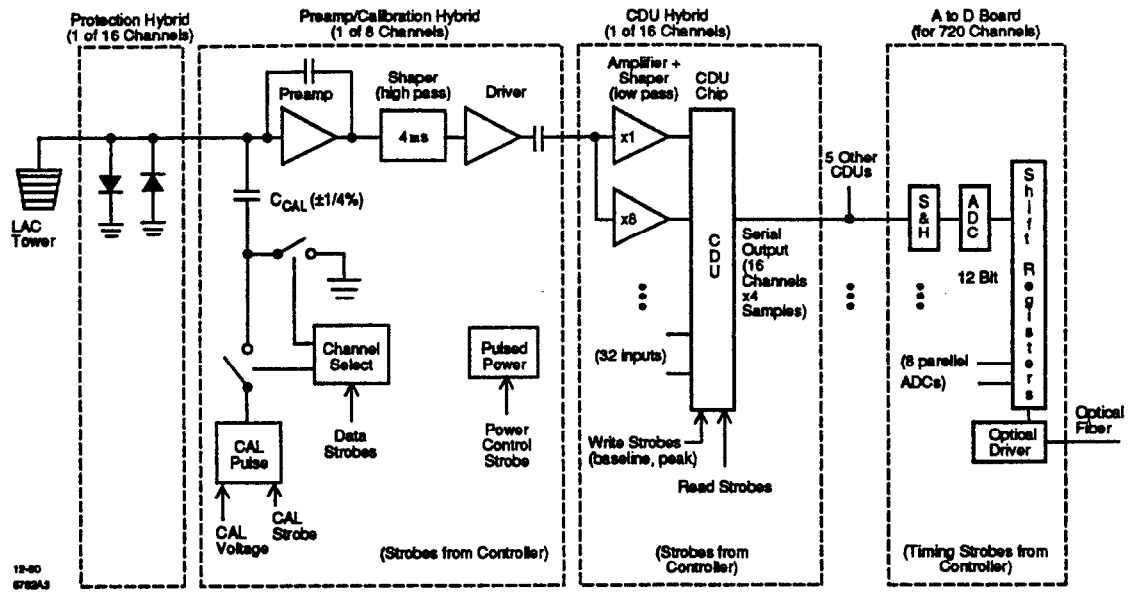

Figure A3.7 Block diagram of the LAC front-end electronics.

between the long (8.3 ms) beam-crossings to reduce power consumption. The data is converted from electronic to optical after the digitization.

Figure A3.7 lays out a simple block diagram of the electronics. Processing of a signal pulse involves preamplification, shaping, dual gain post-amplification, sampling and storage, digitization, serialization, and optical conversion for readout.

The Tophats

The front-end electronics are installed directly on the feedthroughs of the vacuum vessel flanges in units referred to as "tophats". A barrel tophat consists of a printed circuited mother board enclosed in a aluminum cylinder, 41 cm in diameter, 13 cm in height. The enclosure provides mechanical protection and electrical shielding for the various components and also acts as a heat sink with chilled water circulated through tubing around the base. The endcap tophats are mechanically different due to the differing flange arrangement, but they are functionally identical to the barrel tophats. There are a total of 48 tophats on the barrel (one per flange) and 8 tophats on each endcap (one per flange group). Barrel tophats process a total of 720 channels while the endcap tophats process 576.

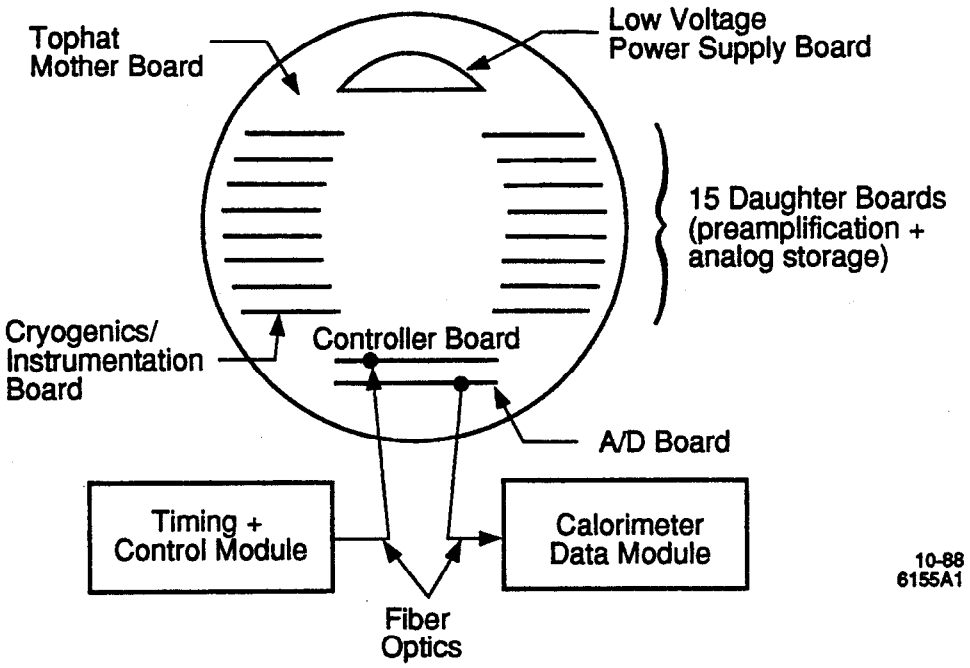

Figure A3.8 Layout of the electronics for a LAC tophat.

Figure A3.8 shows the layout of the electronics in a barrel tophat. Each tophat contains: (1) a controller board; (2) a power supply board; (3) a cryogenics/monitor board; (4) an analogue-to-digital (A/D) board; and (5) 15 daughterboards. The description of these components follows.

The Controller Board

This board regulates the operations of the various components of the tophat. It interprets and executes commands received from a Fastbus Timing and Control Module (refer to Section A3-4). The commands, for example, specify the run mode (normal or calibration) or a DAC voltage for calibration. The controller board also receives and distributes timing signals for the various tophat components.

The Cryogenics/Monitor Board

This board extracts various status parameters of the calorimeter and tophat components, including power supply voltages and currents, temperatures and liquid levels inside

the cryostat (via the instrumentation feedthroughs on the dewar), and daughterboard temperatures.

The Power Supply Board

This board regulates the voltage to the preamplifiers, which are turned on and off between beam-crossings. An external power supply provides the board with only an average current, while local capacitors store the electrical energy. This scheme lowers cable costs and reduces power consumption from approximately 500 W to 60 W per tophat.

The Daughter Boards

The daughterboards perform the primary functions for analogue processing the data. They contain three types of custom circuit hybrids: three 16-channel input protection hybrids, six 8-channel preamplifier and calibration hybrids, and three 16-channel analog storage and multiplexing hybrids.

The Preamplifier Hybrids: These hybrids provide the circuitry for amplifying and pulse shaping the charge signals. The preamplifiers used are low noise, Hitachi 2SK190 field-effect transistors. Ringing (in the LC circuit arising from the tower capacitance in series with the inductance from the lead wires) is damped by a feedback scheme called an 'electronically cooled resistor'.[77]

Unipolar pulse shaping in the preamplifier hybrid channels is performed by a CR high pass filter followed by an RC low pass filter. Since the collision rate of the SLC is only 120 Hz, bipolar shaping was deemed unnecessary. A shaping time of 4 μs was chosen to optimize the signal-to-noise ratio for the second electromagnetic section, which has the best intrinsic resolution.

Each preamplifier hybrid also contains a circuit for calibrating the electronics. A reference voltage specified by a 12-bit 0-2.5 volt DAC on the tophat controller board, is switched onto a calibration capacitor on the preamp which converts the voltage into the charge that gets injected into the preamplifier inputs. The calibration capacitors have been

laser-trimmed to provide a 0.25% accuracy in the injected charge. More than one channel can be calibrated at a time, the group of channels being specified by the controller board.

As mentioned above, to reduce power consumption the amplifiers are powered down between beam crossings. Out of the 8.3ms beam-crossing time, approximately one millisecond is required to power up and stabilize the electronics before the beams collide.

Input Protection Hybrids: The inputs to the FET's on the preamps are protected against large current spikes which might occur from high voltage breakdown in the LAC towers or blocking capacitors. This protection is provided by two stages of diode pairs to ground. The first stage diodes are packaged in a custom hybrid separate from the preamp hybrid and are designed to handle almost 200 amperes for several microseconds. They absorb most of the energy, while the remainder is absorbed by the second stage diodes, which are incorporated into the preamplification hybrids. High current, low noise diodes had to be selected.

CDU Hybrids: Signals are amplified further and then sampled in the 16 channel CDU hybrids. Each signal is split into a pair of post-amplifiers which provide gains of ×1 and ×8. The two amplified signals are then sampled twice to obtain a measurement at the baseline and at the signal peak. One input signal therefore yields four measurements, or data "buckets". Sampling for the 16×2 channels is performed in parallel by a custom integrated circuit, the Calorimeter Data Unit (CDU). Sampling times for the baseline and signal are specified by clock signals from the tophat controller board. Sampled signals are stored in analogue form in capacitors in the CDU until the controller board specifies the readout command and generates the clocking pulses. The 64 analogue outputs are then delivered to a serial data stream of 1.6μs intervals.

The A/D Board

The analogue signals out of the daughter boards are digitized by the tophat A/D board. The CDU output is digitized by a 3.2μs per conversion 12-bit CMOS A/D

converter. After digitization, a parity bit and three framing bits are added to produce a 16-bit data word.The A/D board has eight channels for parallel processing, with each channel servicing two daughterboards. The converted data from the eight channels are loaded into a chain of parallel/serial shift registers, which are clocked at 32 MHz by pulses from the controller board. The serial bit stream is then converted into a series of light pulses by an optical driver, and the optical data is sent to the Fastbus data acquisition system over optical fibers. For redundancy, each A/D board has two drivers; only one, however, is read out.

In terms of ADC counts the gain of the electronics is 1400 ADC counts/8.4pC at low gain, and 7.6 times that at high gain. One ADC count at high gain is therefore about 5000 electrons.

A3-3.2 Performance of the LAC Frontend Electronics

Using the internal calibration circuits, tests were performed in the lab[78] to study linearity, gain, noise and crosstalk in the frontend electronics. The results of the tests are shown in Figure A3.9 through Figure A3.12. The gain is linear over the entire signal range, with residuals from a straight line fit under 1% at the high end and 1 ADC count at the low end. The noise is a linear function of input capacitance with a slope of 2600 e^-/nF and an offset of about 2500 e^-; the non-zero offset is the intrinsic noise of the readout system from preamplification to digitization, and it corresponds to approximately 0.8 ADC counts. Crosstalk measurements, performed by pulsing one tophat channel and recording the response from all 720 channels, found less than 0.6% crosstalk between neighboring channels within a preamplifier hybrid and negligible crosstalk between daughterboards. (Crosstalk in the detector, however, is significant due to the capacitive coupling between neighboring towers.)

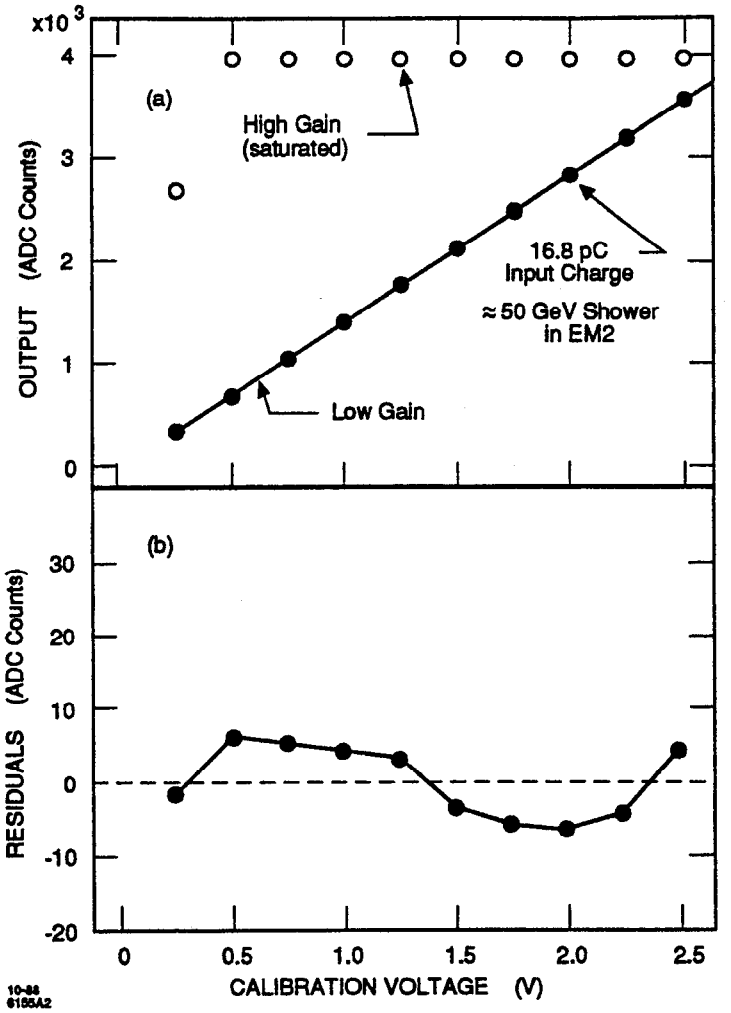

Figure A3.9 (a) Response of the electronics to large calibration voltages. A 2 V pulse corresponds to the largest signal expected in the LAC. (b) The residuals from a least squares fit of the low gain response.

A3-4 The Fastbus Data Acquisition System

Online data acquisition for the SLD is based on Fastbus with an 8800 VAX serving as the host computer. The organization of the full SLD system is shown in Figure A3.13, and the organization of the LAC part is shown in Figure A3.14. The LAC Fastbus system requires only three types of modules (other than the standard system interconnect and system extender modules): 32 Calorimeter Data Modules (CDM's), one Timing and Control Module (TCM)[79] and one Aleph Event Builder (AEB).[80] This section discusses the designs and functions of these modules and the data acquisition process for the LAC.

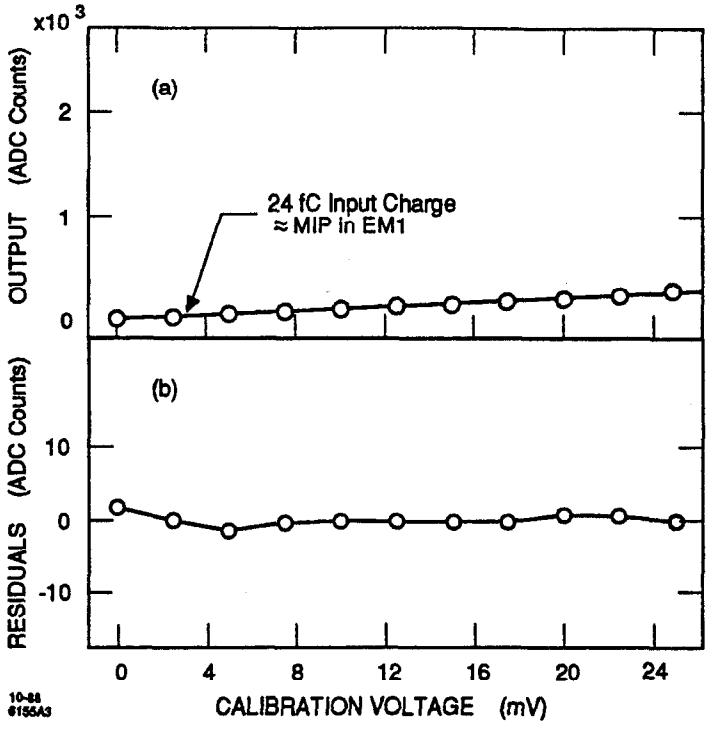

Figure A3.10 (a) Response of the electronics to small calibration voltages. Only the high gain response is shown. A 2.8mV pulse corresponds to the smallest signal expected for a minimum ionizing particle. (b) The residuals from a least squares fit of the high gain response.

A3-4.1 The Calorimeter Data Modules

The CDM's perform the actual function of acquiring and processing the digitized data from the front-end electronics. A block diagram in Figure A3.15 provides a simplified view of the CDM architecture. An auxiliary card in the Fastbus backplane of a CDM receives the optical data, converts the signals from optical to electrical, deserializes and demultiplexes the signals, and deliveries them to the CDM. Each CDM contains four channels for parallel processing data, with two channels for every tophat.

In each CDM channel, the data is processed by a custom chip called the Digital Correction Unit[81] (DCU). In normal data taking mode, the DCU performs the operations of (1) selecting the gain by comparing the raw data with a reference threshold value; (2) calibrating the data by applying a 16 segment piece-wise linear correction; and (3) subtracting the baseline from the signal for the selected gain. The DCU can be also set to a

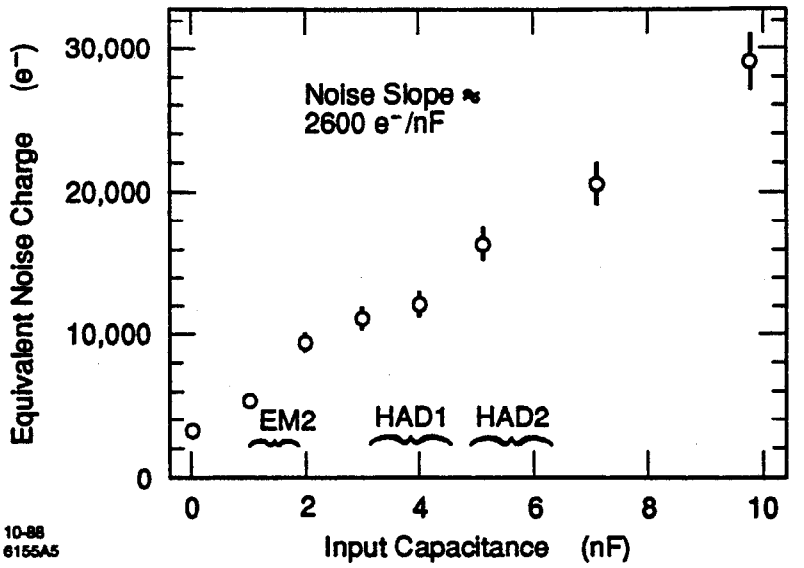

Figure A3.11 The noise as a function of capacitance input to the preamplifier. Indicated are the capacitance ranges in three of the four calorimeter sections.

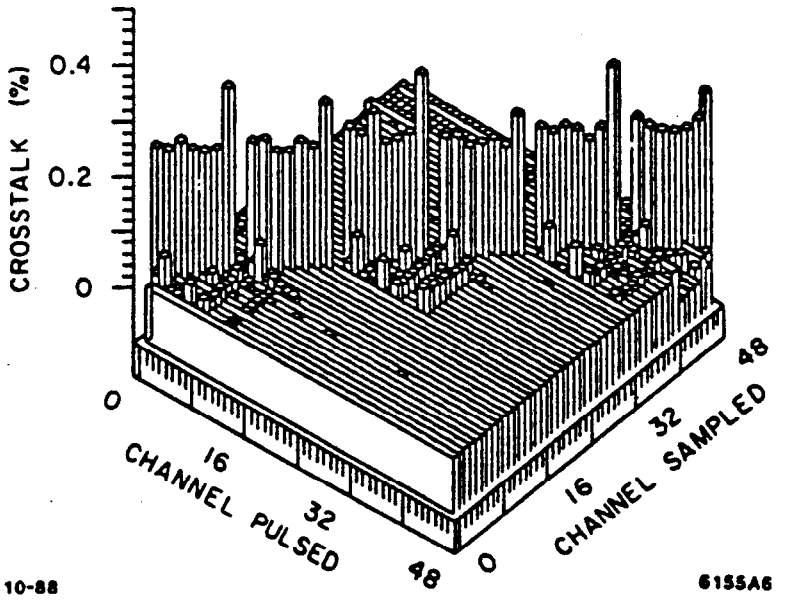

Figure A3.12 Crosstalk within one daughterboard at high gain. The six 8×8 subpatterns correspond to the six preamplifier hybrids (8 channels each) on the daughterboard

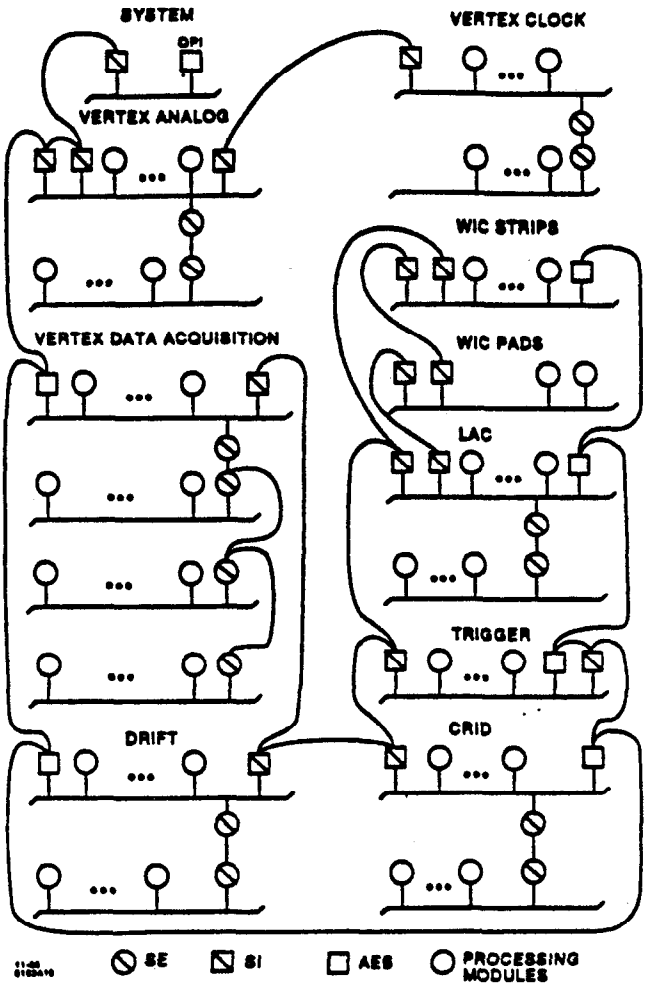

Figure A3.13 The SLD Fastbus system.

"pass-through" mode where all four buckets of information are effectively unprocessed. This mode is required for diagnostics and calibration measurements.

Each CDM channel also contains a Motorola 68020 microprocessor CPU, clocked at 16MHz, for additional analysis of the data from the DCU. Such analysis includes calculating the calibration constants, applying corrections for crosstalk, and various energy sums used in the trigger.

The CDM's contain memory for storing processed data and the calibration constants used by the DCU.

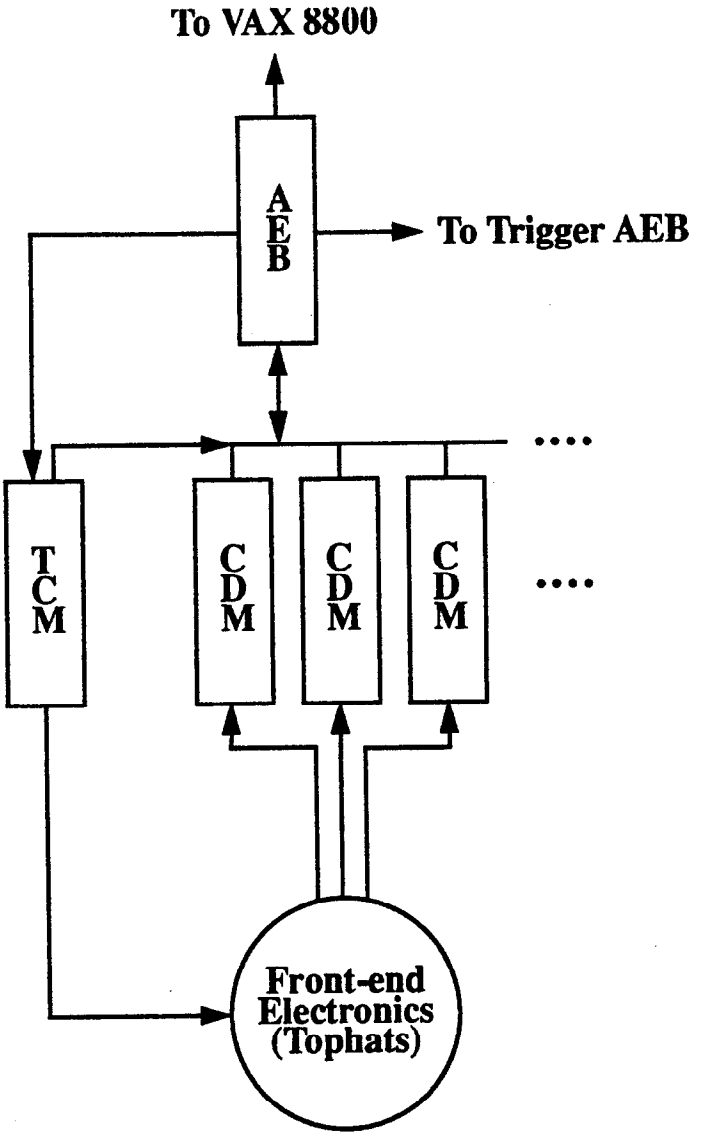

Figure A3.14 Schematic of the LAC Fastbus system.

A3-4.2 The Timing and Control Modules

The TCM performs two major functions: (1) it provides slow (32MHz) timing signals for the frontend electronics and the CDM modules and (2) it transmits command operations to the front-end electronics. The timing signals include the pulses which specify when the preamps should power up or power down, the pulses which specify to the CDU when to sample the baseline and signal, and clock pulses for reading out the CDU sample and hold units. The command operations include those which specify a DAC voltage for

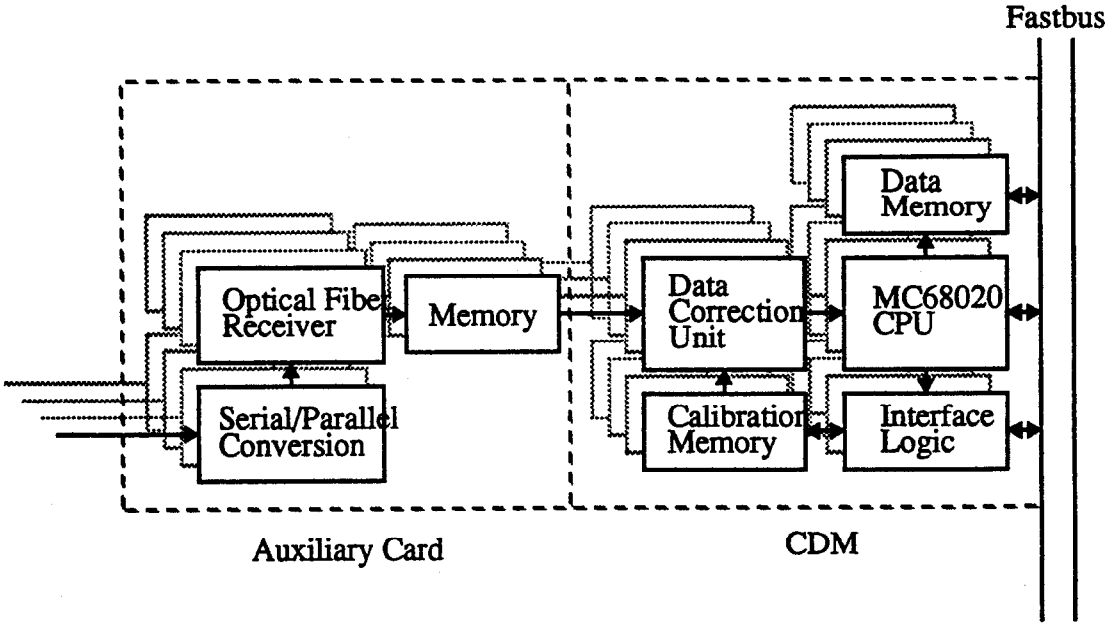

Figure A3.15 Block diagram of the CDM and its auxiliary card.

calibration and the run mode in which the electronics are to operate. The TCM synchronizes all timing and command signals relative to a signal it receives from the SLC approximately 1 ms prior to a collision.

Communication from the TCM is transmitted over two paths. To the CDM's it is transmitted over the Fastbus backplane. To the front-end electronics, specifically to the tophat controller board, it is sent over a standard three-wire SLD protocol which consists of lines referred to as COMMAND, CLOCK, and DATA.

Timing and command sequences are specified and constructed through *sequencer programs*. Software[82] on the host VAX and in the AEB provide routines for constructing a sequencer program and for subsequently downloading a program to the TCM. In the TCM a state machine and various fast timers coordinate the execution of the programs after each beam crossing.

A3-4.3 The Aleph Event Builder

The AEB was designed at CERN for the ALEPH experiment, and adopted for the SLD. It is a general purpose Fastbus computer which serves as a master module to the TCM and CDM slave modules. The CPU in the AEB is also the Motorola 68020 microprocessor (MC68020), but, unlike in the CDM's, a Fastbus coprocessor is included. From the view of the programmer, this coprocessor provides the instructions for various Fastbus operations as simply additional instructions to the set from the MC68020. It also causes Fastbus errors to be viewed as additional MC68020 exceptions, which are handled by the operating system.

The main functions of the AEB are (1) to coordinate and control the operations of the TCM and CDM's and (2) to collect the data from the CDM's and forward them to the VAX.

A3-4.4 The Data Acquisition Run Modes and Online Software

The LAC data acquisition system has four major run modes: (1) normal data acquisition, (2) cosmic data acquisition, (3) calibration and (4) diagnostic testing.

In normal data acquisition mode, the run command and timing signals are sent from the TCM to the tophats as specified from the VAX. Data from the tophats is sent to the CDM's, where the DCU's are set to perform the gain selection, calibration and peak--minus-baseline subtraction. The calibrated data is then further processed in the CDM CPU's to form energy sums for the SLD trigger system. If the trigger accepts the event, threshold cuts are applied to compact the data. The AEB synchronizes the data from all CDM's, appends channel labels and acquisition information, and delivers the event to the VAX.

In cosmic data mode, the configuration and acquisition process is the same except for the TCM pulse which specifies to the CDU chips when to sample the signal peak. In the TCM two internal timers define a 100μs gate or "cosmic window" in which the

front-end electronics await a cosmic trigger. The CDU sample-peak signal is sent if the trigger signal arrives, otherwise a time-out signal is sent after the window closes.

In calibration mode, the electronic channels are injected with reference charges from the preamplifier hybrid calibration system. The DAC voltages are specified from the AEB through a command operation sent from the TCM. The resulting data is analyzed in the CDM's, with the DCU registers set in pass-through mode. Calibration constants are calculated in the CDM and loaded into the CDM calibration memory. Summary statistics are delivered to the VAX for inspection.

In diagnostic test mode, the DCU is again run in pass-through mode. The 1× and 8× peak and baseline raw data are sent directly to the VAX for functionality tests and crosstalk measurements.

References

1. B. J. Bjorken and S. L. Glashow, Phys. Lett. **11**, 255 (1964).
2. S. Weinberg, Phys. Rev. Lett. **19**, 1264 (1967); A. Salam, in *Elementary Particle Theory*, edited by N. Svartholm. (Almquist and Wiksells, 1969)
3. S. L. Glashow, J. Iliopoulos, and L. Maiani, Phys. Rev. **D2**, 1285 (1970).
4. J. J. Aubert *et al.*, Phys. Rev. Lett. **33**, 1404 (1974)
5. J.-E. Augustin *et al.*, Phys. Rev. Lett. **33**, 1406 (1974).
6. G. S. Abrams *et al.*, Phys. Rev. Lett. **33**, 1453 (1974).
7. G. Goldhaber *et al.*, Phys. Rev. Lett. **37**, 255 (1976); I. Peruzzi *et al.*, Phys. Rev. Lett. **37**, 569 (1976); J. E. Wiss *et al.*, Phys. Rev. Lett. **37**, 1531 (1976).
8. Chen *et al.*, Phys. Rev. Lett. **51**, 634 (1983).
9. D. Decamp *et al.*, Phys. Lett. **235B**, 399 (1990); P. Abreu *et al.*, Phys. Lett. **241B**, 435 (1990); B. Adeva *et al.*, Phys. Lett. **237B**, 136 (1990); G. S. Abrams *et al.*, Phys. Rev. Lett. **63**, 2173 (1989); B. Adeva *et al.*, Phys. Lett. **240B**, 497 (1990).
10. D. Hitlin, CALT-68-1722 (1991) and the references therein.
11. G. F. Bertsch *et al.* (Particle Data Group), Phys. Lett. **239B**, 1 (1990).
12. D. Coffman *et al*, Phys. Rev. Lett. **68**, 282 (1992).
13. R. Rückl, *Habilitationsschrift*, Universität München, 1984 (unpublished).
14. Z. Bai *et al*, Phys. Rev. Lett. **65**, 1309 (1990).
15. I. I. Y. Bigi and M. Fukugita, Phys. Lett. **91B**, 121 (1980).
16. H. Albrecht *et al.*, Phys. Lett. **158B**, 525 (1985); C. Bebek *et al.*, Phys.Rev. Lett. **56**, 1893 (1986); R. M. Baltrusaitis *et al.*, Phys. Rev. Lett. **56**, 2136 (1986).
17. J. Donoghue, Phys. Rev. D **33**, 1516 (1986).
18. M. Bauer, B. Stech and M. Wirbel, Z. Phys. C **34**, 103 (1987). The revised values for a_1 and a_2 are from B. Stech, in *Proc. of the Topical Seminar on Heavy Flavors, San Miniato, 1987*, edited by F. L. Navarria. (North-Holland, 1988)
19. J. C. Anjos *et al.*, Phys. Rev. Lett. **62**, 125 (1989); H. Albrecht *et al.*, Phys. Lett. **195B**, 102 (1987); J. C. Anjos *et al.*, Phys. Lett. **223B**, 267 (1989).

20. R. M. Baltrusaitis *et al.* Phys. Rev. Lett. **55**, 150 (1985).

21. G. Altarelli *et al.*, Phys. Lett. **99B**, 141 (1981).

22. J. Adler *et al.* Phys. Lett. **196B**, 107 (1987); Mark III Memorandum 4/87-1 (1987).

23. D. Coffman *et al*, SLAC-PUB-5447 (1991), submitted to Phys. Rev. D. The statistical and systematic errors for $B(D^+ \to K^-\pi^+\pi^+\pi^0)$ have been modified for use in this thesis for the analysis of $D^+ \to K^{*+}\pi^0 \to (K^0\pi^+)\pi^0$ (Chapter 7). In the reference, $B(D^+ \to K^-\pi^+\pi^+\pi^0)$ is derived from a measurement of $\sigma B(D^+ \to K^-\pi^+\pi^+\pi^0)$ and the value for σ_{D^+} given in Reference [24]; the statistical and systematic errors in $B(D^+ \to K^-\pi^+\pi^+\pi^0)$ respectively contain factors from the statistical and systematic errors in σ_{D^+}. The branching fractions reported in Reference [22] are also derived from measurements of σB and the same σ_{D^+}, but the errors from σ_{D^+} have been treated as factors which contribute only to the systematic errors in the branching fractions. To be consistent and to simplify further error propagation, the errors are recalculated for $B(D^+ \to K^-\pi^+\pi^+\pi^0)$ in the same manner.

24. J. Adler *et al.*, Phys. Rev. Lett. **60**, 89 (1988).

25. Z. Bai *et al.* Phys. Rev. Lett. **66**, 1011 (1991).

26. J. C. Anjos *et al.*, Phys. Rev. Lett. **65**, 2630 (1990).

27. A. J. Buras, J.-M. Gérard and R. Rückl, Nucl. Phys.**B262**, 204 (1985).

28. B. Yu. Blok and M. A. Shifman, Yad Fiz. **45**, 211 (1987); **45**, 478 (1987); **45**, 841 (1987); **46**, 1310 (1987) [Sov. J. Nucl. Phys.**45**, 135 (1987); **45**, 301 (1987); **45**, 522 (1987); **46**, 767 (1987)].

29. M. A. Shifman, Int. J. Mod. Phys. A **3**, 2769 (1988).

30. H. Albrecht *et al.*, Phys. Lett. **158B**, 525 (1985). The absolute branching ratio is obtained using $B(D^0 \to \bar{K}^0\pi^+\pi^-) = 6.4\pm0.5\pm1.0\%$ from Reference [22].

31. N. Isgur and M. B. Wise, Phys. Lett. **232B**, 113 (1984); **237B**, 527 (1990); M. Voloshin and M. Shifman, Sov. J. Nucl. Phys. **45**, 292 (1987); **47**, 511 (1988); B. Grinstein, Nucl. Phys. **339B**, 253 (1990); J. D. Bjorken, SLAC-PUB-5362 (1990); H. Georgi, Phys. Lett. **240B**, 447 (1990).

32. J. Donoghue, UMHEP-355 (1991).

33. B. Grinstein, HUTP-91/A028 (1991).

34. I. I. Y. Bigi, in *SLAC Summer Institute on Particle Physics, Stanford, 1987.* edited by E. C. Brennan. (SLAC, 1988)

35. M. Piccolo *et al.*, Phys. Lett. **70B**, 260 (1977).

36. L. L. Chau, Phys. Rep. **95C**, 1 (1983).

37. L. Wolfenstein, Phys. Lett. **164B**, 170 (1985); J. F. Donoghue *et al.*, Phys Rev. **D33**, 179 (1986).

38. I.I. Y. Bigi, in *Proc. of the Beijing Charm Physics Symposium, Beijing, 1987*, edited by M. Ye and T. Huang. (Gordon and Breach, 1987)

39. J. C. Anjos *et al.*, Phys. Rev. Lett. **60**, 1239 (1988).

40. G. Gladding, in *Proc. 5th Int. Conf. on Physics in Collision, Autun, 1985.* edited by B. Aubert and L. Montanet. (Editions Frontieres, 1986); G. Gladding, in *Proc. of the Int. Symposium on Production and Decay of Heavy Flavors, Stanford, 1988*, edited by E. Bloom and A. Fridman. (NY Acad. Sci., 1988).

41. H. Yamamoto, Ph.D. thesis, California Institute of Technology (1985).

42. I. I. Y. Bigi and A. I. Sanda, Phys. Lett. **171B**, 320 (1986).

43. R. Ammar *et al.*, CLNS 91/1058 CLEO 91-2 (1991).

44. D. Bernstein *et al.*, Nucl. Instrum. Methods **226**, 301 (1984).

45. J. Roehrig *et al.*, Nucl. Instrum. Methods **226**, 319 (1984).

46. J. S. Brown *et al.*, Nucl. Instrum. Methods **221**, 503 (1984).

47. W. Toki *et al.*, Nucl. Instrum. Methods **219**, 479 (1984).

48. R. Fabrizio *et al.*, Nucl. Instrum. Methods **227**, 220 (1984).

49. M. Breidenbach *et al.*, IEEE Trans. **NS-25, 1**, 706 (1978).

50. J. J. Thaler *et al.*, IEEE Trans. **NS-30, 1**, 236 (1983).

51. S. Neddermeyer *et al.*, Rev. Sci. Instrum. **18** 488 (1947).

52. M. Burchell, Mark III Memorandum 7/88-4 (1988).

53. J.J. Becker *et al.*, Nucl. Instrum. Methods **A235**, 502 (1985).

54. R. Schindler, Mark III Memorandum, 4 February 1983; D. Hitlin, Mark III Memorandum 6/83-4.

55. S. Wasserbaech, Ph.D. thesis, Stanford U. (1989).

56. L. Parrish, Mark III Memorandum 7/88-4 (1988).

57. R. M. Sternheimer and R. F. Peierls, Phys. Rev. **B11** (1971) 3681.

58. D. Coffman *et al.*, Phys. Lett. **263B**, 135 (1991).

59. T. Sjöstrand, Comput. Phys. Commun. **39**, 347 (1986).

60. J. Izen, Mark III Memorandum 11/86-3 (1986).

61. Professor G. Gladding, University of Illinois at Urbana-Champaign, provided the covariances among the number of produced D^+D^- events and the branching fractions for $D^+ \to \bar{K}^0\pi^+$, $K^-\pi^+\pi^+$, $\bar{K}^0\pi^+\pi^-\pi^+$, and $\bar{K}^0\pi^+\pi^0$.

62. J. Hauser, Ph.D. thesis, California Institute of Technology (1985).

63. J. Adler *et al.* Phys. Rev. Lett. **60**, 1375 (1988).

64. B. B. Rossi, High-Energy Particles (Prentice-Hall, 1952).

65. J. C. Anjos *et al.*, Phys. Rev. Lett. **62**, 1587 (1989).

66. B. Grinstein *et al.*, Phys. Rev. D **39**, 799 (1989).

67. F. J. Gilman and R. L. Singleton, Phys. Rev. D **41**, 142 (1990).

68. J. G. Korner and G. A. Schuler, Z. Phys. C **38**, 511 (1988); **41**, 690 (1989).

69. R. C. Verma and A. N. Kamal, Phys. Rev. D **43**, 829 (1991). This reference gives $B(D^+ \to K^+\pi^0) = 1.9\times\tan^2\theta_c\times B(D^+ \to \bar{K}^0\pi^+)$ and $B(D^+ \to K^{*0}\pi^+) = (0.67\pm0.11)\times10^{-2}\times B(D_s^+ \to \phi\pi^+)$ and the amplitude relations $\sqrt{2}A(D^+ \to K^+\rho^0) = -\tan^2\theta_c\times A(D^0 \to K^{*-}\pi^+)$ and $\sqrt{2}A(D^+ \to K^{*+}\pi^0) = -\tan^2\theta_c\times A(D^0 \to K^-\rho^+)$. The branching fraction predictions are obtained using $B(D^+ \to \bar{K}^0\pi^+) = 3.2\pm0.5\pm0.2\%$ (Reference [24]), $B(D_s^+ \to \phi\pi^+) = 3.3\pm1.1\%$ (provided by CLEO in CLNS 91/1108 CLEO 91-9), $B(D^0 \to K^{*-}\pi^+) = 5.3\pm0.4\pm1.0\%$ (Reference [22]), $B(D^0 \to K^-\rho^+) = 10.8\pm0.4\pm1.7\%$ (Reference [22]) and $\tan\theta_c = 0.2267$. Phase space factors are included in the numbers for $B(D^+ \to K^+\rho^0)$ and $B(D^+ \to K^{*+}\pi^0)$.

70. L. L. Chau, Phys. Rev. D **42**, 1837 (1990).

71. I. I. Y. Bigi, private communication.

72. SLD Design Report, SLAC-273, (1984).

73. W. Willis and V. Radeka, Nucl. Instrum. Methods **120**, 221 (1974).

74. V. Radeka, IEEE **NS-24**, **1** 293 (1977).

75. R. Dubois *et al.*, IEEE **NS-33, 1** 194 (1986).

76. C.W. Fabjan *et al.* Phys. Lett. **60B**, 105 (1975); C. W. Fabjan *et al.*, Nucl. Instrum. Methods **141**, 61 (1977).

77. V. Radeka, IEEE **NS-24, 1** 293 (1977).

78. E. Vella *et al.* IEEE **NS-36, 1** 822 (1989).

79. Jack Hoeflich, University of Illinois, Internal SLD Memorandum.

80. A. Marchioro *et al.*, IEEE **NS-34, 1** 133 (1987); K. Einsweiler *et al.*, IEEE **NS-35, 1** 316 (1988).

81. S. Mackenzie *et al.*, IEEE **NS-34, 1** 250 (1987).

82. J. Labs and M. Huffer, SLD Below Line Documentation BELMAN-15 (1990).